Silica Coated Core-Shell Quantum Dot-based Electro-Immunosensor for Interferon Gamma TB Disease Biomarker

UNIVERSITY *of the*
WESTERN CAPE

By

Sixolile Mini
(BSc Honours)

A thesis submitted in partial fulfillment of the requirements for the degree

of

MAGISTER SCIENTIAE IN NANOSCIENCE

In the

Faculty of Science
University of the Western Cape, South Africa

Supervisor: Prof Emmanuel Iwuoha

Co-supervisor (s): Dr Usisipho Feleni and Dr Lindsay Wilson

November 2019

ABSTRACT

Tuberculosis (TB) is a disease that results from infection by *Mycobacterium tuberculosis,* which is regarded the most common infecting organism. TB has killed countless numbers of people particularly in underdeveloped countries. TB bacteria can remain inactive or in dormant state for years without causing symptoms or spreading to other subjects, but as soon as the immune system of the host becomes weakened, the bacteria become active and infect mainly the lungs along with other parts of body. TB cases are further aggravated by other illnesses that affect the immune system, such as human immune virus (HIV), which is very prevalent in resource-poor countries. Interferon-gamma (IFN-γ) is a TB biomarker that has found to have all the qualities that are needed to help and cure Tuberculosis disease. Early diagnosis and treatment are essential measures for effectively controlling the disease. Traditional microbial culture-based tests are the most common methodologies currently used. Usually, these methods involve cell culture, cell counts, and cell enrichment, but this process is time-consuming and laborious, especially for the slow-growing bacteria like M. tuberculosis. Sputum smear is one of the methods currently used to detect acid fast bacilli (AFB) in clinical specimens or fluorescent staining. It is a cost-effective tool for diagnosing patients with TB and to monitor the progress of treatment especially in developing countries. The traditional method of inoculating solid medium such as Lowerstein-Jensen (L-J) or 7H10/7H11 media is also used currently it is slow and takes 6-8 weeks of incubation to diagnose the infection and further more time to determine the susceptibility patterns. The microscopic observation drug susceptibility (MODS) assay they are also used currently they rely on light microscopy to visualize the characteristic cording morphology of *M. tuberculosis* in liquid culture. MODS has shorter time to culture positivity (average 8 days) compared with LJ medium (average ~26 days), they are very expensive. The Gen-Probe assay specific for *M. tuberculosis* complex is a rapid detection that is also used, nucleic acid amplification (NAA) test results can be obtained as fast as in two hours (provided if a positive culture is present); it also has a high sensitivity of 99% and specificity of 99.2%. It holds the disadvantage of needing of positive culture that can take several days. Enzyme-linked immunosorbent assay (ELISA), is a test that uses antibodies and colour change to identify a substance. ELISA is an assay that uses a solid-phase enzyme immunoassay (EIA) to detect the presence of a substance, usually an antigen, in a liquid sample or wet sample. It can be used to detection of Mycobacterium antibodies in tuberculosis. The Amplified Mycobacterium Tuberculosis Direct Test (AMTDT) is used for the detection of M. tuberculosis it enables the amplification and detection of M. tuberculosis rRNA directly from respiratory specimens. The diagnostic methods employing gene

technology based on the amplification of DNA or RNA are expected to improve the speed, sensitivity, and specificity of Mycobacterium tuberculosis detection. TB rapid cultivation detection technique, such as MB/BacT system, BactecMGIT 960 system and flow cytometry. The BACTEC MGIT960 system (Becton Dickinson, Sparks, MD) performs incubation and reading of the tubes continuously inside the machine using a predefined algorithm to interpret the fluorescent signal and giving the results as positive or negative. When performing DST, the BACTEC MGIT960 interprets the results as susceptible or resistant to the antibiotic under study. Results are available within 8 days. A recent meta-analysis of the published studies found high accuracy and high predictive values associated with the use of BACTEC MGIT960. These methods are more sensitive and rapid than the traditional microbial culture-based methods. However, they cannot provide the detection results in real-time and most of these methods are centralized in large stationary laboratories because complex instrumentation and highly qualified technical staff are required. Recently, Food and Drug Administration (FDA) approved two new assays that were introduced. These two assays detect in vitro a specific immune response to M. tuberculosis. These tests are the QuantiFERON-TB Gold In-Tube (Cellestis/Qiagen, Carnegie, Australia) and the T-SPOT.TB assay (Oxford Immunotec, Abingdon, United Kingdom). Both assays use whole blood from the patient and measure the production of interferon gamma after the whole blood is exposed to specific antigens from M. tuberculosis. These tests are based on the knowledge that IFN-γ is a product of an active cell-mediated immune response induced by M. tuberculosis. However, TB detection remains a major obstacle due to several drawbacks of these methods. To date, the number of diagnosis approaches for TB has increased as the disease continues to be a major public health problem worldwide and most conventional detection technologies present difficulties in recognizing the presence of M. tuberculosis, since they are time consuming, do not provide clinically reliable results and significantly lack of sensitivity.

This thesis focused on developing two binary and one ternary-electrochemically quantum dots, all synthesised at room temperature in aqueous media for detecting (IFN-γ). Copper telluride (CuTe) and Zinc telluride (ZnTe) was prepared to check how does the two quantum dot behave individual and also to check on how they behave when they are combined and formed ternary quantum dots (CuZnTe). The electrochemical studies of the binary CuTe quantum dots, ZnTe quantum dots and the ternary CuZnTe core-shell quantum dots reveal that ternary quantum dots were stable and showed a significant enhancement in the conductivity of CuZnTe core-shell solution compared to that of CuTe and ZnTe, all studied in solution. The three different quantum dots were capped with three different capping reagents which are tetraethyl orthosilicate (TEOS), thioglycolic acid (TGA), (3-mercaptopropyl) trimethoxysilane (MPS). In the study, a label-free electrochemical immunosensor for the detection of interferon gamma (IFN-γ) was prepared for the first time using ternary quantum dots. The biosensor consists of water-soluble silica coated Copper Zinc telluride (CuZnTe core-shell) quantum dots conjugated to a gold electrode. The antibody-antigen were then conjugated on the CuZnTe core-shell QD modified gold electrode. Results from synthesis of two different binary quantum dots are also presented in the study and compared to the results of the CuZnTe core-shell QDs. The CuTe quantum dots had a small average size which was confirmed through HRTEM, SAXS and XRD analysis. The average core size calculated was 7.91 nm for HRTEM. However, the tendency to aggregate was also largest within the MPS-TGA-CuTe QDs this was confirmed by SAXS measurements and HRTEM. The capping of CuTeQDs was confirmed by FTIR via the specific S-H, Si-CH_2-S and Si-O-Si signature bands of TGA, MPS and TEOS respectively. The CuTe QDs exhibited a large blue shift of the band gap (caused by the quantum confinement effect) which was determined through UV-vis absorption studies. PL studies confirmed that the TGA-CuTe QDs emits light at 370 nm, MPS-TGA-CuTe QDs emits light at 385 nm and TEOS-MPS-TGA-CuTe QDs emits light at 382 nm. Cyclic voltammetry studies confirmed good electrochemical properties when immobilized on an electrode surface. In summary, the novel immunosensor, equipped with prominently conductivity of CuTe QDs, is ideal for the development of electrochemical immunosensor. This study represented a successfully synthesized three different capping reagents with ZnTe QDs. In ZnTe system, a remarkable red shift in UV absorbance and an energy transfer from the core to the shell were observed. The optical absorption peak was observed at 229 nm wavelength while that of bulk is 324 nm indicating the blue shift in absorption edge also the band gap calculated from absorption spectra was at 4.42 eV while the bulk ZnTe has 4.30 eV showing quantum size effect. The capped ZnTe QDs which were well dispersed with an average particle size between 3-20 nm and a cubic zinc blende crystalline structure from the XRD. The proposed immunosensor was successfully applied for the determination of IFN-γ.

The electrochemical studies of the binary CuTe quantum dots, ZnTe quantum dots and the ternary CuZnTe core-shell quantum dots reveal that ternary quantum dots were stable and showed a significant enhancement in the conductivity of CuZnTe core-shell solution compared to that of CuTe and ZnTe, all studied in solution. The fluorescence and UV-vis studies of the CuZnTe core-shell quantum dots showed that the ternary quantum dots have distinctive band at 325 nm at it was the only one that had a red shift. After the addition of TEOS it increased to longer wavelengths. With the SAXS, it was showed that the CuZnTe core-shell are the only quantum dots do not agglomerate after the addition of the capping reagents, also it showed a very narrow tube that indicated that the quantum dots are uniform and these results were in correlation with TEM results. SAXS results also confirmed that the diameter of the core-shell increases as the capping reagents are added to the CuZnTe quantum dots. Successful detection of the studied analytes on the binary and ternary quantum dot platforms widens the scope of biocompatible nanostructured platforms upon which other biomolecules of interest can be immobilized for a wide range of analytical purposes. We observed a linear relationship between the electrochemical signal and IFN-γ concentration from 2 ng/mL to 10 ng/mL and lower detection limit of 0.33 ng/ml (method detection limit technique) in buffer solution. Specificity was high and measurement of IFN-γ concentrations took less time than one reported before. IFN-γ levels of tuberculous in patients, for instance, have been shown to be around 1048pg/mL before treatment and 2233pg/mL after treatment. The fact that our sensor requires a very small sample volume and gives an almost instantaneous result makes it convenient in medical settings. The as-proposed immunosensor demonstrated promising potential usage in the diagnosis of tuberculosis in time owing to its simple operation, excellent sensitivity and stability. This electrochemical biosensing technique serve as a promising alternative even for other diseases this can be a solution that need sensor that is cheap, sensitive and stable.

KEYWORDS

Biosensors

Capping agents

Cyclic voltammetry (CV)

Differential pulse voltammetry (DPV)

Electrochemical Impedance Spectroscopy

Interferon-gamma (IFN-γ)

Mycobacterium tuberculosis

Quantum dots

ABBREVIATIONS

AuE	Gold electrode
CuTeQDs	Copper telluride quantum dots
CuZnTe core-shellQDs	Copper zinc telluride quantum dots
CV	Cyclic voltammetry
DPV	Differential pulse voltammetry
ECL	Electro-chemiluminescent
EDC	1-ethyl-3(3-dimethylaminopropyl) carbodiimide hydrochloride
EDS	Energy dispersive spectrometry
EDX	Energy dispersive x-ray spectroscopy
E-gap	Band gap
Egd	Direct band gap
Egi	Indirect band gap
EIS	Electrochemical impedance spectroscopy
ELISA	Enzyme-linked immunosorbent assay
EMB	Ethambutol
f.c.c	face centred cubic
FT-IR	Fourier Transformation Infrared spectroscopy
FWHM	Full-width-at-half-maximum
HIV	Human immunodeficiency virus
HRSEM	High resolution scanning electron microscopy
HRTEM	High resolution transmission electron microscopy
IFN-γ	Interferon gamma
INH	Isoniazid
LOD	Limit of detection
MBTDT	Amplified Mycobacterium Tuberculosis Direct Test
MDR TB	Multidrug-resistant
MPS	(3-mercaptopropyl) trimethoxysilane
NHS	N-Hydroxysuccinimide
p_a	Anodic peak potential
PBS	Phosphate buffer solution
p_c	Cathodic peak potential
PCR	Polymerase chain reach

PDDF	Pair distance distribution function
PL	Photoluminescence
POC	Point of care
PS	Palmsens
PZA	Pyrazinamide
QDs	Quantum dots
RIF	Rifampin
SAED	Selected area electron diffraction
SAXS	Small-angle x-ray scattering
SM	Streptomycin
TB	Tuberculosis
TEOS	Tetraethyl orthosilicate
TGA	Thioglycolic acid
UV-Vis	Ultraviolet-visible spectrophotometry
WHO	World Health Organisation
XRD	X-ray diffraction
ZnTeQDs	Zinc telluride quantum dots

DECLARATION

I declare that ‘‘*Silica-coated core-shell (CuZnTe core-shell) quantum dots (QDs) for the development of electro-immunosensor for interferon gamma TB disease biomarker*’’ is my own work, that it has not been submitted before for any degree or examination in any other university, and that all the sources I have used or quoted have been indicated or acknowledged as complete references.

Sixolile Mini 15 November 2019

Signed ………………

Acknowledgment

First and foremost, I would like to thank God for giving me the strength, the ability, and clear mind to complete my work.

To my supervisor: A special thanks to my supervisor, Prof Emmanuel Iwuoha, for guidance, support and for believing in me throughout the study. Adding to that I would also like to also thank Dr. Lindsay Wilson and Dr. Usisipho Feleni for putting effort on grooming me as a researcher and helping me accomplish my work.

To my family: ORhadebe I say a big thank you for your love, motivation, and support throughout the period of the study. If it was not for you I would have never be here. Thank you for putting my needs first, you always put my education first. I owe you everything. To my in-laws the **Manyala and Bunge** family thank you for supporting me throughout my studies, you are the best. To my better half **Xolisa Manyala** thank for standing by me throughout this journey. I appreciate the love and support you have given to me. I am very grateful for always encouraging me and believing in my abilities and also understanding the long hours spent in the laboratory. Thank you for taking care of me every time I was busy with my thesis, you are the best husband ever.

To my friends: Zandile Leve, Juliat Louw, Siphokazi Tshoko, Nokwanda Mangema, Siphamandla Nqunqa, Sabelo Sifuba, Bangile Rholihlahla, Muziwenkosi Memela, Zolani Myalo thank you all for being my brothers and sisters at the Chemistry department and outside chemistry. Thank you for supporting me and believing in me. To my other sisters Siphosethu Kimbili, Fikile Mavuso, Zizipho (Zee), Ayola Nkunkwana, Ivana, Anastatia Magwaza, Okuhle Nyalela, Khathu Ravuku, Chwayita Mabhece, Zanele Ngingi, Sihle Kondleka, Amanda Magantolo, Bongiswa (Bongie) and Bulelwa (Mambush) thank you for being there when I started this journey and your support has been consistent throughout my studied you are the best friends that anyone could ask for.

To Chemistry Department: To the staff and Sensor Lab researchers, thank you for your friendship and support.

Dedication

I dedicate this work to Pentecostal Unit of God (P.U.G), this is proof that I have learnt and grown in this church. It made me who I am, to know that God is with me throughout my life has been a blessing. This is proof to my family (Ibandla) in everything Inkosi inathi. This is to our generation Inkululekweni, Inkosi has been with us and he is going to continue to be with us. I want to motivate everyone eNkululekweni that are studying or those that want to study that you can get to this level ngoba Inkosi inathi sinazo zonke izinto. I would also like to dedicate this to the following generation Nikukhanya and generations that will follow after you. If you listen to uTata uzophumelela. Inkosi isinikile umntu uba simamele xa ethetha ngoba ngaye soya empumelelweni. This is to show you that if you listen and pray Inkosi will be with you even with your studies and you can get to where I am and beyond.

UYehova usenzela konke Okuhle!

Table of contents

List of Figures

List of Tables

Chapter one

Summary

This chapter gives a brief background on the aspects involved in this project namely; Tuberculosis, quantum dots, sensors, Interferon gamma. Focused in this chapter is the relationship between these aspects and their contribution towards the success of this study. Also included in this chapter are the project's rationale and motivation, the aim and specific objectives of the study as well as the thesis outline.

1.1 Background

Tuberculosis disease is one of the top 10 causes of mortality in the world. It is a disease that affects all age groups old people, young people, and children. Tuberculosis is a disease caused by a bacteria called *Mycobacterium tuberculosis,* Robert Koch found the bacteria in 1882 *(*Medline Plus, 2018*)*. From the statistics given by WHO, this disease has killed 1.7 million people (together with 0.4 million among people with HIV). The top seven countries that have an uppermost number of people infected by the disease are Indonesia, China, Philippines, Pakistan, Nigeria, and South Africa (WHO, 2015b). It was also stated that an estimated incidence of 454,000 cases of active TB in South Africa only, and out of the 454,000 incident cases it is estimated that 73% (330,000) people died from the disease (GHE, 2018). Viewing that this disease is one of the foremost problems in this country, the HIV statics indicates that out of 270,000 people infected by HIV it was found that 110,000 were killed by the disease. Which confirms that TB is the highest killer disease in South Africa and people that were infected by HIV are found to be killed by TB in most cases. South African is one of the under developing countries, the main reasons why they have the highest number of TB is because it is over-crowded (since TB is a respiratory disease spread easily through coughing and breathing), poor health seeking behavior (mainly in rural areas which constitute larger population percentages), leading to delayed detection of diseases (because the samples has to go to the lab and take weeks to get back results) and poverty does play a major role in the increase accidents of TB (Phetlhu, 2018). A number of people are poor and are obliged to settle in low-income areas, particularly in inner cities where housing is densely crowded. Recurrence of TB in these circumstances results in heavy contact of household members. TB preferentially affects the economically active age group; three-quarters of all cases occur between the ages of 14 and 54 years old and 17% of those who die from TB are between 15 and 49 years. One case of TB will, on average, cause the household income to fall by 25% and the death of an adult from TB causes 15 years of lost income (Aggarwal, 2019). In a crowded household it easy to infect each other, Tuberculosis is easily passed. An individual can get infected by inhaling air that contains TB bacteria, this means that when an infected person sings, breath, or a cough the next person can become infected. After a breath, these bacteria are mainly captured by the alveolar macrophages, but they can evade the host immune system and remain in the dormant stage for a long period of time, at which point they can reactivate to a virulent form under immune-compromised conditions of the host. TB mostly affects the lungs (because that is what humans use to breath in and out), but it can also affect the spine, the kidneys, or the brain causing disease namely pulmonary TB, spondylitis TB, renal TB, meninges TB respectively (Jeanes and Grady, 2016).

TB bacteria can remain inactive or in a dormant state for years without causing symptoms or spreading to other subjects that are called a latent TB. This is possible because *M. tuberculosis* can continue in slow growing as well as in fast-growing stages which makes treatment challenging. But as soon as the immune system of the host becomes weakened, the bacteria become active and infects mainly the lungs along with other parts of the body. TB disease cases are then further affected by other illnesses which affect the immune system, such as HIV, which is very common in resource-poor countries. Unfortunately, in spite of continuous efforts at national and global levels, only imperfect success has been done in the detection and management of TB worldwide (Srivastava, Van Rijn and Jongsma, 2016). In detection and management of TB, some patients were found out to be resistant to the treatment. The problem is that *M. tuberculosis* infections are both hard to detect and hard to treat, and they also grow differently according to a person immune system. The rapid diagnosis and treatment of infectors are considered crucial for the effective control of TB because one patient is known to transmit the disease to 12–15 people/year on average through respiratory tract infection(He *et al.*, 2011).

The heavy global public health burden of TB worldwide demands for the development of more rapid and sensitive detection methods. The new development TB detection methods have to have the following characteristics portability, real-time, sensitivity, rapid, and accurate methods for M. tuberculosis detection is essential to effectively prevent TB infection (Tortoli *et al.*, 1999). Researchers are developing new, simple, direct, easy to use, sensitive and specific diagnostic techniques for detecting tuberculosis using biosensor. Currently, there are methods that are used to test for TB. Traditional microbial culture-based tests are the most common methodologies currently used. Usually, these methods involve cell culture, cell counts, and cell enrichment, but this process is time-consuming and laborious, especially for the slow-growing bacteria like M. tuberculosis (Lazcka, Del and Mu, 2007).

1.2 Problem Statement and motivation

Tuberculosis (TB) is an ancient disease that has infected humans for thousands of years. Despite countless campaigns, and even with management and control strategies currently in place to achieve a TB free world, tuberculosis continues to cause a serious health problem worldwide. TB continues to claim lives in South Africa despite the interventions of government and private bodies. Hence there is an urgent need to assess the control strategies. A number of studies have been done on TB especially, over the past two decades. However, despite diagnostic tests that detect the disease and effective therapy, there are still millions of people worldwide who are infected with TB. To date, many methods and techniques have been developed for rapid detection of *M. tuberculosis*, such as polymerase chain reaction (PCR), latex agglutination, enzyme-linked immunosorbent assay (ELISA), radiometric detection, gen probe amplified *M. Tuberculosis* direct test (AMTDT), TB rapid cultivation detection technique, such as MB/BacT system, BactecMGIT 960 system and flow cytometry. These methods are more sensitive and rapid than the traditional microbial culture-based methods. However, they cannot provide the detection results in real-time and most of these methods are centralized in large stationary laboratories because complex instrumentation and highly qualified technical staff are required. As a result, the development of portable, real-time, sensitive, rapid, and accurate methods for *M. tuberculosis* detection is essential to effectively prevent TB infection. Recent efforts to identify the highest priorities in the field of TB diagnostics have revealed the urgent need for biomarker-based assays that will enable more efficient, affordable, and accessible diagnosis for those in need. The biomarkers that are used need to be a biomarker that can be used in a point-of-care test, that are of real-time, with high sensitivity and that can be used for the treatment of Tuberculosis. Interferon-gamma (IFN-γ) is a TB biomarker that has found to have all the qualities that are needed to be used to help and cure Tuberculosis disease. Over the past two decades, bio-sensing technologies (biosensors and biochips) has received a considerable amount of attention due to its use in medical diagnoses. The importance of biosensors results from their high specificity and sensitivity. Biosensors have shown tremendous promise in biomedical studies and are being aggressively studied to further improve the detection platforms for such applications. The sensing surface of biosensors can be improved by the incorporation of nanomaterials such as quantum dots (QDs), gold nanoparticles, magnetic nanoparticles or carbon nanotubes. These nanomaterials have unique physicochemical properties, which offer greater sensitivity than conventional reporter molecules. Quantum dots have found to be the best interesting nanomaterial is the one that is mostly used in research facilities. One of the main factors which make QDs particularly interesting and desirable to biomedical science is their tunable size. QDs are semiconductor nanocrystals that are a few nanometers in diameter and due to their high surface area, favorable electronic properties and good biocompatibility they can be incorporated into biosensors for the detection of very low levels of TB biomarkers. The proposed study seeks to develop a gold electrode that will be used and it will be immobilized with quantum dots. CuZnTe core-shell quantum dots are semiconductor nanocrystals which exhibit quantum mechanical behavior.

Quantum dots will act as a mediator and has large surface area for attachment of biomolecule (antibody) then observed to study the target protein or the behavior of the cells. The immobilized electrode will be used to detect the interferon gamma which is a TB biomarker.

1.3 Aims and Objectives

This study is focussed on the development of an electrochemical immunosensor for the detection of interferon gamma- a TB biomarker. The sensor development involved the preparation of a core-shell CuZnTe core-shell QD capped with tetraethyl orthosilicate (TEOS), thioglycolic acid (TGA), and (3-mercaptopropyl) trimethoxysilane (MPS) on a chip modified with antibody bioelectrode immunosensor. The sensor will be modified with antibody. The intention of such a device is to eliminate invasive procedures and to create a friendly and comfortable environment for patients to be tested making the process much more familiar. It will also allow health care practitioners to receive results promptly and at POC thus allowing adequate treatment to commence and therefore allowing individualization of treatment regimes.

The proposed aim will be achieved through the following objectives:

i. Synthesis of novel silica coated copper zinc telluride quantum dots (CuZnTe core-shell QDs)

ii. Spectroelectrochemical characterization of CuZnTe core-shell QDs by Ultraviolet-Visible (UV-vis) absorption and Photoluminescence (PL) spectroscopy.

iii. Microscopic and spectroscopic characterization of CuZnTe core-shell QDs by Fourier Transform Infra-red (FTIR) spectroscopy and High-Resolution Scanning/Transmission Electron Microscopy (HR-SEM/TEM).

iv. Electro-analysis of CuZnTe core-shell QDs using Cyclic Voltammetry (CV), Deep Wave Voltammetry (SWV) and Electrochemical Impedance Spectroscopy (EIS).

v. Fabrication of the immunosensor (gold electrode with antibody)

vi. Incubation of the immunosensor in blocking buffer solution (Bovine serum albumin).

vii. Detection of interferon gamma using the sensor

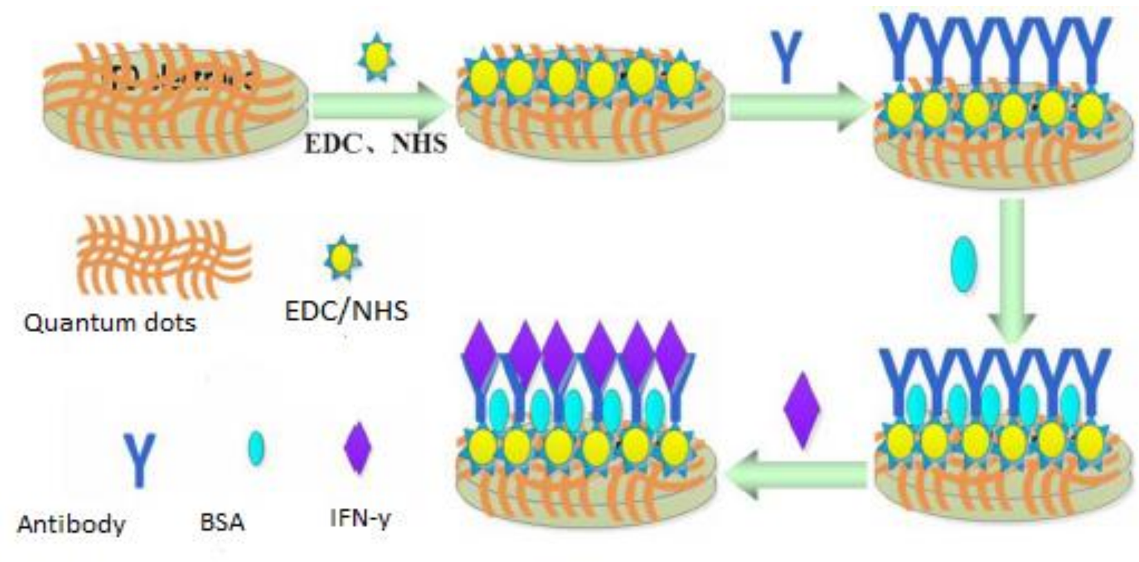

Figure 1.1: Schematic representation of for development of AuE/QDs/Antibody/BSA/IFN-γ biosensor.

1.4 Thesis layout

This thesis is presented in seven chapters

Chapter 1: Gives brief background information on the project, problem statement, and motivation as well as aims and objectives.

Chapter 2: Provides a detailed literature review

Chapter 3: Consists of reagents, procedures, and instrumentations used for synthesized TEOS-MPS-TGA-CuTe quantum dots. The detection of interferon gamma using these quantum dots.

Chapter 4: Consists of reagents, procedures, and instrumentations used for synthesized TEOS-MPS-TGA-ZnTe quantum dots. The detection of interferon gamma using these quantum dots.

Chapter 5: The above material CuTe QDs and ZnTe QDs were combined together to make the success of this study. CuZnTe core-shell was used for the detection of interferon gamma in TB liquid.

Chapter 6: Represents conclusion and recommendations

References

Abd-elsalam, K. A. and Alghuthaymi, M. A. (2015) ‘Journal of Nanotechnology and Materials Science’, pp. 38–40. doi: 10.15436/2377-1372.15.013.

Abd Rahman, S. *et al.* (2017) ‘Thiolate-Capped CdSe/ZnS Core-Shell Quantum Dots for the Sensitive Detection of Glucose’, *Sensors (Basel, Switzerland)*, 17(7), pp. 1–12. doi: 10.3390/s17071537.

Abdelbar, M. F. *et al.* (2016) ‘Spectrochimica Acta Part A : Molecular and Biomolecular Spectroscopy Photo-induced interaction of thioglycolic acid (TGA) -capped CdTe quantum dots with cyanine dyes’, *SAA*. Elsevier B.V., 168, pp. 1–11. doi: 10.1016/j.saa.2016.05.029.

Adegoke, O. *et al.* (2016) ‘Biosensors and Bioelectronics An ultrasensitive SiO 2 -encapsulated alloyed CdZnSeS quantum dot-molecular beacon nanobiosensor for norovirus’, *Biosensors and Bioelectronic*. Elsevier, 86, pp. 135–142. doi: 10.1016/j.bios.2016.06.027.

Aggarwal, A. N. (2019) ‘J Clin Tuberc Other Mycobact Dis Quality of life with tuberculosis’, *J Clin Tuberc Other Mycobact Dis*. Elsevier, 17, p. 100121. doi: 10.1016/j.jctube.2019.100121.

Ali, M. and Sarma, D. D. (2007) ‘Synthesis of ZnSe Quantum Dots and ZnSe – ZnS Core / Shell Nanostructures’, 7(6). doi: 10.1166/jnn.2007.748.

Alia, N. *et al.* (2018) ‘Results in Physics Optical and structural properties of cadmium sulphide quantum dots based thin films as potential sensing material for dengue virus E-protein’, *Results in Physics*. Elsevier, 11(October), pp. 734–739. doi: 10.1016/j.rinp.2018.10.032.

Ambika, S. *et al.* (2019) ‘Structural , morphological and optical properties and solar cell applications of thioglycolic routed nano cobalt oxide material’, *Energy Reports*. Elsevier Ltd, 5, pp. 305–309. doi: 10.1016/j.egyr.2019.02.005.

Andrews, E. *et al.* (2015) ‘Electrocatalytic Reduction of CO 2 at Au Nanoparticle Electrodes : Effects of Interfacial Chemistry on Reduction Behavior’, 162(12), pp. 1373–1378. doi: 10.1149/2.0541512jes.

Arshad, A. *et al.* (2016) ‘Aqueous synthesis of tunable fluorescent , semiconductor CuInS 2 quantum dots for bioimaging’, *Arabian Journal of Chemistry*. The Authors, pp. 4–11. doi: 10.1016/j.arabjc.2016.10.002.

Asano, H. *et al.* (2017) ‘Synthesis of colloidal Zn(Te,Se) alloy quantum dots’, *Materials Research Express*. IOP Publishing, 4(10), pp. 0–10. doi: 10.1088/2053-1591/aa8b84.

Attar, A. R., Blumling, D. E. and Knappenberger, K. L. (2011) ‘Photodissociation of thioglycolic acid studied by femtosecond time-resolved transient absorption spectroscopy’, *Journal of Chemical Physics*, 134(2), pp. 1–9. doi: 10.1063/1.3526746.

Bands, R. (no date) ‘Raman Bands RAMAN DATA AND ANALYSIS Raman Spectroscopy for Analysis and Monitoring’, pp. 2–3.

Banyal, S. *et al.* (2013) ‘Advances in nanotechnology for diagnosis and treatment of tuberculosis’, pp. 289–297. doi: 10.1097/MCP.0b013e32835eff08.

Baustian, J. J. (1988) ‘system’.

Bhatia, S. K. *et al.* (1989) ‘Use of thiol-terminal silanes and heterobifunctional crosslinkers for immobilization of antibodies on silica surfaces', *Analytical Biochemistry*, 178(2), pp. 408–413. doi: 10.1016/0003-2697(89)90662-3.

Buzea, C., Pacheco, I. I. and Robbie, K. (2007) 'Nanomaterials and nanoparticles: Sources and toxicity', *Biointerphases*, 2(4), pp. MR17-MR71. doi: 10.1116/1.2815690.

Chang, C. *et al.* (2012) 'Biosensors and Bioelectronics Amplified surface plasmon resonance immunosensor for interferon-Gamma based on a streptavidin-incorporated aptamer', *Biosensors and Bioelectronic*. Elsevier, 37(1), pp. 68–74. doi: 10.1016/j.bios.2012.04.038.

Chatterjee, B. *et al.* (2019) 'Nanozymes and aptamer-based biosensing', *Materials Science for Energy Technologies*. The Authors. doi: 10.1016/j.mset.2019.08.007.

Chegou, N. N. *et al.* (2014) 'Beyond the IFN- c horizon : biomarkers for immunodiagnosis of infection with Mycobacterium tuberculosis', pp. 1472–1486. doi: 10.1183/09031936.00151413.

Chen, J. B., Neves, M. A. D. and Thompson, M. (2016) 'Sensing and Bio-Sensing Research Biosensor surface attachment of the ovarian cancer biomarker HSP10 via His-tag modi fi cation', *SBSR*. The Authors, 11, pp. 107–112. doi: 10.1016/j.sbsr.2016.10.006.

Chen, X., Liu, F. and Jiang, Q. (2012) 'Synthesis and Properties of Water-Soluble Silica-Coated ZnSe / ZnS Semiconductor Quantum Dots', pp. 6–11. doi: 10.1007/s10904-011-9606-3.

Choudhary, A. K. (2015) 'Biosensor based on piezoelectric crystal probe', 6(8), pp. 91–95.

Choudhary, Y. S. and Nageswaran, G. (2019) 'Sensing and Bio-Sensing Research Branched mercapto acid capped CdTe quantum dots as fluorescence probes for Hg 2 + detection', *Sensing and Bio-Sensing Research*. Elsevier, 23(February), p. 100278. doi: 10.1016/j.sbsr.2019.100278.

Christine, A. *et al.* (2016) 'The electrochemical behavior of core-shell CdSe / CdS magic-sized quantum dots linked to cyclodextrin for studies o .... The electrochemical behavior of core-shell CdSe / CdS magic-sized quantum dots linked to cyclodextrin for studies of the encapsulation of bioactive compounds', *Journal of Solid State Electrochemistry*. Journal of Solid State Electrochemistry, (April). doi: 10.1007/s10008-016-3221-8.

Claude, L. U. and Lyon, B. (2015) 'Development of electrochemical biosensors for environmental pollutant and food safety monitoring Zhenzhong Guo To cite this version : HAL Id : tel-01128300 Délivrée par'.

Compagnone, D. *et al.* (2015) 'Chemical Sensors and Biosensors in Italy : A Review of the 2015 Literature', pp. 1–22. doi: 10.3390/s17040868.

Congiu, M. *et al.* (2015) 'A novel and large area suitable water-based ink for the deposition of cobalt sulfide films for solar energy conversion with iodine-free electrolytes', *Solar Energy*. Elsevier Ltd, 122(December 2015), pp. 87–96. doi: 10.1016/j.solener.2015.08.032.

Cranfill, P. J. *et al.* (2016) 'Quantitative Assessment of Fluorescent Proteins', 13(7), pp. 557–562. doi: 10.1038/nmeth.3891.Quantitative.

Crevel, R. Van, Ottenhoff, T. H. M. and Meer, J. W. M. Van Der (2002) 'Innate Immunity to Mycobacterium tuberculosis', 15(2), pp. 294–309. doi: 10.1128/CMR.15.2.294.

Dalmoro, V. *et al.* (2013) 'A synergistic combination of tetraethylorthosilicate and multiphosphonic acid offers excellent corrosion protection to AA1100 aluminum alloy', *Applied Surface Science*. Elsevier B.V., 273, pp. 758–768. doi: 10.1016/j.apsusc.2013.02.131.

Das, R., Nath, S. S. and Bhattacharjee, R. (2011) 'Luminescence of copper nanoparticles', *Journal of Luminescence*. Elsevier, 131(12), pp. 2703–2706. doi: 10.1016/j.jlumin.2011.05.019.

Decade, T. F. and Musterman, M. I. (2018) 'Interferon-gamma (IFN-γ): Exploring its implications in infectious diseases', 1(2), pp. 64–79.

Dhar, R., Singh, S. and Kumar, A. (2015) 'Effect of capping agents on optical and antibacterial properties of cadmium selenide quantum dots', 38(5), pp. 1247–1252.

Dhasade, S. S., Han, S. H. and Fulari, V. J. (2012) 'A nanostructured copper telluride thin film grown at room temperature by an electrodeposition method A nanostructured copper telluride thin film grown at room temperature by an electrodeposition method', (September). doi: 10.1088/1674-4926/33/9/093002.

Diego, S. (2015) 'The Application of Fluorescent Quantum Dots to Confocal , Multiphoton , and Electron Microscopic Imaging', pp. 112–116. doi: 10.1177/0192623307310950.

Ding, S. *et al.* (2017) 'Rapid and Label-free Detection of Interferon Gamma via an Electrochemical Aptasensor Comprised of a Ternary Surface Monolayer on a Gold Interdigitated Electrode Array Rapid and Label-free Detection of Interferon Gamma via an Electrochemical Aptasensor Comprised of a Ternary Surface Monolayer on a Gold Interdigitated Electrode Array Agriculture and Biological Engineering Department , Institute of Food and Agricultural'. doi: 10.1021/acssensors.6b00581.

Ding, S. and Lu, M. (2018) 'Highly sensitive biosensors with interdigitated electrode arrays'.

Dingran Chang, Sandy Zakaria, Mimi Deng, Nicholas Allen, K. T. and Y. L. (2016) 'Integrating Deoxyribozymes into Colorimetric Sensing Platforms'. doi: 10.3390/s16122061.

Ebrahim, S. *et al.* (2017) 'CdTe quantum dots capped with different stabilizing agents for sensing of ochratoxin A', *Journal of Luminescence*. Elsevier, 182, pp. 154–159. doi: 10.1016/j.jlumin.2016.09.038.

Eleanor Adachi1, Idemudia John Airuoyo2, Lakshmi Krishna2, R. C. (2016) 'Developing a Process for Studying Annealing Effects on Mobilities in Silicon Quantum Dots', 1527(1986), p. 163111.

Epa, U. S. and Osa, A. (2007) 'Nanotechnology White Paper', (February).

Fang, T. *et al.* (2012) '3-Mercaptobutyric Acid as an E ff ective Capping Agent for Highly Luminescent CdTe Quantum Dots : New Insight into the Selection of Mercapto Acids'.

Farid, S. *et al.* (2015) 'Detection of Interferon gamma using graphene and aptamer based FET-like electrochemical biosensor', *Biosensors and Bioelectronics*. Elsevier, 71, pp. 294–299. doi: 10.1016/j.bios.2015.04.047.

Feleni, U. (2013) 'Palladium Telluride Quantum Dots Biosensor for the Determination of Indinavir Drug By Usisipho Feleni (BSc Honours) A thesis submitted in partial fulfilment of the requirements for the degree of Magister Scientiae in Nanoscience Faculty of Science Unive', (November).

Feleni, U. (2017) 'Quantum Dots-Amplified Electrochemical Cytochrome P450 Phenotype Sensor for Tamoxifen , a Breast Cancer Drug', (May).

Feynman, R. P. (1992) ‘There ’ s Plenty of Room at the Bottom’, 1(i), pp. 60–66.

Freitas, D. V, Dias, J. M. M. and Passos, S. G. B. (2014) ‘Electrochemical synthesis of TGA-capped CdTe and CdSe quantum dots’, pp. 3247–3254. doi: 10.1039/c4gc00300d.

G. J. NETTO, R. D. S. & P. A. D. I. (no date) ‘Diagnostic molecular pathology: current techniques and clinical applications, part I’, 75246, pp. 379–383.

Gabriella, L. and Pacoste, C. (2017) ‘Development of Copper Selenide Quantum Dots-Based Therapeutic Drug Monitoring Biosensors for Toremifene – In the Department of Chemistry , University of the Western Cape’.

Gadalla, A. *et al.* (2017) ‘CHARACTERIZATION OF CdSe CORE AND CdSe / ZnS CORE / SHELL QUANTUM DOTS SYNTHESIZED USING A MODIFIED METHOD’, 14(7), pp. 239–249.

Garcia-gutierrez, D. F. *et al.* (2018) ‘Influence of the Capping Ligand on the Band Gap and Electronic Levels of PbS Nanoparticles through Surface Atomistic Arrangement Determination’. doi: 10.1021/acsomega.7b01451.

Gfroerer, T. H. (2000) ‘Photoluminescence in Analysis of Surfaces and Interfaces’, pp. 9209–9231.

GHE (2018) ‘Drug Resistant TB India | Categories, DOTs-Plus, treatment’. Available at: https://www.tbfacts.org/drug-resistant-tb-india/.

Ghosh, S. *et al.* (2011) ‘Aqueous synthesis of ZnTe/dendrimer nanocomposites and their antimicrobial activity: Implications in therapeutics’, *Nanoscale*, 3(3), pp. 1139–1148. doi: 10.1039/c0nr00610f.

Goftman, V. V *et al.* (2016) ‘Multicolored silica coated CdSe core / shell quantum dots’, 9917, pp. 1–6. doi: 10.1117/12.2225212.

Goletti, D. *et al.* (2016) ‘Tuberculosis biomarkers : from diagnosis to protection’, 8. doi: 10.4081/idr.2016.6568.

Gomaa, E. A. and Salem, S. E. (2016) ‘Cyclic Voltammetry Study of Copper Chloride Salt with Ceftazidime Antibiotic’, 3(3).

Grieshaber1, D. *et al.* (2008) ‘Electrochemical Biosensors - Sensor Principles and Architectures’, (January), pp. 1400–1458.

Grossi, M. and Riccò, B. (2017) ‘Electrical impedance spectroscopy (EIS) for biological analysis and food characterization : a review’, pp. 303–325.

Han, A. Z. *et al.* (2017) ‘SC’, *Sensors & Actuators: B. Chemical*. Elsevier B.V. doi: 10.1016/j.snb.2017.11.157.

Hao, J. *et al.* (2019) ‘A facile route to synthesize CdSe / ZnS thick-shell quantum dots with precisely controlled green emission properties : towards QDs based LED applications’, *Scientific Reports*. Springer US, (February), pp. 1–8. doi: 10.1038/s41598-019-48469-7.

Hasan, S. (2014) ‘A Review on Nanoparticles : Their Synthesis and Types’, *Research Journal of Recent Sciences Res . J . Recent . Sci . Uttar Pradesh (Lucknow Campus),* 4(February), pp. 1–3. doi: 10.3233/978-1-61499-057-4-57.

Hasan, S. (2015) ‘A Review on Nanoparticles : Their Synthesis and Types Biosynthesis : Mechanism’, 4, pp. 9–11.

He, W. *et al.* (2015) ‘Electrodeposition and Characterization of CuTe and Cu 2 Te Thin Films’, 2015.

He, X. *et al.* (2011) ‘Biosensing technologies for mycobacterium tuberculosis detection: Status and new developments’, *Clinical and Developmental Immunology*, 2011. doi: 10.1155/2011/193963.

Hodlur, R. M. and Rabinal, M. K. (2014) ‘A new selenium precursor for the aqueous synthesis of luminescent CdSe quantum dots’, *CHEMICAL ENGINEERING JOURNAL*. Elsevier B.V., 244, pp. 82–88. doi: 10.1016/j.cej.2014.01.064.

Hossain, M. and Norazmi, M. (2013) ‘Pattern Recognition Receptors and Cytokines in Mycobacterium tuberculosis Infection — The Double-Edged Sword ?’, 2013.

Ibrahim, I. *et al.* (2016) ‘Cadmium Sulphide-Reduced Graphene Photoelectrochemical Sensing Platform for Copper (II) Ions’, (Ii), pp. 1–18. doi: 10.1371/journal.pone.0154557.

Ishizaki, T. *et al.* (2005) ‘An investigation into the effect of ionic species on the formation of ZnTe from a citric acid electrolyte’, 50, pp. 3509–3516. doi: 10.1016/j.electacta.2004.12.028.

Jameel (2010) ‘Review of Literature’, pp. 1–35. doi: 10.3390/healthcare3041243.Sleep.

Jeanes, C. and Grady, J. O. (2016) ‘Diagnosing tuberculosis in the 21st century – Dawn of a genomics revolution ?’, *International Journal of Mycobacteriology*. Asian-African Society for Mycobacteriology, 5(4), pp. 384–391. doi: 10.1016/j.ijmyco.2016.11.028.

Jiang, H. and Ju, H. (2007) ‘Electrochemiluminescence sensors for scavengers of hydroxyl radical based on its annihilation in CdSe quantum dots film/peroxide system’, *Analytical Chemistry*, 79(17), pp. 6690–6696. doi: 10.1021/ac071061j.

Jimenez-lópez, J. *et al.* (2016) ‘Automated determination of Rifamycins making use of MPA – CdTe quantum dots’, *Journal of Luminescence*. Elsevier, 175, pp. 158–164. doi: 10.1016/j.jlumin.2016.02.036.

Jorge, P. *et al.* (2007) ‘Optical fiber sensing using quantum dots’, *Sensors*, 7(12), pp. 3489–3534. doi: 10.3390/s7123489.

Joseph, J., Nagashri, K. and Suman, A. (2016) ‘Journal of Photochemistry & Photobiology , B : Biology Synthesis , characterization and pharmacological studies of copper complexes of fl avone derivatives as potential anti-tuberculosis agents’, *JPB*. Elsevier B.V., 162, pp. 125–145. doi: 10.1016/j.jphotobiol.2016.06.033.

Jun-Jie Zhu, Jing-Jing Li, Hai-Ping Huang, F.-F. C. (2013) ‘Quantum Dots’, pp. 9–25. doi: 10.1007/978-3-642-44910-9.

Kaviyarasu, K. *et al.* (2016) ‘Solution processing of CuSe quantum dots : Photocatalytic activity under RhB for UV and visible-light solar irradiation’, *Materials Science & Engineering B*. Elsevier B.V., 210, pp. 1–9. doi: 10.1016/j.mseb.2016.05.002.

Ke, S. *et al.* (2019) ‘Construction of silica-encapsulated gold-silver core-shell nanorod : Atomic facets enrichment and plasmon enhanced catalytic activity with high stability and reusability’, *Materials & Design*. The Authors, 177, p. 107837. doi: 10.1016/j.matdes.2019.107837.

KENAN koça,b, FATMA Z. Tepehanb, G. G. T. (2011) ‘OF SELF-ASSEMBLED QUANTUM DOTS THIN FILMS ON A GLASSY SUBSTRATE’, 8(4), pp. 239–247.

Kennedy, R. O. *et al.* (1990) ‘n k n o w a n n t g i e n’, 18(3), pp. 136–140.

Khene, S., Moeno, S. and Nyokong, T. (2011) ‘Voltammetry and electrochemical impedance spectroscopy of gold electrodes modified with CdTe quantum dots and their conjugates with nickel tetraamino phthalocyanine’, *Polyhedron*. Elsevier Ltd, 30(12), pp. 2162–2170. doi: 10.1016/j.poly.2011.06.002.

Kobayashi, Y., Correa-Duarte, M. A. and Liz-Marzán, L. M. (2001) ‘Sol−Gel Processing of Silica-Coated Gold Nanoparticles’, *Langmuir*, 17(20), pp. 6375–6379. doi: 10.1021/la010736p.

Koç, K., Tepehan, F. Z. and Tepehan, G. G. (2012) ‘Growth kinetics of MPS-capped CdS quantum dots in self-assembled thin films’, pp. 1–7.

Krug, K. *et al.* (2012) ‘Electrochemical Cu Growth on MPS-Modi fi ed Au (111) Electrodes’, (111).

Kuhar, N. *et al.* (2018) ‘Challenges in application of Raman spectroscopy to biology and materials’. Royal Society of Chemistry, pp. 25888–25908. doi: 10.1039/c8ra04491k.

Kumar, B. R. and Hymavathi, B. (2017) ‘Journal of Asian Ceramic Societies X-ray peak profile analysis of solid-state sintered alumina doped zinc oxide ceramics by Williamson – Hall and size-strain plot methods’, *Integrative Medicine Research*. Taibah University, 5(2), pp. 94–103. doi: 10.1016/j.jascer.2017.02.001.

Kumar, P. and Singh, K. (2009) ‘Wurtzite ZnSe quantum dots : Synthesis , characterization and PL properties’, 1(1), pp. 59–69.

Labiadh, H. and Hidouri, S. (2017) ‘ZnS quantum dots and their derivatives : Overview on identity , synthesis and challenge into surface modifications for restricted applications’, *Journal of King Saud University - Science*. King Saud University, 29(4), pp. 444–450. doi: 10.1016/j.jksus.2016.12.001.

Lazcka, O., Del, F. J. and Mu, F. X. (2007) ‘Pathogen detection : A perspective of traditional methods and biosensors’, 22, pp. 1205–1217. doi: 10.1016/j.bios.2006.06.036.

Lecture, N. (2017) ‘Advanced Nanochemistry By Dr Masikini Milua SensorLab , Department of Chemistry University of the Western Cape . Email : mmasikini@uwc.ac.za’.

Li, G. *et al.* (2017) ‘Evaluation of a New IFN- γ Release Assay for Rapid Diagnosis of Active Tuberculosis in a High-Incidence Setting’, 7(April). doi: 10.3389/fcimb.2017.00117.

Li, H., Shih, W. Y. and Shih, W. H. (2007) ‘Stable aqueous ZnS quantum dots obtained using (3-mercaptopropyl) trimethoxysilane as a capping molecule’, *Nanotechnology*, 18(49). doi: 10.1088/0957-4484/18/49/495605.

Li, X. *et al.* (2009) ‘Glucose Biosensor Based on Nanocomposite Films of CdTe Quantum Dots and Glucose Oxidase’, 25(11), pp. 6580–6586. doi: 10.1021/la900066z.

Li, Y. *et al.* (2011) ‘ChemComm Aqueous synthesis of CdTe nanocrystals : progresses and perspectives’, pp. 9293–9311. doi: 10.1039/c1cc11331c.

Liu, C. *et al.* (2015) ‘An electrochemical aptasensor for detection of IFN-γ using graphene and a dual signal amplification strategy based on the exonuclease-mediated surface-initiated enzymatic polymerization’, *Analyst*, 140(22), pp. 7784–7791. doi: 10.1039/c5an01591j.

Liu, X. *et al.* (2008) ‘Glucose biosensor based on gold nanoparticle-catalyzed luminol electrochemiluminescence on a three-dimensional sol-gel network’, *Electrochemistry Communications*, 10(9), pp. 1250–1253. doi: 10.1016/j.elecom.2008.06.009.

Liu, Y. *et al.* (2010) ‘Aptamer-based electrochemical biosensor for interferon gamma detection’, *Analytical Chemistry*, 82(19), pp. 8131–8136. doi: 10.1021/ac101409t.

Lu, L. *et al.* (2007) ‘Raman analysis of CdSe / CdS core – shell quantum dots with different CdS shell thickness’, 406221. doi: 10.1088/0953-8984/19/40/406221.

Lu, X. *et al.* (2019) ‘Analytica Chimica Acta Target-driven switch-on fl uorescence aptasensor for trace a fl atoxin B1 determination based on highly fl uorescent ternary CdZnTe quantum dots’, *Analytica Chimica Acta*. Elsevier Ltd, 1047, pp. 163–171. doi: 10.1016/j.aca.2018.10.002.

Ma, Y. *et al.* (2014) ‘Highly bright water-soluble silica coated quantum dots with excellent stability’, *Journal of Materials Chemistry B*, 2(31), pp. 5043–5051. doi: 10.1039/c4tb00458b.

Madras, T. (2016) ‘Chapter - INTRODUCTION TO NANOMATERIALS’, (December 2011).

Malecha, K. *et al.* (2019) ‘Optical Sensors Based on II-VI Quantum Dots’, pp. 1–24. doi: 10.3390/nano9020192.

Malhotra, S. *et al.* (2017) ‘BIOSENSORS : PRINCIPLE , TYPES AND APPLICATIONS’, (2), pp. 3639–3644.

Manchandani, P. *et al.* (no date) ‘Quantum Dots as multifunctional nanoparticles - A review’, pp. 1–8.

Manuscript, A. (2015) ‘Analytical Methods’. doi: 10.1039/C5AY01412C.

Matea, C. T. and Mocan, T. (2017) ‘Quantum dots in imaging , drug delivery and sensor applications’, pp. 5421–5431.

Medline Plus (2018) ‘Tuberculosis (TB) Causes, Symptoms, Warning Signs, & Diagnosis’.

Min, K. *et al.* (2008) ‘A simple and direct electrochemical detection of interferon-γ using its RNA and DNA aptamers’, *Biosensors and Bioelectronics*, 23(12), pp. 1819–1824. doi: 10.1016/j.bios.2008.02.021.

Moradian, R. *et al.* (2013) ‘Structural , optical , and electrical properties of thioglycolic acid-capped CdTe quantum dots thin films’, pp. 1–6.

Morales-saavedra, O. G. *et al.* (2015) ‘Fabrication and photophysical studies of CdTe quantum-dots dispersed in’, *Revista Mexicana de Trastornos Alimentarios*. Universidad Nacional Autónoma de México, Centro de Ciencias Aplicadas y Desarrollo Tecnológico, 13(6), pp. 566–575. doi: 10.1016/j.jart.2015.10.013.

Musa, I., Qamhieh, N. and Said, K. (2019) ‘Results in Physics Germanium antimony quantum dots morphology and Raman spectroscopy fabricated by inert gas condensation’, *Results in Physics*. Elsevier, 13(April), p. 102311. doi: 10.1016/j.rinp.2019.102311.

Nagaveni, V. B. *et al.* (2018) ‘Journal of Science : Advanced Materials and Devices Synthesis , crystal structure and excellent photoluminescence properties of copper (II) and cobalt (II) complexes with Bis’, *Journal of Science: Advanced Materials and Devices*. Elsevier Ltd, 3(1), pp. 51–58. doi: 10.1016/j.jsamd.2018.01.001.

Ndangili, P. M. (2011) ‘Electrochemical and optical modulation of selenide and telluride ternary alloy quantum dots genosensors’, (November).

Ndangili, P. M. *et al.* (2017) ‘Gallium-Induced Perturbation of Zinc Selenide Quantum Dots

Electronics', pp. 7054–7062. doi: 10.1002/slct.201700748.

Niu, Z. and Li, Y. (2013) 'Removal and Utilization of Capping Agents in Nanocatalysis Removal and Utilization of Capping Agents in Nanocatalysis'. doi: 10.1021/cm4022479.

Nwabisa, A. (2010) 'DEVELOPMENT OF ELECTROCHEMICAL ZnSe QUANTUM DOTS BIOSENSORS FOR LOW-LEVEL DETECTION OF 17 β -ESTRADIOL ESTROGENIC', (November).

Onwudiwe, D. C., Hrubaru, M. and Ebenso, E. E. (2015) 'Synthesis , Structural and Optical Properties of TOPO and HDA Capped Cadmium Sulphide Nanocrystals , and the Effect of Capping Ligand Concentration', 2015.

Orth, F. O. R. T. W., Exas, T. and Aprimer, Q. (2002) 'QuantumDots: APrimer'.

Osipovich, N. P. *et al.* (2016) 'Cyclic voltammetry as a sensitive method for in situ probing of chemical transformations in quantum dots', *Physical Chemistry Chemical Physics*, 18(15), pp. 10355–10361. doi: 10.1039/c6cp01085g.

Owens, G. J. *et al.* (2016) 'Progress in Materials Science Sol – gel based materials for biomedical applications', 77, pp. 1–79. doi: 10.1016/j.pmatsci.2015.12.001.

Pal, C. *et al.* (2017) 'Charge transport in lead sul fi de quantum dots / phthalocyanines hybrid nanocomposites', *Organic Electronics*. Elsevier B.V, 44, pp. 132–143. doi: 10.1016/j.orgel.2017.02.014.

Park, Y., Jeong, S. and Kim, S. (2017) 'Medically translatable quantum dots for biosensing and imaging', *Journal of Photochemistry and Photobiology C: Photochemistry Reviews*. Elsevier B.V., 30, pp. 51–70. doi: 10.1016/j.jphotochemrev.2017.01.002.

Pauw, B. R., Kästner, C. and Thünemann, A. F. (2017) 'Nanoparticle Size Distribution Quantification : Results of a SAXS Inter-Laboratory Comparison', 1, pp. 1–21.

Phetlhu, D. R. (2018) 'Nurses ' Knowledge of Tuberculosis , HIV , and Integrated HIV / TB Care Policies in Rural Western Cape , South Africa', *Journal of the Association of Nurses in AIDS Care*. Elsevier Inc, 29(6), pp. 876–886. doi: 10.1016/j.jana.2018.05.008.

Piersimoni, C. *et al.* (2006) 'Current perspectives on drug susceptibility testing of Mycobacterium tuberculosis complex: The automated nonradiometric systems', *Journal of Clinical Microbiology*, 44(1), pp. 20–28. doi: 10.1128/JCM.44.1.20-28.2006.

Priyanka, R. (2014) 'Interferons and Interferon Therapy', 6(12), pp. 400–403.

Qu, H. *et al.* (2014) 'Silica-coated ZnS quantum dots as fluorescent probes for the sensitive detection of Pb 2 + ions'. doi: 10.1007/s11051-014-2762-y.

Quesada-gonza, D. (2018) 'Chem Soc Rev diagnostic applications'. doi: 10.1039/C7CS00837F.

Qutub, N. and Sabir, S. (2012) 'Optical , Thermal and Structural Properties of CdS Quantum Dots Synthesized by A Simple Chemical Route', 8(2), pp. 111–120.

Quyet Van Le, Jong Beom Kim, Soo Young Kim, Byeongdu Lee, and D. R. L. (2017) 'Structural Investigation of Cesium Lead Halide Perovskites for High-Efficiency Quantum Dot Light Emitting Diodes'. doi: 10.1021/acs.jpclett.7b01709.

Rahman, I. A. and Padavettan, V. (2012) 'Synthesis of Silica Nanoparticles by Sol-Gel : Size-Dependent Properties , Surface Modification , and Applications in Silica-Polymer

Nanocomposites — A Review', 2012. doi: 10.1155/2012/132424.

Ram, C. *et al.* (2017) 'Computational study of leading edge jet impingement cooling with a conical converging hole for blade cooling', *ARPN Journal of Engineering and Applied Sciences*, 12(22), pp. 6397–6406. doi: 10.1039/b000000x.

Raquel, S. *et al.* (2017) 'Corrosion Mechanism Suggested Based on Electrochemical Analysis and SVET for Uncoated Tinplate and Post Coated With a Hybrid Film 2 . Experimental Procedures', 20(6), pp. 1735–1747.

Ricardo Adriano Dorledo de Faria, Hassan Iden, Luiz Guilherme Dias Heneine, T. M. & Y. M. (2019) '3-Aminophenylboronic Acid Functionalized Sensitive Glucose Detection'. doi: 10.3390/s19071686.

Rountree, K. J. *et al.* (2017) 'A Practical Beginner ' s Guide to Cyclic Voltammetry'. doi: 10.1021/acs.jchemed.7b00361.

Rubio, F., Rubio, J. and Oteo, J. L. (2006) 'A FT-IR Study of the Hydrolysis of Tetraethylorthosilicate (TEOS).', 7010. doi: 10.1080/00387019808006772.

Sakai, R. T. *et al.* (2012) 'Progress in Organic Coatings Electrochemical study of TEOS , TEOS / MPTS , MPTS / MMA and TEOS / MPTS / MMA films on tin coated steel in 3 . 5 % NaCl solution', *Progress in Organic Coatings*. Elsevier B.V., 74(2), pp. 288–301. doi: 10.1016/j.porgcoat.2012.01.001.

Salah, T. (2016) 'Nanobiotechnology and Its Agricultural Applications', (April 2014).

Salavati-Niasari, M. *et al.* (2013) 'Surfactant-Free Fabrication of Copper Sulfides (CuS, Cu2S) via Hydrothermal Method', *Journal of Cluster Science*, 24(4), pp. 1181–1191. doi: 10.1007/s10876-013-0608-x.

Sánchez-vergara, M. E. *et al.* (2012) 'Determination of the Optical GAP in Thin Films of Amorphous Dilithium Phthalocyanine Using the Tauc and Cody Models', pp. 10000–10013. doi: 10.3390/molecules170910000.

Santos, C. I. do L. *et al.* (2016) 'Synthesis, Optical Characterization, and Size Distribution Determination by Curve Resolution Methods of Water-Soluble CdSe Quantum Dots', *Materials Research*, 19(6), pp. 1407–1416. doi: 10.1590/1980-5373-mr-2016-0121.

Sapsford, K. E. *et al.* (2006) 'Biosensing with Luminescent Semiconductor Quantum Dots', pp. 925–953.

Selvan, S. T. (2010) 'Silica-coated quantum dots and magnetic nanoparticles for bioimaging applications „ Mini-Review … a …', (October), pp. 110–115. doi: 10.1116/1.3516492.

Sepulveda, D., Aroca, M. A. and Osma, J. F. (2017) 'Bioelectrochemical Detection of Mycobacterium tuberculosis ESAT-6 in an'. doi: 10.3390/s17102178.

Series, I. O. P. C. and Science, M. (2016) 'Green Luminescent Copper Nanoparticles'. doi: 10.1088/1757-899X/149/1/012187.

Shah, N. (2009) 'CREATION OF BIOACTIVE SURFACES TO MODULATE CELL BEHAVIOR USING SURFACE INITIATED PHOTOINIFERTER- MEDIATED GRAFT'.

Shahraki, M. R. and Irani, M. (2014) 'The Effects of Ecstasy on Liver Function Tests, Blood Glucose, and Lipids Profile of Male Rats', *International Journal of High Risk Behaviors and Addiction*, 3(4). doi: 10.1039/c2py20863f.

Shanehsaz, M., Mohsenifar, A. and Hasannia, S. (2013) ‘Detection of Helicobacter pylori with a nanobiosensor based on fluorescence resonance energy transfer using CdTe quantum dots’, pp. 195–202. doi: 10.1007/s00604-012-0906-2.

Shenouda, A. Y., Sayed, E. and Sayed, M. El (2015) ‘Electrodeposition , characterization and photo electrochemical properties of CdSe and CdTe’, *Ain Shams Engineering Journal*. Faculty of Engineering, Ain Shams University, 6(1), pp. 341–346. doi: 10.1016/j.asej.2014.07.010.

Shukla, R. N. (2006) ‘Strategies and techniques of node placement in wireless sensor networks : a Survey’, pp. 2–5.

Sigal, G. B. *et al.* (2017) ‘Biomarkers of Tuberculosis Severity and Treatment Effect: A Directed Screen of 70 Host Markers in a Randomized Clinical Trial’, *EBioMedicine*, 25, pp. 112–121. doi: 10.1016/j.ebiom.2017.10.018.

Simão, E. P. *et al.* (2016) ‘Biosensor based on cysteine monolayer and monoclonal antibody for specific detection of aflatoxin b1 in rice’, *Journal of the Brazilian Chemical Society*, 27(6), pp. 1040–1047. doi: 10.5935/0103-5053.20150361.

Singh, A. *et al.* (2015) ‘Surface functionalization of quantum dots for biological applications’. Elsevier B.V., 215, pp. 28–45. doi: 10.1016/j.cis.2014.11.004.

Sirajuddin, M., Ali, S. and Badshah, A. (2013) ‘Journal of Photochemistry and Photobiology B : Biology Drug – DNA interactions and their study by UV – Visible , fluorescence spectroscopies and cyclic voltametry’, *Journal of Photochemistry & Photobiology, B: Biology*. Elsevier B.V., 124, pp. 1–19. doi: 10.1016/j.jphotobiol.2013.03.013.

Smith, I. (2003) ‘Mycobacterium tuberculosis Pathogenesis and Molecular Determinants of Virulence’, 16(3), pp. 463–496. doi: 10.1128/CMR.16.3.463.

Sobczak, E., Nietubyc, R. and Mac, S. (2002) ‘Three-Dimensional Quantum Dot “ Crystal ” Formation in CdTe / ZnTe Superlattices’, 448(1), pp. 445–448.

Sögaard, C., Funehag, J. and Abbas, Z. (2018) ‘Silica sol as grouting material : a physio - chemical analysis’, *Nano Convergence*. Springer Singapore, pp. 1–15. doi: 10.1186/s40580-018-0138-1.

Song, Y. *et al.* (2014) ‘Novel aqueous synthesis methods for ZnTe / ZnSe’, *RSC Advances*. Royal Society of Chemistry, 5, pp. 6271–6278. doi: 10.1039/C4RA12727G.

Sovan Kumar Patra, BhavyaBhushanb and Priyam, A. (2016) ‘Dalton Transactions’. doi: 10.1039/b000000x.

Sowjanya, K. and Yadla, A. K. (2016) ‘Fundamental Aspects of Biosensors’, 6(6), pp. 1–4.

Srivastava, S. K., Van Rijn, C. J. M. and Jongsma, M. A. (2016) ‘Biosensor-based detection of tuberculosis’, *RSC Advances*, 6(22), pp. 17759–17771. doi: 10.1039/c5ra15269k.

Stawski, T. M. *et al.* (2019) ‘Mechanism of silica – lysozyme composite formation unravelled by in situ fast SAXS’, pp. 182–197. doi: 10.3762/bjnano.10.17.

Stober, W. E. R. N. E. R. (1968) ‘Controlled Growth of Monodisperse Silica Spheres in the Micron Size Range 1’, 69, pp. 62–69.

Sunday, C. E. (2014) ‘No Title’, (March).

Talluri, B., Prasad, E. and Thomas, T. (2018) ‘Superlattices and Microstructures Ultra-small (

r < 2 nm), stable (> 1 year) copper oxide quantum dots with wide band gap', *Superlattices and Microstructures*. Elsevier Ltd, 113, pp. 600–607. doi: 10.1016/j.spmi.2017.11.044.

Tang, X. *et al.* (2017) 'Ultrathin and Highly Passivating Silica Shells for Luminescent and Water-Soluble CdSe/CdS Nanorods'. doi: 10.1021/acs.langmuir.7b00615.

Tashkhourian, J. *et al.* (2016) 'Spectrochimica Acta Part A : Molecular and Biomolecular Spectroscopy A rapid and sensitive assay for determination of doxycycline using thioglycolic acid-capped cadmium telluride quantum dots', *SPECTROCHIMICA ACTA PART A: MOLECULAR AND BIOMOLECULAR SPECTROSCOPY*. Elsevier B.V., 152, pp. 119–125. doi: 10.1016/j.saa.2015.07.063.

'The SAXS Guide' (2013).

Tortoli, E. *et al.* (1999) 'Use of BACTEC MGIT 960 for recovery of mycobacteria from clinical specimens: Multicenter study', *Journal of Clinical Microbiology*, 37(11), pp. 3578–3582. doi: 10.1128/JCM.40.2.607.

Valizadeh, A. *et al.* (2012) 'Quantum dots : synthesis , bioapplications , and toxicity', *Nanoscale Research Letters*. Nanoscale Research Letters, 7(1), p. 1. doi: 10.1186/1556-276X-7-480.

Varshney, R. *et al.* (no date) 'Characterization of Copper Nanoparticles Synthesized by a Novel Microbiological Method'.

Wang, C., Wang, T. and Zhang, Y. (2014) 'Construction of a quantum repeater based on a quantum dot in an optical microcavity system'. doi: 10.1088/1612-2011/11/6/065202.

Wang, M., Chen, Z. and Cao, C. (2014) 'Preparation of magnetic CuInS 2 – ZnS nanocomposites for bioimaging', 120, pp. 50–53. doi: 10.1016/j.matlet.2014.01.031.

Wang, X. *et al.* (2017) 'Fabrication of Electrochemical Immunosensor for Interferon- γ Determination and Its Application of Tuberculosis Diagnosis', 12(April 1993), pp. 7262–7271. doi: 10.20964/2017.08.67.

Wang, Y., Mazurek, G. H. and Alocilja, E. C. (2016) 'Measurement of Interferon Gamma Concentration Using an Electrochemical Immunosensor', 163(5), pp. 140–145. doi: 10.1149/2.0271605jes.

Wen, W. *et al.* (2018) 'Recent advances in emerging 2D nanomaterials for biosensing and bioimaging applications', *Materials Today*. Elsevier Ltd, 21(2), pp. 164–177. doi: 10.1016/j.mattod.2017.09.001.

WHO (2015a) 'Global Tuberculosis Report'.

WHO (2015b) 'WHO | Definitions and reporting framework for tuberculosis', *Who*. Available at: http://www.who.int/tb/publications/definitions/en/.

Wilkins, M. D. *et al.* (2018) 'Sensing and Bio-Sensing Research Quantum dot enabled lateral flow immunoassay for detection of cardiac biomarker NT-proBNP', *Sensing and Bio-Sensing Research*. Elsevier, 21(July), pp. 46–53. doi: 10.1016/j.sbsr.2018.10.002.

Wolcott, A. *et al.* (2006) 'Silica-Coated CdTe Quantum Dots Functionalized with Thiols for Bioconjugation to IgG Proteins', pp. 5779–5789. doi: 10.1021/jp057435z.

Wuister, S. F. and Meijerink, A. (2003a) 'Synthesis and luminescence of (3-mercaptopropyl) - trimethoxysilane capped CdS quantum dots', 103, pp. 338–343.

Wuister, S. F. and Meijerink, A. (2003b) ‘Synthesis and luminescence of CdS quantum dots capped with a silica precursor’, 105, pp. 35–43. doi: 10.1016/S0022-2313(03)00095-4.

Xia, J. *et al.* (2015) ‘Biosensors and Bioelectronics Single electrode biosensor for simultaneous determination of inter- feron gamma and lysozyme’, *Biosensors and Bioelectronic*. Elsevier, 68, pp. 55–61. doi: 10.1016/j.bios.2014.12.045.

Xingli Zou, X. L. and X. X. (2017) ‘We are IntechOpen , the world ’ s leading publisher of Open Access books Built by scientists , for scientists TOP 1 %’.

Ying Liu, Timothy Kwa, and A. R. (2012) ‘NIH Public Access’, 33(30), pp. 1–18. doi: 10.1016/j.biomaterials.2012.06.089.Simultaneous.

Zhang, B. *et al.* (2008) ‘A novel method to enhance quantum yield of silica-coated quantum dots for biodetection’. doi: 10.1088/0957-4484/19/46/465604.

Zhang, Y. *et al.* (2015) ‘Fabrication of an interferon-gamma-based ITO detector for latent tuberculosis diagnosis with high stability and lower cost’. doi: 10.1007/s10008-015-2936-2.

Zhang, Y. *et al.* (2016) ‘Electrochemical immunosensor for interferon- γ based on disposable ITO detector and HRP-antibody-conjugated nano gold as signal tag’, *Materials Science & Engineering C*. Elsevier B.V., 59, pp. 577–584. doi: 10.1016/j.msec.2015.10.066.

Zhong, X. *et al.* (2005) ‘Glucose biosensor based on self-assembled gold nanoparticles and polymer onto gold substrate’, 104, pp. 191–198. doi: 10.1016/j.snb.2004.04.114.

Zhou, J. G., Williams, Q. L. and Wu, R. (2010) ‘Thioglycolic acid on the gold (111) surface and Raman vibrational spectra’, *Journal of Chemical Physics*, 132(6), pp. 1–8. doi: 10.1063/1.3319711.

Zhou, X. *et al.* (2005) ‘Preparation of silica encapsulated CdSe quantum dots in aqueous solution with the improved optical properties’, 242, pp. 281–286. doi: 10.1016/j.apsusc.2004.08.022.

Zi, L. *et al.* (2014) ‘Thioglycolic acid-capped CuInS 2 / ZnS quantum dots as fl uorescent probe for cobalt ion detection’, *Journal of Luminescence*. Elsevier, 148, pp. 359–363. doi: 10.1016/j.jlumin.2013.12.051.

Zook, J. D. and Associates, D. (2008) ‘Sensors as Information Transducers’, 9, pp. 329–359.

Chapter two

Summary

This chapter covers the role of quantum dots and their applications in the field of sensors. Also, this chapter gives an introduction of quantum dots detailing their composition and properties. Biosensors are the most recently studied electro-analytical techniques for the quantitative and qualitative detection of various species, due to the negative impacts they pose on human health and the environment. They have drawn much attention due to their portability, low cost and lower detection limits, which have earned biosensors application in a wide range of fields. This study gives a detailed background on the various aspects involved in this study. These include biosensors, tuberculosis, interferon gamma, and quantum dots.

Ternary quantum dots based electrochemical immunosensor

Abstract

Electrochemical immunosensors have shown promising possibilities as a molecular detection tool, mainly due to their fast response, low cost, high sensitivity and uncomplicated operation for analyte detection. The use of antibody as a bio-recognition element for such constructs has been widely explored with promising results for molecular detection. However, frequent attempts are made to improve sensitivity and selectivity. Thus, the implementation of quantum dots (QDs) in combination with antibody has recently gained interest in the research worldwide. QDs have specific remarkable properties such as quantum confinement effect, accredited to their small size. When combined with antibody the quantum dots have shown to provide a stable microenvironment. High maintenance of the biological activity of the antibody has been shown when immobilized on a QD modified electrode surface. In the case of electrochemical immunosensor, the QDs provide a key element for the biosensor function. This literature review summarizes a number of studies on the combination of QD and antibody in electrochemical biosensors, their structure and function.

2.1 Introduction

Nanotechnology has improved our lives for the better. Nanoparticle-based assays have shown significant improvements in diagnosis, treatment, and prevention of TB (Banyal *et al.*, 2013). However, the lack of detecting on time or not properly monitored are still currently the main causes of enormous death in the world. There is quite a lot of disease that claims lives in this world and tuberculosis is found to be one of those leading causes of deaths worldwide (WHO, 2015b). If tuberculosis is detected on time, it can be prevented. Today, multiple technologies and tools exist that are able to detect disease; therefore, why so many people are still dying due to these diseases? There are two main possible reasons in a few reasons that can be the main cause. First, the lack of equipment, especially in the developing countries, where the costs are not affordable for the whole population or even for medical centers. Second, the time frame between the moment when the symptoms are appreciable by the patient and when diagnostics is accomplished by a specialist (Quesada-gonza, 2018). Then, how can these problems be solved? Should a doctor be present for a single patient, ready at any time with accurate and fast diagnostics or is this a utopia? Now, instead of having a real doctor, imagine having a small device that is portable, easy-to-use, give realistic results, and able to monitor several parameters and variables similar to a portable laboratory. When all the data has been collected the device, it can decide in a few minutes either by itself or by immediate communication with a specialist/ medical doctor what action is required by the patient. The tests can be done at home or even in the field without requiring any kind of medical knowledge by the user (Quesada-gonza, 2018). With the research and findings of the portable device, there was still a gap in a good biomarker that will be used on this device. In research by (Sigal *et al.*, 2017), Interferon gamma was found to the best biomarkers to be used in the detection of tuberculosis. Interferons (IFN) are cytokines that are responsible for the activity of the immune system (Priyanka, 2014).

Therefore, a sensitive determination of these cytokines is of great importance to clinical tuberculosis detection. Interferon-gamma (IFN-γ) is released by the T helper cells under stimulation with antigens, is used to determine prior exposure to infectious diseases and serves as an active diagnosis marker for tuberculosis (Chegou *et al.*, 2014). An increasing amount of evidence indicates that IFN-γ plays a crucial role in the pathogenesis of a chronic inflammatory disease such as tuberculosis (Liu *et al.*, 2015). In addition, it has been reported that IFN-γ takes part in the development of pleural effusion of tuberculosis, and the protein may be a powerful biological marker with high sensitivity and specificity (Decade and Musterman, 2018). Detections of IFN-γ were tried by an immuno-sensing technique that utilizes the antibody, the

ELISA method. This technique has a high sensitivity, whereas it is a labor-intensive and time-consuming traditional method (Min *et al.*, 2008).

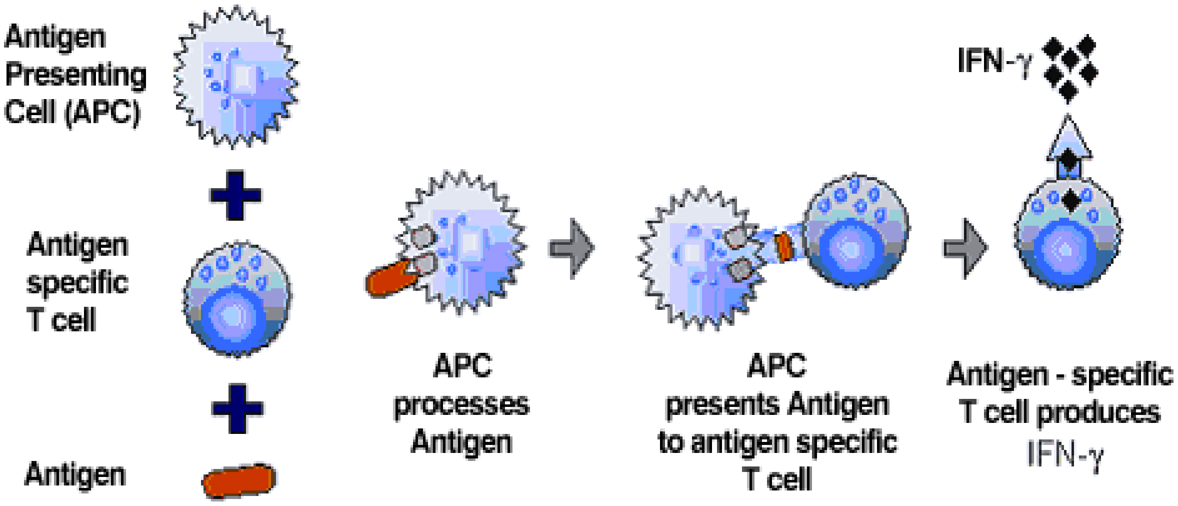

Figure 2.1: Schematic representation of sensitized T-cells in infected individuals will result in far higher levels of IFN-γ release.

2.2 Nanotechnology

“There is a plenty of room at the bottom”, that is how nanotechnology was introduced by physicist Richard Feynman (Feynman, 1992). Nanotechnology is a combination of science, engineering, and technology shepherded at the measurement of a nanoscale, which is about 1 to 100 nanometers. Nanoscience and nanotechnology are the study and application of extremely small things/objects and can be used through all the other science fields, such as chemistry, biology, physics, materials science, and engineering (Abd-elsalam and Alghuthaymi, 2015). Nanotechnology means control of science that comprises synthesis and development of numerous nanomaterials (Hasan, 2014). The definition of a nanomaterial is a material having particles or constituents of nanoscale dimensions, or one that is produced by nanotechnology, or a material that has a size in the nano-scale. The nanomaterial is also a new evolution of understanding and utilization of materials. The nanomaterials that are being made are used in different industries, from medical treatments to solar and oxide fuel batteries for energy storage, to wide incorporation into diverse materials of everyday use such as cosmetics or clothes (Hasan, 2015). Nanomaterials have unique properties, these unique properties of these various types of intentionally produced nanomaterials give them novel electrical, catalytic, magnetic, mechanical, thermal, or imaging features that are highly desirable for applications in commercial, medical, military, and environmental sectors (Madras, 2016). As new uses for materials with these special properties are identified, the number of products containing such nanomaterials and their possible applications continues to grow (Buzea, Pacheco and Robbie, 2007). Currently, there are four types of nanomaterials namely composites, carbon-based materials, dendrimers and metal-based materials (Madras, 2016). Composites combine nanoparticles with other nanoparticles or with larger, bulk-type materials. Nanoparticles, such as nanosized clays, are already being added to products ranging from auto parts to packaging materials, to enhance mechanical, thermal, barrier and flame-retardant properties (Salah, 2016). Carbon-based materials, these nanomaterials are composed mostly of carbon, most commonly taking the form of a hollow sphere, ellipsoids, or tubes (Epa and Osa, 2007). Spherical and ellipsoidal carbon nanomaterials are referred to as fullerenes, while cylindrical ones are called nanotubes. These particles have many potential applications, including improved films and coatings, stronger and lighter materials, and applications in electronics. Metal-based nanomaterials include quantum dots, nanogold, nanosilver and metal oxides, such as titanium dioxide (Madras, 2016).

2.3 Quantum dots

A quantum dot is a closely packed semiconductor crystal comprised of hundreds or thousands of atoms, and whose size is on the order 2-10 nanometers (Park, Jeong and Kim, 2017). Quantum dots (QDs), often described as ‘artificial atoms’, exhibit discrete energy levels, and their bandgap can be precisely modulated by varying the size (Valizadeh *et al.*, 2012). Changing the size of quantum dots changes their optical properties. QDs are nanometer-scale semiconductor crystals composed of groups II to VI or III to V elements and are defined as particles with physical dimensions smaller than the exciton Bohr radius. QDs exhibit unique luminescence characteristics and electronic properties such as wide and continuous absorption spectra, narrow emission spectra, and high light stability (Santos *et al.*, 2016). They absorb white light and then reemit a specific colour a few nanoseconds later depending on the bandgap of the material (Valizadeh *et al.*, 2012). QDs are one of the first nanotechnologies to be integrated with the biological sciences and are widely anticipated to eventually find application in a number of commercial consumer and clinical products. For example, CdSe/ ZnS quantum dots are presently the most common commercially available product as secondary antibody conjugates (Diego, 2015). Quantum dots are advantageous because of their small size, brightness, independence of emission on the excitation wavelength, and stability under relatively harsh environments (Valizadeh *et al.*, 2012). They also have excellent photostability and overcome the limitations associated with photobleaching (Cranfill *et al.*, 2016). Due to the small structures of QDs, some physical properties such as optical and electron transport characteristics are quite different from those of the bulk materials (Valizadeh *et al.*, 2012). In order to use QDs under ambient conditions, they must be stabilized or passivated, because of their high reactivity and surface area. QD range is typically between 2-10 nm in diameter (Jorge *et al.*, 2007). QDs consist of a semiconductor core, over coated by a shell (e.g., ZnS) to improve optical properties, and a cap enabling improved solubility in aqueous buffers (Manchandani *et al.*). When choosing a stabilizer, one has to take into account the absorption and luminescence spectra profile; also the quantum yield and the lifetime depend on the environment composition (Matea and Mocan, 2017). Semiconductor nanocrystals or quantum dots (QDs) from groups II-VI (e.g. CdSe) and III-V (e.g. InP) have been widely studied and found applicable in various biological systems. These applications include molecular histopathology, disease diagnosis, biological imaging among others (G. J. NETTO, R.D. SAAD). There is an increasing interest in the development of nano-theranostics platforms for simultaneous sensing, imaging and therapy. QDs have great potential for such applications, with promising results published in the fields of sensors, drug delivery and biomedical imaging (Jorge *et al.*, 2007). Very good reviews have been published on the use of QDs in new sensing strategies, giving either a general overview of the field, or a more focused discussion on biosensing applications and future trends (Sapsford *et al.*, 2006). *Bard et al.* was the first to study and observe the electrochemiluminescence (ECL) sensor of Si quantum dots (QDs) in 2002 (Jiang and Ju, 2007), and QDs have since attracted particular attention because of their simultaneous excitation, high fluorescence quantum yield, and stability against photo bleaching. QD sensors have been fabricated over the past decade and applied to various fields (Malecha *et al.*, 2019).

2.4 Sensors

A sensor is a device that detects and responds to an input from the physical environment or events. The specific input that it detects could be heat, moisture, pressure, light or any one of the other environment phenomena (Shukla, 2006). A signal of the input is then generated meaning it is converted to human-readable display at the sensor location or transmitted electronically over a network for reading or further processing (Zook and Associates, 2008). A sensor's sensitivity specifies how much the sensor's output variates when the measured quantity changes, it is the relation between output signal and measured property. A good sensor must be sensitive to the measured property only smallest changes in the measured property must be detected by the sensor, be insensitive to any other property likely to be encountered in its application, reproduce the same results repeatedly, the reading must not vary when repeatedly measured under the same conditions, have a signal output that is proportional or bear a mathematical relationship to the amount of species present in the sample, have good signal-to-noise ratio, which determines the limit of the detection, have a fast response time, not influence the measured property, be accurate, be cost effective, be environmentally friendly (Baustian, 1988). The sensitivity and selectivity aspects of chemical sensing are affected by the phase, dimensional, and temporal aspects of the desired determination (Grieshaber1 *et al.*, 2008). There are three main types of sensors based on the property of the entity sensed: physical sensors, chemical sensors and biosensors (Compagnone *et al.*, 2015). Chemical sensor is a device that converts chemical information (which may initiate from a chemical reaction of the analyte or from a physical property of the system) ranging from the concentration of a specific sample component to total composition analysis into an analytically useful signal. Chemical sensors contain usually two basic functional components connected in series: chemical recognition system (receptor) and physico-chemical (transducer). The receptor then transforms the chemical information into a form of energy which can be measured by the transducer. The receptor part of chemical sensors may be based upon various principles: physical change (where no chemical reaction takes place- absorbance, refractive index, conductivity, temperature or mass change), chemical change (in which a chemical reaction with participation of the analyte gives rise to the analytical signal), and biochemical change (in which a biochemical process is the source of the analytical signal such as biocomplexing-immunosensors and biocatalytic enzyme cells). The transducer: This converts the energy carrying the chemical information about the sample into a useful output signal with a defined sensitivity. Physical sensor is a device that provides information about a physical parameter of the system. They are different from chemical sensors in that they measure parameters such as temperature, humidity, speed, depth/pressure, turbidity that regulates the transfer or flux of mass or energy. The analytical device called biosensor is designed for the detection of an analyte by linking a biological recognition component (enzyme, antibody, cell receptor, DNA, microorganisms, organelles, nucleic acids etc.) with a physicochemical signal transducer (Baustian, 1988). This biomimetic component recognises and binds with the analyte under study, then the signal transducer (electrode, optical detector, piezo crystal etc.) converts the biochemical response into electric and optic signals which are amplified, measured and decoded by an appropriate electronic unit (Sunday, 2014). Biosensor consists of 3 parts, the biological recognition component (enzyme, antibody, cell receptor, DNA, microorganisms, organelles, nucleic acids etc.), the transducer (which functions based on electrochemical; optical or piezoelectric principles), and the signal processors that are primarily responsible for the display of the results in a user-friendly way (Choudhary, 2015). Biosensors can be grouped according to their biological element or their transduction principle (Malhotra *et al.*, 2017). The biosensor is described as an affinity sensor when the detected event is the binding of the sensing element and the analyte. Furthermore, if analytical signal is produced after binding with the analyte without chemically changing it except for converting an auxiliary substrate, the biosensor is called a catalytic sensor.

2.4.1 Quantum dot based sensor

Quantum dots have become more attractive nanoparticles for potential use in bio-sensing applications due to the decent stability, sensitivity, good conversion efficiency, and simplicity in preparation. Most of QDs sensors involve QDs functionalized with biomolecules through physical adsorption, electrostatic interaction, covalent binding and specific affinity interaction for analytical applications in DNA analysis, immunoassay, and detection of other biological molecules. (Alia *et al.*, 2018) developed a biosensor where cadmium sulphide quantum dots composited with polyamidoamine dendrimer (CdSQDs-PAMAM) thin film had been successfully developed for use in the detection of dengue virus (DENV) E-proteins. (Ibrahim *et al.*, 2016) have reported an electrochemical biosensor based on reduced graphene oxide (rGO)/cadmium sulphide quantum dots (CdSQDs) nanocomposite for the detection of Mycobacterium tuberculosis. More research based on sensor was done by (Li *et al.*, 2009) a Luminous composite ultrathin films of CdTe quantum dots/silk fibroin co-assembled with layered doubled hydroxide: Enhanced photoluminescence and biosensor application. The prepared (CdTe QDs@SF/LDH) n UTFs were employed as a biosensor using immunoglobulin lgG as a model biomolecule. Quantum dots (QDs) functionalized with bio-recognition antibodies provide a viable method to increase sensitivity and specificity by enabling a 2-part recognition scheme, wherein both the label and capture agent are specific to the target of interest (Wilkins *et al.*, 2018).

2.4.2 Antibody-based biosensors

Antibody-based biosensors are called immunosensors, they ; are affinity ligand-based analytical devices that use antibody or antigen as the specific sensing element and transduce the antigen-antibody interactions directly into signals that are related to analyte concentration (Sowjanya and Yadla, 2016). The basic principle is the specific binding of an antibody to an antigen to form a stable complex. Immunoanalysis is done by measuring several signals associated with the antigen-antibody interactions of known antigen concentrations (Kennedy *et al.*, 1990). The areas where biosensors show particular importance are clinical assay, disease diagnostics, food security, bioprocess, and environmental monitoring. The importance of biosensors results from their high specificity and sensitivity, which allows the detection of a broad spectrum of analytes in complex sample matrices (saliva, serum, and urine) with minimum samples pre-treatment.

In a study done by (He *et al.*, 2011) on Biosensing Technologies for Mycobacterium tuberculosis detection: Status and New Developments, has shown that the rapid development of biosensor technology has opened enormous opportunities for *M. tuberculosis* detection. However, there are still many considerable challenges and issues remained for reliable and effective use in routine applications with biosensors. Sensitivity was found to be one of the challenges, and a solution to this problem is to combine nanotechnology and biosensing technology. This has shown great application in the medical diagnostics, clinical medicine, environmental monitoring, food quality control, defense, and other industries (Wen *et al.*, 2018).

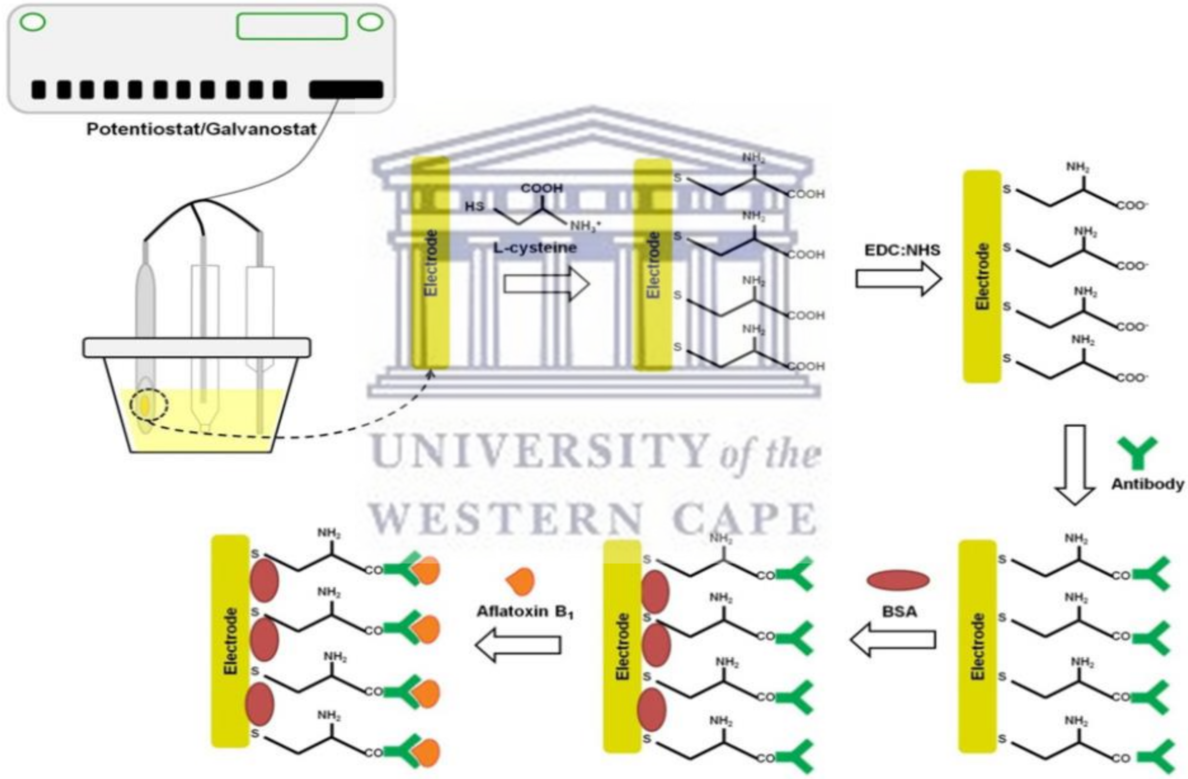

Figure 2.2: Schematic representation of the immunosensor fabrication. Steps of electrode modification consisting in cysteine (Cys) adsorption, COOH activation, antibody immobilization, remaining biding sites blockage by bovine serum albumin (BSA) and sample evaluation.

2.4.3 Electrochemical-immunosensor

Biosensing through the binding between the fragment antigen-binding of the antibody with the epitope interface of the antigen is an affinity-based recognition, therefore, making possible the use of electrical circuitry for the transduction (Chatterjee *et al.*, 2019). These type of biosensors, commonly-named electro-immunosensors, can detect with high selectivity based on the antigen-antibody affinity and, under the appropriate conditions, can be used without the need of lab facilities or highly-trained personnel (Sepulveda, Aroca and Osma, 2017). These electrochemical biosensors convert chemical affinity from an immobilized recognition element binding to the target/analyte molecule into measurable amperometric signal. In order for these sensors to function properly they need to have a specific biomarker. More efficacious treatment regimens are needed for tuberculosis, however, drug development is impeded by a lack of reliable biomarkers of disease severity and of treatment effect (Chen, Neves and Thompson, 2016).

2.5 Interferon gamma

(Sigal *et al.*, 2017) conducted a directed screen of host biomarkers in participants enrolled in a tuberculosis clinical trial to address this need of a good biomarker for the detection of this disease. On the study Interferon gamma was found to be the best biomarker to the time-to-detection. Interferon gamma (IFN-γ) is an important cytokine that possesses antiviral, anti-proliferative, differentiation inducing, and immuno-regulatory properties. This cytokine is produced by a number of immune cell types including T-helper (CD4) cells and cytotoxic T-cells. The detection and quantification of IFN-γ is important for understanding what immune cells are taking part in the immune response and how vigorous this response is(Liu *et al.*, 2010). Interferon-gamma (IFN-γ) is used to determine disease specific immune responses and can be used to serve as an active marker to diagnose infectious diseases like tuberculosis. Detection of IFN-γ was tried traditionally with antibody-based immuno-sensing techniques which are sensitive and specific to cytokines (Farid *et al.*, 2015). In the table below a few examples of detection of IFN- γ and their detection limits.

Type of immunosensor	Analyte	Detection limit	References
Electrochemical immunosensor	Interferon-γ	0.12pg/ml	(Wang *et al.*, 2017)
Electrochemical sensor	IFN- γ	0.06 nM IFN- γ	(Liu *et al.*, 2010)
Immunosensor	IFN-γ	33 pM	(Chang *et al.*, 2012)
Electrochemical biosensor	IFN-γ	1.14_10_3 nM	(Wang *et al.*, 2017)
Label free aptasensor	IFN-γ	11.56 pM	(Ding *et al.*, 2017)

Table 2.1: Electrochemical biosensors for Interferon gamma (IFN-γ) limit of detection.

References

Abd-elsalam, K. A. and Alghuthaymi, M. A. (2015) ‘Journal of Nanotechnology and Materials Science’, pp. 38–40. doi: 10.15436/2377-1372.15.013.

Alia, N. *et al.* (2018) ‘Results in Physics Optical and structural properties of cadmium sulphide quantum dots based thin fi lms as potential sensing material for dengue virus E-protein’, *Results in Physics*. Elsevier, 11(October), pp. 734–739. doi: 10.1016/j.rinp.2018.10.032.

Banyal, S. *et al.* (2013) ‘Advances in nanotechnology for diagnosis and treatment of tuberculosis’, pp. 289–297. doi: 10.1097/MCP.0b013e32835eff08.

Baustian, J. J. (1988) ‘system’.

Buzea, C., Pacheco, I. I. and Robbie, K. (2007) ‘Nanomaterials and nanoparticles: Sources and toxicity’, *Biointerphases*, 2(4), pp. MR17-MR71. doi: 10.1116/1.2815690.

Chatterjee, B. *et al.* (2019) ‘Nanozymes and aptamer-based biosensing’, *Materials Science for Energy Technologies*. The Authors. doi: 10.1016/j.mset.2019.08.007.

Chegou, N. N. *et al.* (2014) ‘Beyond the IFN- c horizon : biomarkers for immunodiagnosis of infection with Mycobacterium tuberculosis’, pp. 1472–1486. doi: 10.1183/09031936.00151413.

Chen, J. B., Neves, M. A. D. and Thompson, M. (2016) ‘Sensing and Bio-Sensing Research Biosensor surface attachment of the ovarian cancer biomarker HSP10 via His-tag modi fi cation’, *SBSR*. The Authors, 11, pp. 107–112. doi: 10.1016/j.sbsr.2016.10.006.

Choudhary, A. K. (2015) ‘Biosensor based on piezoelectric crystal probe’, 6(8), pp. 91–95.

Compagnone, D. *et al.* (2015) ‘Chemical Sensors and Biosensors in Italy : A Review of the 2015 Literature’, pp. 1–22. doi: 10.3390/s17040868.

Cranfill, P. J. *et al.* (2016) ‘Quantitative Assessment of Fluorescent Proteins’, 13(7), pp. 557–562. doi: 10.1038/nmeth.3891.Quantitative.

Decade, T. F. and Musterman, M. I. (2018) ‘Interferon-gamma (IFN-γ): Exploring its implications in infectious diseases’, 1(2), pp. 64–79.

Diego, S. (2015) ‘The Application of Fluorescent Quantum Dots to Confocal , Multiphoton , and Electron Microscopic Imaging’, pp. 112–116. doi: 10.1177/0192623307310950.

Epa, U. S. and Osa, A. (2007) ‘Nanotechnology White Paper’, (February).

Feynman, R. P. (1992) ‘There ’ s Plenty of Room at the Bottom’, 1(i), pp. 60–66.

G. J. NETTO, R. D. S. & P. A. D. I. (no date) ‘Diagnostic molecular pathology: current techniques and clinical applications, part I’, 75246, pp. 379–383.

Grieshaber1, D. *et al.* (2008) ‘Electrochemical Biosensors - Sensor Principles and Architectures’, (January), pp. 1400–1458.

Hasan, S. (2014) ‘A Review on Nanoparticles : Their Synthesis and Types’, *Research Journal of Recent Sciences Res . J . Recent . Sci . Uttar Pradesh (Lucknow Campus),* 4(February), pp. 1–3. doi: 10.3233/978-1-61499-057-4-57.

Hasan, S. (2015) ‘A Review on Nanoparticles : Their Synthesis and Types Biosynthesis : Mechanism’, 4, pp. 9–11.

He, X. *et al.* (2011) ‘Biosensing technologies for mycobacterium tuberculosis detection: Status and new developments’, *Clinical and Developmental Immunology*, 2011. doi: 10.1155/2011/193963.

Ibrahim, I. *et al.* (2016) ‘Cadmium Sulphide-Reduced Graphene Photoelectrochemical Sensing Platform for Copper (II) Ions’, (Ii), pp. 1–18. doi: 10.1371/journal.pone.0154557.

Jiang, H. and Ju, H. (2007) ‘Electrochemiluminescence sensors for scavengers of hydroxyl radical based on its annihilation in CdSe quantum dots film/peroxide system’, *Analytical Chemistry*, 79(17), pp. 6690–6696. doi: 10.1021/ac071061j.

Jorge, P. *et al.* (2007) ‘Optical fiber sensing using quantum dots’, *Sensors*, 7(12), pp. 3489–3534. doi: 10.3390/s7123489.

Kennedy, R. O. *et al.* (1990) ‘n k n o w a n n t g i e n’, 18(3), pp. 136–140.

Li, X. *et al.* (2009) ‘Glucose Biosensor Based on Nanocomposite Films of CdTe Quantum Dots and Glucose Oxidase’, 25(11), pp. 6580–6586. doi: 10.1021/la900066z.

Liu, C. *et al.* (2015) ‘An electrochemical aptasensor for detection of IFN-γ using graphene and a dual signal amplification strategy based on the exonuclease-mediated surface-initiated enzymatic polymerization’, *Analyst*, 140(22), pp. 7784–7791. doi: 10.1039/c5an01591j.

Madras, T. (2016) ‘Chapter - INTRODUCTION TO NANOMATERIALS’, (December 2011).

Malecha, K. *et al.* (2019) ‘Optical Sensors Based on II-VI Quantum Dots’, pp. 1–24. doi: 10.3390/nano9020192.

Malhotra, S. *et al.* (2017) ‘BIOSENSORS : PRINCIPLE , TYPES AND APPLICATIONS’, (2), pp. 3639–3644.

Manchandani, P. *et al.* (no date) ‘Quantum Dots as multifunctional nanoparticles - A review’, pp. 1–8.

Matea, C. T. and Mocan, T. (2017) ‘Quantum dots in imaging , drug delivery and sensor applications’, pp. 5421–5431.

Min, K. *et al.* (2008) ‘A simple and direct electrochemical detection of interferon-γ using its RNA and DNA aptamers’, *Biosensors and Bioelectronics*, 23(12), pp. 1819–1824. doi: 10.1016/j.bios.2008.02.021.

Park, Y., Jeong, S. and Kim, S. (2017) ‘Medically translatable quantum dots for biosensing and imaging’, *Journal of Photochemistry and Photobiology C: Photochemistry Reviews*. Elsevier B.V., 30, pp. 51–70. doi: 10.1016/j.jphotochemrev.2017.01.002.

Priyanka, R. (2014) ‘Interferons and Interferon Therapy’, 6(12), pp. 400–403.

Quesada-gonza, D. (2018) ‘Chem Soc Rev diagnostic applications’. doi: 10.1039/C7CS00837F.

Salah, T. (2016) ‘Nanobiotechnology and Its Agricultural Applications’, (April 2014).

Santos, C. I. do L. *et al.* (2016) ‘Synthesis, Optical Characterization, and Size Distribution Determination by Curve Resolution Methods of Water-Soluble CdSe Quantum Dots’, *Materials Research*, 19(6), pp. 1407–1416. doi: 10.1590/1980-5373-mr-2016-0121.

Sapsford, K. E. *et al.* (2006) ‘Biosensing with Luminescent Semiconductor Quantum Dots’, pp. 925–953.

Sepulveda, D., Aroca, M. A. and Osma, J. F. (2017) ‘Bioelectrochemical Detection of Mycobacterium tuberculosis ESAT-6 in an’. doi: 10.3390/s17102178.

Shukla, R. N. (2006) ‘Strategies and techniques of node placement in wireless sensor networks : a Survey’, pp. 2–5.

Sigal, G. B. *et al.* (2017) ‘Biomarkers of Tuberculosis Severity and Treatment Effect: A Directed Screen of 70 Host Markers in a Randomized Clinical Trial’, *EBioMedicine*, 25, pp. 112–121. doi: 10.1016/j.ebiom.2017.10.018.

Sowjanya, K. and Yadla, A. K. (2016) ‘Fundamental Aspects of Biosensors’, 6(6), pp. 1–4.

Sunday, C. E. (2014) ‘No Title’, (March).

Valizadeh, A. *et al.* (2012) ‘Quantum dots : synthesis , bioapplications , and toxicity’, *Nanoscale Research Letters*. Nanoscale Research Letters, 7(1), p. 1. doi: 10.1186/1556-276X-7-480.

Wen, W. *et al.* (2018) ‘Recent advances in emerging 2D nanomaterials for biosensing and bioimaging applications’, *Materials Today*. Elsevier Ltd, 21(2), pp. 164–177. doi: 10.1016/j.mattod.2017.09.001.

WHO (2015) ‘WHO | Definitions and reporting framework for tuberculosis’, *Who*. Available at: http://www.who.int/tb/publications/definitions/en/.

Wilkins, M. D. *et al.* (2018) ‘Sensing and Bio-Sensing Research Quantum dot enabled lateral flow immunoassay for detection of cardiac biomarker NT-proBNP’, *Sensing and Bio-Sensing Research*. Elsevier, 21(July), pp. 46–53. doi: 10.1016/j.sbsr.2018.10.002.

Zook, J. D. and Associates, D. (2008) ‘Sensors as Information Transducers’, 9, pp. 329–359.

Chapter three

Summary

This chapter describes the synthesis of water-soluble and biocompatible copper telluride quantum dots (CuSe QDs) produced by a simple, inexpensive and reproducible aqueous method. The QD materials were capped with various capping agents such as thioglycolic acid (TGA), (3-mercaptopropyl) trimethoxysilane (MPS) and tetraethyl orthosilicate (TEOS) to improve their stability and solubility. Also, this chapter describes the various chemicals and analytical techniques employed, followed by a detailed experimental procedure based on the synthesis of CuTe QDs. Some techniques used for QDs characterization, such as electrochemical (Cyclic voltammetry), microscopic (HRTEM), spectroscopic methods (UV-Vis absorption, photoluminescence and FTIR) are also presented in the chapter.

Synthesis and properties of water-soluble silica coated Copper telluride quantum dots

Abstract

Copper telluride quantum dots (CuTe QD) materials functionalised with thioglycolic acid (TGA), (3-mercaptopropyl) trimethoxysilane (MPS) and tetraethyl orthosilicate (TEOS) were synthesized by a reproducible aqueous colloidal technique at room temperature. The impact of the capping agents on the size and the confirmation of the crystallinity of the CuTe QD materials, were investigated by small angle X-ray scattering (SAXS) and X-ray diffraction (XRD) spectroscopic techniques, respectively. X-ray diffraction analysis (XRD) confirmed formation of copper telluride species of non-stoichiometric form CuTe (for the TGA, MPS and TEOS capped CuSe QDs). XRD and high resolution electron microscopy (HRTEM) confirmed that TGA capped CuTe QDs had the smallest average particle core size when dried, with average diameter of 5 –7 nm. The CuTe quantum dots were found to be crystalline, spherical in shape and have a different size due to the capping reagents. Whereas small-angle x-ray scattering (SAXS) and HRTEM found that MPS-TGA-CuTe QDs had the high ability to aggregate. The capping of CuTe QDs was confirmed by Fourier transform infrared spectroscopy (FTIR) via the specific S-H, Si-CH_2-S and Si-O-Si signature bands of TGA, MPS and TEOS. UV-vis absorption confirmed a large blue shift of the band gap compared to the bulk material for all formed QDs which is attributed to the quantum confinement effect, Cu only it was 430 nm (with a corresponding band gap of 5.11 eV) and Cu-TGA had an absorption of 230 nm (with a corresponding band gap of 3.91 eV). Photoluminescence (PL) measurements showed that the QDs emits light at 370 nm (TGA-CuTe QDs), 385 nm (MPS-TGA-CuTe) and 382 nm (TEOS-MPS-TGA-CuTe QDs). The electrochemical properties investigated through cyclic voltammetry of the formed CuTe QDs makes them a possible alternative as an electron mediator for electrochemical biosensors. The biosensor was prepared by the self-assembly on a gold electrode that was functionalised with TEOS-MPS-TGA-CuTeQDs, followed by the Antibody and 1-ethyl-3(3-dimethylaminopropyl) carbodiimide hydrochloride (EDC) and N-Hydroxysuccinimide (NHS). The characteristic properties of cyclic voltammetric reduction peak at – 0.4V was used to detect the response of the biosensor to Interferon gamma (IFN-γ). The developed electrochemical biosensor system gave low limit of detection value of 0.042 ng/mL. The *LOD* value is lower thereby indicating that the sensing device would be suitable for monitoring IFN-γ.

3.0 Introduction

Nanotechnology is the root in science, life without it is hard to imagine. Nanotechnology has been used for different applications such as medicine, food, fuel cells, electronics etc. It is rapidly growing by producing nanoproducts and nanoparticles (NPs) that are different in sizes, shapes, physical and chemical properties. Amongst these different nanoparticles there are quantum dots in which its interest has grown over the years due to their unique physical, chemical and biological properties compared to their bulk compound (Jameel, 2010). Quantum dots are semiconductors nanoparticles, their typical dimensions ranging from 1-10 nm (Freitas, Dias and Passos, 2014). Quantum dots have different groups which are group II-VI, III-V, or IV-VI (Jun-Jie Zhu, Jing-Jing Li, Hai-Ping Huang, 2013). They offer advantages including tunable emission spectra, high photostability, resistance to photobleaching, and controllable surface characteristics. The control over surface properties of QDs is important to maintain desirable fluorescent properties and aqueous solubility. Quantum dots are behold to strong quantum confinement effects, and their emission spectra are size-dependent (Wolcott *et al.*, 2006). Quantum dots are then capped which involves introduction of additional layers or coating on the core structure. They can be prepared readily in aqueous media or made water soluble by appropriate capping with hydrophilic ligands. In the aqueous synthesis, QDs are stabilized by some functional ligands, such as mercaptopropionic acid (MPA) and glutathione(GSH), among others, and exhibit some unique properties such as lower cost, less toxicity, water solubility, and biocompatibility (Jimenez-lópez *et al.*, 2016). Quantum dots are capped to make them stable, reduce or eliminate toxicity, improve luminescent properties, avoid agglomeration, biocompatibility and make the quantum dots soluble (Lecture, 2017). Functionalization of the nanoparticle surface is also important to prepare the surface to be exploited for bioconjugation purposes (Wolcott *et al.*, 2006). Generally, quantum dots with capping ligands have been used in highly-sensitive bioanalytical assays such as detection and labelling of biomolecules (Tashkhourian *et al.*, 2016). Since their quantum size effects are understood, fundamental and applied research on these systems has become increasingly popular. One of the most interesting applications is the use of nanocrystals as luminescent labels for biological systems (Wuister and Meijerink, 2003a). Quantum dots (QDs) functionalized with bio-recognition antibodies provide a viable method to increase sensitivity and specificity by enabling a 2-part recognition scheme, wherein both the label and capture agent are specific to the target of interest. For immuno-recognition of a target analyte, immuno-fluorescent probes can be synthesized by linking QDs to targets.

QDs conjugated to biological surfaces generate narrow photoluminescence spectra that enable measuring the concentration of the target analyte (Wilkins *et al.*, 2018). QDs are one of the first nanotechnologies to be integrated with the biological sciences and are widely anticipated to eventually find application in a number of commercial consumer and clinical products (Valizadeh *et al.*, 2012). In this paper, the synthesis and luminescence properties of CuTe quantum dots is described. In this work, we demonstrate the growth of an amorphous silica shell onto as-synthesized water-soluble CuTe QDs. There were three capping reagents that were used Thioglycolic acid (TGA), (3-mercaptopropyl) trimethoxysilane (MPS), and tetraethyl orthosilicate (TEOS). The QDs with and without silica shells have been characterized using electrochemical, spectroscopy and microscopy techniques. This was done to understand the growth of the core shell of the quantum dots after the addition of silica.

3.1 Experimental

3.1.1 Chemicals

All reagents were of analytical reagent grade and purchased from Sigma Aldrich. The material that were used are tetraethyl orthosilicate (TEOS, 90%), thioglycolic acid (TGA, 98%), (3-mercaptopropyl) trimethoxysilane (MPS, 95%), tellurium (Te, 99.997%), sodium hydroxide (NaOH, 98%), copper acetate monohydrate (Cu $(OH)_2CO_3$, 99.0%), sodium borohydride ($NaBH_4$, 98%), sodium phosphate monobasic dihydrate (NaH_2PO_4, 99%) and disodium hydrogen phosphate dibasic (Na_2HPO_2, 98%). De-ionized water, used throughout the experiments, was prepared with a Milli-Q water purification system. Analytical grade nitrogen obtained from Afrox South Africa, was used for degassing buffer solutions. The Phosphate buffer solutions (pH 7.4) was prepared from H_2NaPO_4, HNa_2PO_4 and was used for all the electrochemistry.

3.1.2 Synthesis of silica coated CuTe quantum dots

The quantum dots (QDs) used in this study, was synthesized using the standard procedure described in the literature (Stober, 1968; Wang, Wang and Zhang, 2014). Copper acetate (2 mmol, 0.3993 g) and 400 µL (5.7 mmol) of pure thioglycolic acid (TGA) were dissolved in a three neck round bottomed flask with 25 mL of water and formed a white solution. NaOH (20 g, 5 M) solution was prepared in 100 ml of water and added dropwise to the flask and the solution became clear; and adjusted the pH to 11.8. Then in flask 2, (0.396 g, 3.1 mmol) tellurium and sodium borohydride ($NaBH_4$) (0.227 g, 6.0 mmol) was added together in 25 ml of water, so that the $NaBH_4$ reduces the Tellurium. Flask 2 was heated at 50°C (backfilled with nitrogen) up until the colour changed from black to light purple and to dark purple. Precursor solution of tellurium was then injected to flask 1 to form CuTe, after injection there was a dark-brown colour change. the flask was then backfilled with N_2 and heated up to 100 °C for 1 h, taking aliquots in 20 min intervals. After cooling the reactant solution to room temperature, the TGA-capped CuTe nanoparticles were reacted with (3-mercaptopropyl) trimethoxysilane (MPS) for 1 h under stirring, and aliquots taken at 20 min intervals. To ensure even distribution of MPS, a mini-stir bar was used during the 1 h required for surface priming. After the hour the solution was heated for 5 minutes at 60 °C, it has been found that the average size of quantum dots increases with the increasing heat treatment temperature (Wolcott *et al.*, 2006). In this process, aliquots were taken at different times to check the growth of the quantum dots. After surface priming, tetraethyl orthosilicate (TEOS) (1270 µL, 5.7 mmol) was added to the solution under stirring to initiate silica at the particle surface, aliquots were taken at different times (20 min, 40 min, 60 min) to check the growth of the quantum dots. Then at 14 h and 40 h aliquots were then taken to check the growth of the quantum dots.

3.1.3 Preparation of CuTe/Au modified electrode

Prior to modification, the bare gold electrode (AuE) was polished to a mirror finish with 1.0, 0.3, and 0.05 µm alumina slurries, respectively, and then rinsed thoroughly with distilled water followed by sonication for 20 minutes in ethanol and water, respectively. After the cleaning of electrode, 3.0 µL of CuTe quantum dots solution was drop coated on the gold electrode surface and let to dry overnight. A three electrode system was used for analysis and electrochemical application, and composed of platinum counter electrode, silver/silver chloride reference electrode and gold working electrode. Phosphate buffer (5 ml) was transferred to an electrochemical cell and N_2 bubbled to remove dissolved oxygen. This was done before experiments. The cyclic voltammetric curve started from -1.2 V to +1.2 V/ and back to -1.2 V/.

3.1.4 Preparation of immunosensor system

The CuTe/AuE modified electrode was then activated by drop coating a 30 µL solution containing 1:1 of (EDC/NHS), stored for 30 min in a dark place. After that the CuTe/AuE modified electrode was rinsed carefully with PBS. Subsequently, 10 µL of antibody solution (10 µM) was drop coated on to CuTe/AuE surface. The electrode was then stored for 2 hours at room temperature in a dark place. The electrode was then washed with PBS solution. BSA solution (1%) was used for blocking the nonspecific sites, using 1µL of the solution. The reaction occurred at room temperature for 10 min. 3μL of IFN-γ solution was drop coated on the surface of the electrode and the IFN-γ immunosensor was then washed with PBS solution.

3.2 Instrumentation

The photoluminescence measurements were performed utilising Nanolog, Horiba NanoLog^{TM} 3-22-TRIAX (Horiba Jobin Yvon, USA) and the data was analysed using a FluoroEssence software. The excitation wavelength used was 340 nm. High resolution transmission electron microscopy (HRTEM, Hitachi H800) measurements were performed using a Tecnai G2 F20X-Twin MAT FETEM from FEI (Eindhoven, Netherlands) and it is a 200 kV instrument equipped with Energy dispersive spectroscopy (EDS). Small-angle X-ray scattering (SAXS) (Anton peer, Australia) system using 1 nm diameter quartz capillary positioned at 317mm from the CCD and temperature controlled at 20 °C. Data evaluation was performed with the Generalized indirect Fourier transformation (GIFT) software (which is a versatile tool for the evaluation of small angle scattering data). X-ray diffraction (XRD) was used using a Bruker AXS D8 Advance diffractometer (voltage 40 kV; current 40 mA). The XRD spectra were recorded in the range15-85 θ. Fourier-transform infrared (FTIR) spectroscopy were recorded in the range 4000 - 1000 cm^{-1} using a Perkin Elmer model Spectrum 100 series. Raman spectroscopy samples were prepared on a glass slide and analysed using Xplora Raman spectrometer (Horiba Scientific) utilising a 514 nm He-Cd laser as an excitation source. Data capturing and instrument control were performed using LabSpec software. Ultraviolet-visible (UV-Vis) absorption measurements for CuTe QDs were prepared using a Nicolet evolution 100 UV-Vis spectrophotometer (Thermo Electron Corporation, UK) and the instrument was controlled with VisionPro software. UV-vis absorption spectra were measured over a range from 200 nm - 800 nm. The solutions of quantum dots in water placed in 1 cm quartz cuvette and their absorbance were measured. The cyclic voltammograms for each nanomaterial were collected using an electrochemical workstation connected to three electrodes: gold electrode (working), Ag/AgCl (reference) and silver wire (counter) immersed in a PBS buffer (pH = 7.4) as an electrolyte. The experiments were performed over a potential range of +1200 mV to -1200 mV and a scan rate of 50mV/s. The workstation was controlled using PalmSens (PS) trace software.

3.3 Results and Discussion

3.3.1 Ultraviolet-visible spectroscopy

UV-Vis is used to give the formation, shape and stability of copper nanoparticles and the different capping reagent used in aqueous solutions. The UV absorption spectrum of as-prepared copper acetate monohydrate, copper quantum dots capped by thioglycolic acid is recorded as shown in *Figure 3.1*. The copper bulk material showed a band at wavelength 430 nm (inset). The absorption properties of TGA forms were investigated using also room-temperature UV-Vis spectrophotometry. The absorption spectrum of CuTe QDs obtained a band at 232 nm and 282 nm. These features were assigned to transitions from the ground state to the S1 (282 nm) and S2 (232 nm) excited electronic states, in agreement with previous findings on analogous mercaptocarboxylic acid molecules (Attar, Blumling and Knappenberger, 2011). For instance, Fang and co-workers (Fang *et al.*, 2012) reported the synthesis of CdTe quantum dots prepared by colloidal synthesis route using the branched mercaptopropionic acid, 3 Mercaptoisobutyric acid (3-MIBA) as capping agent. From the obtained UV–vis results, the CuTe QDs exhibited a characteristic band at 320 nm. The CuTe QD prepared in this study showed a band at 336 nm and the band gap was 3.96 eV, which is close to the wavelength of CuTe that was studied. In comparison, the characteristic peak of 3-MIBA observed at 290 nm in the reported study by (Choudhary and Nageswaran, 2019), the peak shifted to 247 nm in the case of CdTe@3-MIBA QDs the study is very similar to this study. These result suggests the possible attachments or interaction of thiol ligands from capping agent with the QDs. The band at 282 nm is attributed to $n\text{-}\sigma^*$ transition, the structure of the capping reagent contains CH_3SH. In *Figure 3.1.*, the thioglycolic acid showed a band at 232 nm and at 282 nm, however, after the formation of the TGA-CuTe QDs the intensity of the TGA peak decreased to 247 nm which indicate the attachment of thiol ligands to the QDs. The TGA-CuTe QDs, had an absorption band appeared at 247 nm and 336 nm respectively. The band at 247nm is attributed to ligand to metal charge transfer (LMCT) transition from S (σ) to Cu^{2+}, between the copper and the sulphur atom from the capping agent (Ambika *et al.*, 2019). Therefore, the band at 336 nm in the TGA-CuTe QDs could be assigned as the LMCT between the copper in the QDs and the capping agent, with a slight shift towards lower energies from the bulk of Cu 430 nm (inset). The blue shift of the peak at 282 nm observed for TGA result from the presence of the electron-donating -OH functional group in TGA. The absorption band at 336 nm where the quantum dots form is attributed $\pi\text{-}\pi^*$ transition.

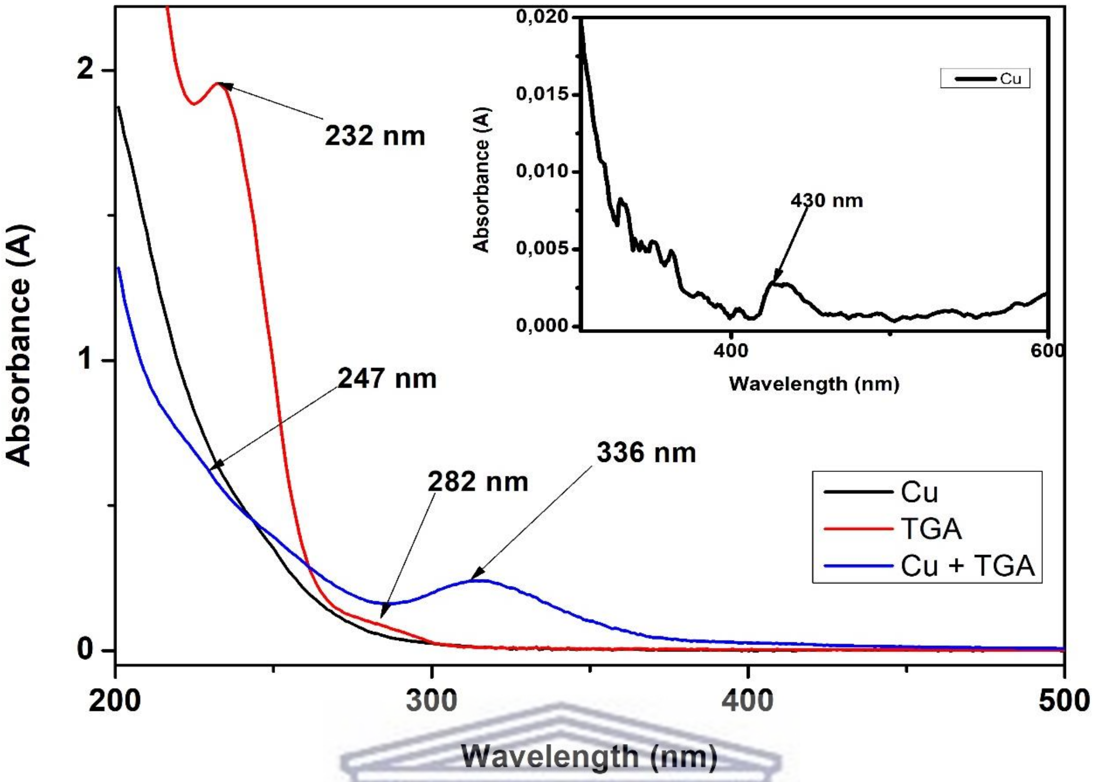

Figure 3.1: Absorbance spectra of Copper (black line), Thioglycolic acid (red line) and copper and TGA (blue line).

From the absorption spectra, the direct and indirect band gap was determined by Tauc-relation (Equation 1).

$$\alpha h\nu = \mathrm{A}\,(h\nu - Eg)^{\mathrm{n}} \qquad (1)$$

Where α is the absorption coefficient, h is Planck constant, υ is the frequency, A is a constant, Eg is the energy band gap and n = 2 for indirect and n = 1/2 for direct allowed electron transitions. The direct band gap energy (Egd) was obtained by plotting $(\alpha h\upsilon)^2$ against $h\upsilon$ and extrapolate the linear portion of the curve $(\alpha h\upsilon)^2 = 0$. The indirect band gap energy (Egi) was determined from $(\alpha h\upsilon)^{1/2}$ against $h\upsilon$ and extrapolation of $(\alpha h\upsilon)^{1/2} = 0$ from the linear region (Sánchez-vergara *et al.*, 2012). The results are shown in *Figure 3.2*, where the copper band gap and TGA-CuTe bang gap are demonstrated. Straight lines were drawn to fit the experimental bandgap curves, and they were extended to intercept the x axis to determine the optical bandgap of the CuTe QDs. It was found that the optical bandgap decreased from 5.11 eV (bulk Cu) to 3.956 eV (TGA-CuTe QDs), is attributed to the increase in particle size. It is believed that as the particle size increased, the number of atoms that formed a particle also increased, consequently rendering the valence and conduction electrons more attractive to the ions′ core within the particles and decreasing the bandgap. This is due to the strong quantum confinement.

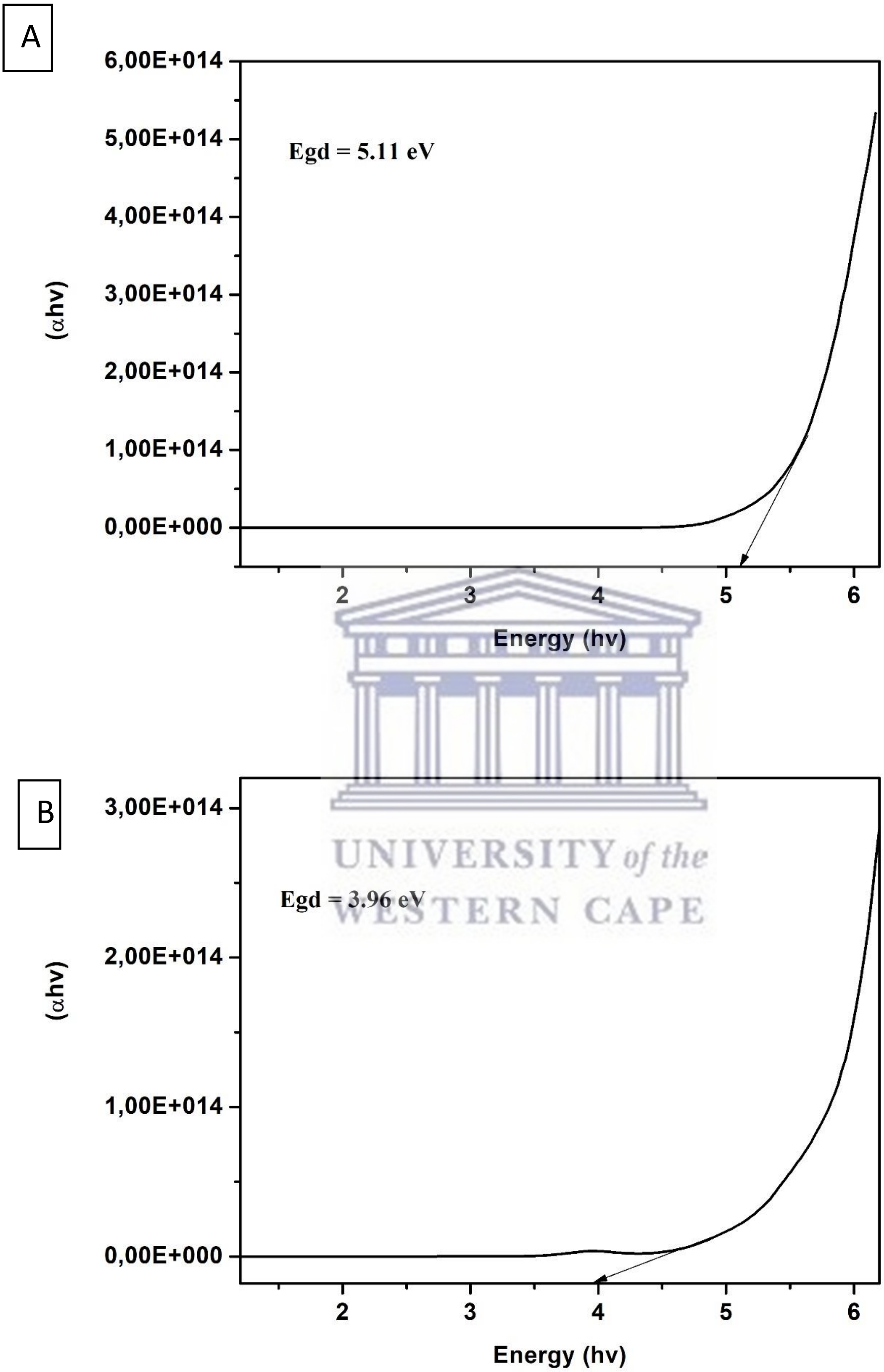

Figure 3.2: A) The direct band gap plot of Copper (bulk) only. B) The direct band gap plot of TGA-CuTe.

The process of creating a layer of amorphous silica on the surface of nanoparticles is called silanization (Rahman and Padavettan, 2012). Silica shows anomalous behaviour in water and shows strong stability at near neutral pH even under high salt concentration. The high stability of silica arises from the strong short range forces of the order of 4 nm (Sögaard, Funehag and Abbas, 2018). The stability of the dispersion, coating QDs with silica layer does not alter the optical properties of QDs. Even though the particle size increases by silica encapsulation of QDs, the sols display the properties of core QDs and do not display large changes in the exciton absorbance or PL. Most developments have been made in the surface activation step of QDs for silanization (Singh *et al.*, 2015). In this work that was done the addition of the TGA-CuTe QDs with silica coating by using (3-mercaptopropyl) trimethoxysilane (MPS) as the first layer of silica, (Kobayashi, Correa-Duarte and Liz-Marzán, 2001) was the first to perform this. The silica shell was then grown in thickness using the conventional Stober process by addition of tetraethyl orthosilicate (TEOS) to the colloidal solution. The diagram below *Figure 3.3* shows the absorption spectra of the process of surface silanization from TGA-CuTe to MPS-TGA-CuTe then a thicker shell TEOS-MPS-TGA-CuTe.

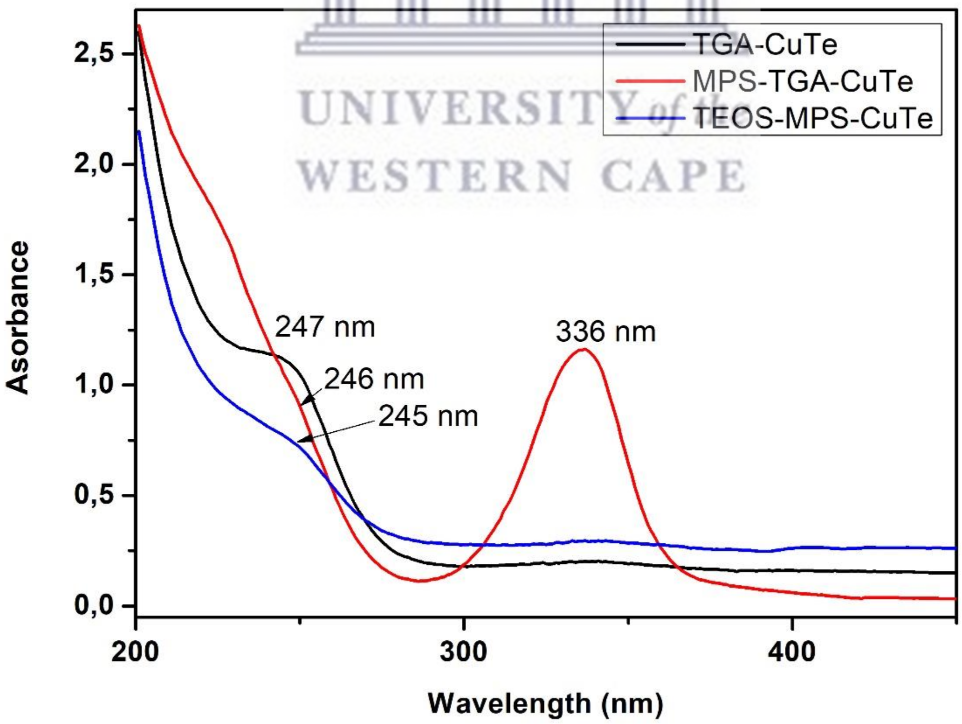

Figure 3.3: UV-vis spectra of TGA-CuTe, MPS-TGA-CuTe and TEOS-MPS-CuTe quantum dots.

In the absorption spectra for MPS-TGA-CuTe QDs bands between 226 - 247 nm could likewise be assigned to transitions caused by the TGA-CuTe and MPS precursors. A very sharp band at 336 nm could be attributed to the formed MPS-TGA-CuTe QDs (Wuister and Meijerink, 2003a). The band gap was calculated and it was Egd = 4.26 eV. This shows a red shift from the TGA-CuTe QDs. The peak positions of core/shell spectra are red-shifted compared to their corresponding core TGA-CuTe QDs. This may indicate an increase in the overall nanoparticle size as a result of growth of the shell around the TGA-CuTe QDs (Ke *et al.*, 2019). The UV-vis absorption spectrum shows the characteristic electron-hole pair (exitonic) peak representative of the band gap energy. During the growth of the quantum dots, smaller particles will dissolve and become the constituents of larger particles, this leads to exitonic peak positions shifting to longer wavelengths as the QD grows to larger diameter. This process is known as Ostwald ripening. An effect of the Ostwald ripening is the increase in size distribution, a phenomenon termed “defocusing”. This effect is seen clearly in the “flattening” of the exitonic peak as particles increase in size during the growth phase (Garcia-gutierrez *et al.*, 2018). Narrow size distributions are reflected in a very sharp exitonic absorption peak (Wolcott *et al.*, 2006). TEOS-MPS-TGA-CuTe show the derivative QD@SiO_2 aqueous solutions exhibited almost identical UV-vis absorption to those of the MPS-TGA-CuTe QDs. These results indicate that the process of silica coating has no effects on the electronic properties of the inorganic QD cores, and the obtained QD@SiO_2 maintains great dispersibility without obvious aggregation of the QDs inside the silica spheres (Ma *et al.*, 2014). The flattening of the band at 336 nm shows the change on the surface of the quantum dot and the red shift of the band at 226 to 249 nm shows the growth of the quantum dots. It is likely that absorption due to light scattering from the silica particles made the absorption features appear less sharp for the QDs (Goftman *et al.*, 2016). This was then proven by the increase of the band gap between MPS-TGA-CuTe and the band gap of TEOS-MPS-TGA-CuTe. The band gap of TEOS-MPS-TGA-CuTe increased to Egd = 4.95 eV, this is an indication of a shell or growth of the quantum dots with the addition of TEOS (Morales-saavedra *et al.*, 2015).

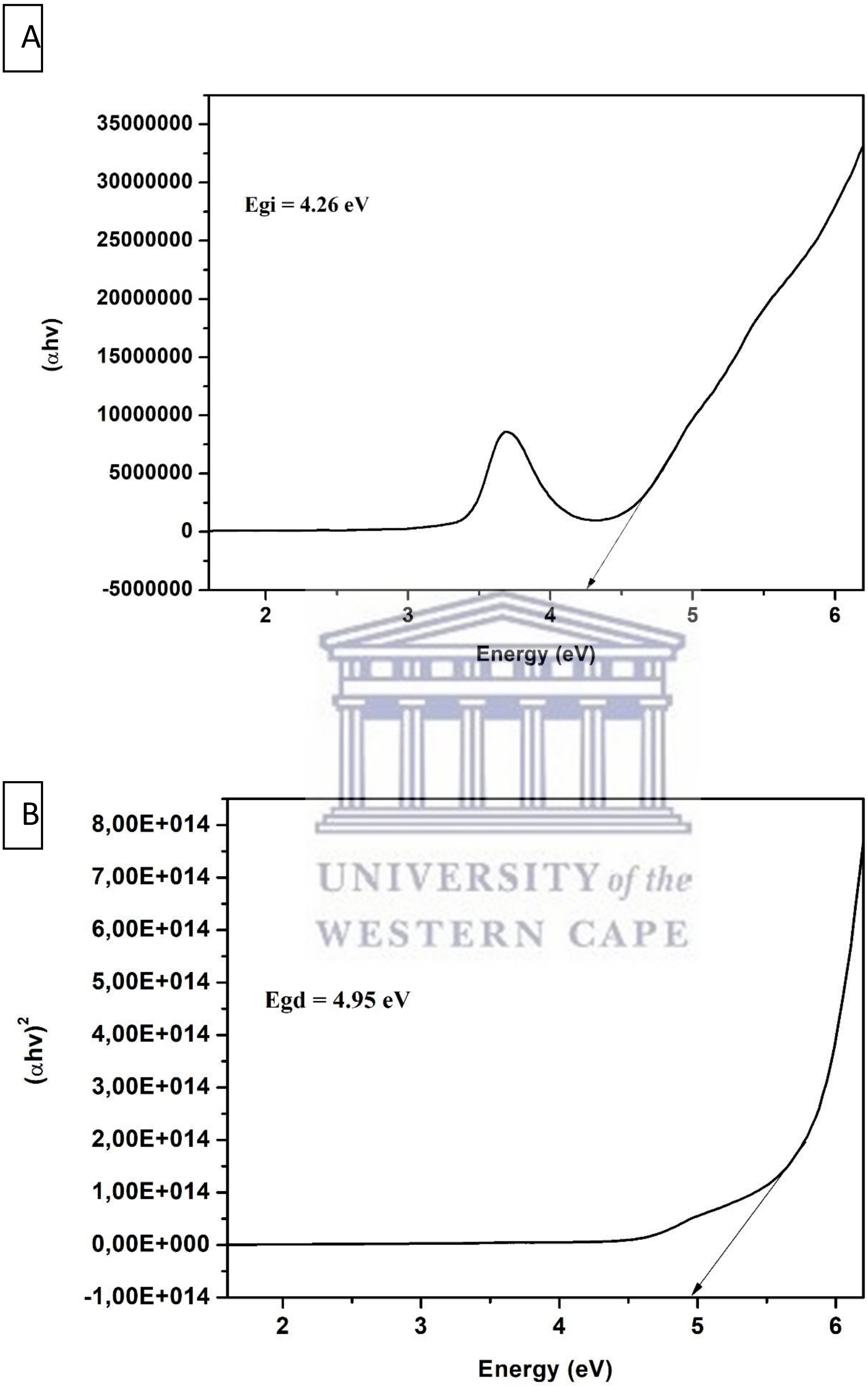

Figure 3.4: A) The direct band gap of MPS-TGA-CuTe. B) The direct band gap plot of TEOS-MPS-TGA-CuTe.

3.3.2 Photoluminescence

Photoluminescence (PL) in metals is very rare owing to their lack of bandgap. In 1969, Mooradian first observed the photoluminescence of bulk copper and extensively used it in explaining the band structure of metals (Gfroerer, 2000). This emission is attributed to direct radiative recombination of the excited electrons in the sp band with the holes in the d band. Visible PL from nanostructures smaller than 15 nm has been reported. Usually the visible photoluminescence from noble metal nanoparticles is due to the inter-band transition between the sp conduction bands and the d bands. The electronic structure of copper atom can explain the photoluminescence spectra of Cu nanoparticles. In the case of copper, 3d valence and 4sp conduction electrons play the role for fluorescence. The outermost d and s electrons of all the constituent atoms of the nanoparticles create six bands (Nagaveni *et al.*, 2018). Five of these bands lie below the Fermi level, which are denoted as d bands and the sixth band, the last band, which lies above the Fermi level, is known as the conduction band or sp band (Series and Science, 2016). Metals can be excited by a low intensity source in the UV region of spectra, Siwach and Sen reported a fluorescence peak of copper nanoparticles at 296 nm with excitation wavelength in the ranges 200–240 and 250–280 nm. Wilcoxon et al. reported that small spherical gold clusters show an emission at 440 nm when excited at 230 nm (Das, Nath and Bhattacharjee, 2011). These finds are similar to the work done in this paper. *Figure 3.5* shows typical absorption and PL spectra of a size series of CuTe QDs. The spectra were measured on as-prepared CuTe solutions which were taken from the reaction mixture and diluted with water. The copper bulk had an emission peak at 477 nm (Talluri, Prasad and Thomas, 2018). For the formation of quantum dots there was a blue-shifting 370 nm compared with bulk CuTe (477 nm) which was caused by quantum confinement effect. The similar results of emission peak of CuTe were found for CuS (Salavati-Niasari *et al.*, 2013). The strong blue-shifting indicated that the particle size was very small. When the capping reagent TGA is added to the bulk material copper, the peak of the copper telluride quantum dots is blue shifted. The narrow band is mostly attributed to the recombination of the carriers trapped in the surface states of the bare copper telluride quantum dots. The emission spectrum undergoes a blue shift from the bulk bandgap indicating the existence of quantum confinement (Kaviyarasu *et al.*, 2016).

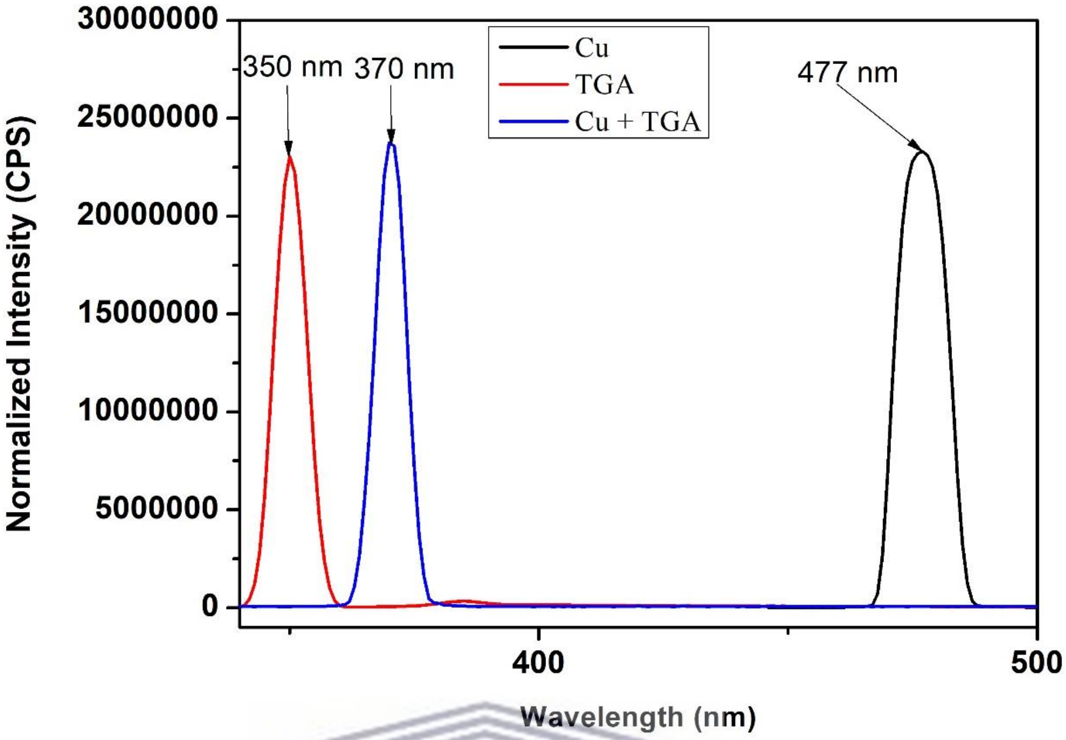

Figure 3.5: PL diagram of Cu, TGA and the addition of TGA-CuTe.

Photoluminescence emission spectra was mainly intended to be used to investigate the outcome of photo generated electron and holes in a semiconductor, since PL emission results from the recombination of free charge carriers. The electronic band structure in which the highest occupied molecular orbital (HOMO) or valence band and lowest unoccupied molecular orbital (LUMO) or conduction band semiconductor material is characterized. Smaller particles have lower values of λmax. *Figure 3.6* shows the change of the PL properties of the QDs in the coating process. TGA-CuTe QDs show a pronounced, relatively luminescence peak at 370 nm. After coating of the MPS-TGA-CuTe, there was a red-shift on the peak from 370 nm to 385 nm (Wuister and Meijerink, 2003). With the increase of the TGA-CuTe wavelength 370 nm (with band gap 5.35 eV), then MPS-CuTe the wavelength increased to 382 nm (with a band gap 5.19 eV) and the TEOS-CuTe increased to 385 nm (with a band gap of 5.15 eV). The reason for the wavelength increase is the formation of a silica shell, which passivates the CuTe surface defects. During the experiment it is found that, in the process of surface silanization, the PL peaks of the QDs red shift. This might originate from re-absorption by larger QDs in the assembly because the PL from the smaller QDs leads to re-absorption by the adjacent larger QDs due to the high QDs concentration. The decrease of the wavelength of luminescent Si particles from TEOS-MPS-TGA-CuTe are ascribed mainly to (a) partial ligand exchange of TEOS for MPS (b) the change of the refraction index of the media (c) the inhomogeneous broadening of the electronic transitions affected by the local morphology. The measurements show that the synthesized QDs are capable of emitting light of wavelengths in the visible region. The decrease of the wavelength can be explained by quenching of the capping agent on the surface (Onwudiwe, Hrubaru and Ebenso, 2015).

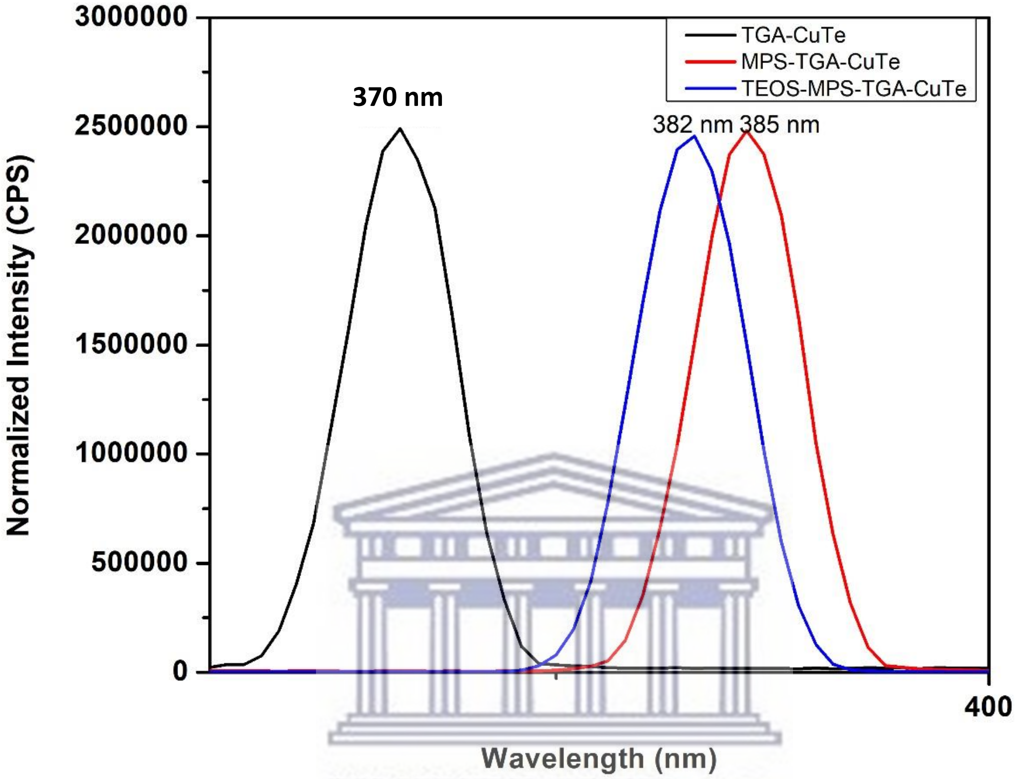

Figure 3.6: PL spectra of TEOS-MPS-TGA-CuTe, MPS-TGA-CuTe, TGA-CuTe quantum dots at 1hour.

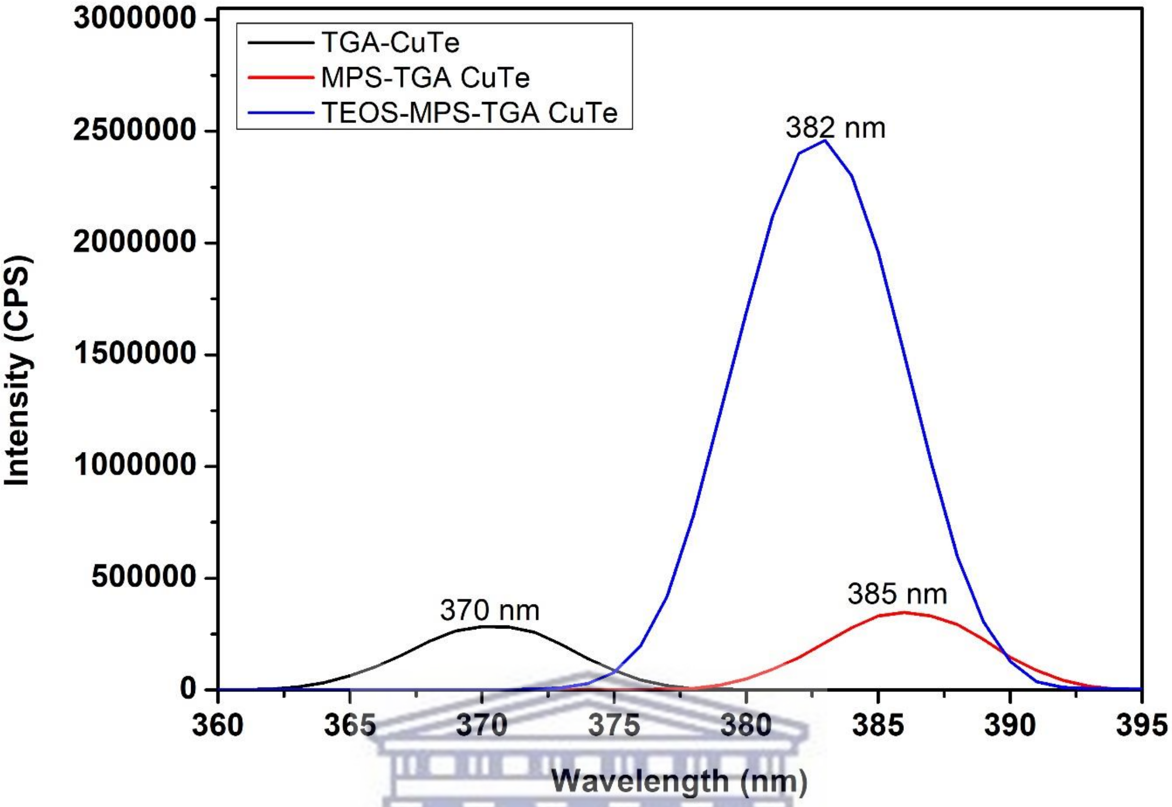

Figure 3.7: Photoluminescence intensity of (black line) TGA-CuTe QDs, (red line) MPS-TGA-CuTe QDs and (blue line) TEOS-MPS-TGA-CuTe QDs.

Figure 3.7 shows the improvement of the PL properties of the QDs in the coating process. The TGA-CuTe QDs showed a small intensity at 370 nm. From TGA-CuTe QDs to MPS-TGA-CuTe QDs the intensity increased, showing the addition of (3-mercaptopropyl) trimethoxysilane (MPS) formed a shell around the QDs (Labiadh and Hidouri, 2017). The addition of tetraethyl orthosilicate (TEOS) formed a thicker shell on the QDs and this is indicated by the extreme high intensity of TEOS-MPS-TGA-CuTe QDs from MPS-TGA-CuTe QDs. Obviously, the PL intensity of the final QDs with a thick rigid shell of silica was much stronger than that of the initial QDs. The reason for the increased PL intensity is the formation of a thick silica shell, which may have a higher potential for the ground-state electron (Zhou *et al.*, 2005). The broad band of all the quantum dots is an evidence of monodispersity of the quantum dots (Wuister and Meijerink, 2003).

3.3.3 X-ray diffraction

Chemical composition and stoichiometry of the CuTe QDs and crystallinity was evaluated through x-ray diffraction (XRD). Powder X-ray diffraction patterns for the CuTe QDs capped with TGA, MPS and TEOS are illustrated in *Figure 3.8* to *Figure 3.10* below.

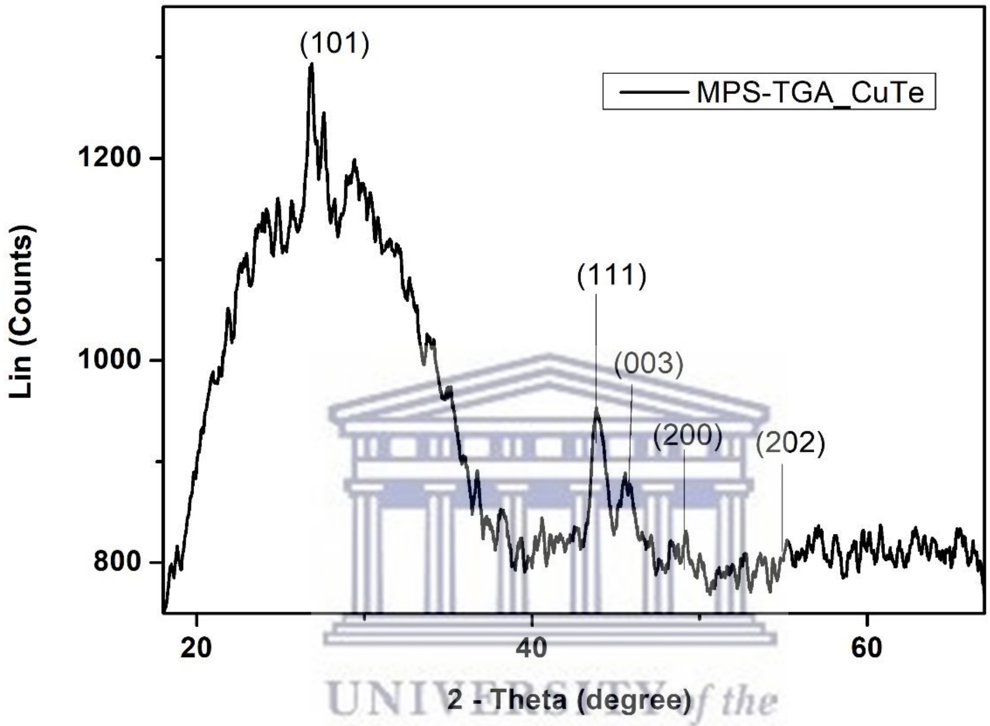

Figure 3.9: The x-ray diffraction of MPS-TGA-CuTe quantum dots.

Investigating the phase purity and crystal structure, the powder products were examined by XRD and the results are shown in *Fig. 3.9*. The diffraction peaks can be indexed to those of pure face centered cubic (f.c.c.) Cu (JCPDS, File No. 04-0836), corresponding to 44° (111). The observation of diffraction peaks for the Cu nanoparticles indicates that these are crystalline in nature (Piersimoni *et al.*, 2006). The phases of copper telluride can be easily distinguished by the powder X-ray diffraction pattern, all of the peaks can be indexed as (003) and (200) (Dhasade, Han and Fulari, 2012). Crystal silicon (c-Si) has peaks at 28°, 47°, and 56° (Baustian, 1988). In this work, the (3-mercaptopropyl) trimethoxysilane (MPS) contains a silicon and the diffraction peaks in *Figure 3.9* are present at 28° and 56° which indicates the presence of crystal silicon. It can be concluded that the nature of the capping group influences the preferable growth direction of quantum dots (Onwudiwe, Hrubaru and Ebenso, 2015).

Three main peaks at diffraction angle 2θ= 46° and 49.5° are clearly observed which be longs to (003) and (200) crystal plane. The peaks at 28°, and 56° corresponding with 101, and 202 respectively show planes which is in good agreement with the JCPDS (Join Committee on Powder Diffraction standers) card no. 00-036-1452 with a = 4.45790, and c = 5.92700 of CuTe with face-centered cubic structure. These positions of diffraction pattern matched well with standard CPDS card no. 49-1411 (a) 3.80 Å, and (c) 21.923 Å cubic of Cu_2Te. The observation of diffraction peaks for the Cu nanoparticles indicates that these are crystalline in nature. The XRD pattern of the QD powder sample is shown in figure 2, which indicated that the QDs had a cubic zinc blende crystalline structure. The broadening of the XRD peaks, therefore, believed to be caused by the quantum confinement (Li, Shih and Shih, 2007; Pal *et al.*, 2017). The peaks with irregularity in baseline are observed to be broad due to the presence of both amorphous and crystalline contents in the synthesized quantum dots (Choudhary and Nageswaran, 2019). The average crystallite size of CuTe QDs, was calculated from the peak width at half-maximum of the (101) plane of the higher intensities in all patterns, using the Debye-Scherrer equation:

$$D = K\lambda/\beta Cos\theta$$

where β the broadening at half band width, λ the wavelength of the X-ray, θ is the angle of diffraction obtained from 2θ value corresponding to maximum intensity peak pattern, and K is a dimensionless shape factor, with a value close to unity. The peak position and resolution were determined by using Gaussian peak fitting method (Gadalla *et al.*, 2017). From different θ values, the calculated average particle size is about 5.67 nm.

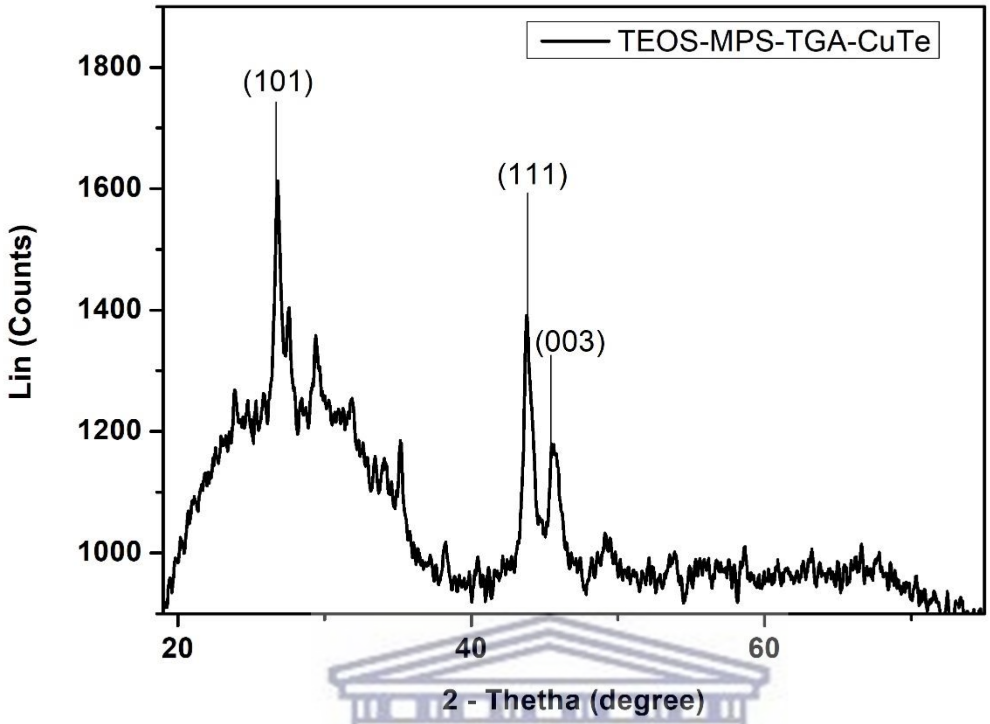

Figure 3.10: The x-ray diffraction of TEOS-MPS-TGA-CuTe quantum dots.

The XRD pattern of the sample is shown above. Diffraction peaks can be indexed to those of pure face centered cubic (f.c.c.), corresponding to the (101), (111), and (003) planes. The XRD patterns of the QDs are considerably broadened due to their small sizes. The XRD patterns exhibit prominent broad peaks at 2θ values of 27°, 42° and 46°. The peak at 25° was shifted to a slight larger angle as the size increases (Kumar and Hymavathi, 2017; Hao *et al.*, 2019). XRD patterns indicated that the lattice parameters of CuTe QDs fitted well to the zinc blende structure which is the dominant crystal phase of bulk CuTe (He *et al.*, 2015). The broad peaks belonging to (101), (111) and (003), from MPS-TGA-CuTe also appear for TEOS-MPS-TGA-CuTe and these peaks are more pronounce in case of sample TESOS-MPS-TGA-CuTe. These results clearly indicate that CuTe has purely cubic zinc blende structure (JCPDS file. 19-0191) and the particle size increases from MPS-TGA-CuTe to TEOS-MPS-TGA-CuTe (Hodlur and Rabinal, 2014). The broadening of the peaks can also be due to the increase of the core-shell. TEOS is used to thicken the shell of the CuTe QDs. The crystal structure (face-centered cubic) was confirmed through selected area electron diffraction (SAED). The crystallite size can be found by applying Sherrer's equation and the average crystallite size is found to be 6.39 nm.

No diffraction peaks from other species could be detected, which indicates that the obtained sample is pure.

3.4.4 High resolution transmission electron microscopy

Particle size, morphology and further assessment of crystallinity was evaluated using high resolution transmission electron microscopy (HRTEM) together with energy dispersive x-ray spectroscopy (EDX) to confirm the chemical composition. HRTEM studies were performed on a nickel grid where samples were sonicated, drop coated and allowed to dry under lamp. In *Figure 3.11* (A), the nanoparticles observed are spherical structure (Abd Rahman *et al.*, 2017) with some of the particles showing aggregation (Qutub and Sabir, 2012). The HRTEM image show the lattice fringes and this shows that the quantum dots have a perfect solid crystalline structure, this finding is close to the find of TGA-CdTe (Ebrahim *et al.*, 2017). As shown in *Figure 3.11*, the quantum dots are spherical morphology with a particle size of about 5.85 nm (Shanehsaz, Mohsenifar and Hasannia, 2013). The selected area diffraction (SAED) pattern in *Figure 3.11 (B)* shows discontinuous rings with bright spots, indicating that the nanoparticles formed are crystalline. The fact that some rings appear in higher intensities (101) indicates that the QDs have a certain preferred orientation of the CuTe planes in contrast to random orientation. Energy dispersive X-ray spectrum shown in *Figure 3.11* (C) revealed the chemical composition of as-prepared CuTe QDs interacting with thioglycolic acid (ref CdTe quantum dots capped).

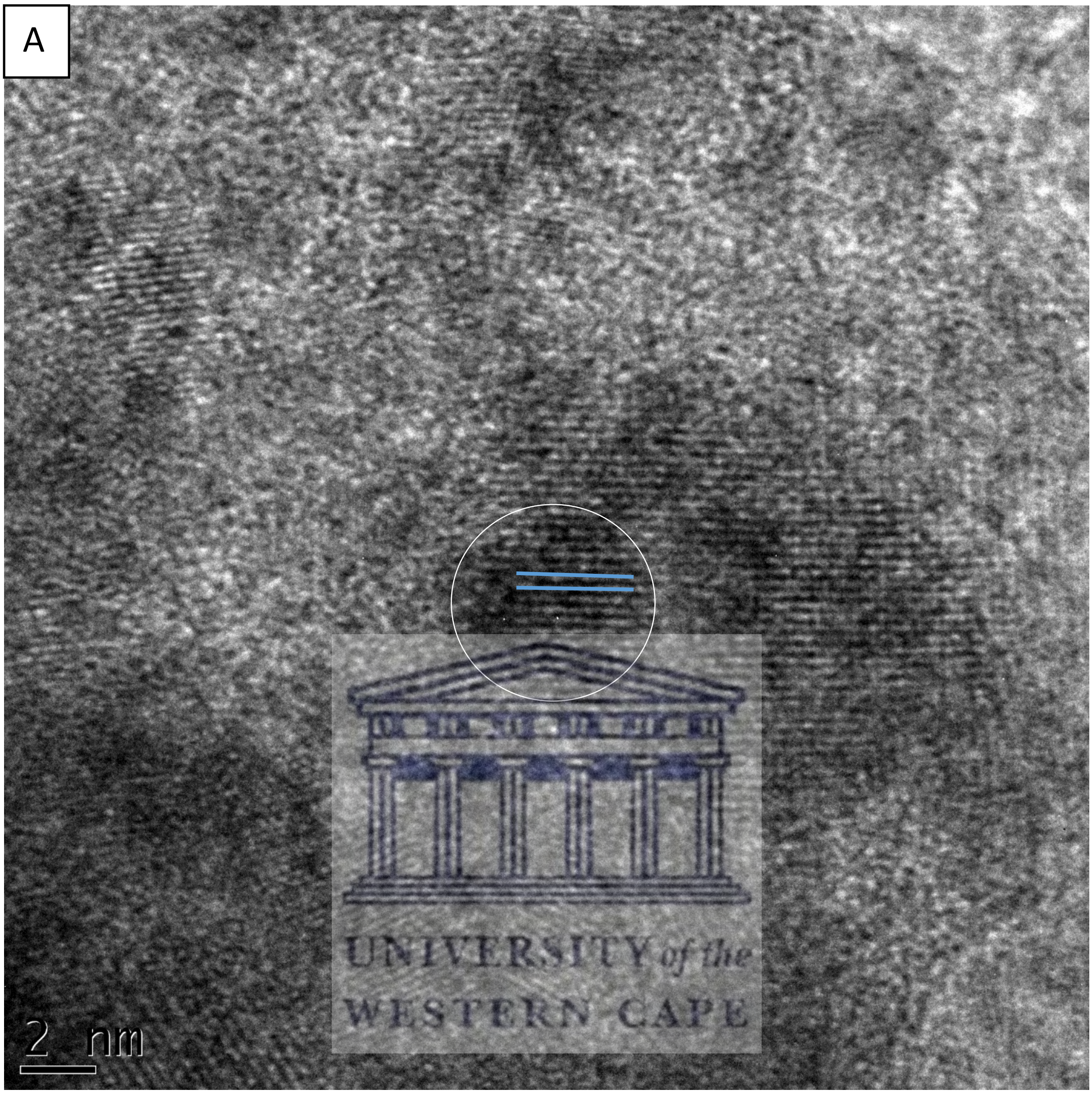
A
2 nm

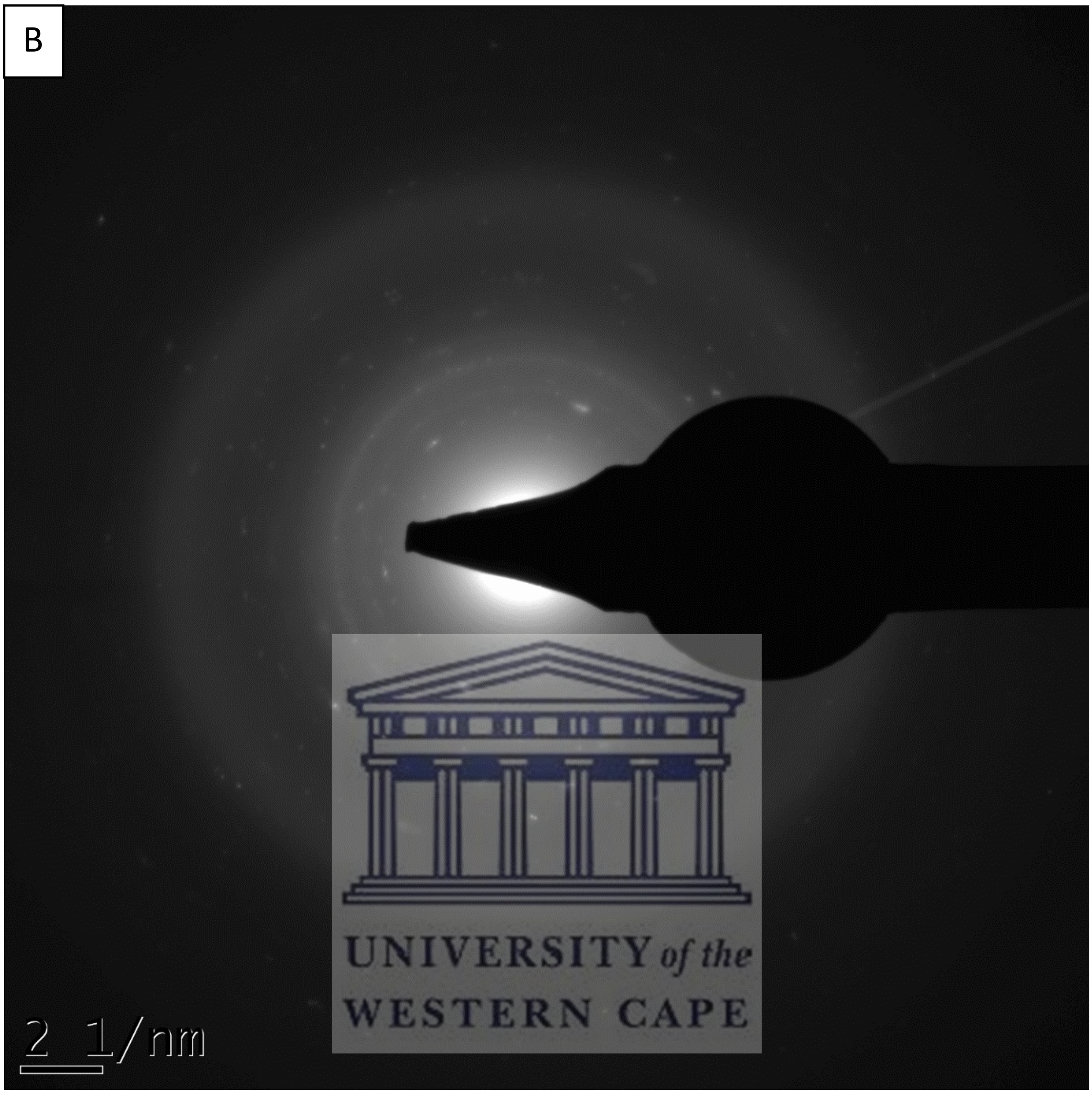
B
2 1/nm

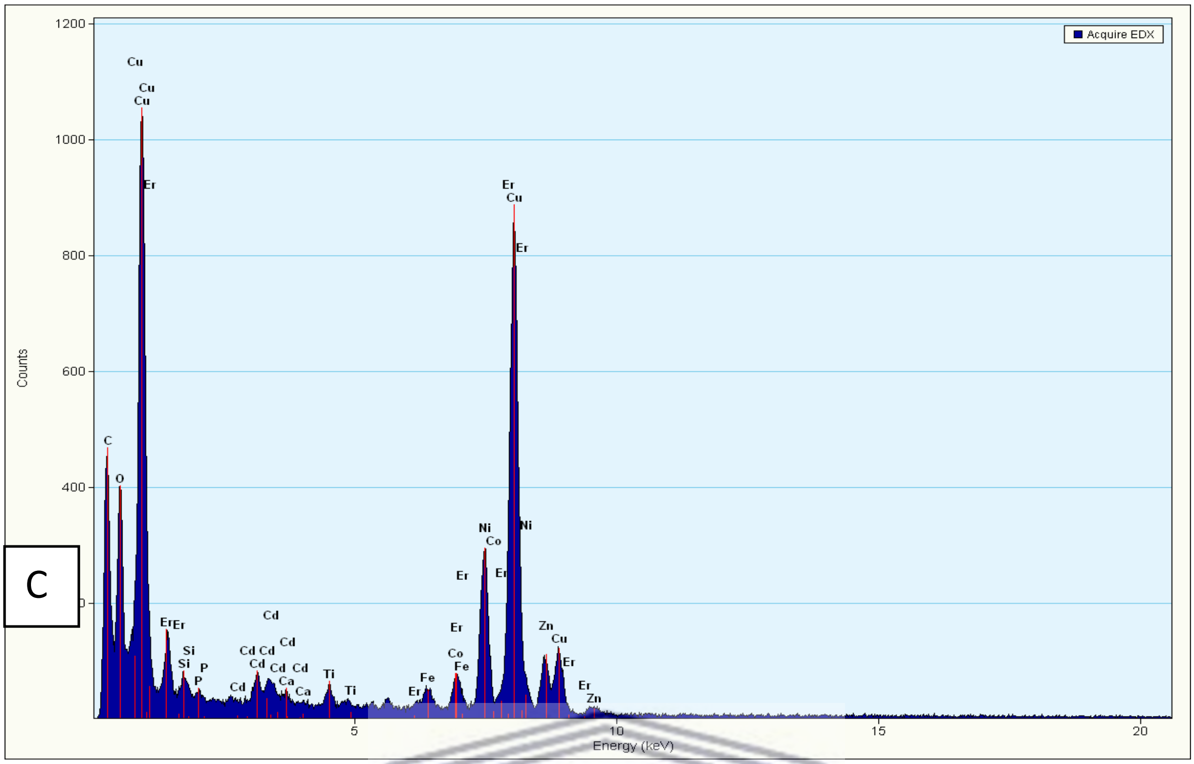

Figure 3.11: A) The TEM image, B) the SAED image and C) the Energy Dispersive X-ray (EDX) spectrum of TGA-CuTe.

Figure 3.12 below shows the TEM image, SAED and the EDX spectrum of MPS-TGA-CuTe. The shape of MPS-TGA-CuTe QDs is nearly spherical and they are crystalline particles, *Fig. 3.12 (***A***)*. The TEM image shows a dark core surrounded by grey shell, the dark core indicating the structure of CuTe cores covered by the silica shells in grey (Hao *et al.*, 2019). The image also shows agglomeration of particles, by being close to each other. The particle size was calculated using Image J and it was found to be about 2 - 3 nm. It's clear that the MPS-TGA-CuTe particle size is larger than that of the TGA-CuTe core. Energy dispersive X-ray spectrum shown in *Figure 3.12* (C) revealed the chemical composition of as-prepared CuTe QDs interacting with TGA and MPS. The spectrum shows Cu, S from TGA and Si from MPS. In the EDX pattern, the presence of Cu and S is clear, and the atomic ratio of S/Cu was calculated as 3:1. In our work, copper acetate and thioglycolic acid were used as a Cu source and as an S source, respectively, in a molar ratio of 1 as explained in the 'Methods' section. On the other hand, MPS molecules contain sulphur due to their thiol group. Therefore, we think that S ratio is a little larger than that of Cu due to the contribution of the thiol group. Also, the oxygen and silicon peaks shown in the EDS pattern correspond to the capping agent of MPS (Koç, Tepehan and Tepehan, 2012). The selected area electron diffraction (SAED) pattern of sample *Figure 3.12 (B)* shows the discontinuous diffraction rings, suggested that the crystalline domains making up these nano-crystalline powders to have certain preferred orientations instead of the random orientations (Kaviyarasu *et al.*, 2016). These results are comparable with the XRD results that were discussed earlier in the study.

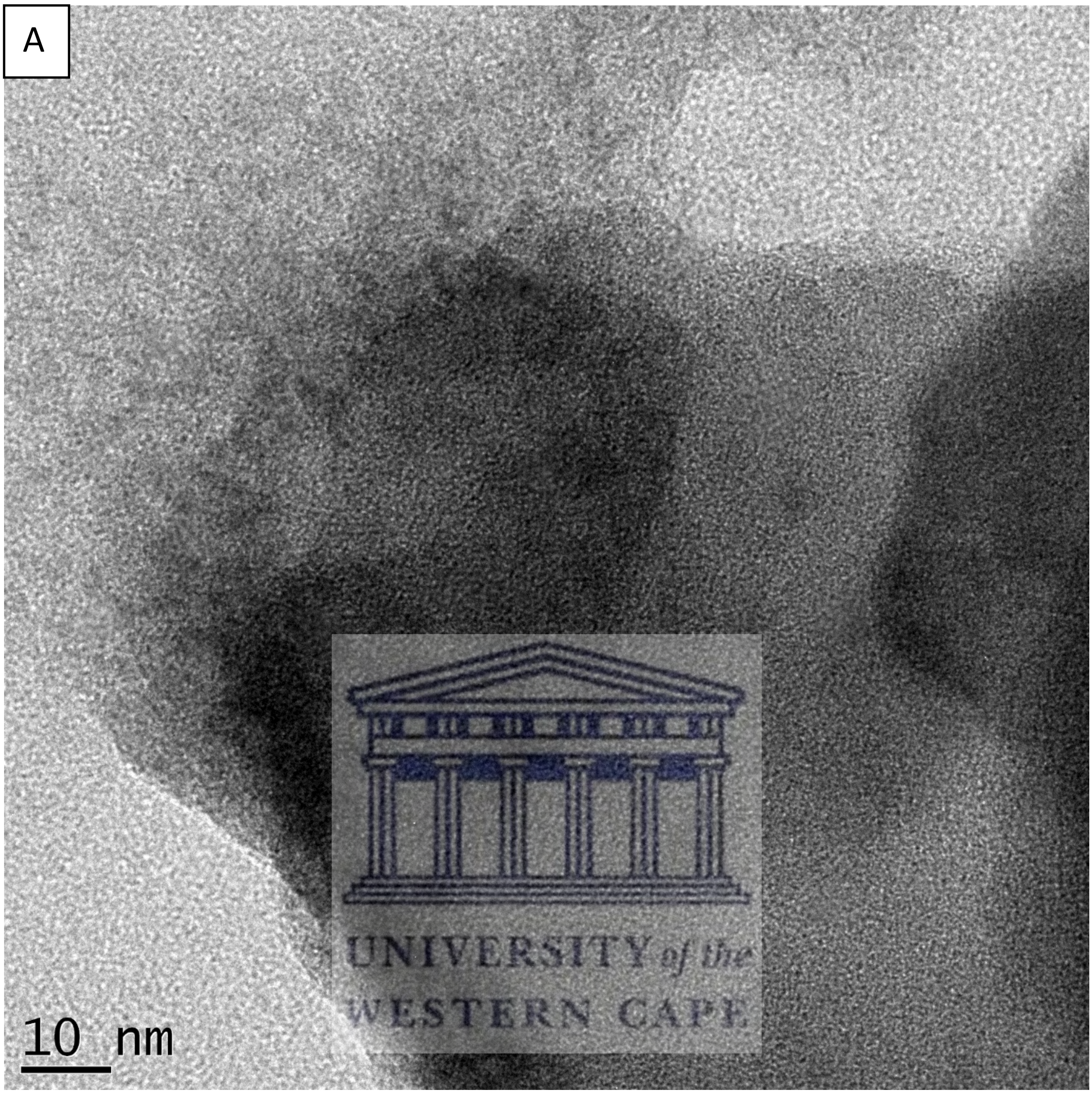
A
10 nm

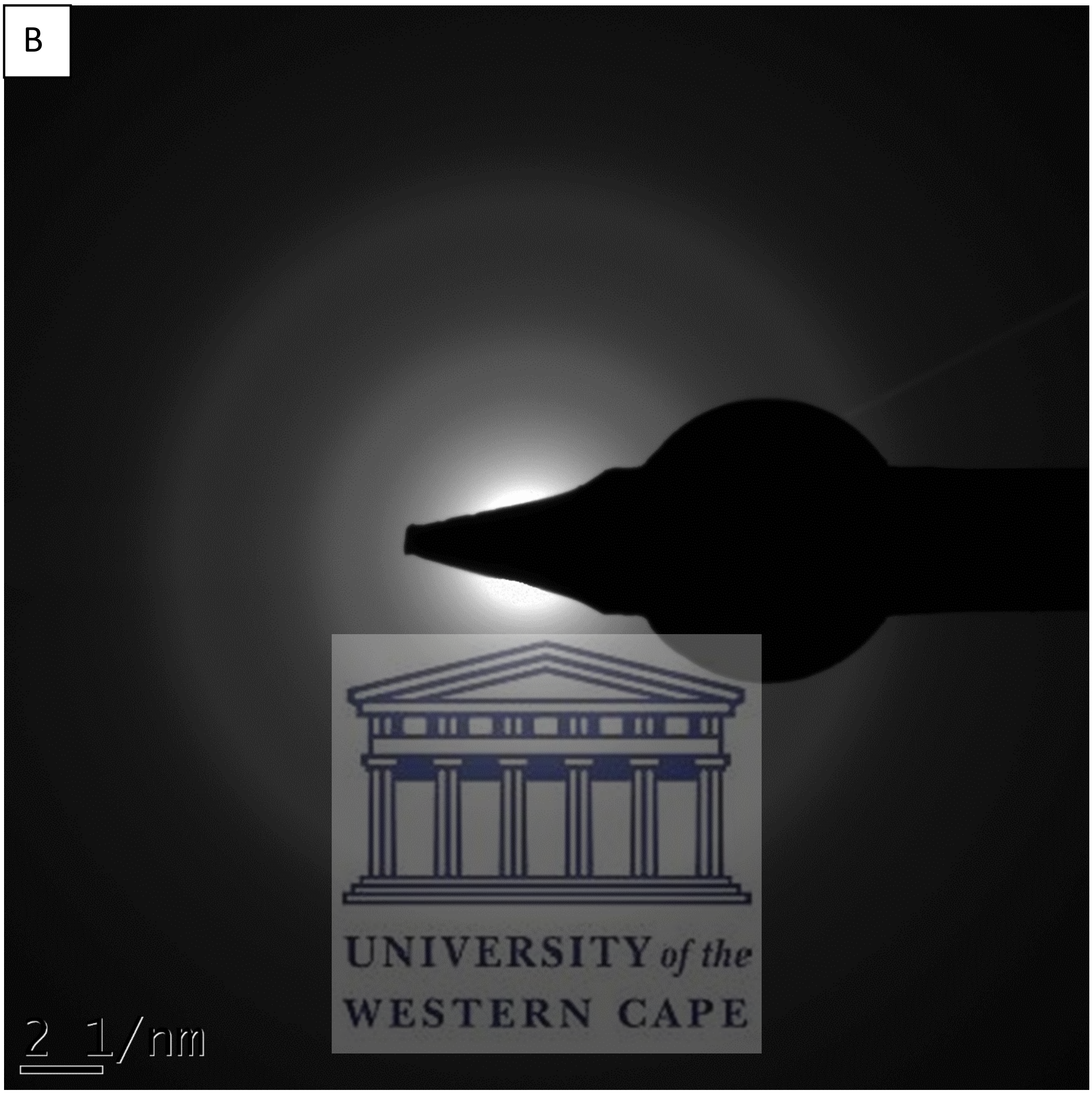
B
2 1/nm

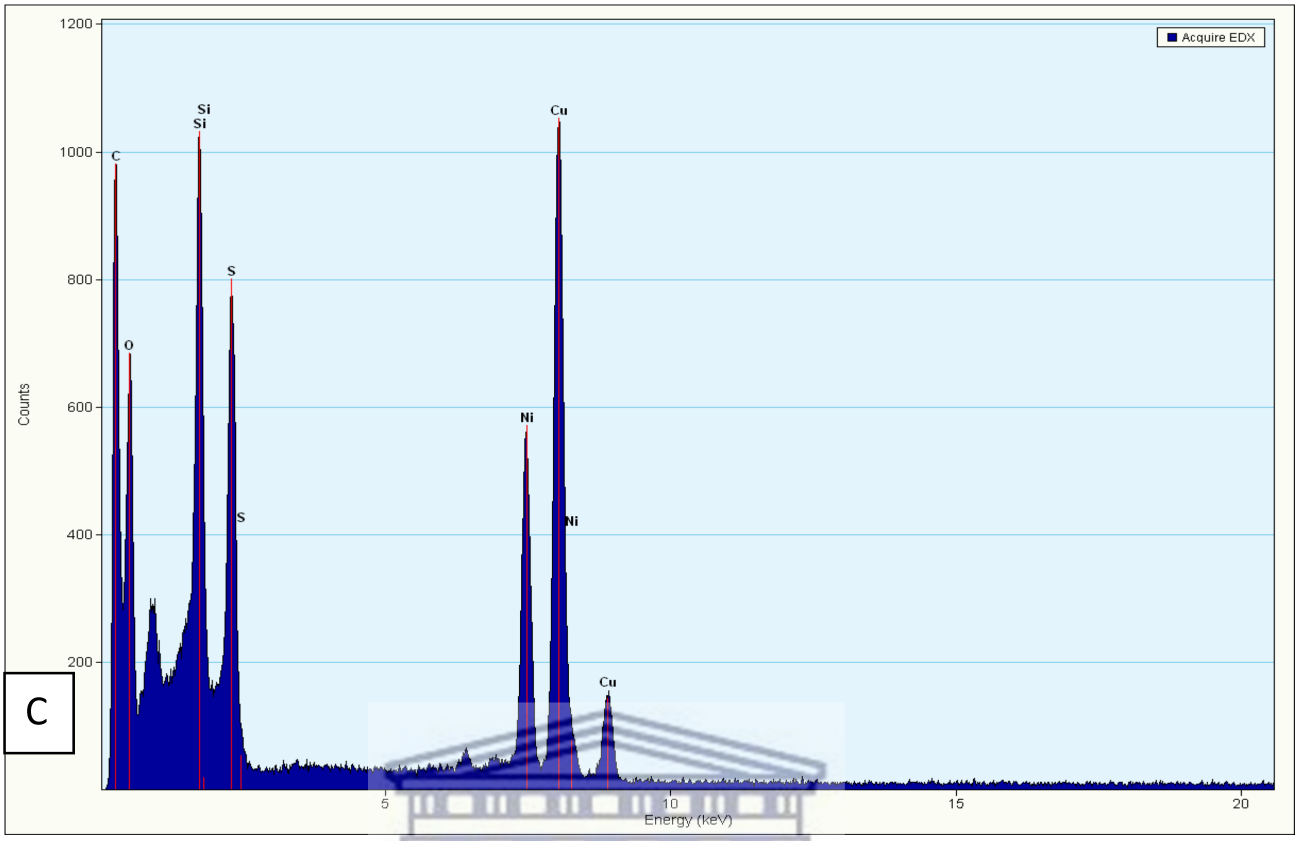

Figure 3.12: A) The TEM image, B) the SAED image and C) the Energy Dispersive X-ray (EDX) spectrum of MPS-TGA-CuTe.

The TEM image seen in *Figure 3.13* ***(A)*** lattice fringes, which indicate that the structure of the quantum dots to be spherical in shape with a smooth surface morphology. The image also shows that the quantum dots are monodispersed. The SAED pattern *(Figure 3.13* ***(B)****)* displays three diffraction rings. From the SAED patterns, it is clear that phase pure copper quantum dots having cubic structure were formed in the reaction ensemble. Selected area electron diffraction (SAED) pattern confirms the amorphous nature of the synthesized QDs which supports the data obtained from XRD (Choudhary and Nageswaran, 2019). The graph above shows the different molecules used, S and Si indicate the presence of capping reagents. The Ni that is present is from the grid that was used. The particle size was calculated using image J is found to be about 6.55 nm. The particle size measured by TEM micrograph is larger than that value calculated by XRD. This might be explained by the fact that, X-ray diffraction results based on the mean size of the sample obtained from XRD pattern which is smaller than that obtained from all the structural layers of sample when using TEM. The size determined by diffraction cannot simply be compared to the sizes determined by other methods. Also in XRD method; system standard errors were not eliminated (Gadalla *et al.*, 2017). All the TEM images show that most of the nanoparticles are nearly spherical and have polycrystalline nature as there are distinct contrast regions within one nanoparticle (Series and Science, 2016).

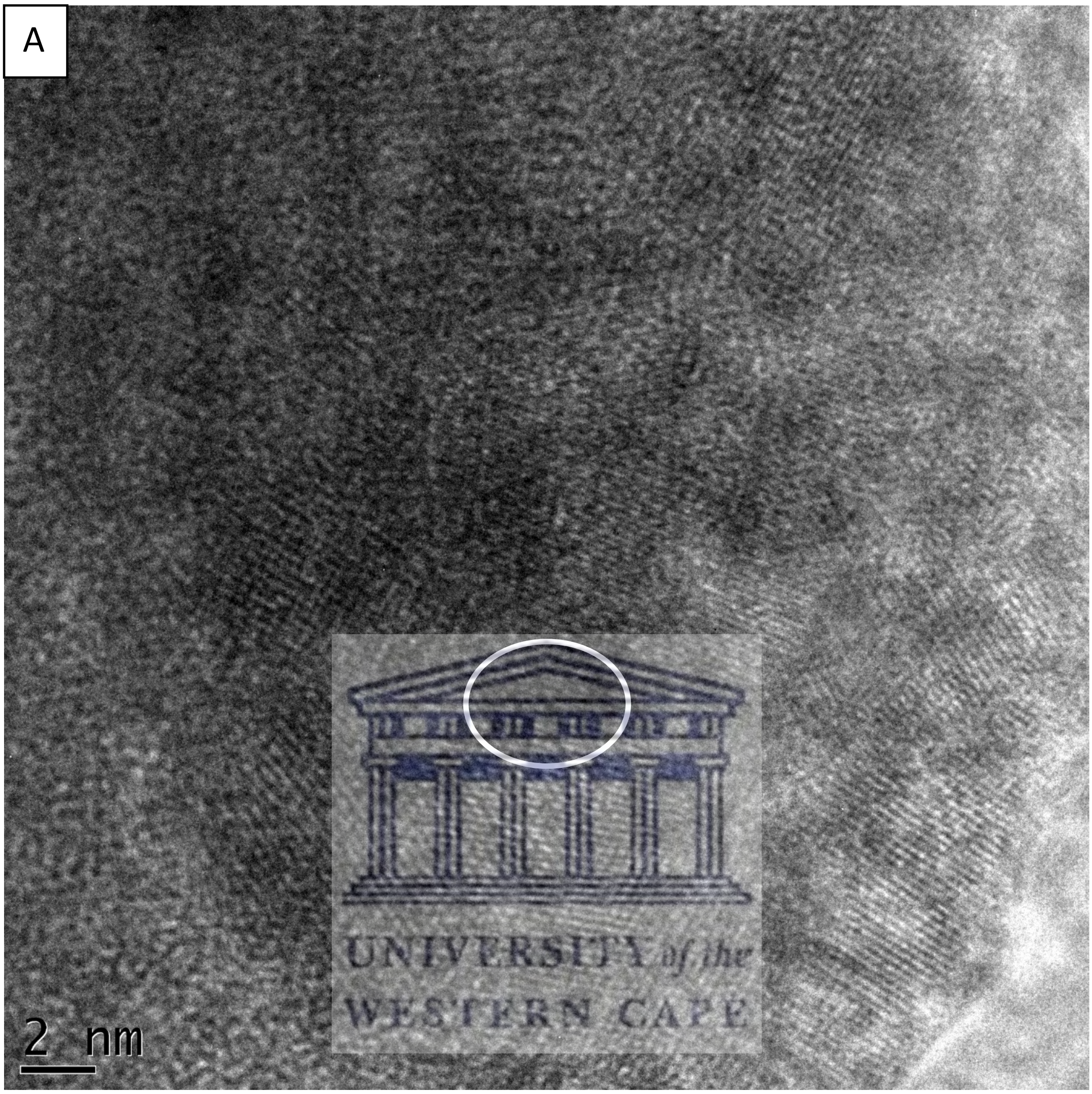
A
2 nm


B
2 1/nm

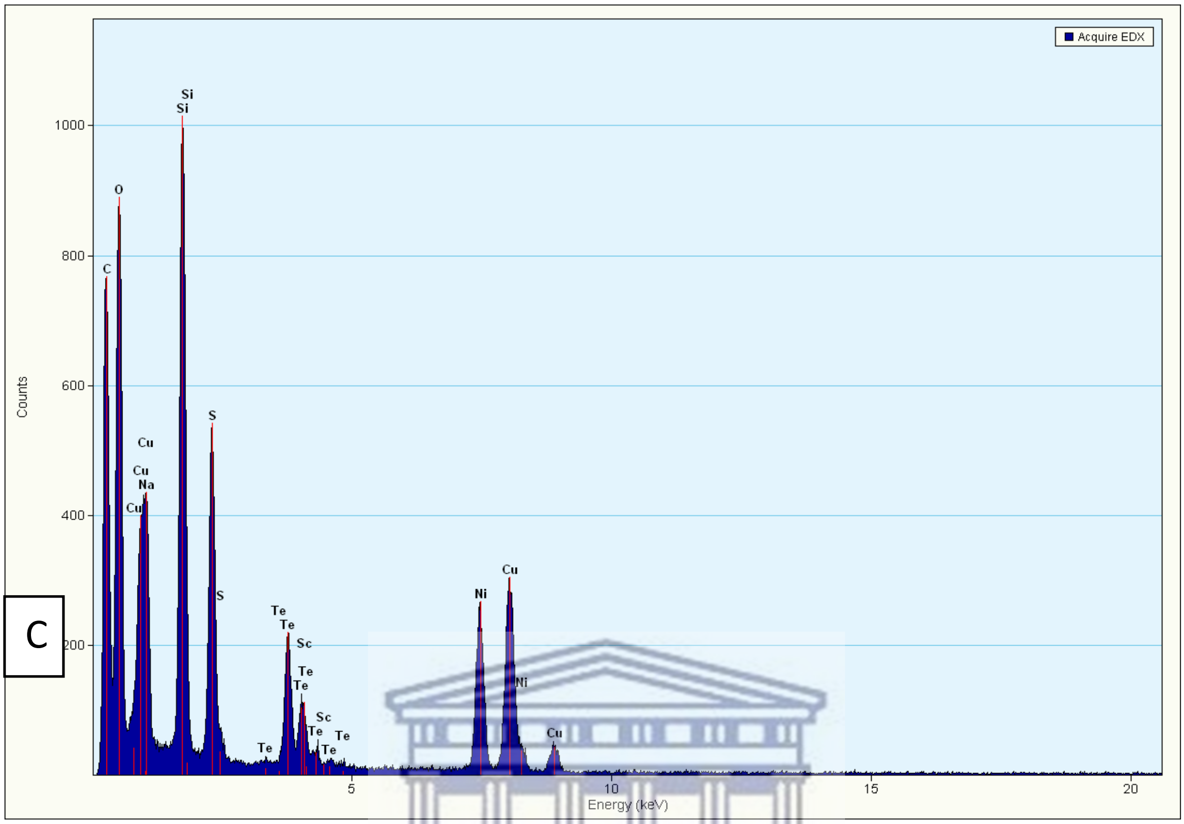

Figure 3.13: A) The TEM image, B) the SAED image and C) the Energy Dispersive X-ray (EDX) spectrum of TGA-CuTe.

3.3.5 Small-angle x-ray scattering

The particle size and size dispersion in aqueous media was investigated using small-angle x-ray scattering (SAXS). Furthermore, information regarding the stability of the nanoparticles in aqueous media (tendency to agglomerate) could also be obtained through this technique. The results from the SAXS analysis was Fourier transformed using GIFT software, into a pair distance distribution function (PDDF) by volume and size distribution by number function NN(r). The results are shown in *Figure 3.14* and *Figure 3.15*.

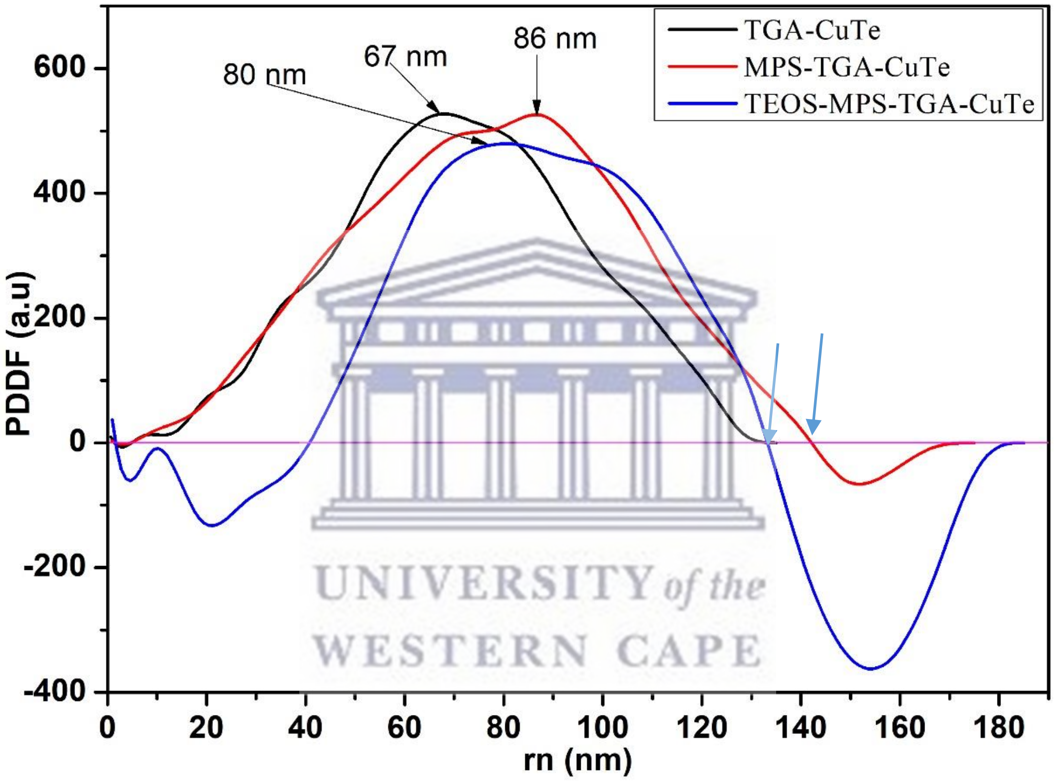

Figure 3.14: Representation of SAXS data in form of PDDF of TGA-CuTe (black-line), MPS-TGA-CuTe (red-line) and TEOS-MPS-TGA-CuTe (blue-line).

In *Figure 3.14*, the PDDF curve of TGA-CuTe (black-line) showed the largest particles detected have a radius of 131.6 nm. From these results, TGA-CuTe shows a globular graph which shows that quantum dots are spherical. The diameter of the TGA-CuTe QDs end at 140 nm and it is clearly represented that it does not have a shell. The PDDF curve of MPS-TGA-CuTe shows that the largest detected particle has the radius of 173 nm (Pauw, Kästner and Thünemann, 2017). The diameter of the of the MPS-TGA-CuTe QDs is at 176 nm, which is bigger than the diameter of TGA-CuTe. This indicates that the outer shell on the QDs is being formed, also the second curve that is in the negative regain compliments the formation of a shell on the QDs. MPS-TGA-CuTe QDs graph is asymmetrical having two peaks that shows agglomeration of the quantum dots these results compliments with HRTEM results ('The SAXS Guide', 2013; Gabriella and Pacoste, 2017). TEOS-MPS-TGA-CuTe graph is symmetrical and has a curve in the negative reign, this indicates that the quantum dots are spherical and have core-shell. This is also proved by the increases of the diameter of TEOS-MPS-TGA-CuTe QDs at 182 nm. The propose reason for smaller diameter to bigger diameter is from the successive addition of capping agents, protecting the core QD's. The core-shell of the MPS-TGA-CuTe it has a smaller curve than that of TEOS-MPS-CuTe, this proves that the core-shell is thickened by the addition of TEOS (Stawski *et al.*, 2019).

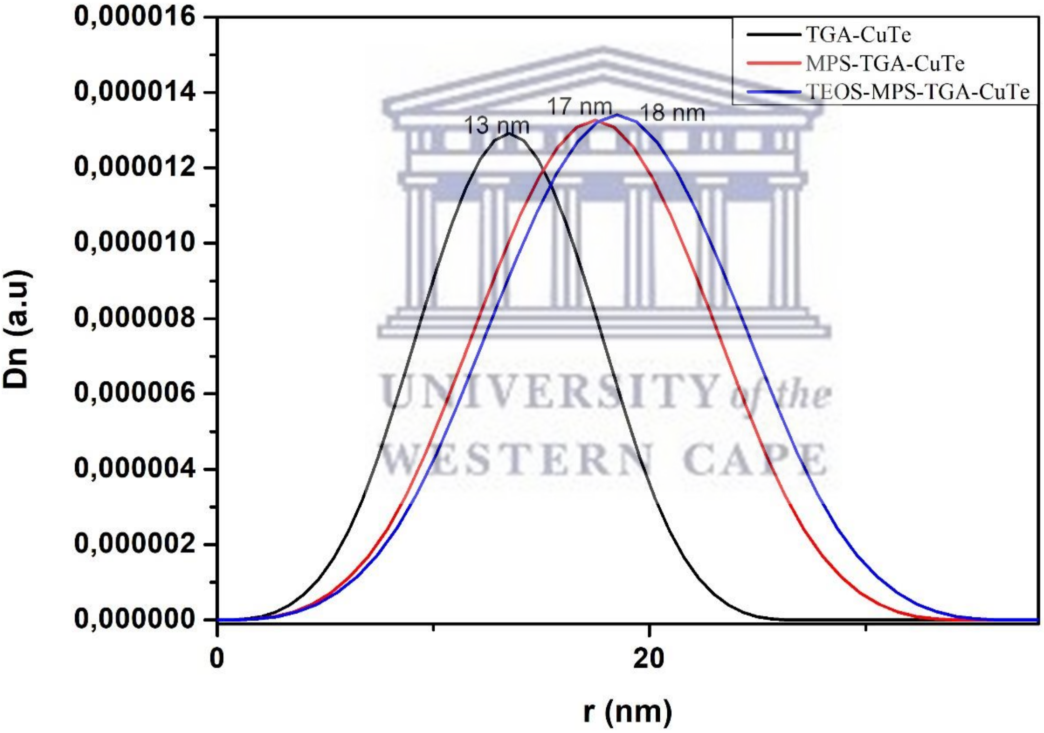

Figure 3.15: Representation of SAXS data in form of particle radius (r) distributed by number of particles for TGA-CuTe (black-line), MPS-TGA-CuTe (red-line) and TEOS-MPS-TGA-CuTe (blue-line).

The *Fig. 3.15* illustrates that TGA-CuTe had a radius of 13 nm (diameter of 26 nm) when diluted in aqueous media. The MPS-TGA-CuTe QDs *(red-line)* have an average particle size of 27 nm in diameter (17 nm radius) in aqueous media. In the case of the TEOS-MPS-TGA-CuTe QDs (blue-line) the most abundant size within the particles is 30 nm in diameter when dispersed in aqueous solution. The broadness observed from the three Qds is due to the formation of poly dispersed particles (Feleni, 2017).

3.3.6 Fourier Transform Infrared Spectroscopy (FTIR)

Further characterization by solid FTIR was performed to evaluate structural properties of the QDs. The samples were precipitated and dried prior to analysis. The results of CuTe quantum dots with different capping reagents are shown in *Figure 3.16 – Figure 3.19*.

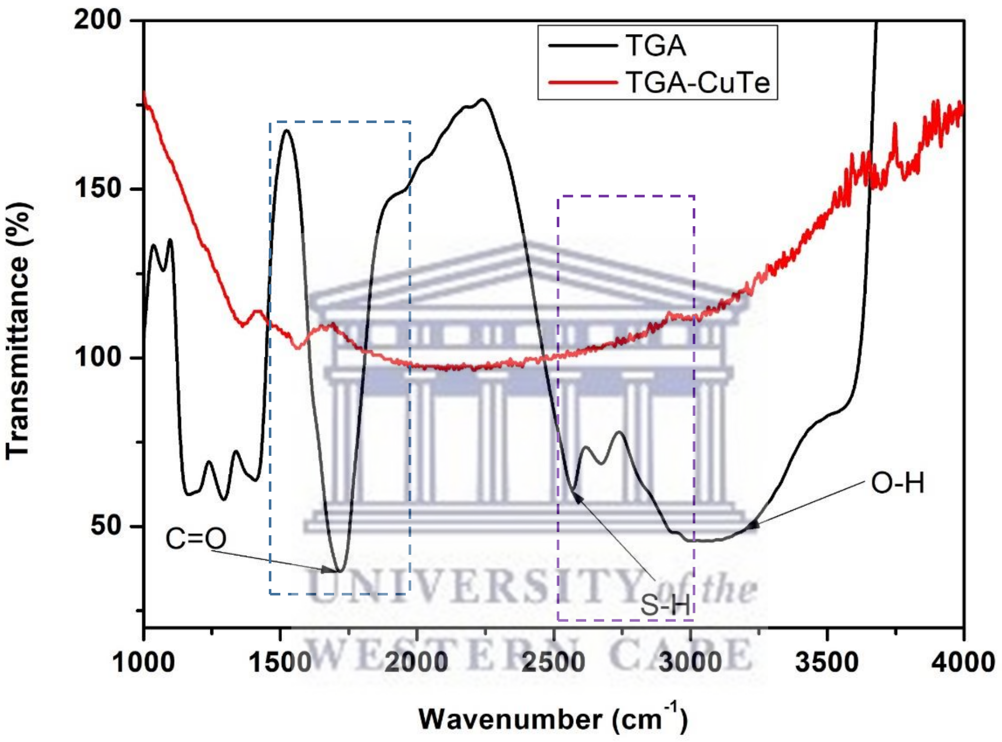

Figure 3.16: FTIR spectra of TGA only and TGA-CuTe QDs.

The characteristic peaks belonging to TGA are seen in *Fig. 3.16*. The peak at 2570 cm^{-1} is attributed to the stretching vibration of the S-H bond and the peak at 1700 cm^{-1} is attributed to vibration of the carboxylic group (Congiu *et al.*, 2015). As can be seen in *Fig. 3.16*, the stretching vibration for TGA (2570 cm^{-1}), does not appear in the complex TGA-CuTe as a result of covalent bonding between thiols and Cu atom on the QDs surface (Manuscript, 2015). The signal of the carbonyl group, at 1700 cm^{-1} for the TGA, is shifted to 1563 cm^{-1} in the TGA-CuTe complex. These spectra showed a shift of the asymmetric vibration of the carboxyl group in implying that the COOH in TGA turned to its anion, which also led to the appearance of the symmetric vibration of the carboxyl anion at 1563 cm^{-1} (Jiang and Ju, 2007). In total, the structure of the obtained QDs could be identified as a CuTe core covered with excess TGA^{2-} anions. This makes the QDs surfaces negatively charged and the QDs become water-soluble (Abdelbar *et al.*, 2016).

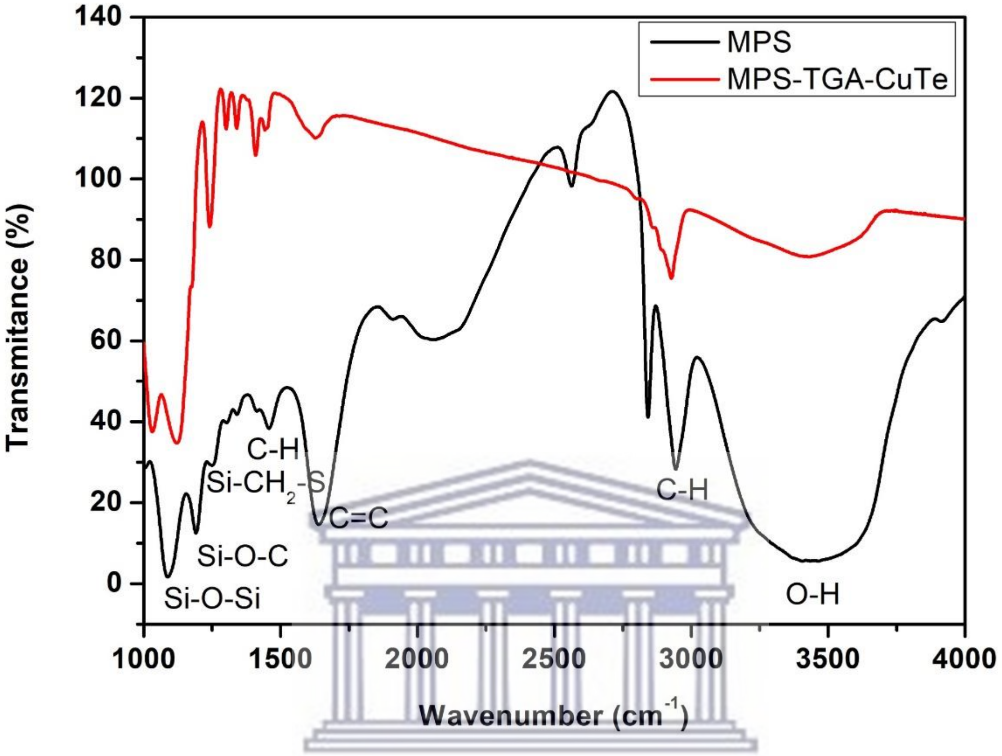

Figure 3.17: FTIR spectra of MPS only and MPS-TGA-CuTe QDs.

The presence of capping molecule at the surface of quantum dots was confirmed by FTIR spectroscopy. FTIR graph of MPS-TGA-CuTe is shown in *Fig. 3.17*. The FTIR analysis shows the characteristic peaks belonging to MPS. The most prominent peak of these are at 1082 cm^{-1} and 1110 cm^{-1} belonging to asymmetric stretching of Si-O-C and Si-O-Si bonds respectively. The peak at 1240 cm^{-1} is for Si-CH$_2$-S stretching (KENAN KOÇ, FATMA Z. TEPEHAN, 2011). The peak at 1405 cm^{-1} comes from asymmetric deformation of C-H in CH$_3$. The peak at 1632 cm^{-1} belongs to C=C bond. The peaks at 2941 cm^{-1} and 3449 cm^{-1} belong to C-H and O-H respectively (Shahraki and Irani, 2014). The FTIR spectroscopy analysis confirms that the siloxane group was introduced on the QD surface after silica coating. There was a shift of the spectrum of MPS-TGA-CuTe all the molecules shifted this indicates the addition of MPS on the surface of the quantum dots. Quantum dots are also bonded with Si-O-Si bonds between themselves. Bonding of MPS to TGA-CuTe quantum dots is done through thiol groups from TGA.

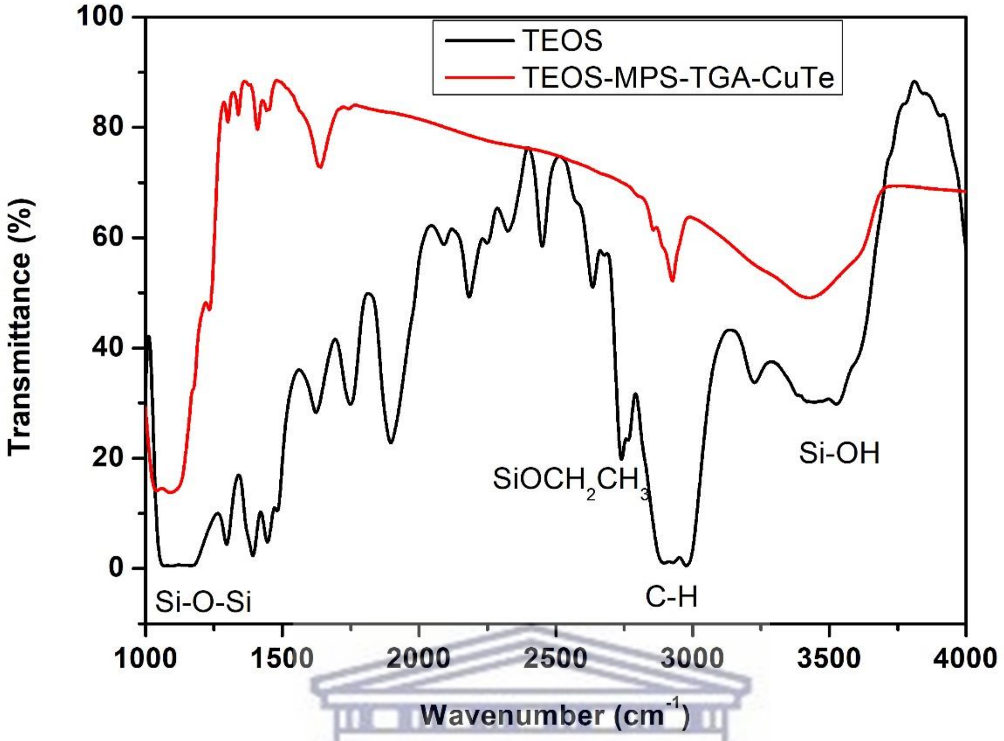

Figure 3.18: FTIR spectra of TEO and TEOS-MPS-TGA-CuTe.

The stepwise silanization based procedure to modify the MPS-TGA-CuTe QDs surface is illustrated in the illustrate in *Fig. 3.18* spectrum. Spectroscopic characterization of the quantum dots coated with TEOS revealed interesting features. The peak at 3500 cm^{-1} has been attributed to the Si–OH stretching of silanol groups, while the band at 1614 cm^{-1} corresponds to the scissoring of the OH bonds of water, revealing the presence of water occluded into porous silica (Koç, Tepehan and Tepehan, 2012). The strong and broad band centered at 1058 cm^{-1} is potentially due to the overlap of the Si-O-Si. The absorption bands between 2974 cm^{-1} have been assigned to the asymmetric stretching vibrations of the C-H bonds of the residual ethoxy moieties from TEOS (Tang *et al.*, 2017). There was a shift of the spectrum of TEOS-MPS-TGA-CuTe all the molecules shifted this indicates the addition of TEOS on the surface of the quantum dots.

In *Fig. 3.19*, the spectrum presents the three different capping reagent which are TGA-CuTe, MPS-TGA-CuTe and TEOS-MPS-TGA-CuTe the difference that they make when they are added to the quantum dots. From the structure of TGA-CuTe that showed the effect of the carbonyl group, at 1700 cm^{-1} for the TGA, is shifted to 1563 cm^{-1} in the TGA-CuTe complex. This shift is due to the deprotonation of the acid –OH group and its participation as a ligand in the formation of the complex with the Cu^{2+} ion (Congiu *et al.*, 2015). In addition, the S-H broad band stretching diminished at approximately 2570 cm^{-1} indicated the formation of S-Cu bonds between the TGA molecule and CuTe core. The addition of MPS showed a shift of carboxylic group and the peak of –OH became broad at 3421 cm^{-1} and there was a slight shift. A new peak of Si-O-Si appeared at 1023 cm^{-1} indicating the silica that was added. With the addition of TEOS to the quantum dots the Si-O-Si peak became broad indicating the thickening of the shell. Another interesting peak is the –OH bonding it became broad and there was a shift to 3432 cm^{-1} (Dalmoro *et al.*, 2013).

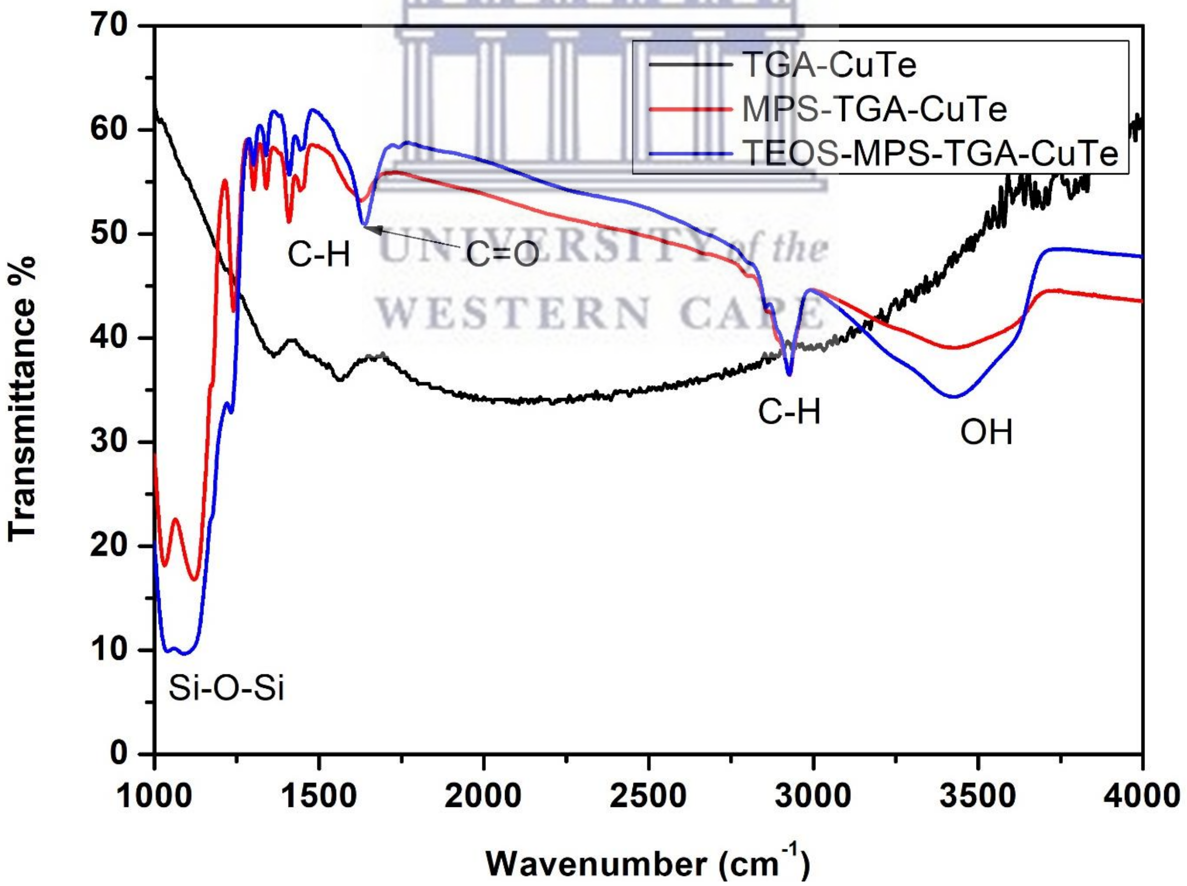

Figure 3.19: The FTIR spectrum showing the effect of different capping reagents on the structure of quantum dots.

3.3.7 Raman

Raman spectra have been an important method for the determination of molecular structure, for locating various chemical bonds or functional groups in molecules and for the quantitative analysis of complex mixtures (Kuhar *et al.*, 2018). A feature of Raman scattering is that each line has a characteristic polarization, and polarization data can provide additional information about molecular structure. Bands below 300 cm^{-1} are caused by lattice vibrations, i.e. translational and torsional motions of the molecules in the lattice (phonon modes) (Dhasade, Han and Fulari, 2012). The lattice vibrational modes of the copper telluride compound have been obtained at room temperature by the Raman spectra. Peak observed in *Figure 3.20* at 123 cm^{-1}, 479 cm^{-1}, 1470 cm^{-1}, 1537 cm^{-1} and 2431 cm^{-1}. The peak at 479 cm^{-1} for TGA-CuTe quantum dots is attributed to the vibration of longitudinal optical phonons (Pal *et al.*, 2017), this peak also indicates that the material is amorphous which is in agreement with TEM and XRD results (Baustian, 1988). The band at 1537 cm^{-1} is due to the C–H_2 out of plane stretch of the TGA capping agent (Abd Rahman *et al.*, 2017). The peaks in the range 670 cm^{-1} - 1700 cm^{-1} are mostly due to C-C and C-H vibrations (Pal *et al.*, 2017). The strong vibration at 2435 cm^{-1} is assigned to S-H vibration band (Zhou, Williams and Wu, 2010).

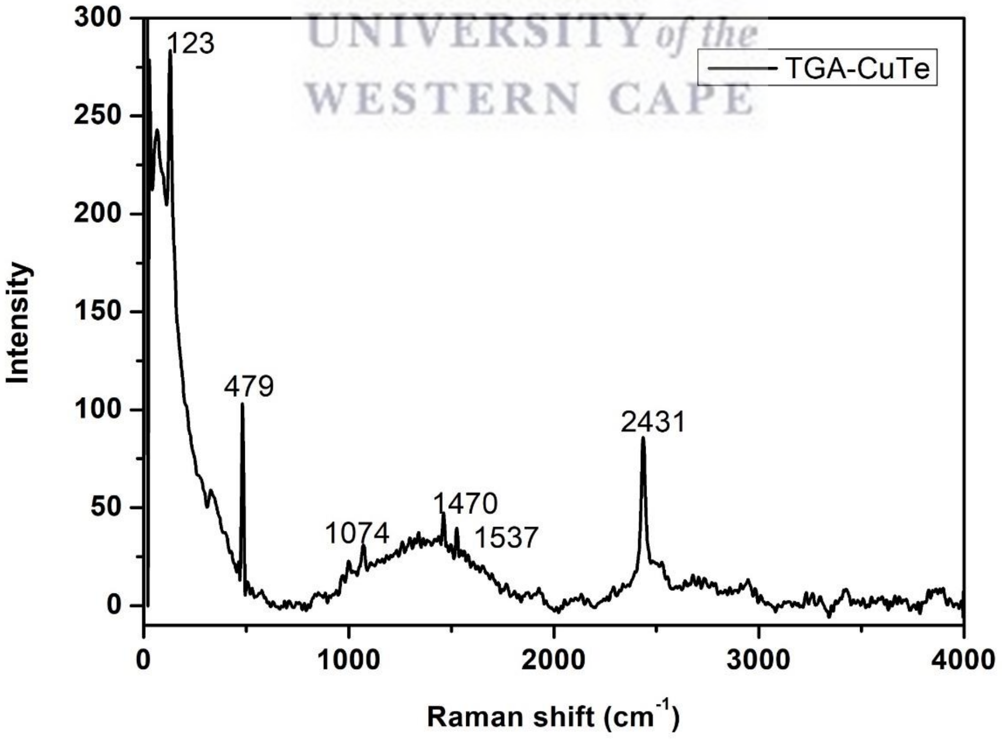

Figure 3.20: Raman spectra of TGA-CuTe

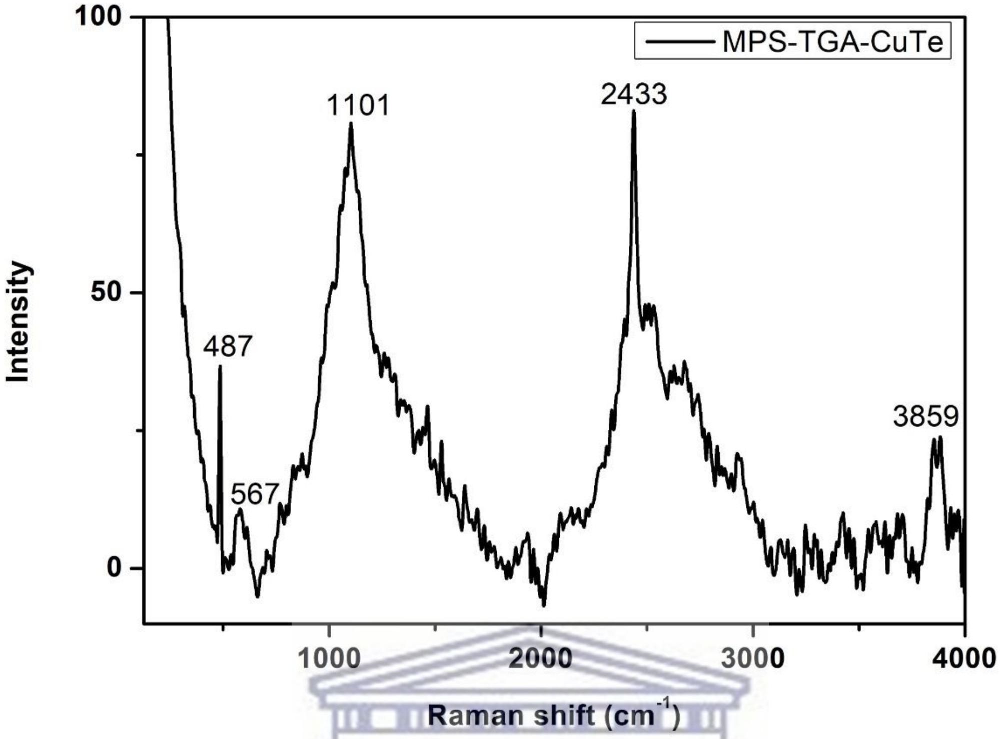

Figure 3.21: Raman spectra of MPS-TGA-CuTe.

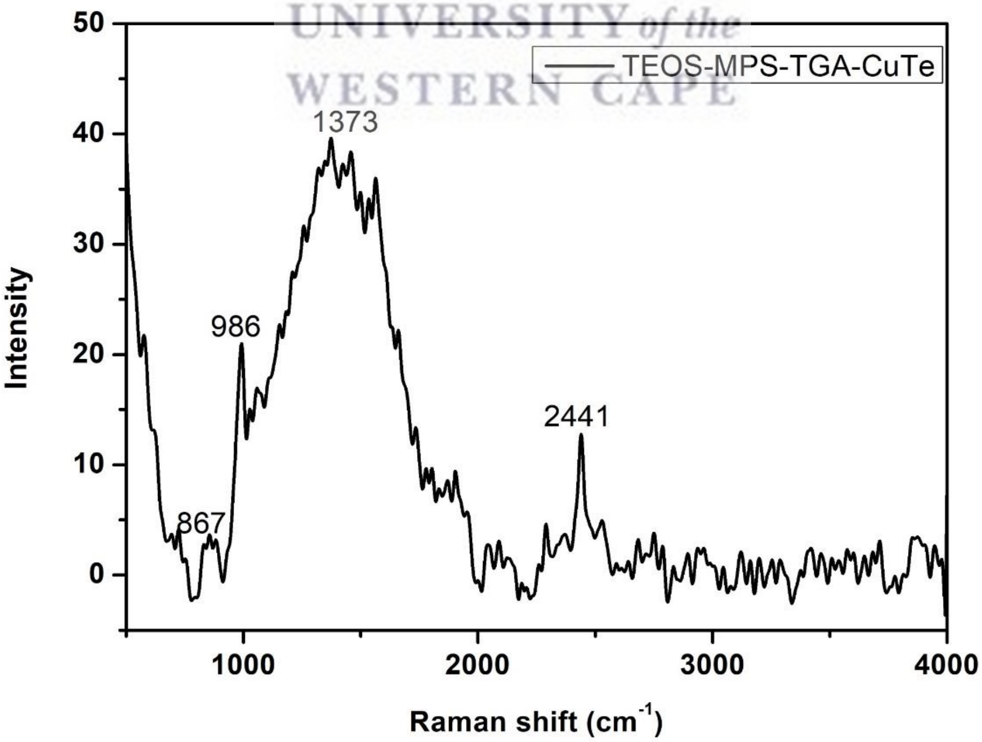

Figure 3.22: Raman spectra of TEOS-MPS-TGA-CuTe.

In *Figure 3.21*, the Raman spectra of MPS-TGA-CuTe is shown. Peak observed in *Figure 3.201* at 487 cm^{-1}, 587 cm^{-1}, 1101 cm^{-1}, 2433 cm^{-1} and 3859 cm^{-1}. The peak at 487 cm^{-1} for MPS-TGA-CuTe quantum dots is attributed to Si-O-Si, the peaks for 587 cm^{-1} and 1101 cm^{-1} are mostly due to C-C and C-H vibrations (Pal *et al.*, 2017). As indicated that in *Figure 3.20* that the strong vibration at 2431 cm^{-1} is assigned to S-H vibration band (Zhou, Williams and Wu, 2010), now in *Figure 3.21* the peak has shifted to 2433 cm^{-1} which indicates that the quantum dots size is increasing (Eleanor Adachi1, Idemudia John Airuoyo2, Lakshmi Krishna2, 2016). The peak at 3859 cm^{-1}, is attributed to O-H group present in the quantum dots (Bands). In *Figure 3.22*, the Raman spectra of TEOS-MPS-TGA-CuTe is shown, with peaks at 867 cm^{-1}, 986 cm^{-1}, 1373 cm^{-1} and 2441 cm^{-1}. The peak at 867 cm^{-1} is attributed to C-C vibrations and the peak at 1373 cm^{-1} is attributed to CH_3. As indicated that in *Figure 3.20* that the strong vibration at 2431 cm^{-1} is assigned to S-H vibration band, in *Figure 3.21* the peak has shifted to 2433 cm^{-1} which indicates that the quantum dots size is increasing (Rubio, Rubio and Oteo, 2006). Now in *Figure 3.22,* the peak has again shifted to 2441 cm^{-1}. Raman spectroscopy is a widely used and powerful tool to reveal ordered and disordered crystal structures of carbon based materials. The Raman spectroscopy results compliments the FTIR results by showing molecules that are present in different capping reagents being present in the CuTe QQs. The spectra *Figure 3.23* below shows Raman spectra of 3 different capping reagents. In this spectra it seen on how these peaks shift which indicates the growth of the quantum dots.

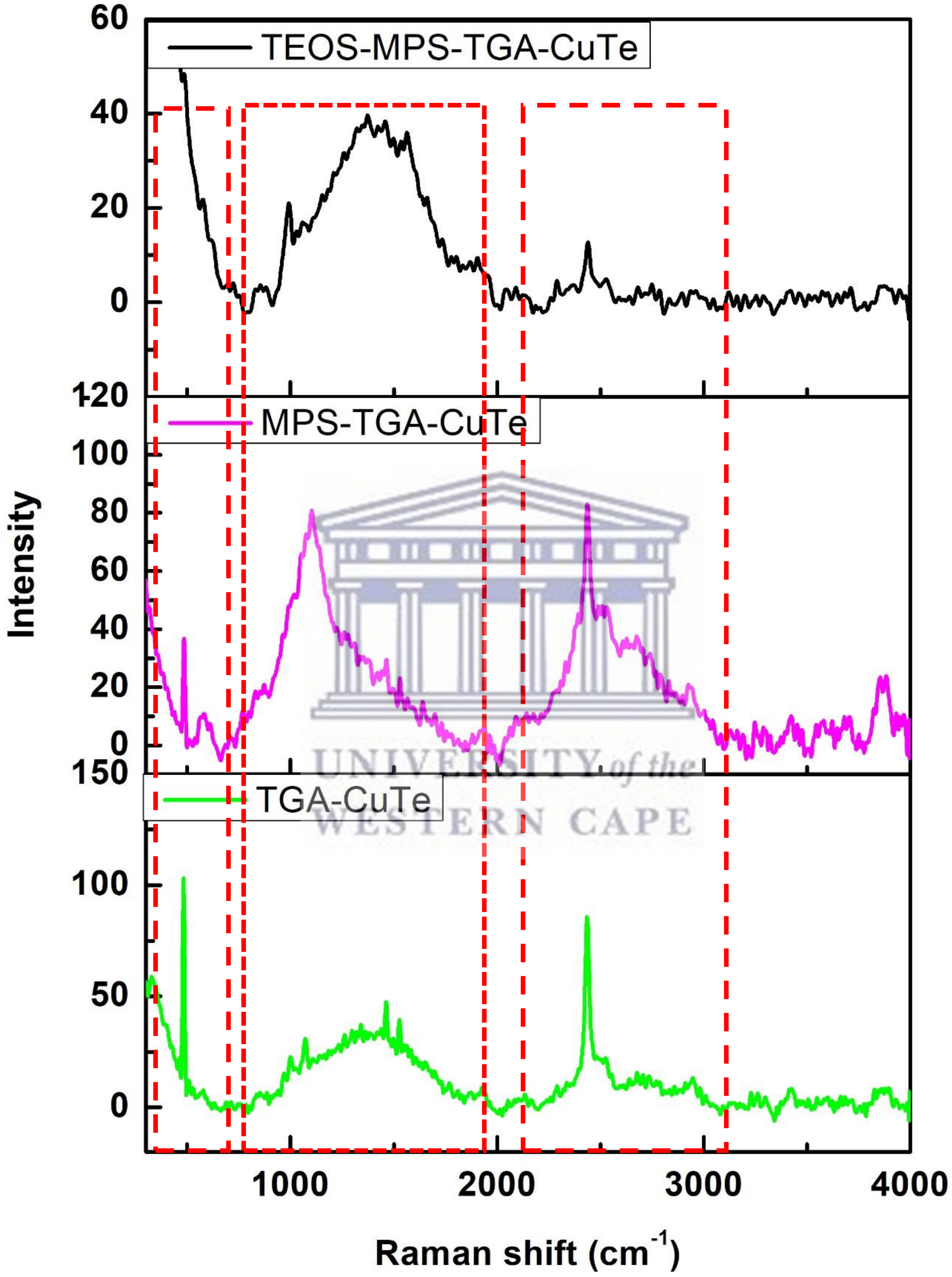

Figure 3.23: Raman spectra of TGA-CuTe (lime-line), MPS-TGA-CuTe (purple-line) and TEOS-MPS-TGA-CuTe (black-line).

3.3.8 Electrochemistry

Cyclic voltammetry

Cyclic voltammetry (CV) is widely used for the evaluation of mode of action and binding strength of compounds interaction. This technique is predominantly useful for metal based compounds due to their accessible redox states. As in CV the scan is revered so the fate of the species in the backward scan can also be studied. The peak potential and peak current of the compound changes, the variation in peak potential and peak current can be exploited for the determination of binding parameters (Sirajuddin, Ali and Badshah, 2013). The electrochemical behaviour of the CuTe QDs when immobilized on a bare gold (Au) electrode was investigated using cyclic voltammetry at scan rates of 50 mV s-1. All the experiments were carried out in 0.1 M phosphate buffer (pH 7.40) with a potential window of -1200 - 1200 mV starting with an anodic sweep from -1200 mV. The resulting cyclic voltammograms are illustrated in Figure 3.24 to Figure 3.36. The electrochemical behaviour of copper, the redox couple cathodic peak appeared at 0.17 V for Cu(II) → Cu(I) and its corresponding anodic peak observed at -0. 18 V. This indicates that the reaction of the complex on the gold electrode surface was a quasi-reversible redox process (Joseph, Nagashri and Suman, 2016).

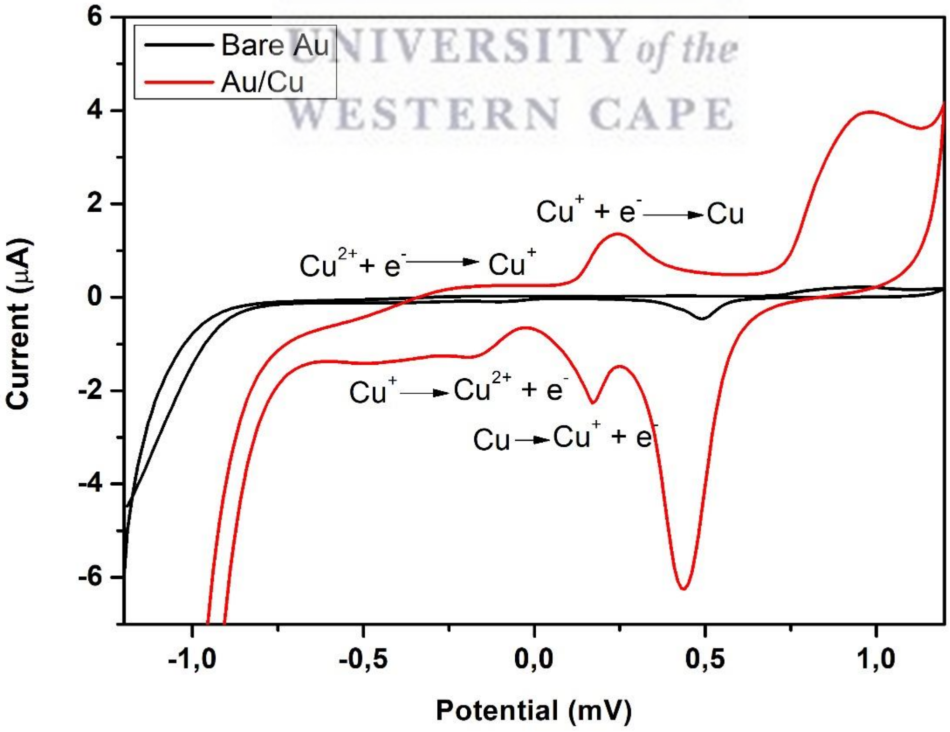

Figure 3.24: Cyclic voltammograms measured with bare Au electrode and Cu in 0.1 phosphate buffer (pH 7.40) at 50mVs-1.

In the presence of complexing agents, Cu^+ is stable in aqueous solution. Thus, Cu^{2+} may undergo a two-step electron transfer from Cu^{2+} to Cu. This causes the Cu^{2+}/Cu^+ redox reaction to be visible in the cyclic voltammetry as two redox peaks, which is illustrated in *Figure 3.24*. Two reduction peaks were observed at -0.25 V and 0.24 V, respectively (He *et al.*, 2015). The first reduction peak was attributed to the reduction of Cu^{2+} to Cu^+ and the second reduction peak was ascribed to further reduction of Cu^+ to Cu. The oxidation peak occurring at 0.16 V was assigned to the one electron oxidation of Cu to Cu^+. Whereas the oxidation at -0.18 V was assigned to the oxidation of Cu^+ to Cu^{2+} (Gomaa and Salem, 2016; Gabriella and Pacoste, 2017). In *Figure 3.25*, the multi scans of cyclic voltammetry of Copper. This was done to check the stability of the peaks and if is there a change in high and low scan rates. As the scan rate increases the peak current also increases.

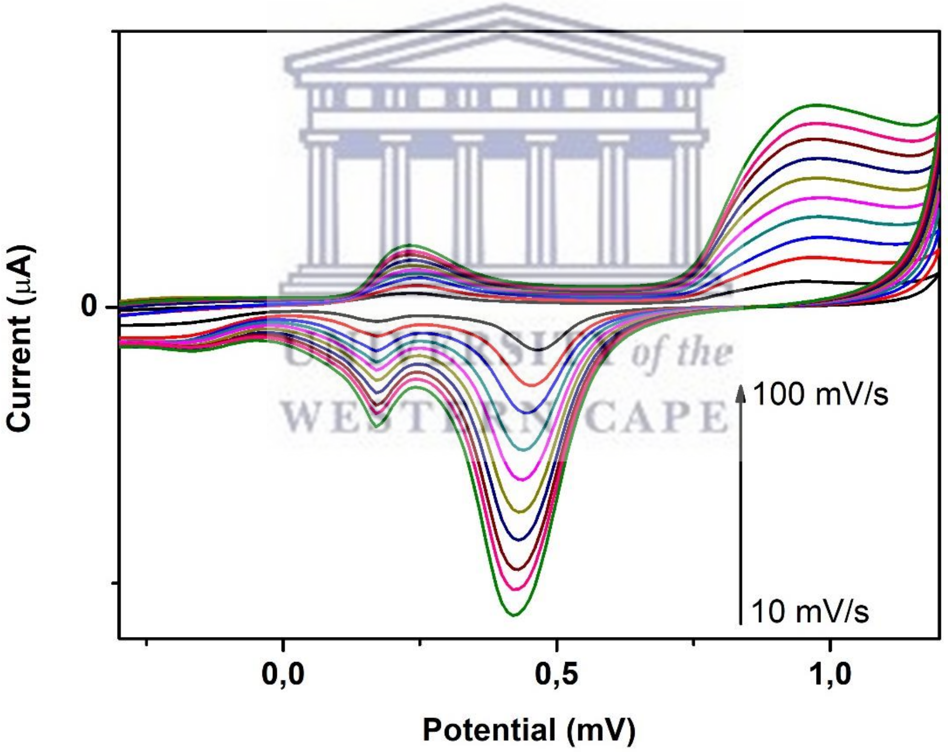

Figure 3.25: The cyclic voltammograms of Cu immobilized on a bare Au at multiple scan rates varying from 10-100 mVs^{-1}.

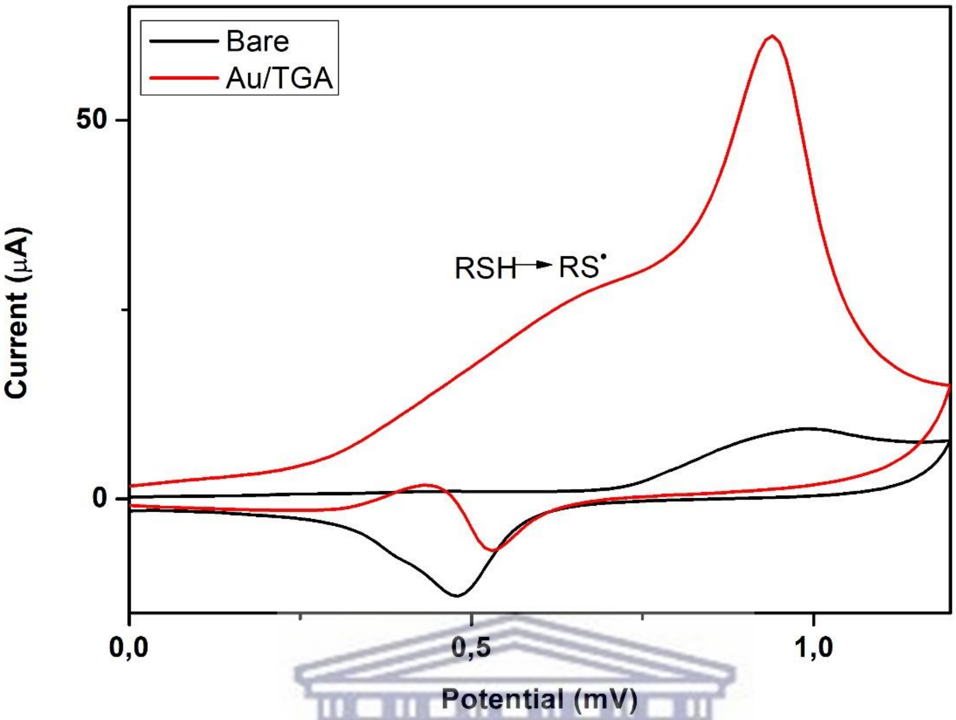

Figure 3.26: Cyclic voltammograms measured with bare Au electrode and Au/TGA in 0.1 phosphate buffer (pH 7.40) with proposed reaction mechanisms responsible for the current peaks at 50mVs^{-1}.

In *Figure 3.26*, the cyclic voltammetry of Au/TGA showed that with this capping reagent the gold peaks from the gold electrode shift to the negative potential (Andrews *et al.*, 2015). The enhancement in gold surface peak is due to the Au-S interaction. The reduction peaks visible in the cyclic voltammogram for the capping agents at 0.64V, could be attributed to reduction of the thiol group (RSH) to form thiol radicals (RS•) (Feleni, 2013). Multiple scan rates in *Figure 3.27* were done to check the consistency of the peaks that appeared. With the increase of the scan rate the current of the peaks also increased and the peaks shift this reflect the continuous change of the concentration gradient with the time (Rountree *et al.*, 2017).

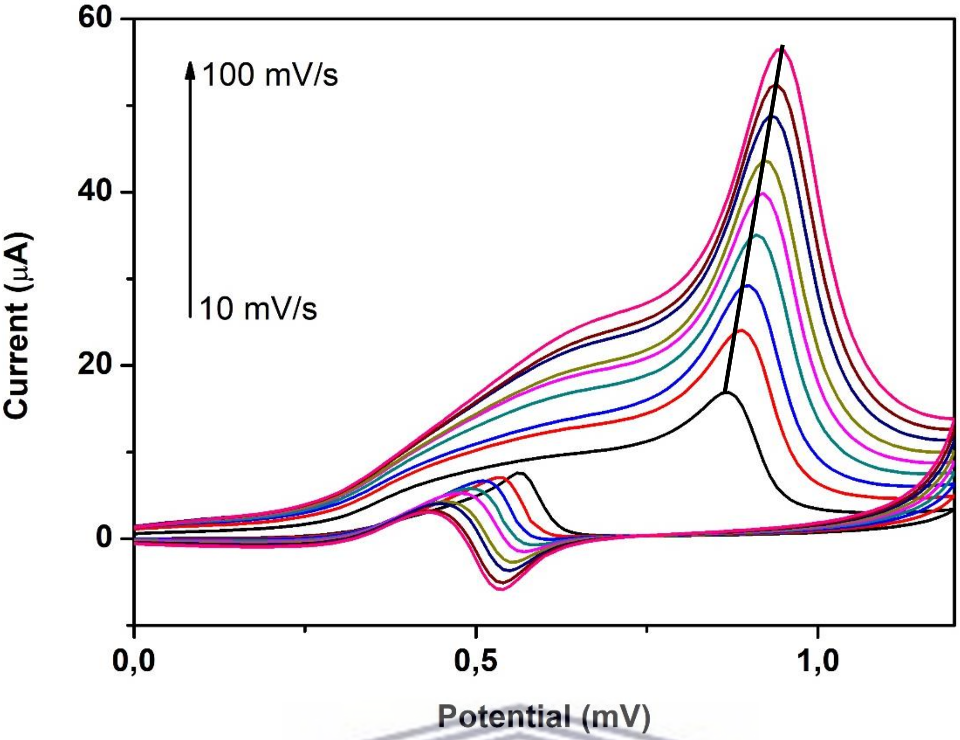

Figure 3.27: The cyclic voltammograms of TGA immobilized on a bare Au at multiple scan rates varying from 10-90 mVs^{-1}.

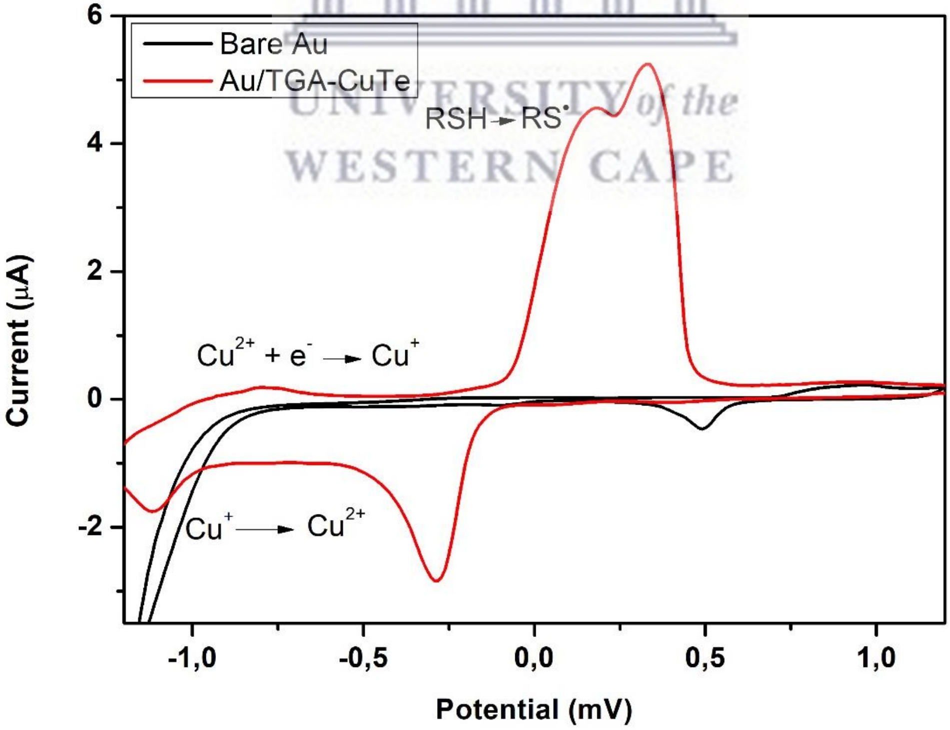

Figure 3.28: Cyclic voltammograms measured with bare Au electrode and TGA-CuTe in 0.1 phosphate buffer (pH 7.40) with proposed reaction mechanisms responsible for the current peaks.

Figure 3.28, shows cyclic voltammograms of bare Au electrode and TGA-CuTe quantum dots immobilized onto the Au electrode and measured in 0.1 M PBS. For the bare electrode, one reduction peak where observed attributed to gold oxide Epc= (0.33 V) and one oxidation peak attributed to the formation of gold oxide Epa= (-0.28 V). As compared to bare Au electrode, the TGA-CuTe quantum dots exhibited three reduction peaks at Epc = -0.79 V, 0.19 V and 0.34 V and two oxidation peaks at Epa = -0.28 V and -1.12 V. The reduction peak at (0.34 V) and the reduction peak occurring at (-0.28 V) showed an increase in peak current than that of bare gold electrode and a shift towards negative potentials. Whereas the reduction peak at -1.12 V was assigned to the reduction of Cu^{2+} to Cu (Feleni, 2013). As TGA is used as a ligand to stabilize CuTe QDs, we also examined the influence of TGA adsorption on the electrochemical behaviour of Te-terminated and Cu terminated CuTe QDs. Observed here is also a shift to more negative potentials as a result of the capping agent, TGA, donating negative charges to the CuTe quantum dots (Osipovich *et al.*, 2016). The quantum dots TGA-CuTe then MPS was added to the quantum dots for a silica core-shell and the behaviour was characterized using cyclic voltammetry. *Figure 3.31* show the cyclic voltammograms of TGA-CuTe and MPS-TGA-CuTe.

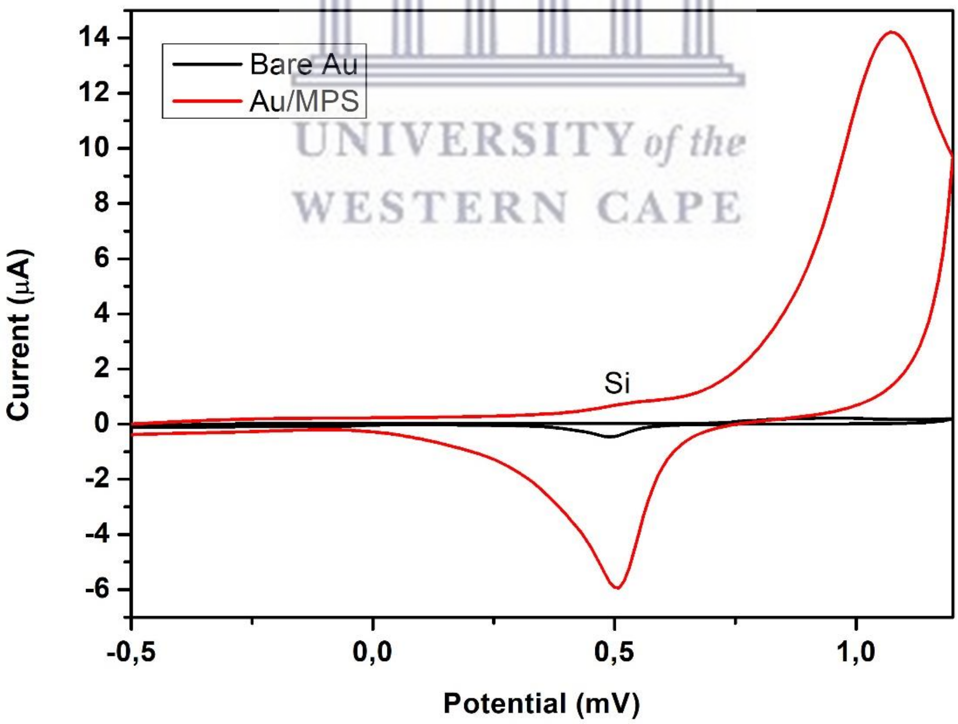

Figure 3.29: Cyclic voltammograms measured with bare Au electrode and Au/MPS.

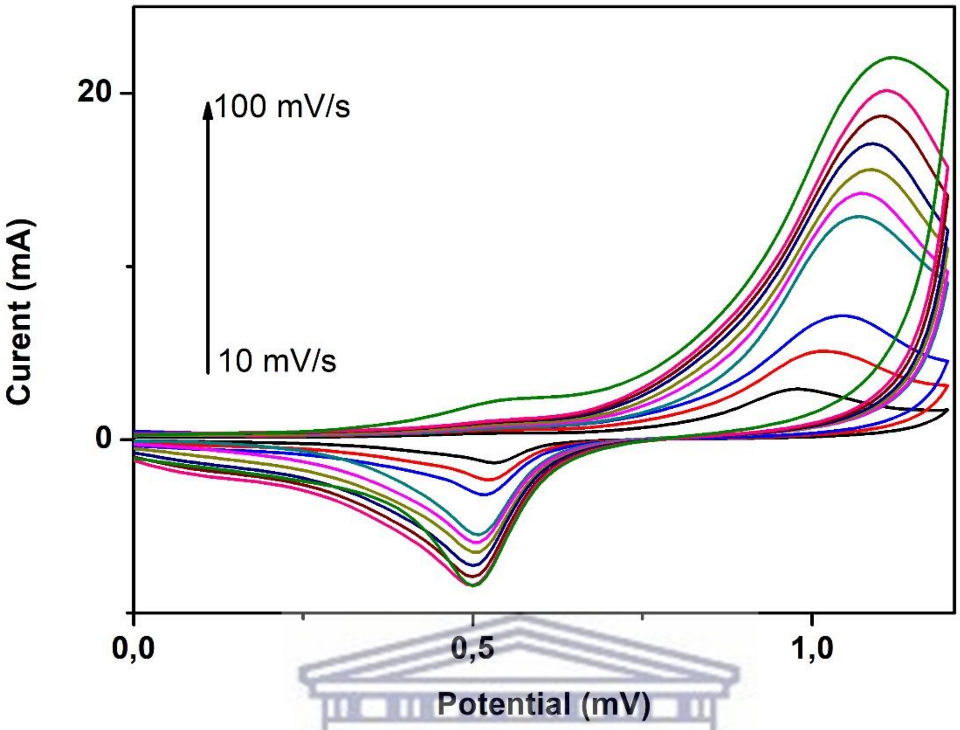

Figure 3.30: The cyclic voltammograms of MPS immobilized on a bare Au at multiple scan rates varying from 10-100 mVs^{-1}.

Cyclic voltammograms recorded at between –1.2 V and +1.2 V in 0.1 M phosphate buffer solution (pH 7.40) are shown in *Fig. 3.29*. The first cycle Au/MPS exhibited clearly one well-defined oxidation peaks at 0.53 V in the forward scan. The peak is an indication that the capping reagent is absorbed on the surface of the electrode. *Figure 3.30* shows multi-scans of Au/MPS at different scan rates. With an increase of the scan rate the current of the peak also increases. In *Figure 3.31*, when MPS is formed on electrode, one can notice an obvious decrease in the cathodic and anodic peak currents. The reason is that the –SH of the MPS solution serving as binding site for the covalent attachment of MPS to electrode surface blocked electron transfer (Zhong *et al.*, 2005). On the cyclic voltammetry of Au/MPS-TGA-CuTe all the peaks are visible. There are four reduction peaks that were observed and are -0.01 V, 0.22 V, 0.33 V and 0.91 V (which is from Au electrode). There were then three oxidation peaks that were observed at 0.39 V (which is also from Au electrode), 0.15 V and 0.36 V. The small peak at 0.01 is attributated to $Cu^{2+} + e^- \rightarrow Cu^+$ and the peak at 0.22 is attributed to $Cu^+ + e^- \rightarrow Cu$ (He *et al.*, 2015). These two peaks shifted to the positive potential with the addition of MPS and with the capping reagent TGA one of the peak dissapeared. Now with the capping reagent MPS all the peaks are visible with a shift and current reduction. The redution peak at 0.33 V is attributed with Si from the (3-mercaptopropyl) trimethoxysilane (MPS). The reduction peak at 0.15 is attributed to $Cu \rightarrow Cu^{+} + e^{-}$ and the last peak at -0.36 V is attributed to $Cu^{+} \rightarrow Cu^{2+} + e^{-}$ and it is also possible that the peak is attributed to Te^{2-} from the telluride that is used. The reduction peaks are seen to be shifting towards more positive potentials while the oxidation peaks are seen to be shifting to more negative potentials indicating an electron transfer and irreversible process (Krug *et al.*, 2012).

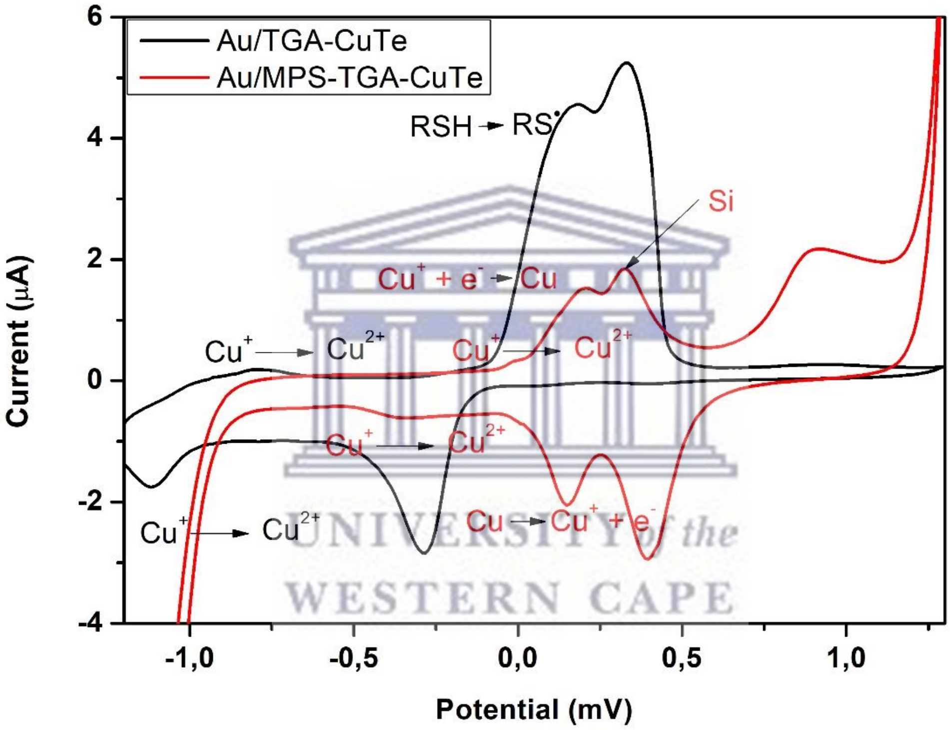

Figure 3.31: Cyclic voltammograms measured with bare Au/TGA-CuTe and Au/MPS-TGA-CuTe in 0.1 M phosphate buffer (pH 7.40).

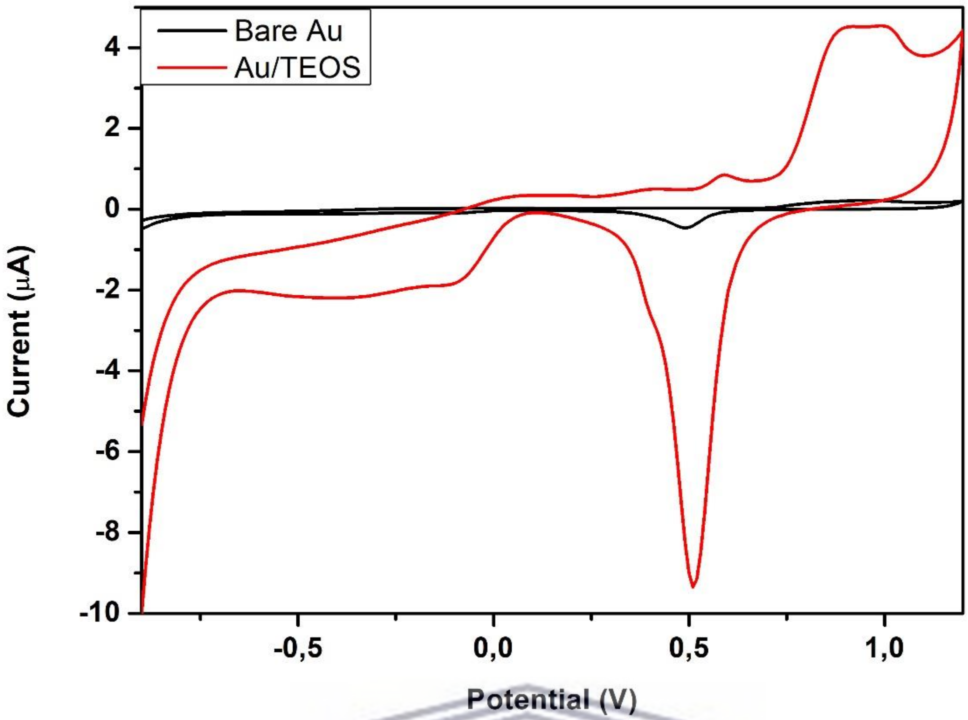

Figure 3.32: Cyclic voltammograms measured with bare Au electrode and Au/TEOS.

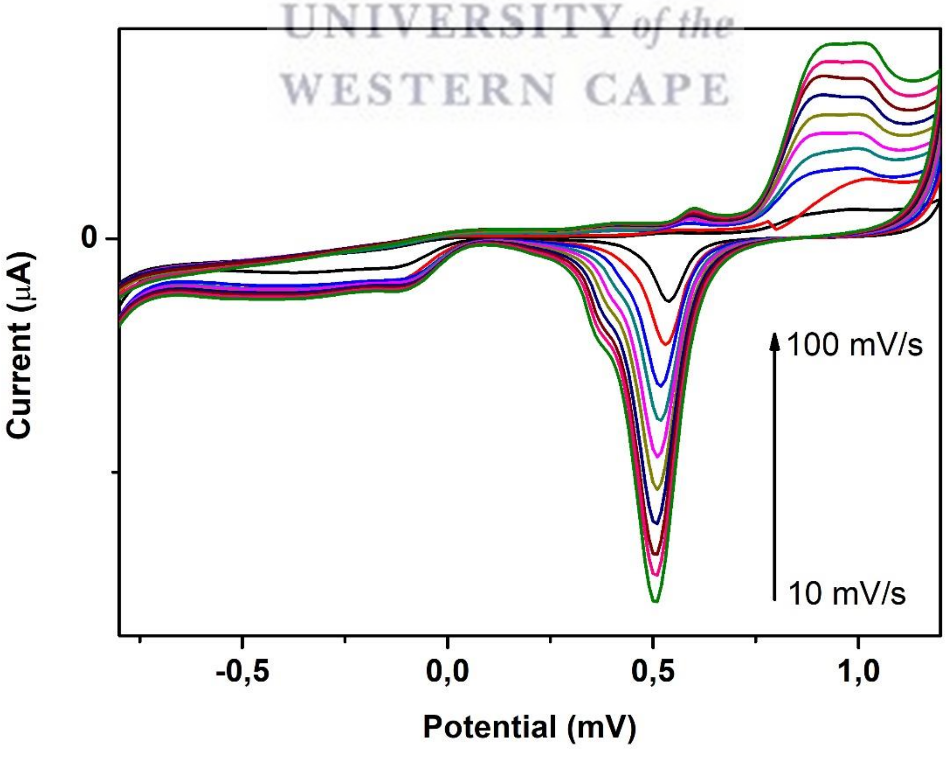

Figure 3.33: The cyclic voltammograms of MPS immobilized on a bare Au at multiple scan rates varying from 10-100 mVs^{-1}.

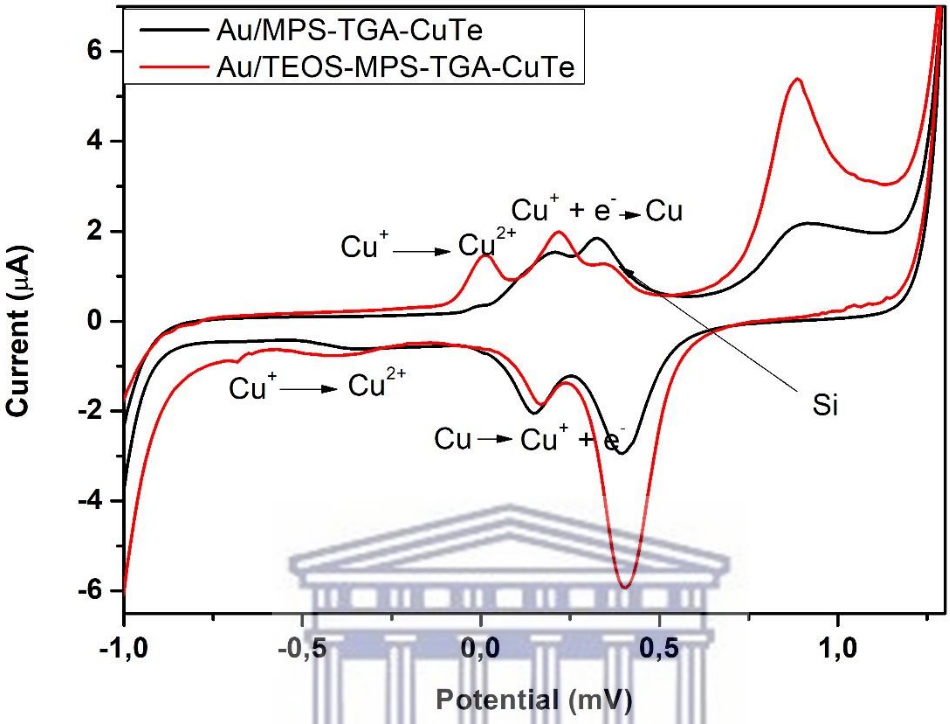

Figure 3.34: Cyclic voltammograms measured with bare Au/MPS-TGA-CuTe and Au/TEOS-MPS-TGA-CuTe in 0.1 phosphate buffer (pH 7.40).

Cyclic voltammetry is a simple and easy mean to show the changes of electrode behaviour after each assembly step, because the electron transfers between the solution species and the electrode must occur by tunnelling through either the barrier or the defects in the barrier from *Fig. 3.30,* shows the details of MPS-TGA-CuTe has been explained. Adding to this composite, silica was added which resulted in a cyclic voltammetry above (Sakai *et al.*, 2012). TEOS-MPS-TGA-CuTe peak at -0.4 V was enhanced from MPS-TGA-CuTe. This peaks shows the grow of the quantum dots and enhancement of the peak is it is clear that it is due to the addition of silica. Most of the peaks that appeared with in this sensor were more visible in the Au/TEOS-MPS-TGA-CuTe (Raquel *et al.*, 2017). Which indicates that the use of these reagents are complimentary with one another.

3.4 Biosensor

Electrochemical impedance spectroscopy (EIS) can give information on the impedance changes of the electrode surface during the modification process. The EIS include a semicircle part and a linear part. The semicircle part at higher frequencies corresponds to the electron-transfer limited process, the semicircle diameter of EIS equals to the electron transfer resistance (*R*et), which controls the electron transfer kinetics of the redox probe at the electrode interface. And the linear part at lower frequencies corresponds to the diffusion process. The EIS was done to check if these quantum dots are working in immunoassay and also will they are able to detect.

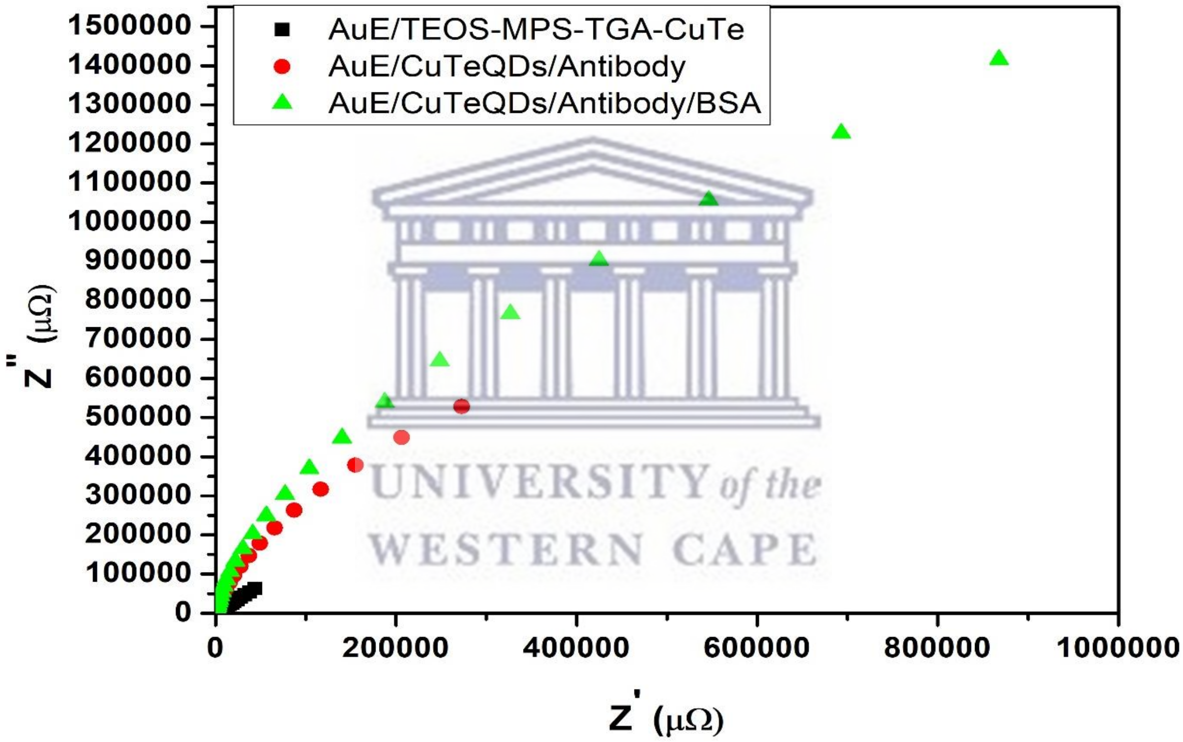

Figure 3.35: Nyquist plot of AuE/Capped-CuTe QDs, AuE/CuTeQDs/Antibody and AuE/CuTeQDs/BSA in 0.1 M PBS, pH 7.40.

The electron transfer capability of different electrodes was investigated by electrochemical impedance analysis and the corresponding results are shown in *Fig. 3.35*. The first investigation was of *AuE/Capped-CuTe QDs, AuE/CuTeQDs/Antibody and AuE/CuTeQDs/BSA in 0.1 M PBS, pH 7.40*. It was obvious that the *AuE/Capped-CuTe QDs* had the lowest Rct among all the electrodes, which might be attributed to the large surface area. These results are in good agreement with the peak current (ipa) values obtained from CVs measurements. In general, the change of impedance during the modification process was measured by EIS experiments. The

Faradaic impedance spectra achieved in each modification process were shown in *Fig. 2.36*. The diameter of semicircle calculated from the Nyquist plot corresponds to the electron transfer resistance (*R*ct). As can be deduced from the impedance spectrum the *R*ct value showed a slight increase when IFN-γ was modified with *AuE/CuTeQDs/BSA*, indicating the successful formation of quantum dots on the surface of AuE (Sepulveda, Aroca and Osma, 2017). When the fabricated immunosensor was used for the detection of IFN-γ, *R*ct was found to increase furtherly with increase of IFN-γ concentration, which could be ascribed to the significant hinder effect of formed protein layer for the diffusion of probe toward the surface of electrode (Liu *et al.*, 2015). It was then repeated three times to show reproducibility of same results. The biosensor's detection limit value was determined in *Figure 3.37* to be a value of 0.042 ng/mL. This indicates that the biosensor is suitable for measuring the low concentrations of IFN-γ and can be customised for higher concentrations(Liu *et al.*, 2010).

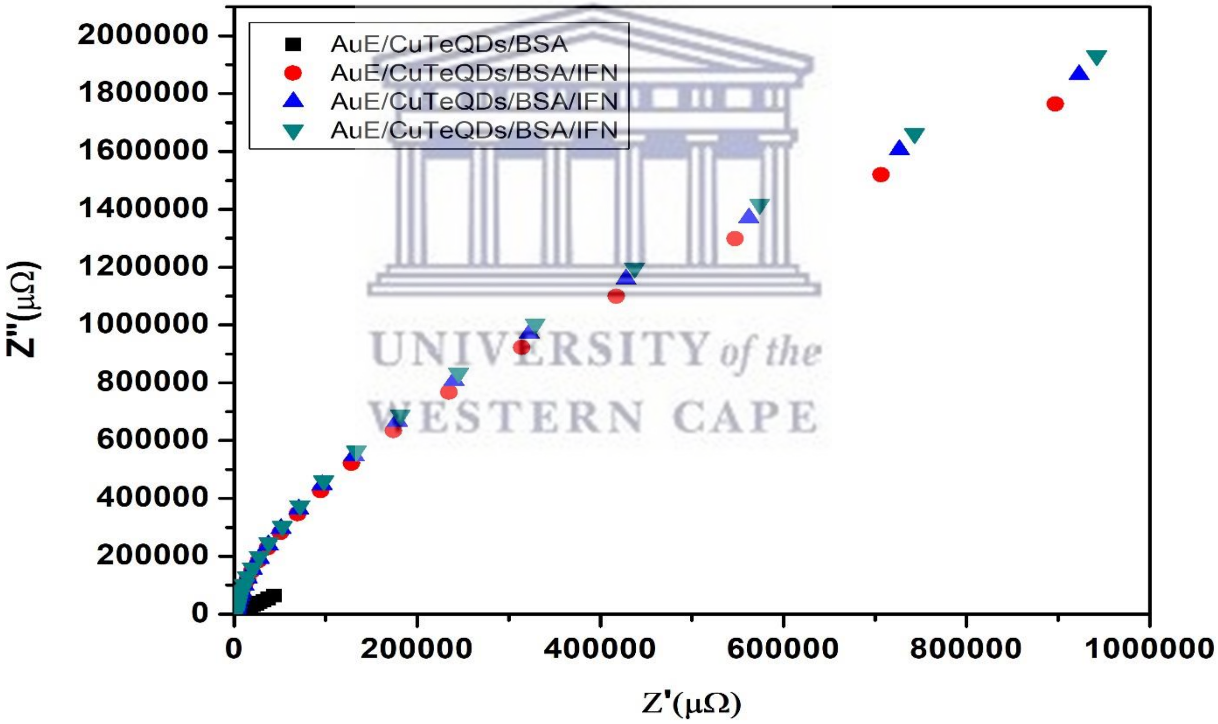

Figure 3.36: Nyquist plot of AuE/CuTeQDs/BSA, AuE/CuTeQDs/BSA/IFN, AuE/CuTeQDs/BSA/IFN and AuE/CuTeQDs/BSA/IFN in 0.1 M PBS, pH 7.40.

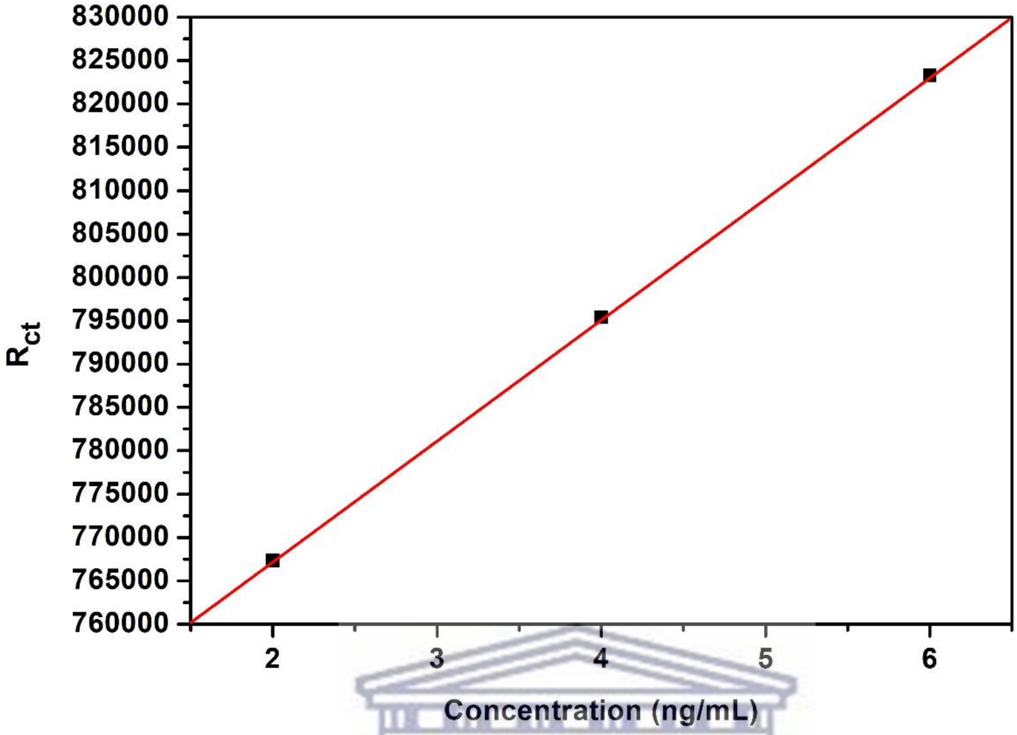

Figure 3.37: Calibration curve of the as-prepared immunosensor upon incubated with different concentrations of IFN-γ (2, 4, and 6 ng/mL).

3.5 Conclusion

Water-soluble copper telluride QDs were successfully synthesized through an aqueous route with the use of different capping agents: TGA, MPS and TEOS. These capping agents have, to the best of our knowledge, never been explored for capping of CuTe QDs before. The type of capping agent had effect on the size distribution and stability of the QDs. The formed nanoparticles had a small average size which was confirmed through HRTEM, SAXS and XRD analysis. HRTEM and XRD analysis showed that TGA-CuTe QDs gave the smallest average core size when dried. The average core size calculated was 7.91 nm for HRTEM. However, the tendency to aggregate was also largest within the MPS-TGA-CuTe QDs. This could be seen by the irregular shape of the PDDF curve from the SAXS measurements.

The capping of CuTeQDs was confirmed by FTIR via the specific S-H, Si-CH_2-S and Si-O-Si signature bands of TGA, MPS and TEOS respectively. The effect on the optical and electrochemical properties of the QDs, which was investigated through UV-vis absorption, PL and CV. The QDs exhibited a large blue shift of the band gap (caused by the quantum confinement effect) which was determined through UV-vis absorption studies. PL studies confirmed that the TGA-CuTe QDs emits light at 370 nm, MPS-TGA-CuTe QDs emits light at 385 nm and TEOS-MPS-TGA-CuTe QDs emits light at 382 nm. Cyclic voltammetry studies confirmed good electrochemical properties when immobilized on an electrode surface. In summary, the novel immunosensor, equipped with prominently conductivity of CuTe QDs, is ideal for the development of electrochemical immunosensor. Anti-IFN-γ can be directly attached to the modified electrode and used to specifically recognize IFN-γ. These makes the QDs possible to use as an electrochemical biosensor as an electron mediator. This immunosensor was easy to fabricate without complicated procedures or expensive instruments and exhibited an excellent performance. The proposed immunosensor was successfully applied for the determination of IFN-γ. The obtained biosensor is a successful development of a user-friendly and inexpensive biosensor for Interferon gamma. Calibration curve drawn from linear region was used to determine the detection limit (0.042ng/mL) of the biosensor system. From these results, we can conclude that biosensor construction method developed in this study possesses excellent acceptable stability and good reliability. Additionally, this indicates that biosensor systems represent a powerful nanotechnology suitable for determining IFN-γ and may be used to develop point-of care and low cost devices for personalized therapy. Therefore, this novel, facile strategy reported here may hold great promise for applications in the clinical diagnosis with further development.

References

Abd Rahman, S. *et al.* (2017) 'Thiolate-Capped CdSe/ZnS Core-Shell Quantum Dots for the Sensitive Detection of Glucose', *Sensors (Basel, Switzerland)*, 17(7), pp. 1–12. doi: 10.3390/s17071537.

Abdelbar, M. F. *et al.* (2016) 'Spectrochimica Acta Part A : Molecular and Biomolecular Spectroscopy Photo-induced interaction of thioglycolic acid (TGA) -capped CdTe quantum dots with cyanine dyes', *SAA*. Elsevier B.V., 168, pp. 1–11. doi: 10.1016/j.saa.2016.05.029.

Ambika, S. *et al.* (2019) 'Structural , morphological and optical properties and solar cell applications of thioglycolic routed nano cobalt oxide material', *Energy Reports*. Elsevier Ltd, 5, pp. 305–309. doi: 10.1016/j.egyr.2019.02.005.

Andrews, E. *et al.* (2015) 'Electrocatalytic Reduction of CO 2 at Au Nanoparticle Electrodes : Effects of Interfacial Chemistry on Reduction Behavior', 162(12), pp. 1373–1378. doi: 10.1149/2.0541512jes.

Attar, A. R., Blumling, D. E. and Knappenberger, K. L. (2011) 'Photodissociation of thioglycolic acid studied by femtosecond time-resolved transient absorption spectroscopy', *Journal of Chemical Physics*, 134(2), pp. 1–9. doi: 10.1063/1.3526746.

Bands, R. (no date) 'Raman Bands RAMAN DATA AND ANALYSIS Raman Spectroscopy for Analysis and Monitoring', pp. 2–3.

Baustian, J. J. (1988) 'system'.

Choudhary, Y. S. and Nageswaran, G. (2019) 'Sensing and Bio-Sensing Research Branched mercapto acid capped CdTe quantum dots as fluorescence probes for Hg 2 + detection', *Sensing and Bio-Sensing Research*. Elsevier, 23(February), p. 100278. doi: 10.1016/j.sbsr.2019.100278.

Congiu, M. *et al.* (2015) 'A novel and large area suitable water-based ink for the deposition of cobalt sulfide films for solar energy conversion with iodine-free electrolytes', *Solar Energy*. Elsevier Ltd, 122(December 2015), pp. 87–96. doi: 10.1016/j.solener.2015.08.032.

Dalmoro, V. *et al.* (2013) 'A synergistic combination of tetraethylorthosilicate and multiphosphonic acid offers excellent corrosion protection to AA1100 aluminum alloy', *Applied Surface Science*. Elsevier B.V., 273, pp. 758–768. doi: 10.1016/j.apsusc.2013.02.131.

Das, R., Nath, S. S. and Bhattacharjee, R. (2011) 'Luminescence of copper nanoparticles', *Journal of Luminescence*. Elsevier, 131(12), pp. 2703–2706. doi: 10.1016/j.jlumin.2011.05.019.

Dhasade, S. S., Han, S. H. and Fulari, V. J. (2012) 'A nanostructured copper telluride thin film grown at room temperature by an electrodeposition method A nanostructured copper telluride thin film grown at room temperature by an electrodeposition method', (September). doi: 10.1088/1674-4926/33/9/093002.

Ebrahim, S. *et al.* (2017) 'CdTe quantum dots capped with different stabilizing agents for sensing of ochratoxin A', *Journal of Luminescence*. Elsevier, 182, pp. 154–159. doi: 10.1016/j.jlumin.2016.09.038.

Eleanor Adachi1, Idemudia John Airuoyo2, Lakshmi Krishna2, R. C. (2016) 'Developing a Process for Studying Annealing Effects on Mobilities in Silicon Quantum Dots', 1527(1986), p. 163111.

Fang, T. *et al.* (2012) '3-Mercaptobutyric Acid as an E ff ective Capping Agent for Highly Luminescent CdTe Quantum Dots : New Insight into the Selection of Mercapto Acids'.

Feleni, U. (2013) 'Palladium Telluride Quantum Dots Biosensor for the Determination of Indinavir Drug By Usisipho Feleni (BSc Honours) A thesis submitted in partial fulfilment of the requirements for the degree of Magister Scientiae in Nanoscience Faculty of Science Unive', (November).

Feleni, U. (2017) 'Quantum Dots-Amplified Electrochemical Cytochrome P450 Phenotype Sensor for Tamoxifen , a Breast Cancer Drug', (May).

Freitas, D. V, Dias, J. M. M. and Passos, S. G. B. (2014) 'Electrochemical synthesis of TGA-capped CdTe and CdSe quantum dots', pp. 3247–3254. doi: 10.1039/c4gc00300d.

Gabriella, L. and Pacoste, C. (2017) 'Development of Copper Selenide Quantum Dots-Based Therapeutic Drug Monitoring Biosensors for Toremifene – In the Department of Chemistry , University of the Western Cape'.

Gadalla, A. *et al.* (2017) 'CHARACTERIZATION OF CdSe CORE AND CdSe / ZnS CORE / SHELL QUANTUM DOTS SYNTHESIZED USING A MODIFIED METHOD', 14(7), pp. 239–249.

Garcia-gutierrez, D. F. *et al.* (2018) 'In fl uence of the Capping Ligand on the Band Gap and Electronic Levels of PbS Nanoparticles through Surface Atomistic Arrangement Determination'. doi: 10.1021/acsomega.7b01451.

Gfroerer, T. H. (2000) 'Photoluminescence in Analysis of Surfaces and Interfaces', pp. 9209–9231.

Goftman, V. V *et al.* (2016) 'Multicolored silica coated CdSe core / shell quantum dots', 9917, pp. 1–6. doi: 10.1117/12.2225212.

Gomaa, E. A. and Salem, S. E. (2016) 'Cyclic Voltammetry Study of Copper Chloride Salt with Ceftazidime Antibiotic', 3(3).

Hao, J. *et al.* (2019) 'A facile route to synthesize CdSe / ZnS thick-shell quantum dots with precisely controlled green emission properties : towards QDs based LED applications', *Scientific Reports*. Springer US, (February), pp. 1–8. doi: 10.1038/s41598-019-48469-7.

He, W. *et al.* (2015) 'Electrodeposition and Characterization of CuTe and Cu 2 Te Thin Films', 2015.

Hodlur, R. M. and Rabinal, M. K. (2014) 'A new selenium precursor for the aqueous synthesis of luminescent CdSe quantum dots', *CHEMICAL ENGINEERING JOURNAL*. Elsevier B.V., 244, pp. 82–88. doi: 10.1016/j.cej.2014.01.064.

Jameel (2010) 'Review of Literature', pp. 1–35. doi: 10.3390/healthcare3041243.Sleep.

Jiang, H. and Ju, H. (2007) 'Electrochemiluminescence sensors for scavengers of hydroxyl radical based on its annihilation in CdSe quantum dots film/peroxide system', *Analytical Chemistry*, 79(17), pp. 6690–6696. doi: 10.1021/ac071061j.

Jimenez-lópez, J. *et al.* (2016) 'Automated determination of Rifamycins making use of MPA – CdTe quantum dots', *Journal of Luminescence*. Elsevier, 175, pp. 158–164. doi: 10.1016/j.jlumin.2016.02.036.

Joseph, J., Nagashri, K. and Suman, A. (2016) 'Journal of Photochemistry & Photobiology , B : Biology Synthesis , characterization and pharmacological studies of copper complexes of flavone derivatives as potential anti-tuberculosis agents', *JPB*. Elsevier B.V., 162, pp. 125–145. doi: 10.1016/j.jphotobiol.2016.06.033.

Jun-Jie Zhu, Jing-Jing Li, Hai-Ping Huang, F.-F. C. (2013) 'Quantum Dots', pp. 9–25. doi: 10.1007/978-3-642-44910-9.

Kaviyarasu, K. *et al.* (2016) 'Solution processing of CuSe quantum dots : Photocatalytic activity under RhB for UV and visible-light solar irradiation', *Materials Science & Engineering B*. Elsevier B.V., 210, pp. 1–9. doi: 10.1016/j.mseb.2016.05.002.

Ke, S. *et al.* (2019) 'Construction of silica-encapsulated gold-silver core-shell nanorod : Atomic facets enrichment and plasmon enhanced catalytic activity with high stability and reusability', *Materials & Design*. The Authors, 177, p. 107837. doi: 10.1016/j.matdes.2019.107837.

KENAN KOÇa,b, FATMA Z. TEPEHANb, G. G. T. (2011) 'OF SELF-ASSEMBLED QUANTUM DOTS THIN FILMS ON A GLASSY SUBSTRATE', 8(4), pp. 239–247.

Kobayashi, Y., Correa-Duarte, M. A. and Liz-Marzán, L. M. (2001) 'Sol−Gel Processing of Silica-Coated Gold Nanoparticles', *Langmuir*, 17(20), pp. 6375–6379. doi: 10.1021/la010736p.

Koç, K., Tepehan, F. Z. and Tepehan, G. G. (2012) 'Growth kinetics of MPS-capped CdS quantum dots in self-assembled thin films', pp. 1–7.

Krug, K. *et al.* (2012) 'Electrochemical Cu Growth on MPS-Modified Au (111) Electrodes', (111).

Kuhar, N. *et al.* (2018) 'Challenges in application of Raman spectroscopy to biology and materials'. Royal Society of Chemistry, pp. 25888–25908. doi: 10.1039/c8ra04491k.

Kumar, B. R. and Hymavathi, B. (2017) 'Journal of Asian Ceramic Societies X-ray peak profile analysis of solid-state sintered alumina doped zinc oxide ceramics by Williamson – Hall and size-strain plot methods', *Integrative Medicine Research*. Taibah University, 5(2), pp. 94–103. doi: 10.1016/j.jascer.2017.02.001.

Labiadh, H. and Hidouri, S. (2017) 'ZnS quantum dots and their derivatives : Overview on identity , synthesis and challenge into surface modifications for restricted applications', *Journal of King Saud University - Science*. King Saud University, 29(4), pp. 444–450. doi: 10.1016/j.jksus.2016.12.001.

Lecture, N. (2017) 'Advanced Nanochemistry By Dr Masikini Milua SensorLab , Department of Chemistry University of the Western Cape . Email : mmasikini@uwc.ac.za'.

Li, H., Shih, W. Y. and Shih, W. H. (2007) 'Stable aqueous ZnS quantum dots obtained using (3-mercaptopropyl) trimethoxysilane as a capping molecule', *Nanotechnology*, 18(49). doi: 10.1088/0957-4484/18/49/495605.

Liu, C. *et al.* (2015) 'An electrochemical aptasensor for detection of IFN-γ using graphene and a dual signal amplification strategy based on the exonuclease-mediated surface-initiated enzymatic polymerization', *Analyst*, 140(22), pp. 7784–7791. doi: 10.1039/c5an01591j.

Liu, Y. *et al.* (2010) 'Aptamer-based electrochemical biosensor for interferon gamma detection', *Analytical Chemistry*, 82(19), pp. 8131–8136. doi: 10.1021/ac101409t.

Ma, Y. *et al.* (2014) 'Highly bright water-soluble silica coated quantum dots with excellent stability', *Journal of Materials Chemistry B*, 2(31), pp. 5043–5051. doi: 10.1039/c4tb00458b.

Manuscript, A. (2015) ‘Analytical Methods’. doi: 10.1039/C5AY01412C.

Morales-saavedra, O. G. *et al.* (2015) ‘Fabrication and photophysical studies of CdTe quantum-dots dispersed in’, *Revista Mexicana de Trastornos Alimentarios*. Universidad Nacional Autónoma de México, Centro de Ciencias Aplicadas y Desarrollo Tecnológico, 13(6), pp. 566–575. doi: 10.1016/j.jart.2015.10.013.

Nagaveni, V. B. *et al.* (2018) ‘Journal of Science : Advanced Materials and Devices Synthesis , crystal structure and excellent photoluminescence properties of copper (II) and cobalt (II) complexes with Bis’, *Journal of Science: Advanced Materials and Devices*. Elsevier Ltd, 3(1), pp. 51–58. doi: 10.1016/j.jsamd.2018.01.001.

Onwudiwe, D. C., Hrubaru, M. and Ebenso, E. E. (2015) ‘Synthesis , Structural and Optical Properties of TOPO and HDA Capped Cadmium Sulphide Nanocrystals , and the Effect of Capping Ligand Concentration’, 2015.

Osipovich, N. P. *et al.* (2016) ‘Cyclic voltammetry as a sensitive method for in situ probing of chemical transformations in quantum dots’, *Physical Chemistry Chemical Physics*, 18(15), pp. 10355–10361. doi: 10.1039/c6cp01085g.

Pal, C. *et al.* (2017) ‘Charge transport in lead sul fi de quantum dots / phthalocyanines hybrid nanocomposites’, *Organic Electronics*. Elsevier B.V, 44, pp. 132–143. doi: 10.1016/j.orgel.2017.02.014.

Pauw, B. R., Kästner, C. and Thünemann, A. F. (2017) ‘Nanoparticle Size Distribution Quantification : Results of a SAXS Inter-Laboratory Comparison’, 1, pp. 1–21.

Piersimoni, C. *et al.* (2006) ‘Current perspectives on drug susceptibility testing of Mycobacterium tuberculosis complex: The automated nonradiometric systems’, *Journal of Clinical Microbiology*, 44(1), pp. 20–28. doi: 10.1128/JCM.44.1.20-28.2006.

Qutub, N. and Sabir, S. (2012) ‘Optical , Thermal and Structural Properties of CdS Quantum Dots Synthesized by A Simple Chemical Route’, 8(2), pp. 111–120.

Rahman, I. A. and Padavettan, V. (2012) ‘Synthesis of Silica Nanoparticles by Sol-Gel : Size-Dependent Properties , Surface Modification , and Applications in Silica-Polymer Nanocomposites — A Review’, 2012. doi: 10.1155/2012/132424.

Raquel, S. *et al.* (2017) ‘Corrosion Mechanism Suggested Based on Electrochemical Analysis and SVET for Uncoated Tinplate and Post Coated With a Hybrid Film 2 . Experimental Procedures’, 20(6), pp. 1735–1747.

Rountree, K. J. *et al.* (2017) ‘A Practical Beginner ’ s Guide to Cyclic Voltammetry’. doi: 10.1021/acs.jchemed.7b00361.

Rubio, F., Rubio, J. and Oteo, J. L. (2006) ‘A FT-IR Study of the Hydrolysis of Tetraethylorthosilicate (TEOS).’, 7010. doi: 10.1080/00387019808006772.

Sakai, R. T. *et al.* (2012) ‘Progress in Organic Coatings Electrochemical study of TEOS , TEOS / MPTS , MPTS / MMA and TEOS / MPTS / MMA films on tin coated steel in 3 . 5 % NaCl solution’, *Progress in Organic Coatings*. Elsevier B.V., 74(2), pp. 288–301. doi: 10.1016/j.porgcoat.2012.01.001.

Salavati-Niasari, M. *et al.* (2013) ‘Surfactant-Free Fabrication of Copper Sulfides (CuS, Cu2S) via Hydrothermal Method’, *Journal of Cluster Science*, 24(4), pp. 1181–1191. doi: 10.1007/s10876-013-0608-x.

Sánchez-vergara, M. E. *et al.* (2012) ‘Determination of the Optical GAP in Thin Films of Amorphous Dilithium Phthalocyanine Using the Tauc and Cody Models’, pp. 10000–10013. doi: 10.3390/molecules170910000.

Sepulveda, D., Aroca, M. A. and Osma, J. F. (2017) ‘Bioelectrochemical Detection of Mycobacterium tuberculosis ESAT-6 in an’. doi: 10.3390/s17102178.

Series, I. O. P. C. and Science, M. (2016) ‘Green Luminescent Copper Nanoparticles’. doi: 10.1088/1757-899X/149/1/012187.

Shahraki, M. R. and Irani, M. (2014) ‘The Effects of Ecstasy on Liver Function Tests, Blood Glucose, and Lipids Profile of Male Rats’, *International Journal of High Risk Behaviors and Addiction*, 3(4). doi: 10.1039/c2py20863f.

Shanehsaz, M., Mohsenifar, A. and Hasannia, S. (2013) ‘Detection of Helicobacter pylori with a nanobiosensor based on fluorescence resonance energy transfer using CdTe quantum dots’, pp. 195–202. doi: 10.1007/s00604-012-0906-2.

Singh, A. *et al.* (2015) ‘Surface functionalization of quantum dots for biological applications’. Elsevier B.V., 215, pp. 28–45. doi: 10.1016/j.cis.2014.11.004.

Sirajuddin, M., Ali, S. and Badshah, A. (2013) ‘Journal of Photochemistry and Photobiology B : Biology Drug – DNA interactions and their study by UV – Visible , fluorescence spectroscopies and cyclic voltametry’, *Journal of Photochemistry & Photobiology, B: Biology*. Elsevier B.V., 124, pp. 1–19. doi: 10.1016/j.jphotobiol.2013.03.013.

Sögaard, C., Funehag, J. and Abbas, Z. (2018) ‘Silica sol as grouting material : a physio - chemical analysis’, *Nano Convergence*. Springer Singapore, pp. 1–15. doi: 10.1186/s40580-018-0138-1.

Stawski, T. M. *et al.* (2019) ‘Mechanism of silica – lysozyme composite formation unravelled by in situ fast SAXS’, pp. 182–197. doi: 10.3762/bjnano.10.17.

Stober, W. E. R. N. E. R. (1968) ‘Controlled Growth of Monodisperse Silica Spheres in the Micron Size Range 1’, 69, pp. 62–69.

Talluri, B., Prasad, E. and Thomas, T. (2018) ‘Superlattices and Microstructures Ultra-small (r < 2 nm), stable (> 1 year) copper oxide quantum dots with wide band gap’, *Superlattices and Microstructures*. Elsevier Ltd, 113, pp. 600–607. doi: 10.1016/j.spmi.2017.11.044.

Tang, X. *et al.* (2017) ‘Ultrathin and Highly Passivating Silica Shells for Luminescent and Water-Soluble CdSe/CdS Nanorods’. doi: 10.1021/acs.langmuir.7b00615.

Tashkhourian, J. *et al.* (2016) ‘Spectrochimica Acta Part A : Molecular and Biomolecular Spectroscopy A rapid and sensitive assay for determination of doxycycline using thioglycolic acid-capped cadmium telluride quantum dots’, *SPECTROCHIMICA ACTA PART A: MOLECULAR AND BIOMOLECULAR SPECTROSCOPY*. Elsevier B.V., 152, pp. 119–125. doi: 10.1016/j.saa.2015.07.063.

‘The SAXS Guide’ (2013).

Valizadeh, A. *et al.* (2012) ‘Quantum dots : synthesis , bioapplications , and toxicity’, *Nanoscale Research Letters*. Nanoscale Research Letters, 7(1), p. 1. doi: 10.1186/1556-276X-7-480.

Wang, C., Wang, T. and Zhang, Y. (2014) ‘Construction of a quantum repeater based on a quantum dot in an optical microcavity system’. doi: 10.1088/1612-2011/11/6/065202.

Wilkins, M. D. *et al.* (2018) ‘Sensing and Bio-Sensing Research Quantum dot enabled lateral flow immunoassay for detection of cardiac biomarker NT-proBNP’, *Sensing and Bio-Sensing Research*. Elsevier, 21(July), pp. 46–53. doi: 10.1016/j.sbsr.2018.10.002.

Wolcott, A. *et al.* (2006) ‘Silica-Coated CdTe Quantum Dots Functionalized with Thiols for Bioconjugation to IgG Proteins’, pp. 5779–5789. doi: 10.1021/jp057435z.

Wuister, S. F. and Meijerink, A. (2003a) ‘Synthesis and luminescence of (3-mercaptopropyl) - trimethoxysilane capped CdS quantum dots’, 103, pp. 338–343.

Wuister, S. F. and Meijerink, A. (2003b) ‘Synthesis and luminescence of CdS quantum dots capped with a silica precursor’, 105, pp. 35–43. doi: 10.1016/S0022-2313(03)00095-4.

Zhong, X. *et al.* (2005) ‘Glucose biosensor based on self-assembled gold nanoparticles and polymer onto gold substrate’, 104, pp. 191–198. doi: 10.1016/j.snb.2004.04.114.

Zhou, J. G., Williams, Q. L. and Wu, R. (2010) ‘Thioglycolic acid on the gold (111) surface and Raman vibrational spectra’, *Journal of Chemical Physics*, 132(6), pp. 1–8. doi: 10.1063/1.3319711.

Zhou, X. *et al.* (2005) ‘Preparation of silica encapsulated CdSe quantum dots in aqueous solution with the improved optical properties’, 242, pp. 281–286. doi: 10.1016/j.apsusc.2004.08.022.

Chapter four

Summary

This chapter describes the procedures for the synthesis of ZnTe QDs using three appropriate reagents. Their properties were investigated using techniques such as spectroscopic (UV, FTIR), microscopic (HRSEM, HRTEM) and electrochemical (CV).

Biocompatibility of silica coated ZnTe quantum dots for the detection of Interferon gamma

Abstract

Bio-electrochemical sensing of Mycobacterium tuberculosis through electro-immunosensors is a promising technique to detect relevant analytes. In this work, an impedance analysis technique was used, as a non-invasive method, to measure and differentiate the manufacturing stages of the sensors. The silica-coated ZnTe quantum dots were prepared via a simple and environmentally friendly process. This work reports on the synthesis of conjugates of zinc telluride quantum dots (ZnTe-QDs) capped with thioglycolic acid, (3-mercaptopropyl) trimethoxysilane (MPS) and tetraethyl orthosilicate (TEOS), respectively had been successfully developed for use in the detection of Interferon gamma (IFN-γ) a TB disease biomarker. The quantum dots were synthesized in the presence of capping agents to improve their stability, solubility and biocompatibility. The capping of ZnTe quantum dots with TGA was confirmed by FTIR, where the SH group at 2570 cm^{-1} from the thiol, the absorption band disappeared from the spectra of TGA-ZnTe. The FTIR also conformed the silica present from MPS and TEOS around 1400 cm^{-1}. The particle size of the quantum dots was estimated from high resolution transmission electron microscopy (HRTEM) measurements to have an average size of 16-20 nm. Optical properties of the materials were confirmed by UV-Vis spectrophotometry which produced absorption bands at 320 nm that corresponded to energy band gap values of 4.04 eV for TGA-ZnTe quantum dots increased to band gap of 4.30 eV for TEOS-MPS-ZnTe QDs. The XRD indicated that the quantum dots are crystalline before the silica coated and amorphous after silica is added to the quantum dots. The cyclic voltammogram of the last capping reagent was added (TEOS) to form a thicker shell on the quantum dots (MPS-TGA-ZnTe). They both have the same peaks anodic at 0.16 V, 0.48 V and 0.89 V and same oxidation peaks at 0.37 V, 0.75 V and -0.49 V, which indicates that there was no change on the surface/core of the quantum dots but only the shell that was affected this was proven by the decrease of the peaks. After silica was assembled on the electrode, both anodic current and cathodic currents decreased, implying the hindrance exerted by silica on the electron-transfer process. In agreement with the Electrochemical Impedance Spectroscopy (EIS) tests performed before and after the functionalization revealed that the sensor was capable to selectively detect IFN-γ at a broad range of concentrations (limit of detection of 0.067). The device presented a stable impedimetric response when immediately prepared.

4.0 Introduction

Nowadays, the quality of the human's life is determined by accuracy of diagnostic, treatment, food control and environmental monitoring. This requires availability of the sensitive multiplex assays, which simultaneously measure multiple analytes in a single cycle of the analysis. Zinc telluride (ZnTe) quantum dots (QDs) belong to an important class of materials, semiconductor nanocrystals, which show quantum confinement phenomenon (Sovan Kumar Patra, BhavyaBhushanb and Priyam, 2016). These quantum dots also have all the properties of a semiconductor nanocrystals. Zinc telluride (ZnTe) has been found to be a very promising candidate for biomedical applications because of friendliness of zinc to biological systems as compared to cadmium (Hao *et al.*, 2019). A prerequisite for the aforementioned high-end applications is that the semiconductor nanocrystals possess tunability of photoluminescence (PL), high photoluminescence quantum efficiency (PL QE), photochemical stability, high monodispersity and desired surface functionality (Chen, Liu and Jiang, 2012; Sovan Kumar Patra, BhavyaBhushanb and Priyam, 2016). One of the main problems encountered in the development of QD-based systems is the selection of a suitable capping ligand in order to achieve adequate solubility of QDs in the dispersion media. There are many capping reagents that are used for quantum dots but each has its different uses and properties. In aqueous synthesis, thiols are predominantly employed as the capping agents (Niu and Li, 2013). Thioglycolic acid (TGA), mercaptopropionic acid, cysteine, glutathione, cystamine and mercaptoethanol are some of the water-soluble thiols which have been used in such synthesis. While the thiol-end of the molecule binds to the particle surface, the other end-groups such as amide(NH_2), carboxylate (COO-) or hydroxide (OH) remains free, which imparts biocompatibility and opens up a window to interact and integrate with other biomolecules (Shah, 2009). Thiol-capping method has been successfully used for synthesis of CdS, CdTe, CdSe, ZnS, ZnO QDs (Sovan Kumar Patra, BhavyaBhushanb and Priyam, 2016). A significant research effort has been devoted to prepare core-shell type QDs with a cross-linked shell that would protect the QDs much better than thiol-based coating. The most widely used approach is silica coating (Selvan, 2010). Silanization of various metal and semiconductor nanoparticle systems have shown great success in protecting their surface characteristics (Wolcott *et al.*, 2006). The silanization of QDs is a laborious process that goes through multiple steps. The first step involves the activation of QD surface for attaching the first layer of silane molecules (often called as primer layer) to QD surface (Singh *et al.*, 2015). Most developments have been made in the surface activation step of QDs for silanization. Earlier *Correa-Duarte et al.* exchanged the citrate coated QDs with silica coating by using (3-mercaptopropyl) trimethoxysilane (MPS) as the first layer of silica followed by solvent exchange in ethanol or water. The silica shell was then grown in thickness using the conventional *Stober* process by addition of tetraethyl orthosilicate (TEOS) to the colloidal solution (Kobayashi, Correa-Duarte and Liz-Marzán, 2001). Encapsulation of hydrophobic QDs into a silicon dioxide (SiO_2) shell is a well-known approach to make QDs soluble in water. Silica coated nanoparticles (NPs) have several advantages. In the first place, silica may provide both chemical and physical shielding from the direct environment, thereby improving the stability. For example, it can prevent aggregation of the nanocrystals, reduce the release of (cytotoxic) ions, or prevent photo-oxidation. Furthermore, the surface chemistry of colloidal silica is well developed and therefore facilitates the solubilisation in water or other hydrophilic solvents, enhances the bio-applicability, and allows modifications of the composite particles for further use (Owens *et al.*, 2016). In addition, silica spheres can contain multiple and different nanocrystals per particle (e.g., gold, magnetite, QDs), which is an idea starting point for a multimodality contrast agent (Goftman *et al.*, 2016).

In general, zinc tellurides, as a class of materials, have been found difficult to synthesize. Therefore, there is a need to devise a new method that has a better control over the nucleation and growth of these nanocrystals. In order to meet these challenges, we developed a super-saturation controlled aqueous approach to obtain ZnTe QDs with high monodispersity, stability and facile tunability of luminescence and particle sizes. To obtain these properties 3 capping reagents were used, starting with Thioglycolic acid then following with (3-mercaptopropyl) trimethoxysilane (MPS) and then silica shell was then grown in thickened by addition of tetraethyl orthosilicate (TEOS). These 3 capping reagent make very stable quantum dots and they will be best to be used for bio-application.

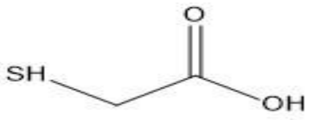

Thioglycolic acid (TGA)

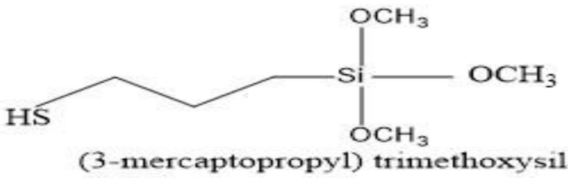

(3-mercaptopropyl) trimethoxysilane (MPS)

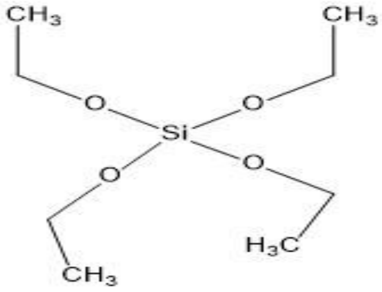

Tetraethyl orthosilicate (TEOS)

4.1 Materials and Method

4.1.1 Chemicals

All reagents were of analytical reagent grade and purchased from Sigma Aldrich. The material that were used are tetraethyl orthosilicate (TEOS, 90%), thioglycolic acid (TGA, 98%), (3-mercaptopropyl) trimethoxysilane (MPS, 95%), tellurium (Te, 99.997%), sodium hydroxide (NaOH, 98%), copper acetate monohydrate (Cu (OH)2CO3, 99.0%), sodium borohydride (NaBH4, 98%), sodium phosphate monobasic dihydrate (NaH2PO4, 99%) and disodium hydrogen phosphate dibasic (Na2HPO2, 98%). De-ionized water, used throughout the experiments, was prepared with a Milli-Q water purification system. Analytical grade nitrogen obtained from Afrox South Africa, was used for degassing buffer solutions. The Phosphate buffer solutions (pH 7.4) was prepared from H2NaPO4, HNa2PO4 and was used for all the electrochemistry.

4.1.2 Synthesis of ZnTe QDs with different stabilizing agents

NaHTe solution was prepared according to the following method. Simply, 0.396 g (3.1 mmol) of tellurium powder and 0.227 g (6.0 mmol) of $NaBH_4$ were loaded in a three neck flask and then 25 mL deionized water was added. The mixture was reacted at 50 °C for appropriate time under N_2 flow to get a deep purple clear solution (Ghosh *et al.*, 2011). ZnTe QDs were prepared by the following procedure. Simply, 400 µl (5.7 mmol) stabilizing agent (TGA) and 0.6146 g (2.8 mmol) $Zn(OH)_2CO_3$ were dissolved in 25 ml ultra-pure water. The pH of mixture was adjusted to pH = 12.0 by drop-wise addition of 20 g (5 M) NaOH solution with stirring in conical flask, then the fresh NaHTe solution was added through a syringe under continually stirring. The TGA injection occurred at 80 °C. The final solution was under reflux at 90 °C for 1 h, with aliquots taken at 20 min intervals. After the hour the solution was cooled down to room temperature (Ali and Sarma, 2007). In the flask containing TGA-capped ZnTe nanoparticles, MPS (330 µL, 1.8 mmol) was added to the solution, period of 20 min aliquots were taken. To ensure even distribution of MPS, a mini-stir bar was used during the 1h required for surface priming. After the hour the solution was heated for 5 min at 60°C. After surface priming, TEOS (1270 µL, 5.7 mmol) was added to the solution under stirring to initiate silica polymerization at the particle surface, aliquots were taken at different times (20 min, 40min, 60min) to check the growth of the quantum dots.

4.1.3 Preparation of ZnTe/Au modified electrode

In the fabrication process of biosensor, a gold electrode was first polished with 1 μm, 5 min, 0.3 μm, 10 min and 0.05 μm, 20 min alumina slurries in polishing pads respectively, followed by ultra-sonication in absolute ethanol and distilled water for 10 min each. ZnTe quantum dots suspension was prepared by adding 3.0 µL of ZnTe QDs into 3.0 µL of deionized water, and the QDs solution was treated with ultrasonic and stirring before, in order to achieve complete dissolution. 3.0 µL of the mixture was drop coated on to the AuE electrode surface. The ZnTe/AuE electrode was then stored at room temperature for 24 h and kept in the dark in order to form a well characterised, self-assembled monolayer on metal electrodes (AuE). This was used as a strategy to immobilise and organise biomolecules at the interface and also give stability and provide electron transfer (Goncolves et al., 2007).

4.1.4 Preparation of immunosensor

After that the ZnTe/AuE modified electrode was rinsed carefully with distilled water to remove unbound ZnTe QDs molecules. The ZnTe/AuE modified electrode was then activated by drop coating a 30 µL solution containing 1:1 of (EDC/NHS), stored for 30 min in a dark place. After that the ZnTe/AuE modified electrode was rinsed carefully with PBS. Subsequently, 10 µL of antibody solution (10 µM) was drop coated on to ZnTe/AuE surface. The electrode was then stored for 2 hours at room temperature in a dark place. The electrode was then washed with PBS solution. BSA solution (1%) was used for blocking the nonspecific sites, using 1µL of the solution. The reaction occurred at room temperature for 10 min. The IFN-γ immunosensor was then washed with PBS solution.

4.2 Instrumentation

Ultraviolet–visible spectroscopy (UV-Vis) of the ZnTe QDs solution was carried out using a Nicolet evolution 100 UV-Vis spectrophotometer (Thermo Electron Corporation, UK) and the instrument was controlled with VisionPro software. The corresponding optical properties was determined at room temperature with photoluminescence measurements performed utilising Nanolog, Horiba NanoLog^{TM} 3-22-TRIAX (Horiba Jobin Yvon, USA) and the data was analysed using a FluoroEssence software. High resolution transmission electron microscope (HRTEM) images of the ZnTe QDs were obtained using a Tecnai G2 F20X-Twin MAT FETEM from FEI (Eindhoven, Netherlands) and it is a 200 kV instrument equipped with Energy Dispersive Spectroscopy (EDS). SAXS was used to determine the structure of particle systems in terms of averaged particle sizes or shapes. SAXSpace (Anton peer, Australia) system using 1nm diameter quartz capillary positioned at 317 mm from the CCD and temperature controlled at 20°C. Data evaluation was performed with the GIFT software (which is a versatile tool for the evaluation of small angle scattering data). X-ray diffraction (XRD) was used to investigate the structural properties of synthesized freshly dried quantum dots and used to detect the crystallinity of QDs. Quantum dots were recorded using a Bruker AXS D8 Advance diffractometer (voltage 40 KV; current 40 mA). FTIR is a technique that was used to investigate chemical bonding or molecular structure of materials due different functional groups. FTIR spectra were recorded in the range 4000 - 1000 cm^{-1} using a Perkin Elmer model Spectrum 100 series. Raman spectroscopy were also prepared on a glass slide and analysed using Xplora Raman spectrometer (Horiba Scientific) utilising a 514 nm He-Cd laser as an excitation source. Data capturing and instrument control were performed using LabSpec software. The cyclic voltammograms for each nanomaterial were collected using an electrochemical workstation connected to three electrodes: gold electrode (working), Ag/AgCl (reference) and silver wire (counter) immersed in a PBS buffer (pH = 7.4) as an electrolyte. To evaluate the electrochemical behaviour of the biosensor materials on gold electrode, the cyclic voltammetric experiments were performed in 0.1 M PBS over a potential range of +1200 mV to -1200 mV at a scan rate of 50 mV/s. The workstation was controlled using PalmSens (PS) trace software.

4.3 Results and Discussion

4.3.1 Ultraviolet-visible spectroscopy

Usually, the nature of the interaction between the conduction and valence bands as well as the size of the band gap determines the optical properties of semiconducting nanocrystals. The absorption of a photon by a semiconductor causes electronic transition from the valence band to the conduction band, which creates an electron-hole pair known as an exciton in the valence band. The lowest-energy electron-hole pair (excitonic) state ($1S_{3/2}$-$1S_e$) is not usually observable in nanocrystals that are heterogeneous in size, shape and composition (Ndangili *et al.*, 2017). Optical properties of synthesized water dispersible QDs were characterized by UV-Vis spectrometry, *Figure 4.1* illustrate the absorption spectra of TGA functionalized ZnTe QDs respectively. TGA capped ZnTe QDs exhibited long emission wavelength and a large Stokes shift. The UV-Vis absorption spectrum of colloidal ZnTe QDs showed weak broad absorption in the UV range. The maximum absorbance was obtained at about 320 nm. This peak was deduced to be associated with electrons transition of d valence electrons from Zn to Zn* exited state (Nwabisa, 2010). The onset of absorption is considerably blue shifted relative to the bulk of ZnTe indicating a significant effect of synthesized ZnTe QDs. The broad peak at 226 nm indicates the capping reagent TGA. The bulk material was calculated by researchers and it was found to be Eg = 2.26 eV (Asano et al., 2017; Ram et al., 2017). When the material synthesized in this study was capped with thioglycolic acid, was expected to have an increase of the bad gap which shows quantum confinement. *Figure 4.1* **(B)** illustrate the band gap of Eg = 4.42 eV this showed an increase, the increase of nanoparticles in this case quantum dots.

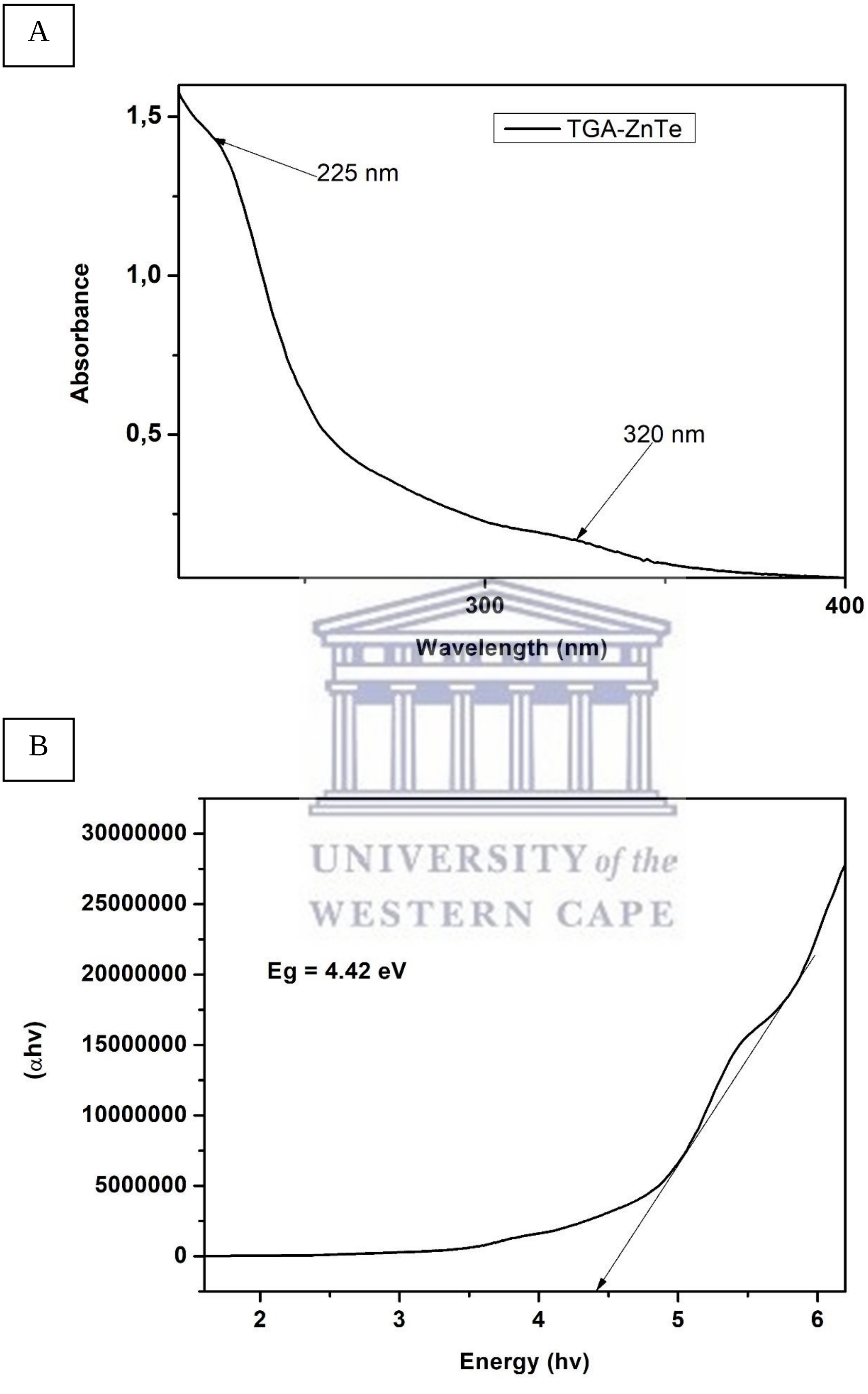

Figure 4.1: A) UV-Vis absorption spectra of TGA-ZnTe QDs synthesized in water and B) The insert corresponding to the band gap plot of TGA-ZnTe.

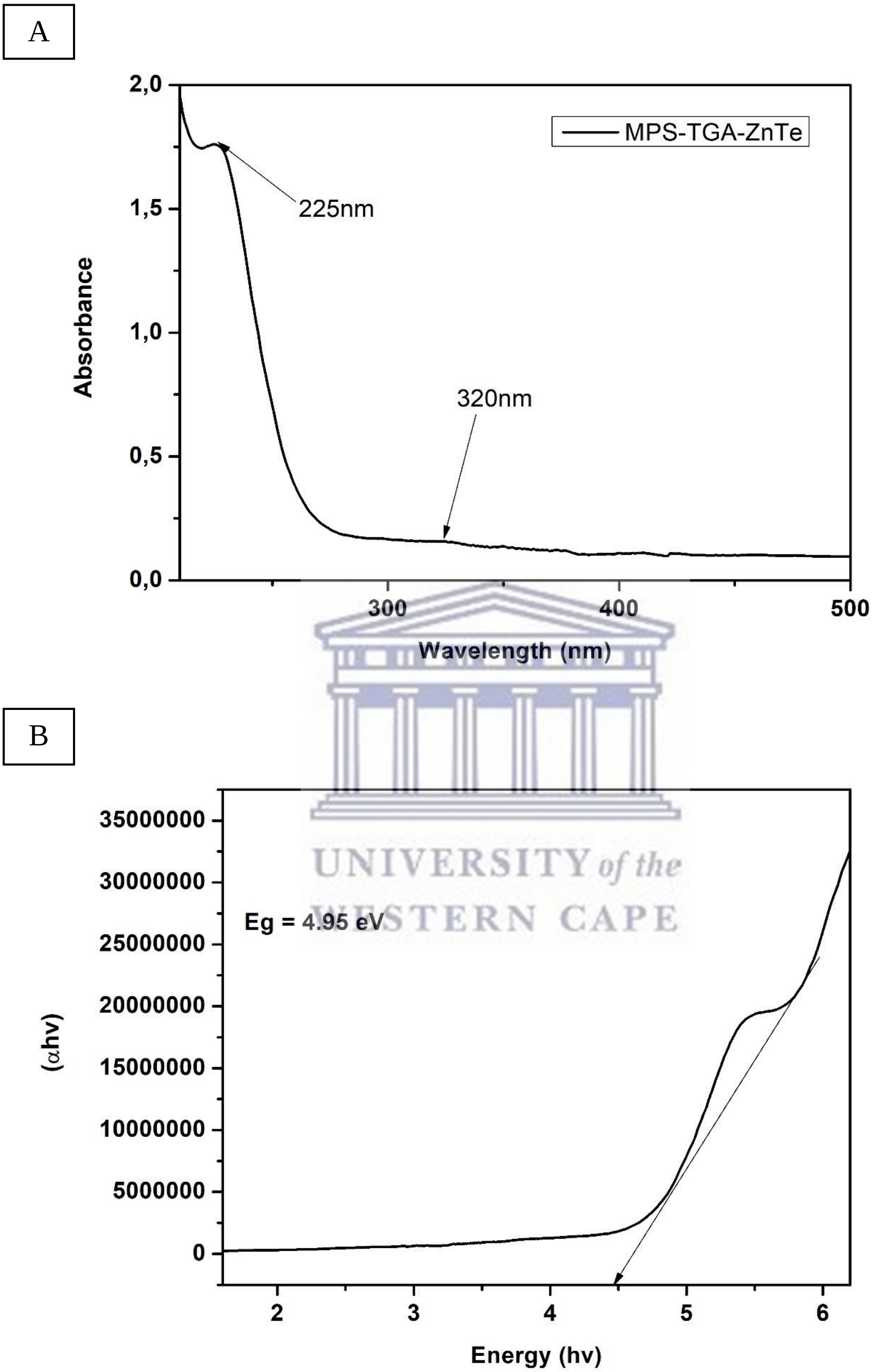

Figure 4.2: A) UV-Vis absorption spectra of MPS-TGA-ZnTe QDs synthesized, B) The insert corresponding to the band gap plot of MPS-TGA-ZnTe.

The TGA-ZnTe QDs gave a peak at 320 nm in the absorption spectra and after the conjugation between TGA-ZnTe QDs and MPS. It has been observed that there is no shift when the MPS was added to the quantum dots. The peak at 320 nm for MPS flatted this is due to the capping reagent absorbing on the surface of the quantum dots. Similar results were obtained by *Li et al* where they had MPS-capped ZnS QDs and the absorption edges of the present ZnS QDs were around 320 nm (Li, Shih and Shih, 2007). Because UV absorption increases dramatically below the wavelength corresponding to the band edge, empirically, the absorption edge was determined as the wavelength with the greatest change in slope, i.e., the wavelength where the absorption curve bent the most and started to deviate from the longer wavelength background absorption. To confirm the quantum confinement band gap of MPS-TGA-ZnTe was calculated using the Tauc plot and they are shown in *Figure 4.2* ***B)*** Eg = 4.92 eV. There was an increase in the band gap of TGA-ZnTe to MPS-TGA-ZnTe this is related to the overlap of the atomic orbitals (Orth, Exas and Aprimer, 2002). *Figure 4.3* ***A)*** then illustrate the difference of all three capping reagents on the absorption spectrum, when TEOS was added on to the quantum dots there was a shift towards longer wavelengths (372 nm) and this indicates particle growth. The TEOS is a silica shell that thickens the quantum dots which add a layer on the quantum dots. The band gap was calculated Eg = 4.58 eV, from the MPS-TGA-ZnTe the band gap decrease. This was not expected because with the addition of TEOS, the band gap is expected to increase.

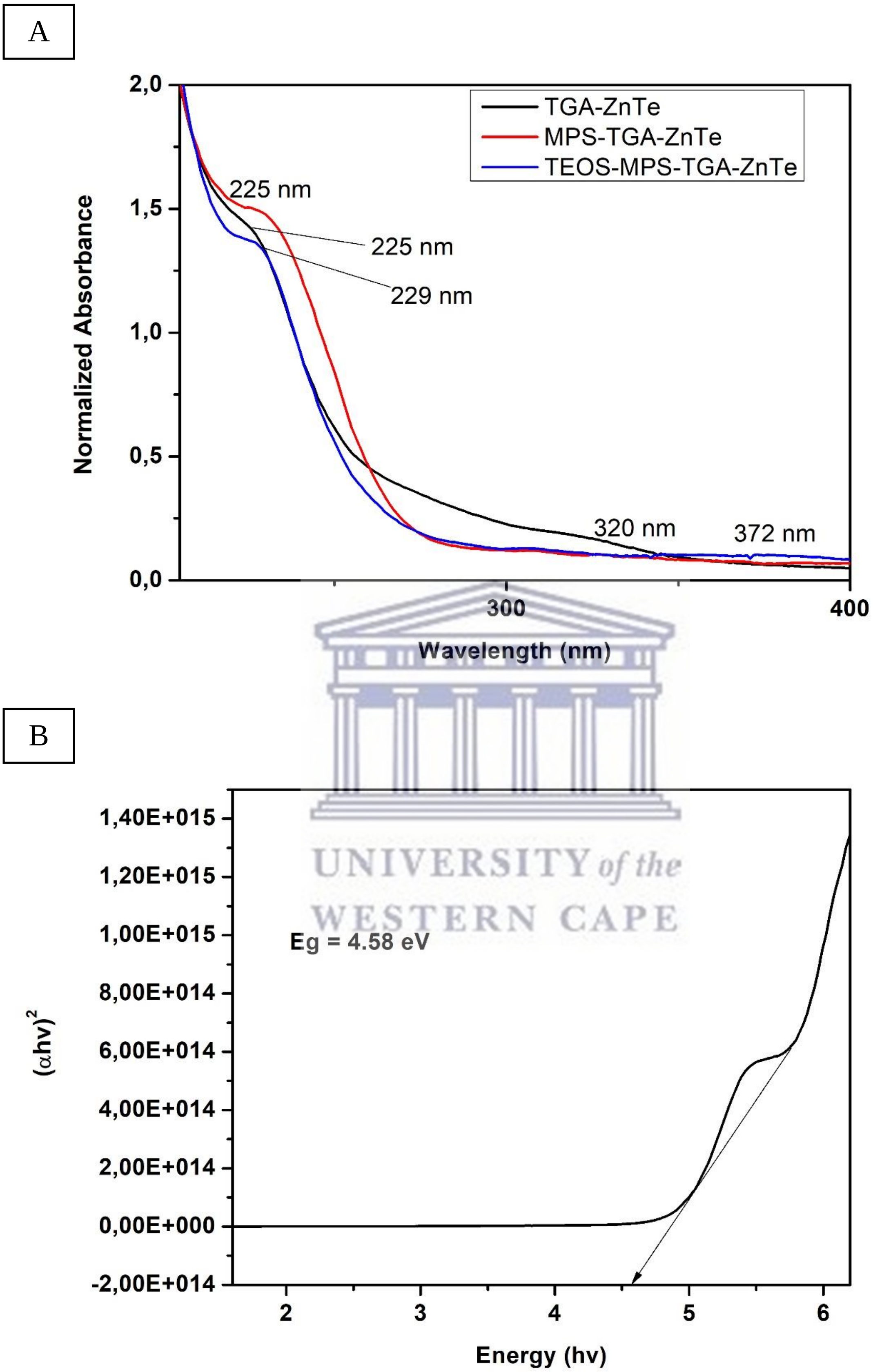

Figure 4.3: A) UV-Vis absorption spectra of TGA-ZnTe, MPS-TGA-ZnTe and TEOS-MPS-TGA-ZnTe QDs synthesized, B) The insert corresponding to the band gap plot of MPS-TGA-ZnTe.

4.3.2 Transmission electron microscopy

The microscopy of Zinc telluride quantum dots was studied using transmission electron microscopy (TEM). The method was used to study the shape and size of the ZnTe quantum dots used as support material for the biosensors developed. The TEM images of the TGA-ZnTe QDs prepared are shown Figure 4.4 A), the size of the synthesised thioglycolic acid capped zinc telluride quantum dots were found to be about 4.5 nm and mono dispersed with minimal aggregation as indicated by the TEM image (Moradian *et al.*, 2013). The dark spots were deduced to be ZnTe quantum dots, it can be seen that the obtained QDs are approximately spherical in shape. These nearly mono dispersed quantum dots exhibited the shape and appearance similar to what was reported by Kumar and co-workers as quantum dots, synthesised by similar chemical method, which exhibit the Wurtzite shape (Kumar and Singh, 2009). In Figure 4.4 B) the image shows lattice fringes which suggest good crystallinity (Ghosh et al., 2011). In contrast, the SAED Pattern Figure 4.4 C) shows well resolved bright rings corresponding to lattice planes this indicates that the degree of crystallinity is higher for the particles synthesized (Sovan Kumar Patra, BhavyaBhushanb and Priyam, 2016). Figure 4.5 shows the TEM of the MPS-capped TGA-ZnTe QDs with the dispersed QDs (individual black dots) can be clearly seen. There is a clear aggregation of particles after the capping of MPS to the ZnTe QDs. Higher magnification images showed that the average size of the particles is about 8.5 nm (Li, Shih and Shih, 2007). Figure 4.6 shows the TEM images of TEOS-MPS-TGA-ZnTe and shows the quantum dots are spherical particles. The average particle size was calculated using Image J and it was found to be 16-20 nm. The ZnTe QDs show good dispersion stability in water, which is the foundation for the growth of SiO_2 shells (Qu *et al.*, 2014). The dispersed QDs (individual black dots) can be clearly seen and the core-shell is t grey surrounding, the core. The SAED of both MPS-TGA-ZnTe (*Figure 4.5* ***C***) and TEOS-MPS-TGA-ZnTe (*Figure 4.6* ***C***) show the rings without the spots which indicate the addition of the shell on the quantum dots had an effect on the shape of the quantum dots and they are amorphous. The TEOS-MPS-TGA-ZnTe quantum dots with core–shell structural characteristics are rather spherical and uniform (Chen, Liu and Jiang, 2012).

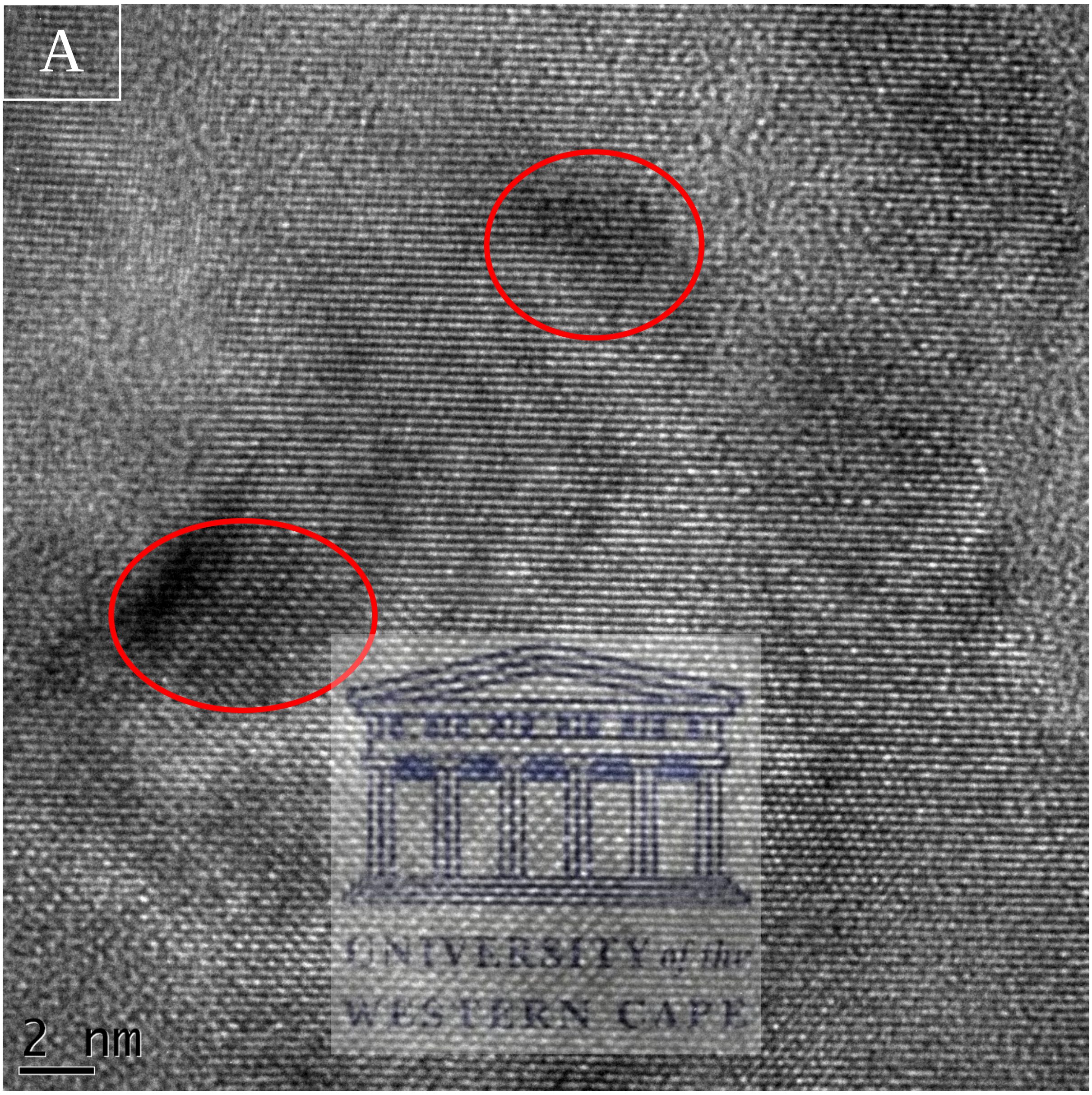
A
2 nm

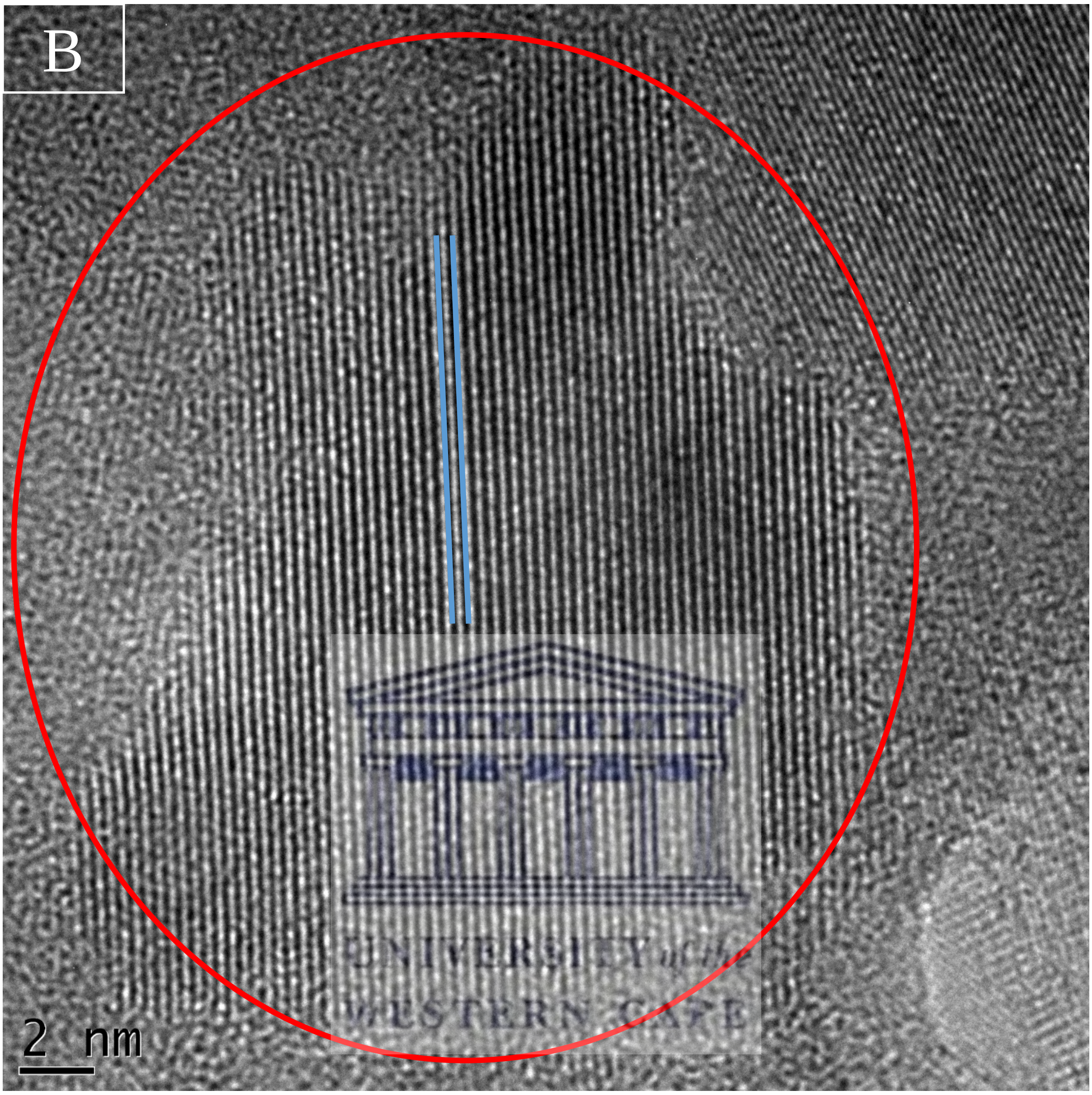
B
2 nm

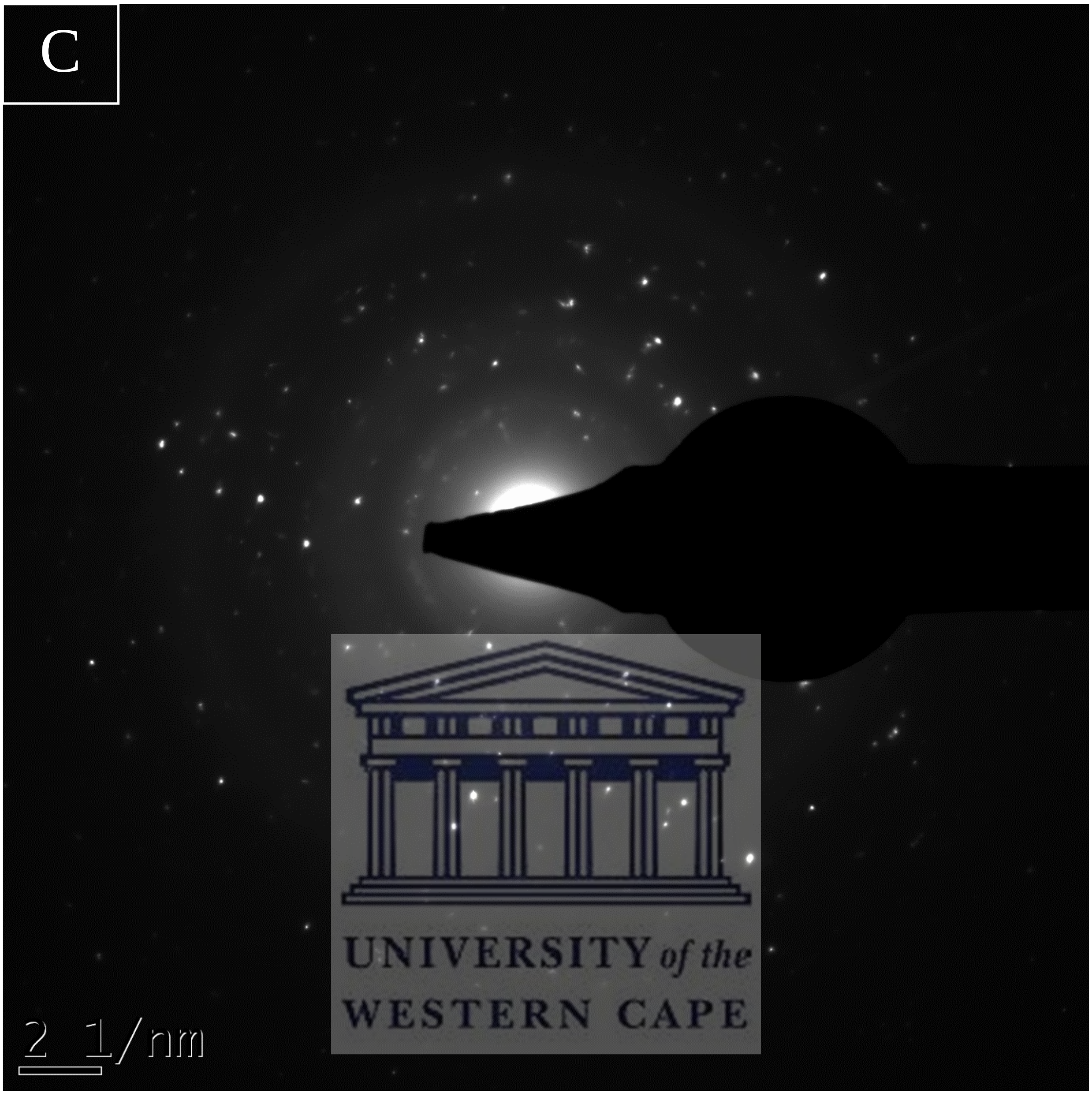

Figure 4.4: A) and B) HRTEM image of TGA-ZnTe QDs and C) SAED (Selected Area Electron Diffraction) pattern of TGA-ZnTe QDs.

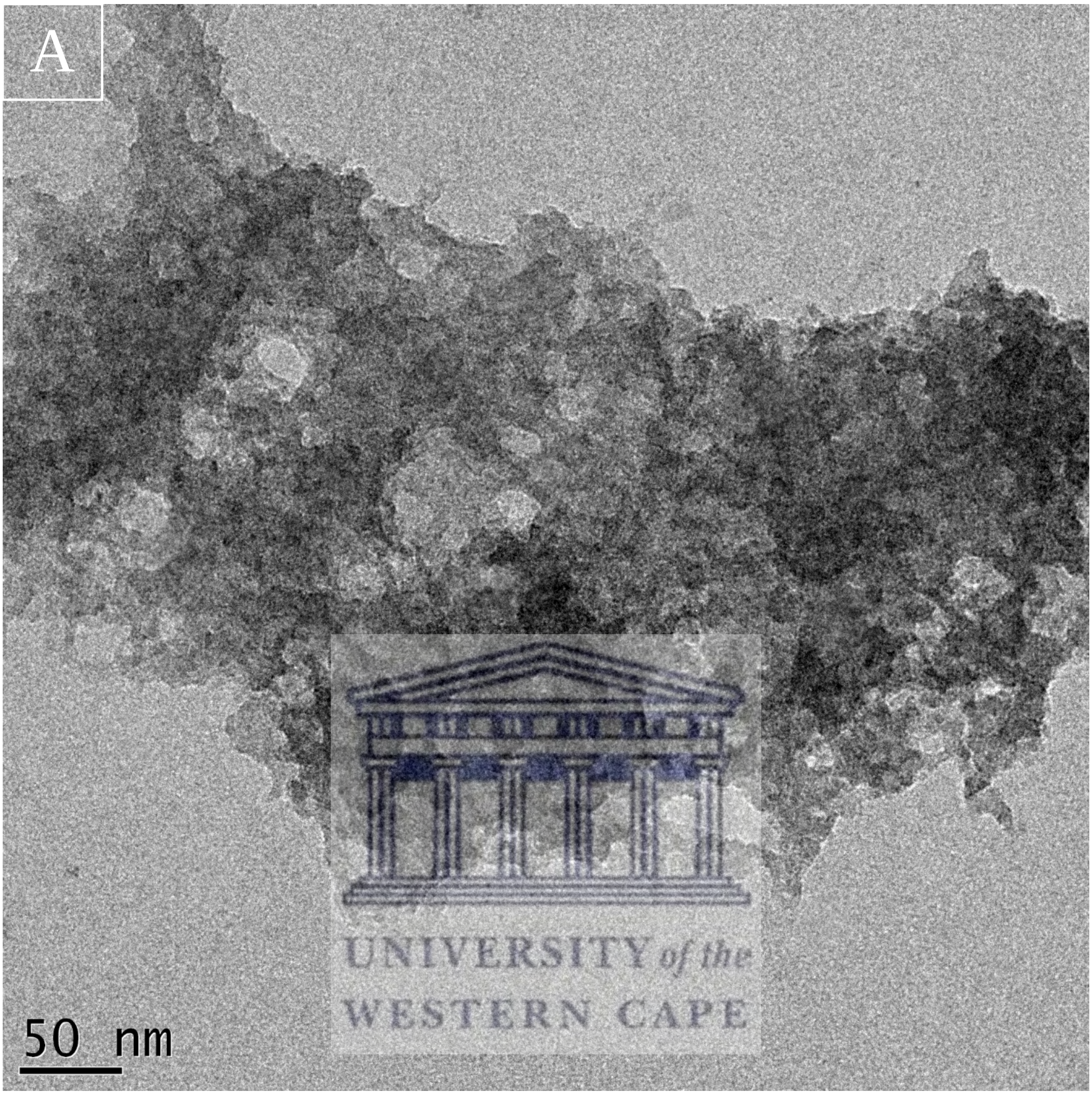
A
50 nm

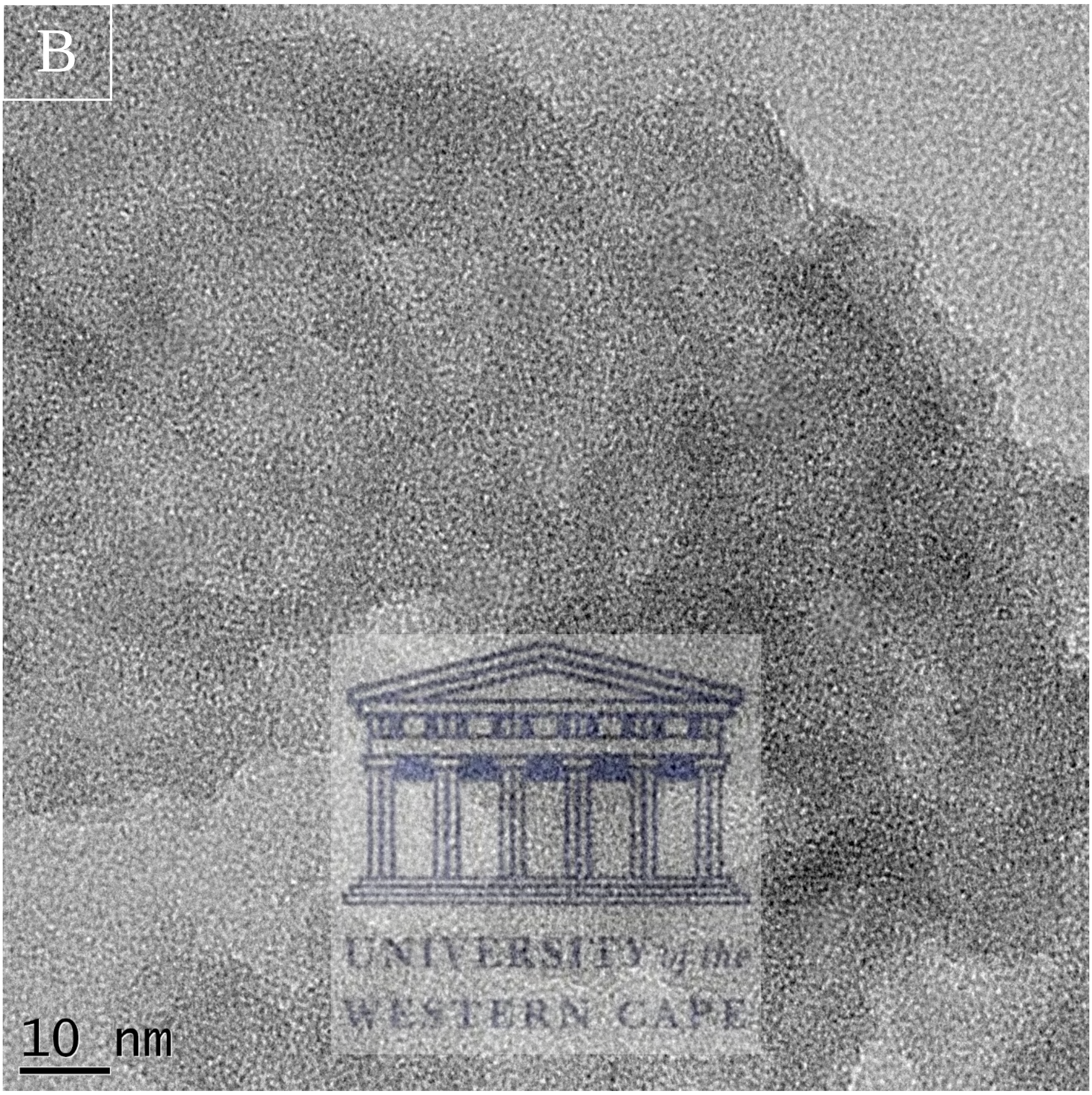
B
10 nm

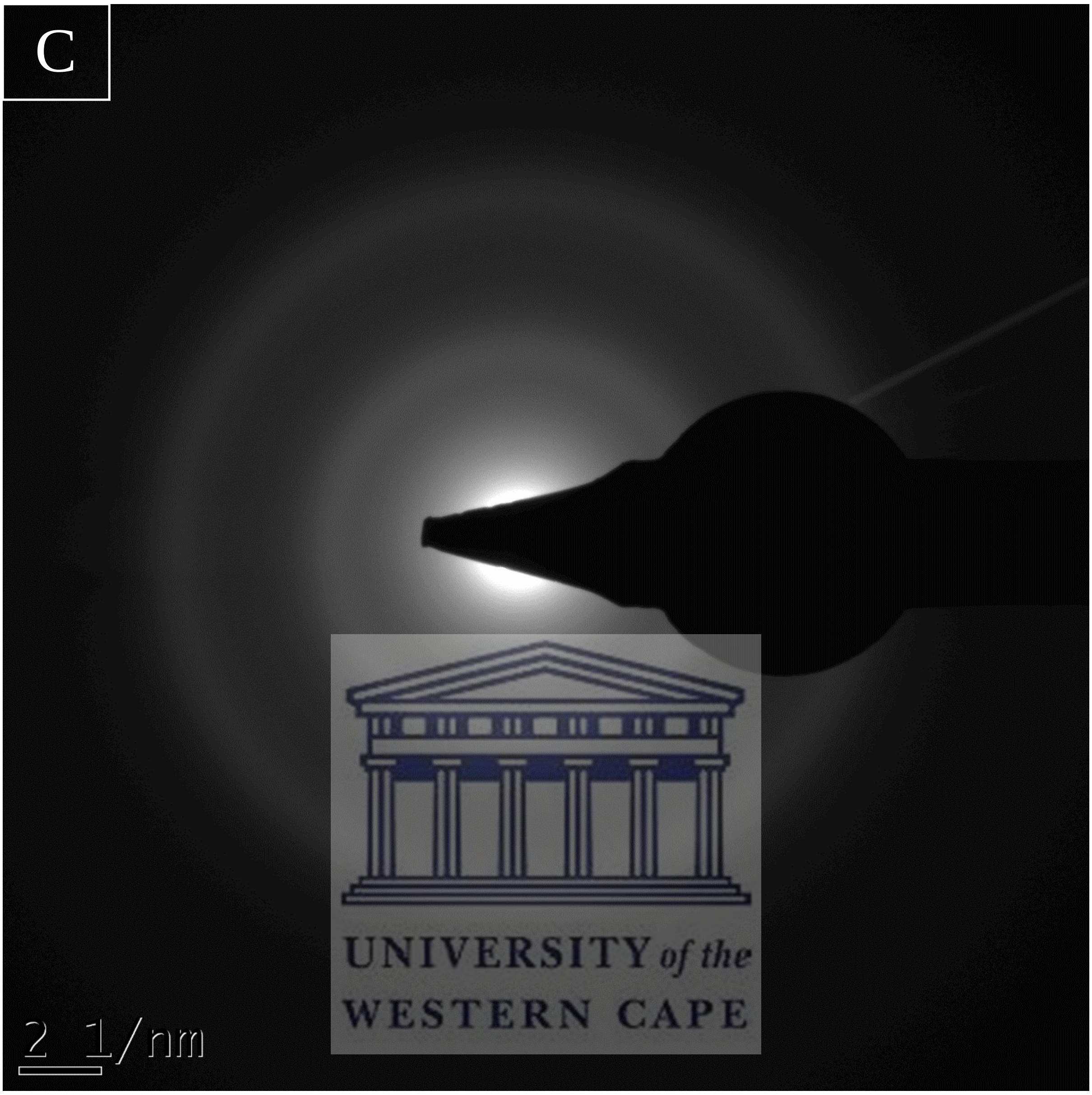

Figure 4.5: A) and B) HRTEM image of MPS-TGA-ZnTe QDs and C) SAED (Selected Area Electron Diffraction) pattern of MPS-TGA-ZnTe QDs.

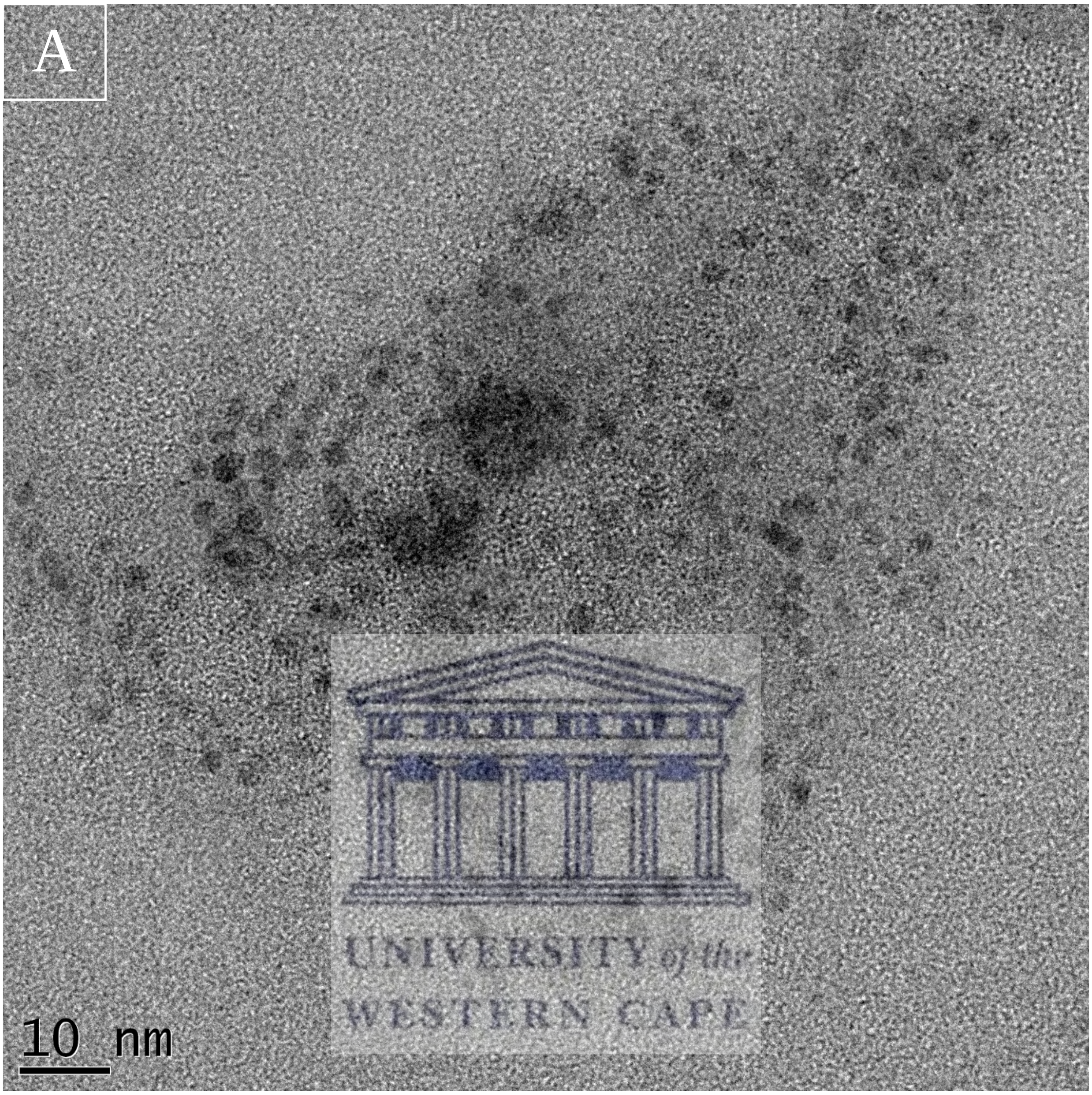
A
10 nm

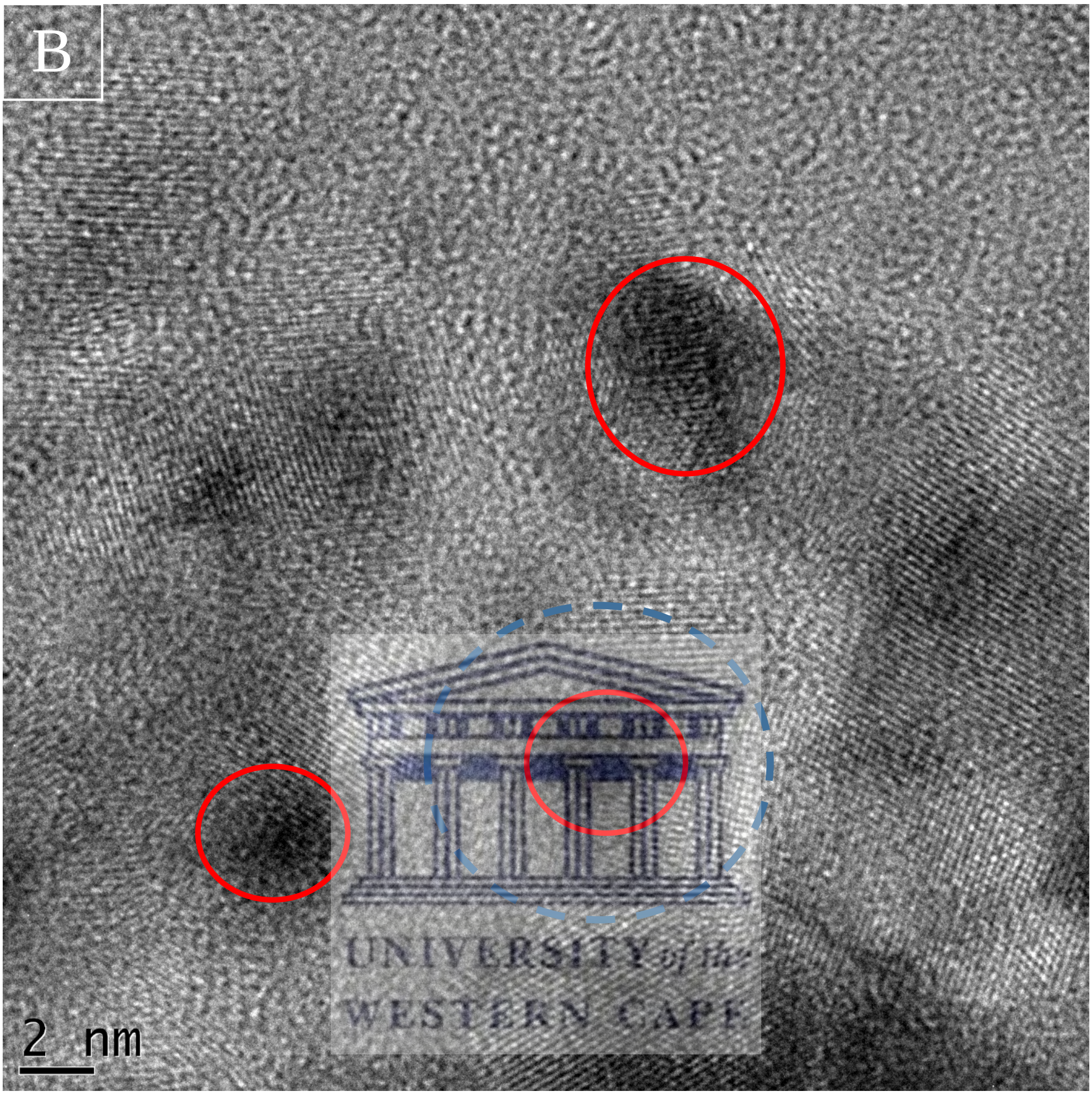
B
2 nm

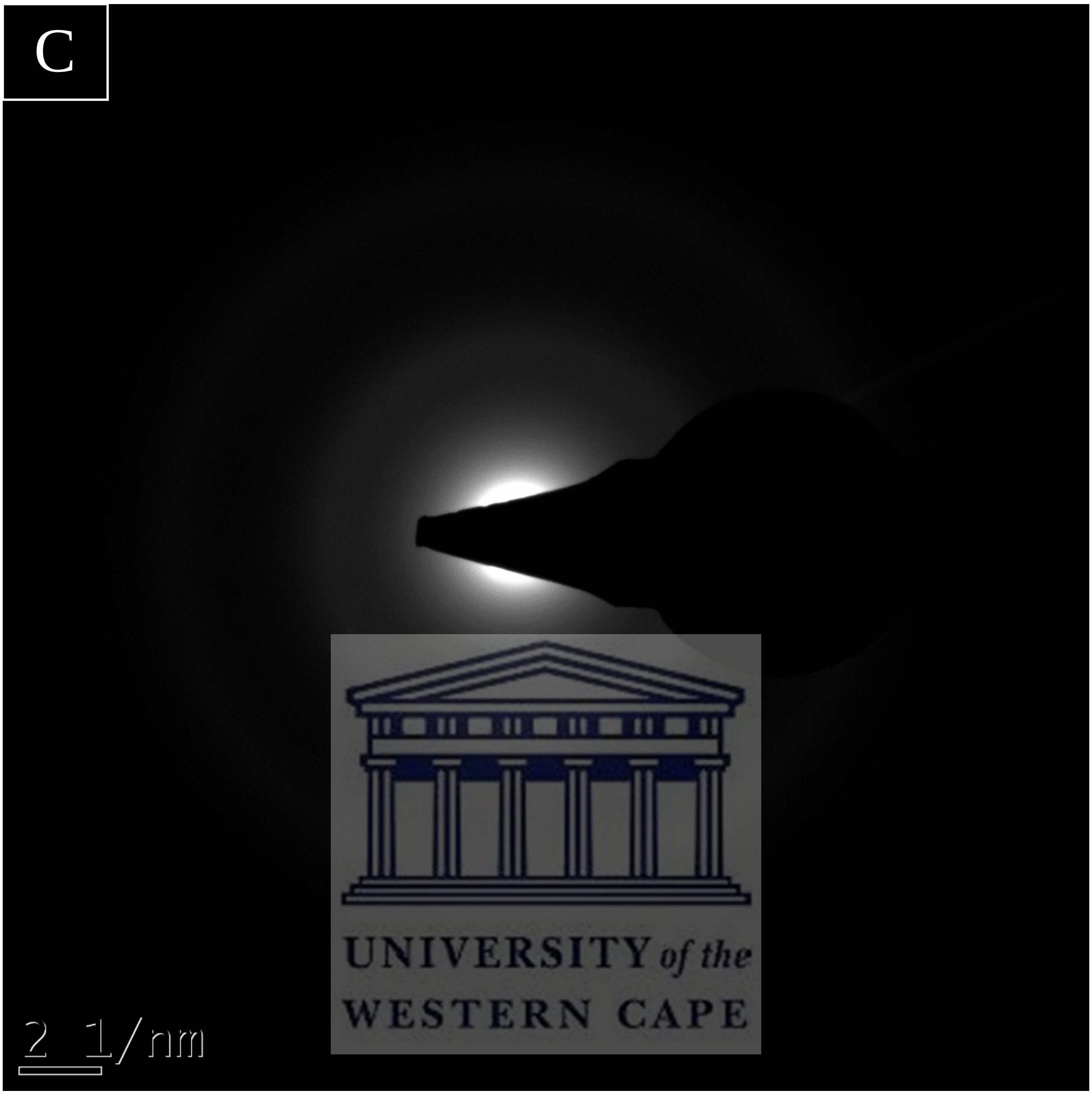

Figure 4.6: A) and B) HRTEM image of TEOS-MPS-TGA-ZnTe QDs and C) SAED (Selected Area Electron Diffraction) pattern of TEOS-MPS-TGA-ZnTe QDs.

4.3.3 Small Angle X-ray Scattering

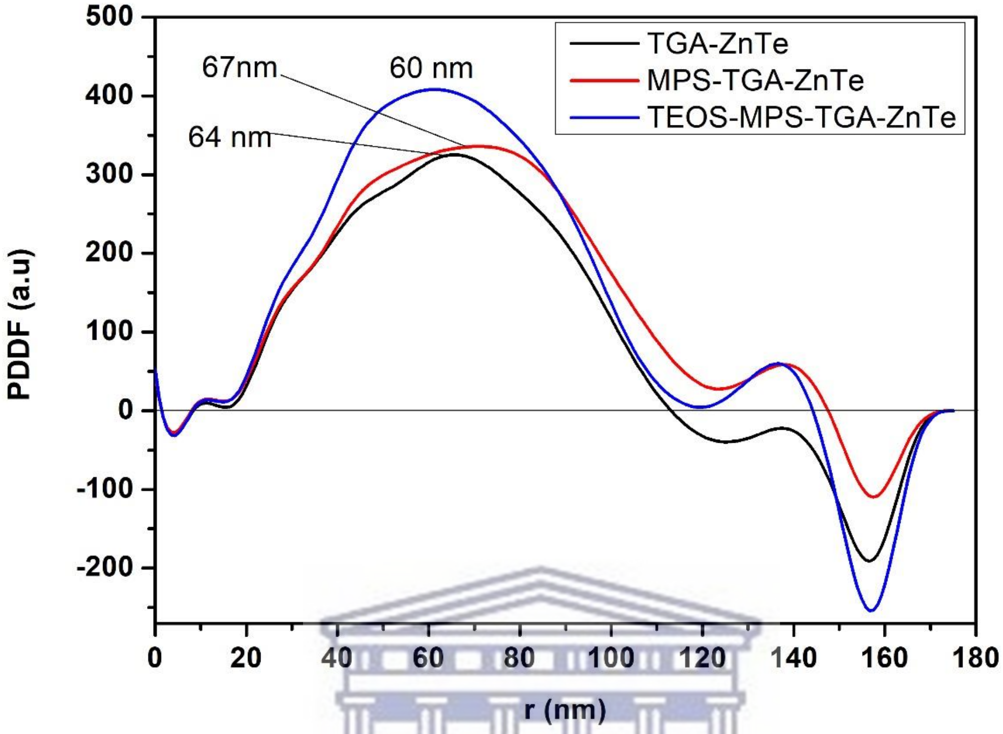

Figure 4.7: SAXS corresponding PDDF plot of TGA-ZnTe, MPS-TGA-ZnTe and TEOS-MPS-TGA-ZnTe.

The Small Angle X-ray Scattering (SAXS) provided more information on the size of the ZnTe quantum dots. The shape of the QDs is displayed in the pair-distance distribution function (PDDF) in the inset of *Figure 4.7* above. The PDDF plot shows a symmetric peak for all three capping reagents, this means that the ZnTe quantum dots are spherical in all the capping reagents (Sobczak, Nietubyc and Mac, 2002). The hump on the curves indicates that the quantum dots agglomerated in TGA-ZnTe and MPS-TGA-ZnTe, these results compliment with HRTEM results discussed previously. The core-shell is also represented on the diagram, in all three of the capping reagents at the end all of them go to the negative area which indicates core-shell ('The SAXS Guide', 2013). The TEOS-MPS-TGA-ZnTe core-shell was the highest indicating the thickening of the shell by TEOS. The diameter of all three capping reagents is equal, but they differ in size, TGA-ZnTe has a narrow shell, then with MPS-TGA-ZnTe the capping became broad this is an indication of increase of the shell and the last one TEOS-MPS-TGA-ZnTe has the largest and also broad curve which indicates the thickness of the core-shell when Silica was added (Stawski *et al.*, 2019). The accurate size of ZnTe quantum dots is displayed in the size by number plot in *Figure 4.8* below. The plot of the three different capping reagents displays a peak at 17 nm indicate the majority of the particles have an average diameter of 6 nm in size with other peak at 61 nm being the agglomerated particles. The average size of the quantum dots at 17 nm decreased which indicate that the core of the quantum dots ZnTe is being reduced with the addition of the shell (MPS and TEOS). The nanoparticles that are agglomerating were increasing indicating that as the capping reagents increases the surface of the quantum dots, they were getting closer to each other making them to agglomerate but only a few. These results are in accordance with the HRTEM analysis that reported the average diameter of QDs at 17 nm. The TGA-ZnTe curve is narrow then when MPS was added the curve broadened and it became more broad when TEOS was added and the bigger number of the ZnTe quantum dots increased.

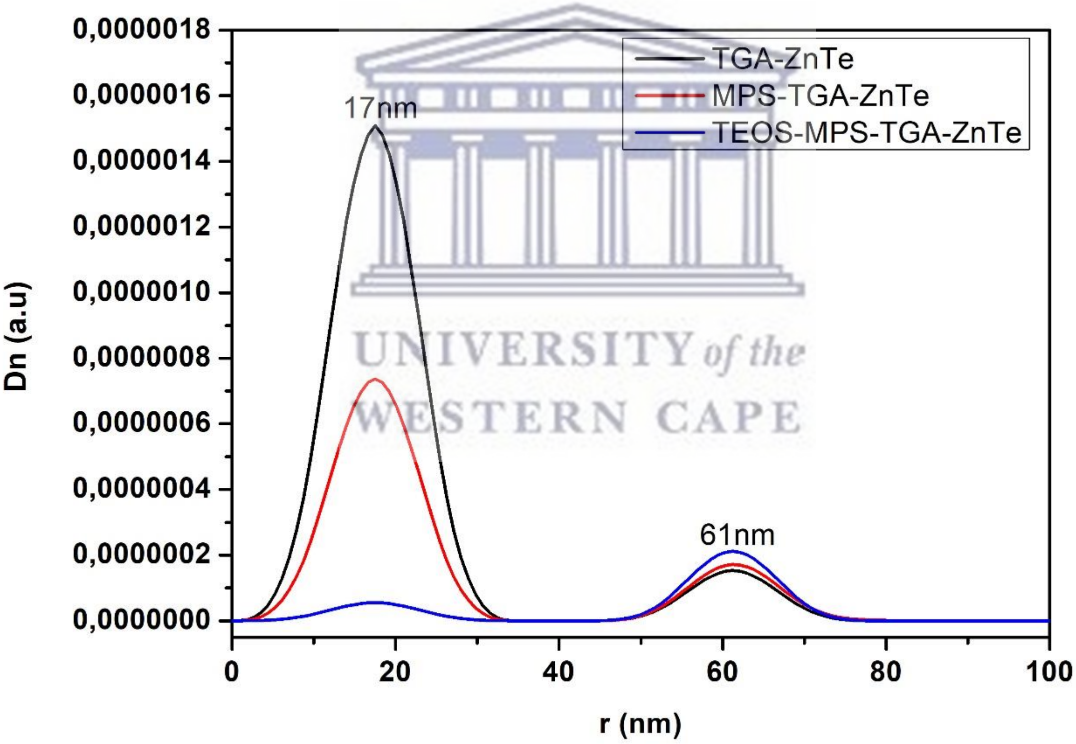

Figure 4.8: SAXS particle size by number plot of TGA-ZnTe, MPS-TGA-ZnTe and TEOS-MPS-TGA-ZnTe.

4.3.4 The X-ray powder diffraction

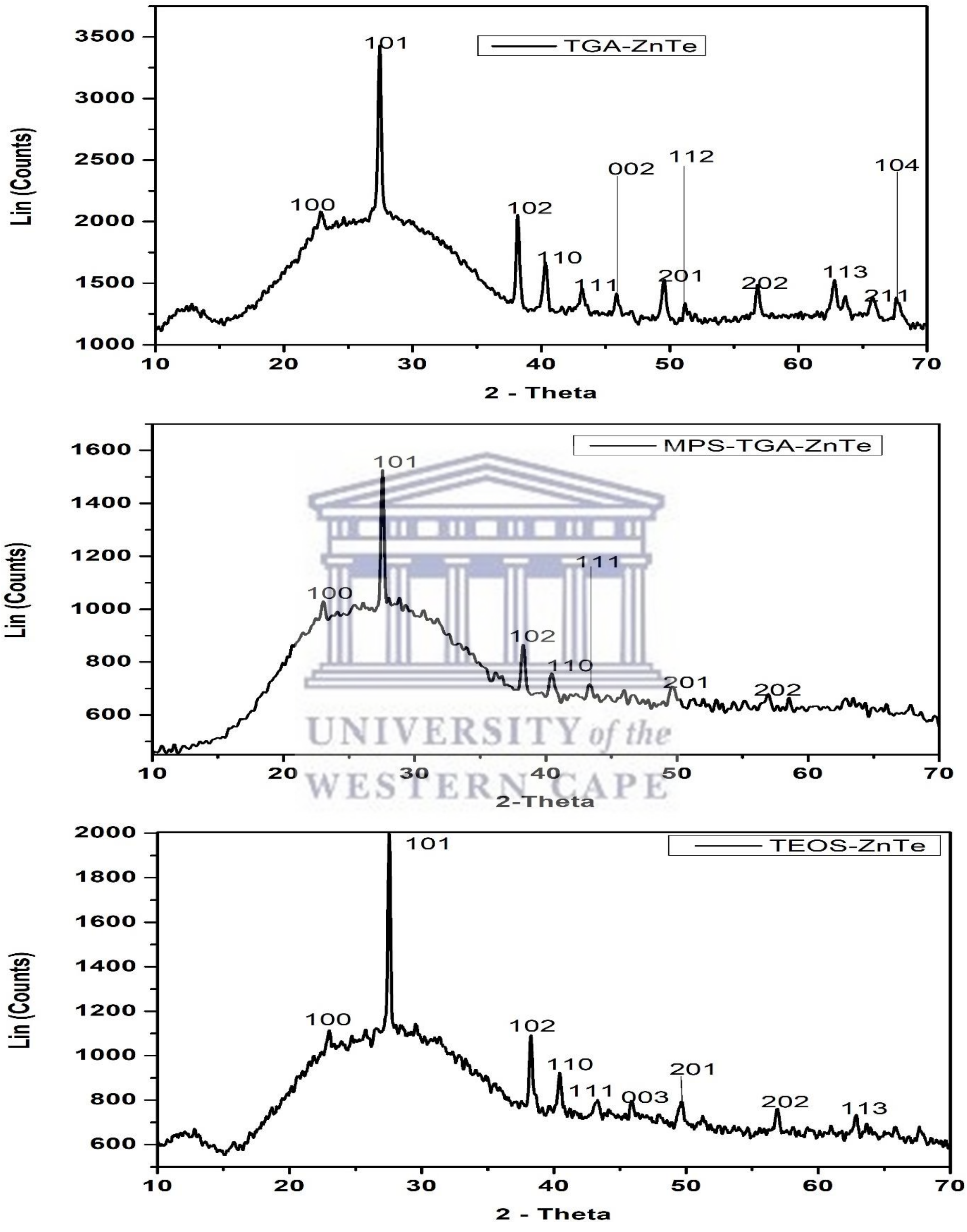

Figure 4.9: X-Ray diffraction (XRD) pattern of TGA-ZnTe, MPS-TGA-ZnTe and TEOS-MPS-TGA-ZnTe QDs synthesised. The XRD of ZnTe QDs is provided for reference (JCPDS Number 36-1452).

The figure above shows the diffraction patterns of ZnTe capped with different capping reagents. The X-ray powder diffraction (XRD) patterns of ZnTe quantum dots are shown in *Figure 4.9*. Diffraction peaks for TGA-ZnTe were observed at $2\theta = 23.14°$, 27.55°, 38.35°, 40.34°, 43.31°, 45.96°, 49.71°, 56.87°, 62.94°, 66.35°and 68.96° which correspond to (100), (101), (102), (110), (111), (002), (201), (112), (202), (113), (211) and (104) respectively. The three distinct diffraction peaks were observed at 2θ values of 27.55°, 38.35° and 40.34°, respectively, corresponding to the (101), (102) and (110) crystalline planes of TGA-ZnTe. The broad nature of the XRD peaks could be attributed to the nano-crystalline nature of ZnTe particles (Qutub and Sabir, 2012). The XRD pattern of MPS-TGA-ZnTe corresponds to the standard ZnTe QDs of cubic zinc blend structure. Comparing the spectra of TGA-ZnTe to MPS-TGA-ZnTe, there is little movement of the TGA-ZnTe peaks as the MPS-TGA-ZnTe shell is formed. This may be a result of the formation of core-shell. The diffractions peaks in the MPS-TGA-ZnTe pattern have strong broad peak, which is attributed to the amorphous silica phase. This correlates with HRTEM findings in *Figure 4.5* ***C)*** that indicates the composites are composed of ZnTe crystals and amorphous SiO_2 after coating. Furthermore, the MPS-TGA-ZnTe quantum dots were coated with tetraethyl orthosilicate, centrifuged and dried. Thus obtained solid nano-powders were characterized by XRD technique. Results indicate that the quantum dots are amorphous, this is due from the broad strong peaks (Gadalla *et al.*, 2017).

4.3.5 FTIR

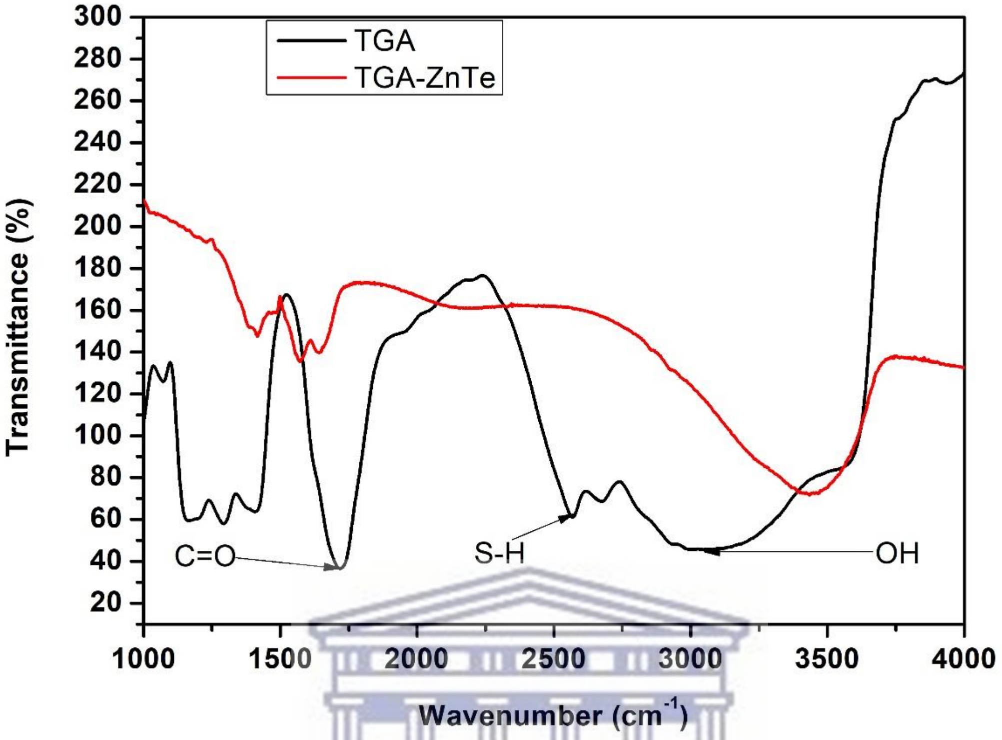

Figure 4.10: FTIR spectra of TGA and TGA-ZnTe.

The presence of capping molecule at the surface of quantum dots was confirmed by FTIR spectroscopy. *Figure 4.10* depicts the FTIR spectra of free TGA and TGA stabilized ZnTe QDs. The proposed structure of a single quantum dot was shown in Figure 4-5. The band at 1401 cm^{-1} was deduced to be due to C-C single bond of the thioglycolic acid capping agent of the TGA-ZnTe QDs (Dhar, Singh and Kumar, 2015). However, the peak at 1639 cm^{-1} might have been due to ν(C=O) from the terminal carboxylic group of the capping reagent, a broad peak at 3400 cm-1 might have been a resultant of ν(OH) from the OH group of carboxylic acid derivative from the thioglycolic acid capping agent, and unbound OH groups from water that was present during synthesis (Nwabisa, 2010). The absence of a CH stretching frequency at 2850 cm^{-1} to 3000 cm^{-1} might have been either due the CH being concealed in the internal core of the quantum dots or the peak was predominated by the presence of the access amount of water within the TGA-ZnTe QDs solution. The peak for S-H (2570 cm^{-1}) vibration was absent in the spectrum of TGA-ZnTe QDs as a result of covalent bonding between thiols and ZnTe atom on the QDs surface (Chen, Liu and Jiang, 2012).

FTIR spec of MPS-TGA-CuTe is shown in *Figure 4.11*, the analysis shows the characteristic peaks belonging to MPS. The most prominent peak of these are at 1110 cm^{-1} belonging to asymmetric stretching of Si-O-Si bonds respectively. The peak at 1240 cm^{-1} is for Si-CH_2-S stretching (Koç, Tepehan and Tepehan, 2012). The peak at 1405 cm^{-1} comes from asymmetric deformation of C-H in CH_3. The peak at 1639 cm^{-1} belongs to C=O bond. The peaks at 2941 cm^{-1} and 3449 cm^{-1} belong to C-H and O-H respectively (Shahraki and Irani, 2014). The FTIR spectroscopy analysis confirms that the siloxane group was introduced on the QD surface after silica coating. There was a shift of the spectrum of MPS-TGA-CuTe all the molecules shifted this indicates the addition of MPS on the surface of the quantum dots.

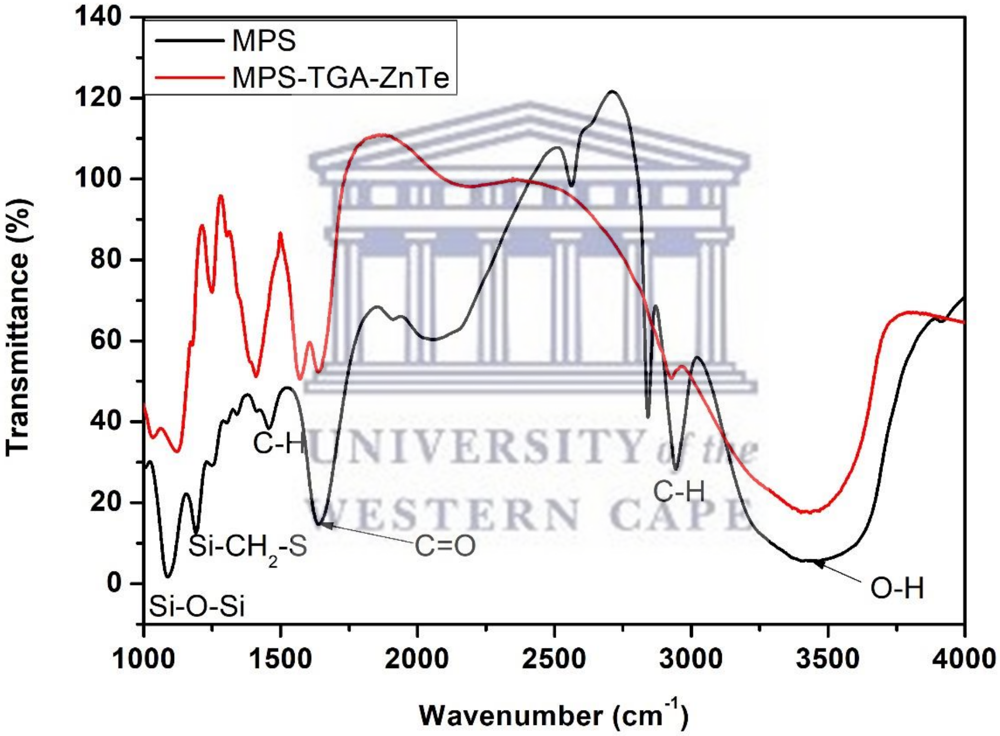

Figure 4.11: FTIR spectra of MPS and MPS-TGA-ZnTe.

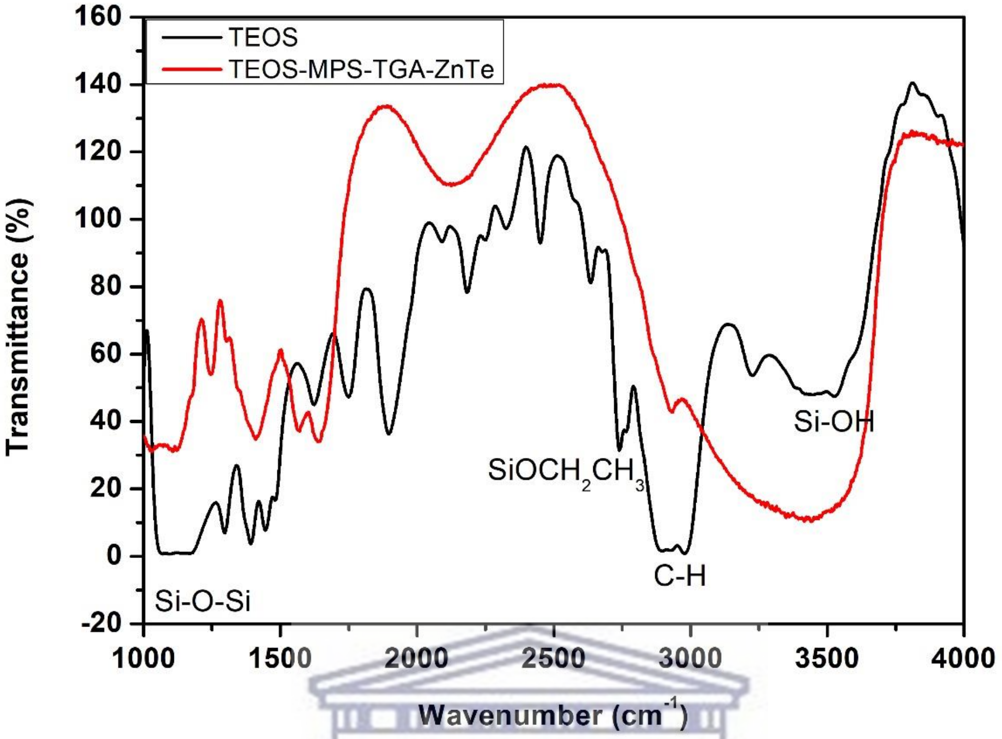

Figure 4.12: FTIR spectra of TEOS and TEOS-MPS-TGA-ZnTe.

For the spectrum of TEOS-MPS-TGA-ZnTe QDs, the broad -OH peak at 3,441 cm^{-1} indicates that a fraction of the Si atoms exist on the surface has been hydroxylated, which gives the QDs very good dispersion in water. The peaks at 1,101 and 800 cm^{-1} are attributed to the Si–O–Si asymmetric and symmetric stretching, respectively (Qu *et al.*, 2014). The FTIR spectra of TGA-ZnTe, MPS-TGA-ZnTe and TEOS-MPS-TGA-ZnTe are shown in *Figure 4.13*. Relative to TGA-ZnTe, the C=O (1639 cm^{-1}), O–H (3440 cm^{-1}) and C–H (1414 cm^{-1}) are associated with TGA. Moreover, no S–H stretching vibration is observed in the 2600–2550 cm^{-1} region, which suggests that S–H from TGA is adsorbed onto the particles' surface in the form of a closed packed monolayer that stabilizes ZnTe QDs in solution (Song *et al.*, 2014). The peaks at 1,101 and 800 cm^{-1} are attributed to the Si–O–Si asymmetric and symmetric stretching, respectively. This peak is present both on the MPS-TGA-ZnTe QDs and TEOS-MPS-TGA-ZnTe QDs, this confirms that the two capping reagents had silica on them (Chen, Liu and Jiang, 2012).

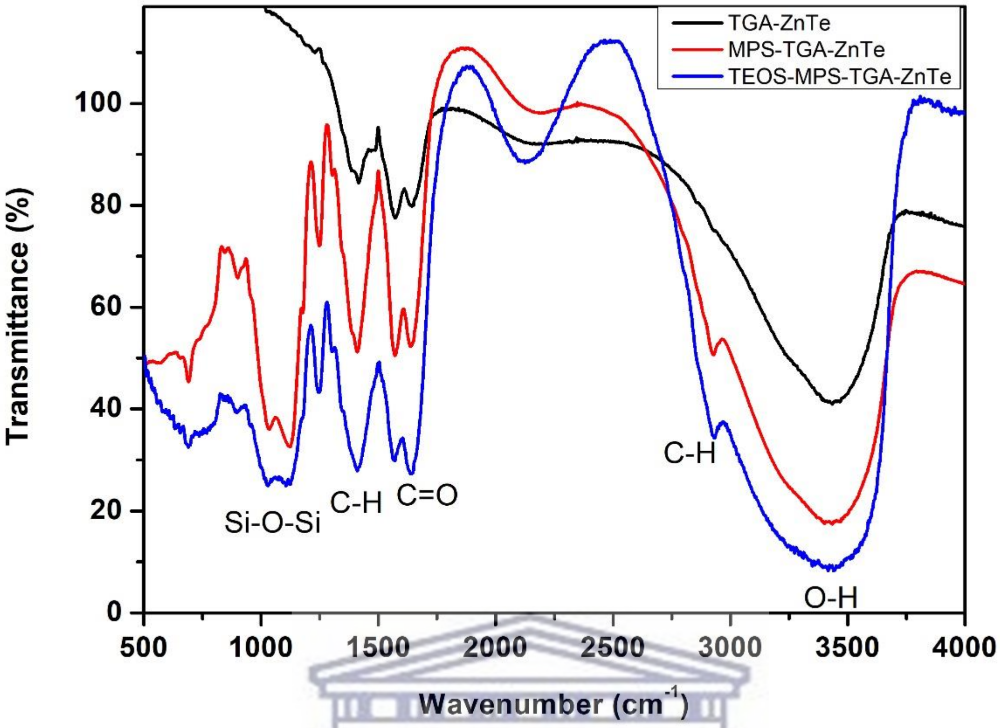

Figure 4.13: The FTIR spectrum showing the effect of different capping reagents on the structure of quantum dots, TGA-ZnTe (black-line), MPS-TGA-ZnTe (red-line) and TEOS-MPS-TGA-ZnTe (blue-line).

4.3.6 Electrochemistry

Cyclic voltammetry was used to study the electrochemical properties of ZnTe quantum dots capped with three different capping reagents. *Figure 4.14* shows the cyclic voltammograms of AuE/TGA-ZnTe, versus bare AuE.

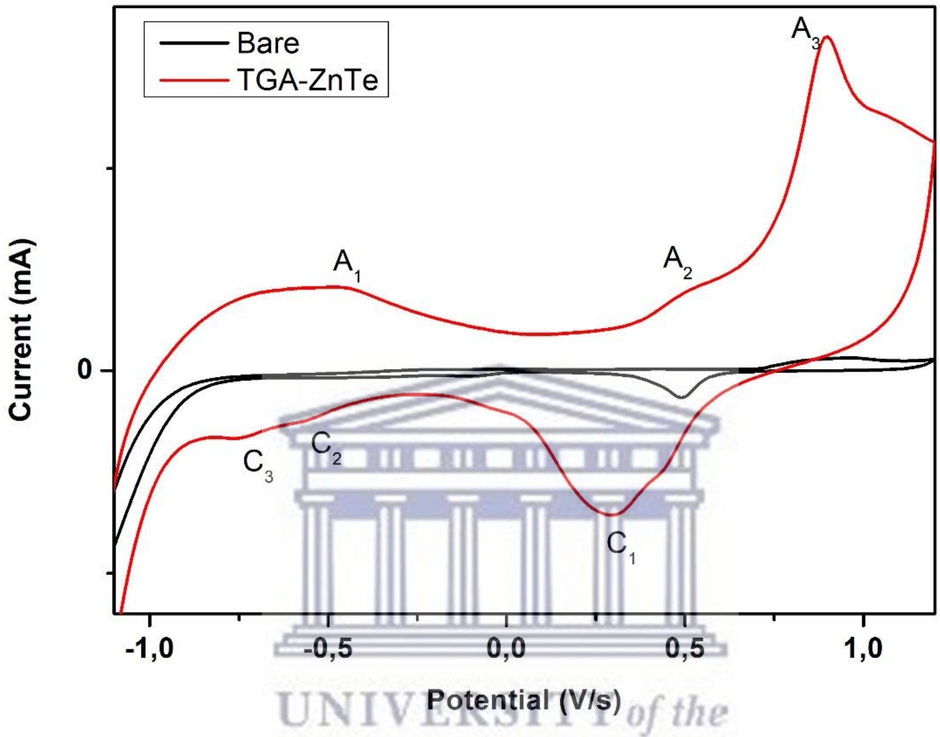

Figure 4.14: Cyclic voltammogram of bare AuE and AuE/TGA-ZnTe in 0.1M PBS, pH 7.4 at 0.5 mV/s.

The cyclic voltammogram scanned from the positive direction from -1.2 V to +1.2 V, and from +1.2 V back to -1.2 V. The cyclic voltammogram of ZnTe-QDs capped with TGA has been reported in literature and three anodic peaks have been observed for CdTe QDs (Khene, Moeno and Nyokong, 2011). The AuE peaks are observed at 0.45 V and 1.0 V at a pH = 7.4 of PBS solution. In AuE/TGA-ZnTe the two gold peaks appeared at A_3 (0.95 V) and C_1 (0.35 V), there was a shift on both peaks which indicates that the quantum dots were absorbed on the surface of the electrode. The peak at 0.89 V (A_3) will have a contribution of the Au and ZnTe-QDs, oxidation peaks hence the enhancement in currents compared to bare Au electrode. Peak (C_1) is shifted to more negative potentials compared the peak observed for gold electrode in blank buffer solution (Feleni, 2013). Systematic studies revealed that the oxidation peak A1 can be assigned to Te-related trap states. The reverse scan shows two peaks at -0.55 V (C_2) and -0.74

(C_3). Peak C_2 and C_3 is associated with the electrochemical reduction of ZnTe-QDs oxidation products which are metallic in nature (Li *et al.*, 2011).

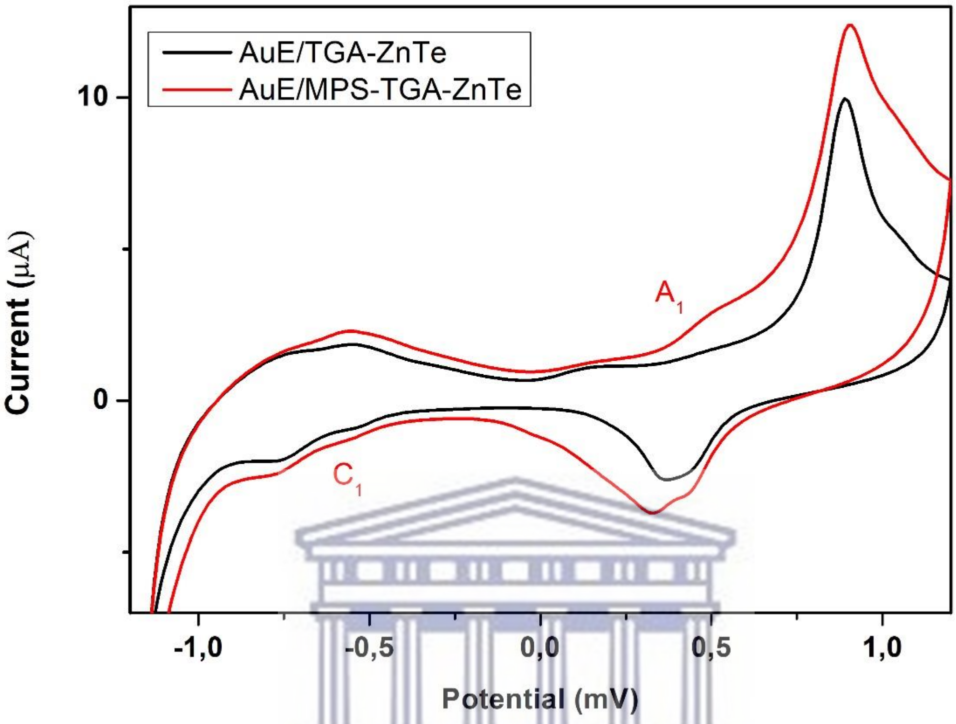

Figure 4.15: Cyclic voltammogram of bare AuE/TGA-ZnTe and AuE/MPS-TGA-ZnTe in 0.1M PBS, pH 7.4 at 50 mV/s.

In *Figure 4.15*, illustrate the effect of addition of (3-mercaptopropyl) trimethoxysilane (MPS) as a capping reagent on TGA/ZnTe. One anodic and cathodic peak was observed from the previous voltammogram of AuE/TGA-ZnTe. The anodic peak A_1 (0.48 V) is due to the MPS, this capping reagent affects mostly the core of the quantum dots. The voltammogram indicates the change on the surface of the quantum dot. In *Figure 4.16* is the cyclic voltammogram of AuE/MPS-TGA-ZnTe and AuE/TEOS-MPS-TGA-ZnTe, the last capping reagent was added to form a thicker shell on the quantum dots (Sakai *et al.*, 2012). They both have the same peaks anodic at 0.16 V, 0.48 V and 0.89 V and same oxidation peaks at 0.37 V, 0.75 V and -0.49 V, which indicates that there was no change on the surface/core of the quantum dots only the shell that was affected by the decrease of the peaks. After silica was assembled on the electrode, both anodic current and cathodic currents decreased, implying the hindrance exerted by silica on the electron-transfer process (Liu *et al.*, 2008).

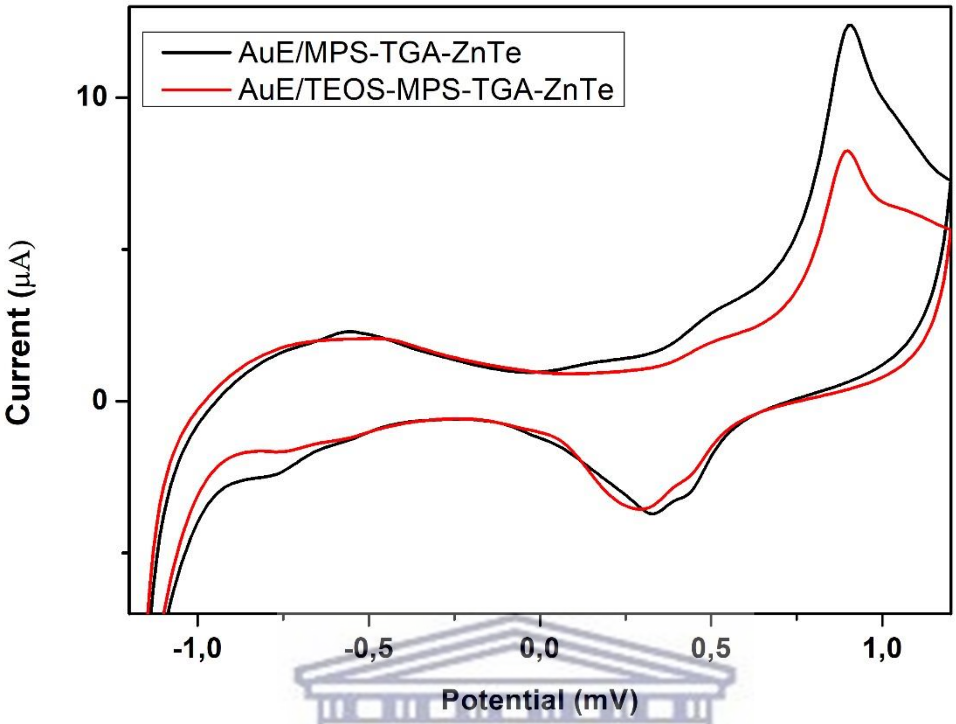

Figure 4.16: Cyclic voltammogram of bare AuE/MPS-TGA-ZnTe and AuE/TEOS-MPS-TGA-ZnTe in 0.1M PBS, pH 7.4 at 50 mV/s.

4.4 Immunoassay

Figure 4.17 and *Figure 4.18* shows the electrochemical impedance spectroscopic (EIS) measurement results that were used to assimilate the electrical characteristics and application perspective of ZnTe QDs. Here, ZnTe QDs were drop coated on the working electrode in a three electrode cell for such measurements. The figures show the Nyquist plot of ZnTe nanostructures. This plot represents the real and imaginary part of impedance and appears to be made up of partial semicircles. The plot was further fitted with an equivalent circuit to estimate the charge transfer resistance (Rct) value.

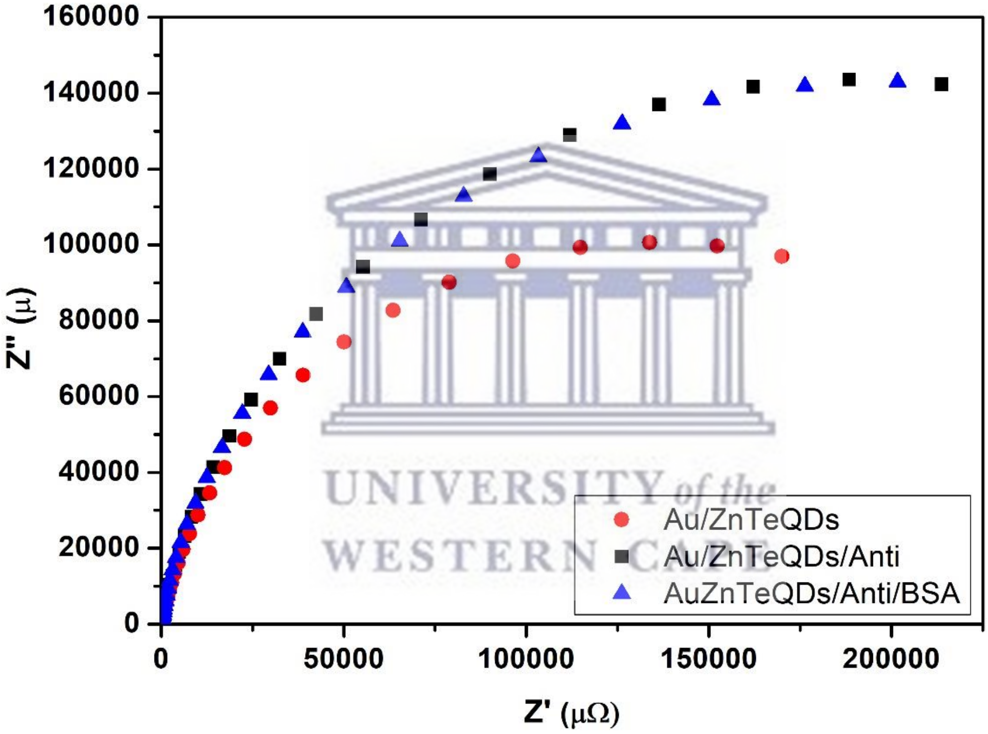

Figure 4.17: Cyclic voltammogram AuE/TEOS-MPS-TGA-ZnTe, AuE/ZnTeQDs/Antibody, and AuE/ZnTeQDs/Antibody/BSA in 0.1M PBS, pH 7.4 at 50 mV/s.

The electrochemical impedance spectroscopy analysis shown by *Figure 4.17*, indicated that the ZnTeQDs modified gold electrode with a small charge transfer. The Anti/ZnTeQDs modified gold electrode showed a charge resistance that is higher than the QDs alone. A great charge transfer resistance indicates the susceptibility of the material to charge opposition and depends on charged species on the electrolyte solution and the charge of the quantum dots immobilised onto the electrode surface (Nwabisa, 2010). It was clearly identified that the TEOS-ZnSe-QDs had much more great charge susceptibility to the charged materials present in PBS solution. Thus, the BSA/Anti/ZnTeQDs composite showed much more resistance to charge transfer in PBS than the pure ZnTeQDs thus indicated that the composite BSA/Anti/ZnSeQDs was better charge conducting material and a better electron conductive than the unmodified TEOS-ZnTeQDs which might be due to presence of the conducting BSA and Anti within the composite (Simão *et al.*, 2016). The proposed immunosensor was incubated with varying amounts of IFN-γ, and tested under optimal conditions. *Figure 4.18* showed the current response of the proposed immunosensor modified with ZnTe QDs, Antibody and BSA in the presence of different concentrations of IFN-γ. As illustrated, there is an increased with increasing IFN-γ concentrations, consistent with the formation of a large quantity of the quantum dots used on the electrode surface. These results indicated that the ZnTe quantum dots attached to the immunosensor surface retained high catalytic activity toward H_2O_2 reduction and also that it was a suitable electron transfer mediator for the electro-immuno process. The biosensor's detection limit value was determined in Figure 4.19 to be a value of 0.067 mg/L. This indicates that the biosensor is suitable for measuring the low concentrations of IFN-γ and can be customised for higher concentrations (Li *et al.*, 2017).

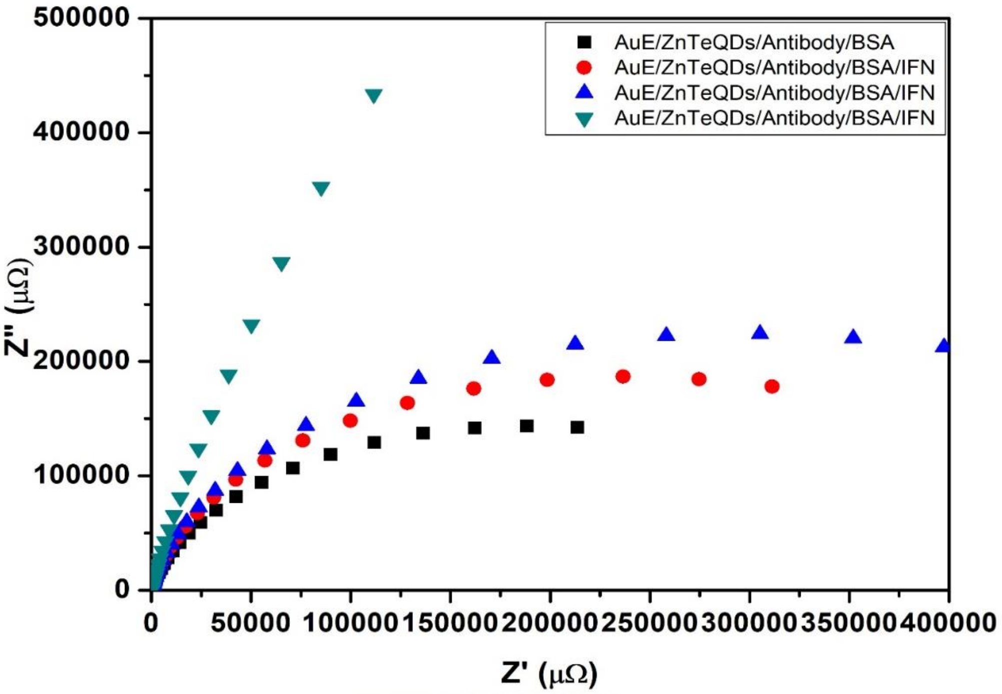

Figure 4.18: Cyclic voltammogram of bare AuE/TEOS-MPS-TGA-ZnTe, AuE/ZnTeQDs/Antibody/BSA/IFN, AuE ZnTeQDs/Antibody/BSA/IFN and AuE/ZnTeQDs/Antibody/BSA in 0.1M PBS, pH 7.4 at 50 mV/s.

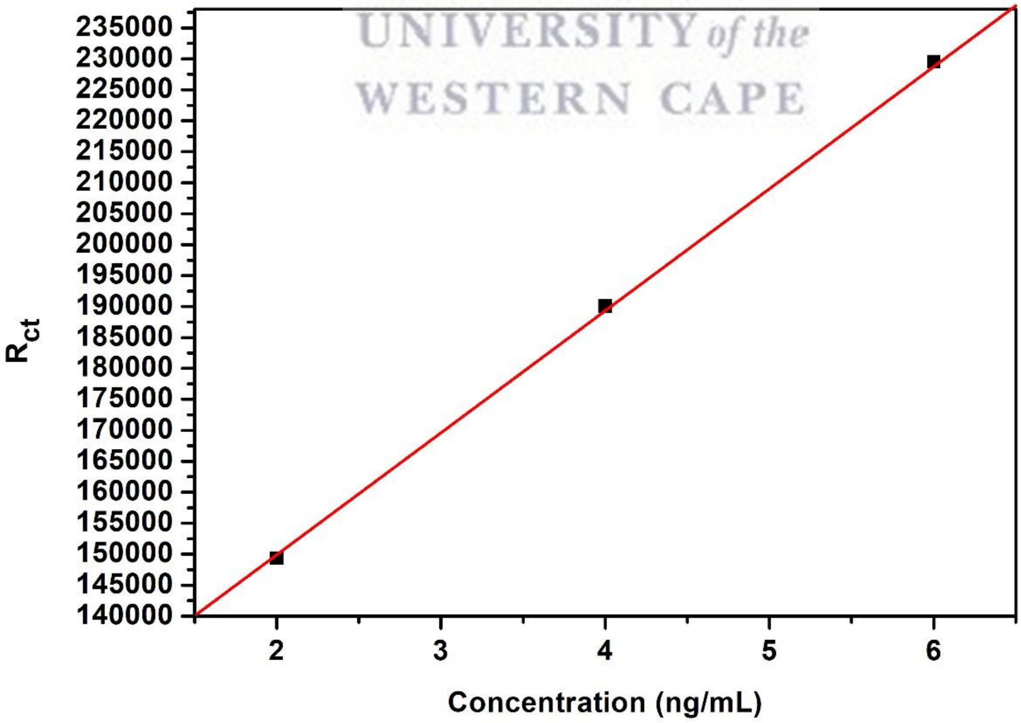

Figure 4.19: Calibration curve of the as-prepared immunosensor upon incubated with different concentrations of IFN-γ (2, 4, and 6 ng/mL).

4.5 Conclusion

This study represented a successfully synthesized three different capping reagents with ZnTe QDs. In ZnTe system, a remarkable red shift in UV absorbance and an energy transfer from the core to the shell were observed. The Optical Absorption peak was observed at 229 nm wavelength while that of bulk is 324 nm indicating the blue shift in absorption edge also the band gap calculated from absorption spectra was at 4.42 eV while the bulk ZnTe has 4.30 eV showing quantum size effect. The capped ZnTe QDs which were well dispersed with an average particle size between 3-20 nm and a cubic zinc blende crystalline structure from the XRD. The silica shell provides a versatile platform for the decoration of the surface with specific functional groups to be later used for bioconjugation (thiols, carboxylic acids) and increased biocompatibility. A calibration plot from the increasing IFN-γ concentrations plotted against increasing current was used to determine low limit of detection (LOD) (0.067 mg/L) values. The concentration range studied is much lower than the range found in clinical samples where the range of maximum Interferon gamma concentration is 2 to 6 mg/L. This means that the biosensor can be applied for IFN-γ detection in patients who are suspected to have the TB disease from their systems very quickly. Thus, there is high expectation that such a device could be developed as a reliable tool for point of care diagnosis for TB and other diseases. In summary, a new disposable electrochemical immunosensor with low cost and simple fabrication was proposed to detect IFN-γ. Therefore, this strategy reported here possessed excellent clinical value in IFN-γ detection.

References

Ali, M. and Sarma, D. D. (2007) 'Synthesis of ZnSe Quantum Dots and ZnSe – ZnS Core / Shell Nanostructures', 7(6). doi: 10.1166/jnn.2007.748.

Asano, H. *et al.* (2017) 'Synthesis of colloidal Zn(Te,Se) alloy quantum dots', *Materials Research Express*. IOP Publishing, 4(10), pp. 0–10. doi: 10.1088/2053-1591/aa8b84.

Chen, X., Liu, F. and Jiang, Q. (2012) 'Synthesis and Properties of Water-Soluble Silica-Coated ZnSe / ZnS Semiconductor Quantum Dots', pp. 6–11. doi: 10.1007/s10904-011-9606-3.

Dhar, R., Singh, S. and Kumar, A. (2015) 'Effect of capping agents on optical and antibacterial properties of cadmium selenide quantum dots', 38(5), pp. 1247–1252.

Feleni, U. (2013) 'Palladium Telluride Quantum Dots Biosensor for the Determination of Indinavir Drug By Usisipho Feleni (BSc Honours) A thesis submitted in partial fulfilment of the requirements for the degree of Magister Scientiae in Nanoscience Faculty of Science Unive', (November).

Gadalla, A. *et al.* (2017) 'CHARACTERIZATION OF CdSe CORE AND CdSe / ZnS CORE / SHELL QUANTUM DOTS SYNTHESIZED USING A MODIFIED METHOD', 14(7), pp. 239–249.

Ghosh, S. *et al.* (2011) 'Aqueous synthesis of ZnTe/dendrimer nanocomposites and their antimicrobial activity: Implications in therapeutics', *Nanoscale*, 3(3), pp. 1139–1148. doi: 10.1039/c0nr00610f.

Goftman, V. V *et al.* (2016) 'Multicolored silica coated CdSe core / shell quantum dots', 9917, pp. 1–6. doi: 10.1117/12.2225212.

Hao, J. *et al.* (2019) 'A facile route to synthesize CdSe / ZnS thick-shell quantum dots with precisely controlled green emission properties : towards QDs based LED applications', *Scientific Reports*. Springer US, (February), pp. 1–8. doi: 10.1038/s41598-019-48469-7.

Khene, S., Moeno, S. and Nyokong, T. (2011) 'Voltammetry and electrochemical impedance spectroscopy of gold electrodes modified with CdTe quantum dots and their conjugates with nickel tetraamino phthalocyanine', *Polyhedron*. Elsevier Ltd, 30(12), pp. 2162–2170. doi: 10.1016/j.poly.2011.06.002.

Kobayashi, Y., Correa-Duarte, M. A. and Liz-Marzán, L. M. (2001) 'Sol−Gel Processing of Silica-Coated Gold Nanoparticles', *Langmuir*, 17(20), pp. 6375–6379. doi: 10.1021/la010736p.

Koç, K., Tepehan, F. Z. and Tepehan, G. G. (2012) 'Growth kinetics of MPS-capped CdS quantum dots in self-assembled thin films', pp. 1–7.

Kumar, P. and Singh, K. (2009) 'Wurtzite ZnSe quantum dots : Synthesis , characterization and PL properties', 1(1), pp. 59–69.

Li, G. *et al.* (2017) 'Evaluation of a New IFN- γ Release Assay for Rapid Diagnosis of Active Tuberculosis in a High-Incidence Setting', 7(April). doi: 10.3389/fcimb.2017.00117.

Li, H., Shih, W. Y. and Shih, W. H. (2007) 'Stable aqueous ZnS quantum dots obtained using (3-mercaptopropyl) trimethoxysilane as a capping molecule', *Nanotechnology*, 18(49). doi: 10.1088/0957-4484/18/49/495605.

Li, Y. *et al.* (2011) 'ChemComm Aqueous synthesis of CdTe nanocrystals : progresses and perspectives', pp. 9293–9311. doi: 10.1039/c1cc11331c.

Liu, X. *et al.* (2008) 'Glucose biosensor based on gold nanoparticle-catalyzed luminol electrochemiluminescence on a three-dimensional sol-gel network', *Electrochemistry Communications*, 10(9), pp. 1250–1253. doi: 10.1016/j.elecom.2008.06.009.

Moradian, R. *et al.* (2013) 'Structural , optical , and electrical properties of thioglycolic acid-capped CdTe quantum dots thin films', pp. 1–6.

Ndangili, P. M. *et al.* (2017) 'Gallium-Induced Perturbation of Zinc Selenide Quantum Dots Electronics', pp. 7054–7062. doi: 10.1002/slct.201700748.

Niu, Z. and Li, Y. (2013) 'Removal and Utilization of Capping Agents in Nanocatalysis Removal and Utilization of Capping Agents in Nanocatalysis'. doi: 10.1021/cm4022479.

Nwabisa, A. (2010) 'DEVELOPMENT OF ELECTROCHEMICAL ZnSe QUANTUM DOTS BIOSENSORS FOR LOW-LEVEL DETECTION OF 17 β -ESTRADIOL ESTROGENIC', (November).

Orth, F. O. R. T. W., Exas, T. and Aprimer, Q. (2002) 'QuantumDots: APrimer'.

Owens, G. J. *et al.* (2016) 'Progress in Materials Science Sol – gel based materials for biomedical applications', 77, pp. 1–79. doi: 10.1016/j.pmatsci.2015.12.001.

Qu, H. *et al.* (2014) 'Silica-coated ZnS quantum dots as fluorescent probes for the sensitive detection of Pb 2 + ions'. doi: 10.1007/s11051-014-2762-y.

Qutub, N. and Sabir, S. (2012) 'Optical , Thermal and Structural Properties of CdS Quantum Dots Synthesized by A Simple Chemical Route', 8(2), pp. 111–120.

Ram, C. *et al.* (2017) 'Computational study of leading edge jet impingement cooling with a conical converging hole for blade cooling', *ARPN Journal of Engineering and Applied Sciences*, 12(22), pp. 6397–6406. doi: 10.1039/b000000x.

Sakai, R. T. *et al.* (2012) 'Progress in Organic Coatings Electrochemical study of TEOS , TEOS / MPTS , MPTS / MMA and TEOS / MPTS / MMA films on tin coated steel in 3 . 5 % NaCl solution', *Progress in Organic Coatings*. Elsevier B.V., 74(2), pp. 288–301. doi: 10.1016/j.porgcoat.2012.01.001.

Selvan, S. T. (2010) 'Silica-coated quantum dots and magnetic nanoparticles for bioimaging applications „ Mini-Review … a …', (October), pp. 110–115. doi: 10.1116/1.3516492.

Shah, N. (2009) 'CREATION OF BIOACTIVE SURFACES TO MODULATE CELL BEHAVIOR USING SURFACE INITIATED PHOTOINIFERTER- MEDIATED GRAFT'.

Shahraki, M. R. and Irani, M. (2014) 'The Effects of Ecstasy on Liver Function Tests, Blood Glucose, and Lipids Profile of Male Rats', *International Journal of High Risk Behaviors and Addiction*, 3(4). doi: 10.1039/c2py20863f.

Simão, E. P. *et al.* (2016) 'Biosensor based on cysteine monolayer and monoclonal antibody for specific detection of aflatoxin b1 in rice', *Journal of the Brazilian Chemical Society*, 27(6), pp. 1040–1047. doi: 10.5935/0103-5053.20150361.

Singh, A. *et al.* (2015) 'Surface functionalization of quantum dots for biological applications'. Elsevier B.V., 215, pp. 28–45. doi: 10.1016/j.cis.2014.11.004.

Sobczak, E., Nietubyc, R. and Mac, S. (2002) 'Three-Dimensional Quantum Dot " Crystal " Formation in CdTe / ZnTe Superlattices', 448(1), pp. 445–448.

Song, Y. *et al.* (2014) ‘Novel aqueous synthesis methods for ZnTe / ZnSe’, *RSC Advances*. Royal Society of Chemistry, 5, pp. 6271–6278. doi: 10.1039/C4RA12727G.

Sovan Kumar Patra, BhavyaBhushanb and Priyam, A. (2016) ‘Dalton Transactions’. doi: 10.1039/b000000x.

Stawski, T. M. *et al.* (2019) ‘Mechanism of silica – lysozyme composite formation unravelled by in situ fast SAXS’, pp. 182–197. doi: 10.3762/bjnano.10.17.

‘The SAXS Guide’ (2013).

Wolcott, A. *et al.* (2006) ‘Silica-Coated CdTe Quantum Dots Functionalized with Thiols for Bioconjugation to IgG Proteins’, pp. 5779–5789. doi: 10.1021/jp057435z.

Chapter five

Summary

This chapter describes the procedures for the synthesis of CuZnTe core-shell QDs using three appropriate reagents. Their properties were investigated using techniques such as spectroscopic (UV, FTIR), microscopic (HRSEM, HRTEM) and electrochemical (CV). It also includes the comparison of CuTe, ZnTe and CuZnTe core-shell. This chapter also shows the detection of interferon gamma.

CuZnTe core-shell Quantum Dots based Electrochemical Immunosensor for Sensing Interferon gamma a TB biomarker.

Abstract

Developing a rapid and accurate technique for the detection of *M. tuberculosis* is crucial to the control of TB. Nevertheless, current point-of-care (POC) detection method has some problems such as slow speed, low rate of accuracy and limited to active TB infection, leading to the inefficient reduction of TB-related deaths. As to the detection of TB, the technique should be fast, accurate, cheap and field-applicable. Electrochemical immunosensors have attracted numerous attention in the last decades owing to its simple operation, excellent sensitivity and high selectivity. Because of the electrochemically inert of most antigen and antibody molecules, electrochemical impedance spectroscopy (EIS) has been employed for the direct determination of immunospecies. In comparison with assay methods, EIS method is cheaper because none additional materials (e.g., labelled antibodies) are required. Therefore, EIS have been widely used in a large number of biological studies. In this study, a novel electrochemical impedance immunosensor for the sensitive detection of IFN-γ was developed for the first time. The sensor was fabricated with CuZnTe modified electrode on which IFN-γ monoclonal antibody was immobilized. The concentration of IFN-γ was determined by detecting the change of impedance values after the specific reaction of IFN-γ antibody. The as-prepared immunosensor demonstrated various advantages such as simple operation, low cost, label-free and high sensitivity, which is superior to the conventional assay. The immunosensor is demonstrated to be a potential method for the early diagnosis of TB infections. A new disposable electrochemical immunosensor with low cost and simple fabrication was proposed to detect interferon-γ (IFN-γ). In this work, a multilayer Gold electrode (AuE) modified with a self-assembled Silica coated Copper Zinc Telluride (CuZnTe core-shell) quantum dots followed by antibodies was fabricated for highly sensitive and rapid detection of IFN-γ. The formation of the antibody complex at the electrode surface causes the impedance to increase. Differential pulse voltammetry (DPV) responses of the IFN-γ/BSA/antibody/CuZnTe core-shell/Au biosensor systems showed catalytic cathodic peaks at -275 mV (-0.3 V) for the IFN-γ reaction. This is the first report of developing an electrochemical IFN-γ biosensor with a ternary surface in biosensor developed. This immunosensor is able to detect IFN-γ with a linear sensing region of 2 ng/ml to 10 ng/ml and lower detection limit of 0.33 ng/ml (method detection limit technique) in buffer solution. The resulting IFN-γ immunosensor shows excellent detection reproducibility, good specificity, and stability for tuberculosis.

5.0 Introduction

Tuberculosis (TB) is a chronic, infectious disease caused by the *Mycobacterium tuberculosis* (MTB), continues to be a major cause of morbidity and mortality throughout the world (Smith, 2003). The World Health Organization 2016 global tuberculosis report estimates that in 2015 two million people died from TB (WHO, 2015). Many studies have confirmed that various cytokines secreted by human peripheral blood immune cells in response to *M. tuberculosis* can be used as diagnostic biomarkers for TB (Goletti *et al.*, 2016). Research conducted over the past decade has brought about the development of commercial molecular assays that are based on the enzyme-linked immunosorbent spot (ELISPOT) assay(Li *et al.*, 2017). Overexpressed IFN-γ production is generally regarded as a good indicator of MTB infection (Hossain and Norazmi, 2013). Interferon gamma (IFN-γ) is a crucial cytokines secreted by immune cell (T cells) that can act as a diagnostic marker for TB disease, it can be used as a good indicator for early diagnosis of TB infection (Crevel, Ottenhoff and Meer, 2002). Therefore, an IFN-γ release assay is a viable alternative to conventional measurements, such as the tuberculin skin test (TST), because the IFN-γ release assay is performed in vitro and is more specific than the TST (Chang *et al.*, 2012). At the present time, antibody-based immunoassays such as ELISA/ELISpot represent the gold standard in IFN-γ detection (Ying Liu, Timothy Kwa, 2012). Although the sensitivities of these detection kits are satisfactory, the assays are still cumbersome, expensive, and time-consuming, involving multiple washing steps and requiring large sample volumes for analysis (Chang *et al.*, 2012; Chen, Liu and Jiang, 2012). Thus, it is necessary to develop other strategies that can simply and directly detect IFN-γ. Analytical methods based on immunosensing techniques have been reported for the detection of IFN-γ (Wang, Mazurek and Alocilja, 2016). Although these approaches have a high sensitivity, they are still hindered by high cost, time-consuming, and low stability of antibody-antigen binding events. Thus, it is very urgent to develop an ultrasensitive, low cost, specific, rapid, and reliable assay method for quantitative detection of IFN-γ.

Biosensors have been used for the detection of a wide variety of biomolecules (proteins, peptides, nucleic acids, etc.) and intact microorganisms (bacteria, viruses). Biosensor-based detection of IFN-γ has been reported. Compared to other methods, electrochemical biosensors are attractive options for measuring IFN-γ due to their sensitivity, speed, and ability to convert a biological event directly to an electronic signal (Wang, Mazurek and Alocilja, 2016). The principle behind electrochemical biosensor is the coupling of a specific antibody with an electrode transducer which functions to convert a binding event into an electrical signal (Dingran Chang, Sandy Zakaria, Mimi Deng, Nicholas Allen, 2016). Because of the electrochemically inert of most antigen and antibody molecules, electrochemical impedance spectroscopy (EIS) has been employed for the direct determination of immunospecies. In comparison with assay methods, EIS method is cheaper because none additional materials (e.g., labelled antibodies) are required. Moreover, the non-destructive testing EIS can be employed for the detection of electrical properties of the biological interface. Therefore, EIS have been widely used in a large number of biological studies (Wang *et al.*, 2017). While these immunoassays are sensitive and specific, they are often limited by the low stability and the need for large sample volumes (Liu *et al.*, 2015).

In comparison with assay methods, EIS method is cheaper because none additional materials (e.g., labelled antibodies) are required. Moreover, the non-destructive testing EIS can be employed for the detection of electrical properties of the biological interface. Therefore, EIS have been widely used in a large number of biological studies. In this study, a novel electrochemical impedance immunosensor for the sensitive detection of IFN-γ was developed (Grossi and Riccò, 2017). The sensor was fabricated with CuZnTe core-shell modified electrode on which IFN-γ monoclonal antibody was immobilized. The concentration of IFN-γ was determined by detecting the change of impedance values after the specific reaction between IFN-γ antigen and IFN-γ antibody. The sensitivity of as-prepared immunosensor was greatly improved by the usage of CuZnTe core-shell QDs. We used a simple and facile synthetic strategy to prepare uniform-size water-soluble CuZnTe core-shell QDs and fabricated a novel immunosensor to effectively detect IFN-γ based on the electrochemical signals. The as-prepared immunosensor demonstrated various advantages such as simple operation, low cost, label-free and high sensitivity, which is superior to the conventional assay. The immunosensor is demonstrated to be a potential method for the diagnosis of TB infections.

5.1 Experiments

5.1.1 Chemicals

All reagents were of analytical reagent grade and purchased from Sigma Aldrich. The material that were used are tetraethyl orthosilicate (TEOS, 90%), thioglycolic acid (TGA, 98%), (3-mercaptopropyl) trimethoxysilane (MPS, 95%), tellurium (Te, 99.997%), sodium hydroxide (NaOH, 98%), copper acetate monohydrate (Cu (OH)2CO3, 99.0%), sodium borohydride (NaBH4, 98%), sodium phosphate monobasic dihydrate (NaH2PO4, 99%) and disodium hydrogen phosphate dibasic (Na2HPO2, 98%). De-ionized water, used throughout the experiments, was prepared with a Milli-Q water purification system. Analytical grade nitrogen obtained from Afrox South Africa, was used for degassing buffer solutions. The Phosphate buffer solutions (pH 7.4) was prepared from H_2NaPO_4, HNa_2PO_4 and was used for all electrochemical characterisation. The Alumina micro polishing pads were obtained from Sigma-Aldrich.

5.1.2 Synthesis of core-shell CuZnTe quantum dots

The quantum dots (QDs) used in this study, was synthesized using the standard procedure described in the literature. In flask 1 0.3993 g of Cu, 0.7024 g of Zn and 400 µL of TGA (5.7 mmol) was added in a flask with 25 ml of water. 2M NaOH was added dropwise to adjust the pH to 11.8. Then in flask 2, 0.396 g of Tellurium (0.46 mmol) and 0.227 g of $NaBH_4$ (6.0 mmol) was added together in 25 ml of water, so that the $NaBH_4$ will reduce the Tellurium. The precursor solution of reduced Tellurium was injected to flask 1 to form CuZnTe core-shell, after injection there a colour change. The flask was degassed under vacuum at 100°C for 1 h. Then, the flask was backfilled with nitrogen and heated up to 100 °C. On a portion of TGA-capped CuTe nanoparticles, 330 µL of MPS (48 mmol in water) was added. To ensure even distribution of MPS, a mini-stir bar was utilized during the 1 h required for surface priming. After surface priming, 1270 µL of TEOS (1.8mmol) was added to the solution under stirring to initiate silica polymerization at the particle surface.

5.1.3 Preparation of IFN-γ immunosensor

In the fabrication process of biosensor, a gold electrode was first polished with 1 µm, 5 min, 0.3 µm, 10 min and 0.05 µm, 20 min alumina slurries in polishing pads respectively, followed by ultra-sonication in absolute ethanol and distilled water for 10 min each. CuZnTe core-shell quantum dots suspension was prepared by adding 3.0 µL of CuZnTe core-shell QDs into 3.0 µL of deionized water, and the QDs solution was treated with ultrasonic and stirring before, in order to achieve complete dissolution. 3.0 µL of the mixture was drop coated on to the AuE electrode surface. The CuZnTe core-shell/AuE electrode was then stored at room temperature for 24 h and kept in the dark in order to form a well characterised, self-assembled monolayer on metal electrodes (AuE). This was used as a strategy to immobilise and organise biomolecules at the interface and also give stability and provide electron transfer (Goncolves et al., 2007). After that the CuZnTe core-shell/AuE modified electrode was rinsed carefully with distilled water to remove unbound CuZnTe core-shell QDs molecules. The CuZnTe core-shell/AuE modified electrode was then activated by drop coating a 30 µL solution containing 1:1 of (EDC/NHS), stored for 30 min in a dark place. After that the CuZnTe core-shell/AuE modified electrode was rinsed carefully with PBS. Subsequently, 10 µL of antibody solution (10 µM) was drop coated on to CuZnTe core-shell/AuE surface. The electrode was then stored for 2 hours at room temperature in a dark place. The electrode was then washed with PBS solution. BSA solution (1%) was used for blocking the nonspecific sites. The reaction occurred at room temperature for 10 min. The IFN-γ immunosensor was then washed with PBS solution.

5.2 Instrumentation

Ultraviolet–visible spectroscopy (UV-Vis) of the ZnTe QDs solution was carried out using a Nicolet evolution 100 UV-Vis spectrophotometer (Thermo Electron Corporation, UK) and the instrument was controlled with VisionPro software. High resolution transmission electron microscope (HRTEM) images of the ZnTe QDs were obtained using a Tecnai G2 F20X-Twin MAT FETEM from FEI (Eindhoven, Netherlands) and it is a 200 kV instrument equipped with Energy Dispersive Spectroscopy (EDS). SAXS was used to determine the structure of particle systems in terms of averaged particle sizes or shapes. SAXSpace (Anton peer, Australia) system using 1nm diameter quartz capillary positioned at 317 mm from the CCD and temperature controlled at 20°C. Data evaluation was performed with the GIFT software (which is a versatile tool for the evaluation of small angle scattering data). FTIR is a technique that was used to investigate chemical bonding or molecular structure of materials due different functional groups. FTIR spectra were recorded in the range 4000 - 1000 cm^{-1} using a Perkin Elmer model Spectrum 100 series. Raman spectroscopy were also prepared on a glass slide and analysed using Xplora Raman spectrometer (Horiba Scientific) utilising a 514 nm He-Cd laser as an excitation source. Data capturing and instrument control were performed using LabSpec software. Immunoassay measurement of materials was carried out by using a Palm Sensor. Electrochemical measurements were carried out in 0.1 M phosphate buffer, pH 7.4, cell solution using a 3 mm diameter Au disk working electrode, a platinum wire counter electrode and a Ag/AgCl (with 3 M KCl salt-bridge) reference electrode supplied by Bioanalytical Systems, Incorporated (BASi). The electrochemical signals were recorded with an IviumStat Electrochemical Interface and Impedance Analyser (Ivium 113 Technologies B.V., Eindhoven, The Netherlands). Differential pulse voltammetry (DPV) was recorded at a scan rate of 50 mV/s. As to EIS experiments, the amplitude of applied potential was 10 mV and the frequency ranges from 10^{-1} to 105 Hz.

5.3 Results and Discussion

5.3.1 Ultraviolet - vis spectroscopy

The UV-vis spectrum of CuZnTe core-shell quantum dots aqueous solution is presented in *Fig 5.1*. Deionized water was used as a reference solution in taking the spectrum of the quantum dots solution. The spectrum of TGA-CuZnTe core-shell has a distinct absorption peak at 256 nm which is attributed to the characteristic absorption of TGA and a broad peak at 320 nm which is attributed to the formation of the quantum dots CuZnTe core-shell. After the addition of MPS, the UV absorption peak observed at 256 nm shifted to 226 nm, which shows are blue shift (Zi *et al.*, 2014). The peak at 320 nm became flattened, which is due to the addition of the silica particles made the absorption features appear less sharp for the QDs (Zhang *et al.*, 2008). With the addition of TEOS to the quantum dots there was a red shift of peaks. The absorption peak of MPS-TGA-CuZnTe core-shell red shifts from 226 to 228 nm and the peak at 320 nm to 325 nm, suggesting that the electronic conjugation within the nanomaterial was restored upon the reduction procedure. The spectra of TEOS-MPS-TGA-CuZnTe core-shell solution exhibits maximum absorption peak at 325 nm. The red shift also indicates the quantum dots growth with addition of silica, making the outer shell thicker (Wang, Chen and Cao, 2014).

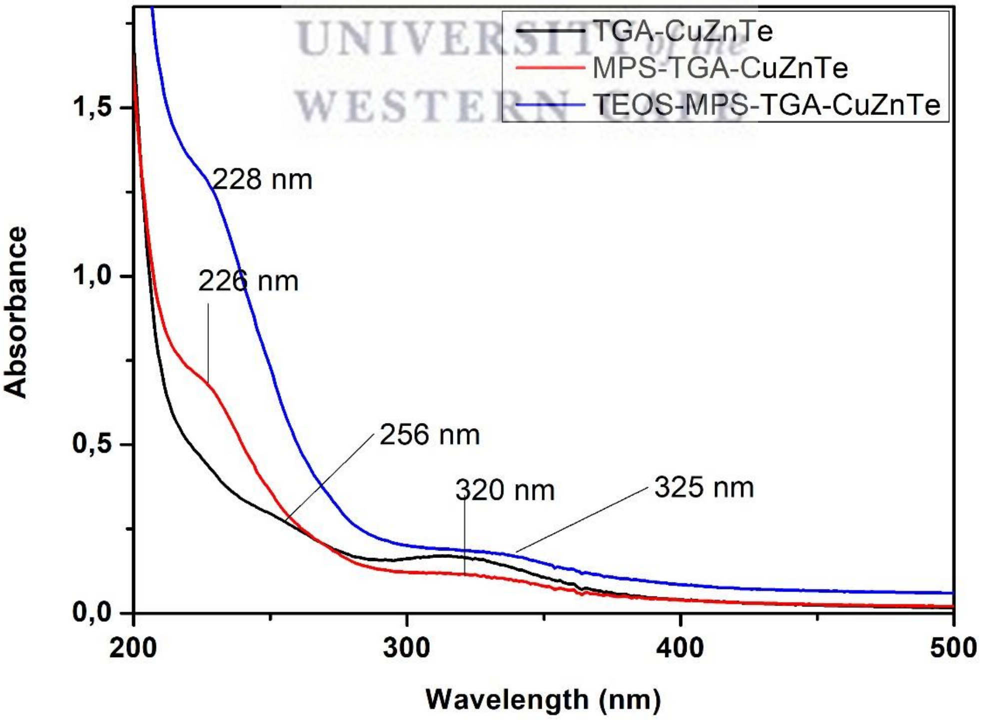

Figure 5.1: UV-Vis spectrum of CuZnTe core-shell quantum dots capped with TGA, MPS and TEOS.

The UV-vis spectra of the silica coated quantum dots are shown in the figure below (*Figure 5.2*). TEOS-CuTe quantum dots show two absorption shoulders at 250 nm and 325 nm. These present a significant blue shift from the absorption edge of bulk CuTe (531 -548 nm). The UV-Vis absorption spectrum of colloidal ZnTe QDs showed weak broad absorption in the UV range. The maximum absorbance was obtained at about 307 nm. This peak was deduced to be associated with electrons transition of d valence electrons from Zn to Zn* exited state (Nwabisa, 2010). The onset of absorption is considerably blue shifted relative to the bulk of ZnTe indicating a significant effect of synthesized ZnTe QDs. The broad peak at 227 nm indicates the capping reagent TGA (Asano *et al.*, 2017; Ram *et al.*, 2017). The spectrum of TEOS-CuZnTe core-shell quantum dots shows an absorption shoulder at 225 nm. Although its shape is similar to the spectra of TEOS-CuTe quantum dots, it is interesting to note that the absorption peak is at the same wavelength as that of the weak absorption of TEOS-CuTe quantum dots and the ternary quantum dots have a more enhanced band. In this case, the broad and low absorption peak can be related to the small particle size due to a reduced mean free path for conduction electrons. At very small sizes, limitation of the mean free path by the particle boundary broadens and decreases peak absorption (Varshney *et al.*).

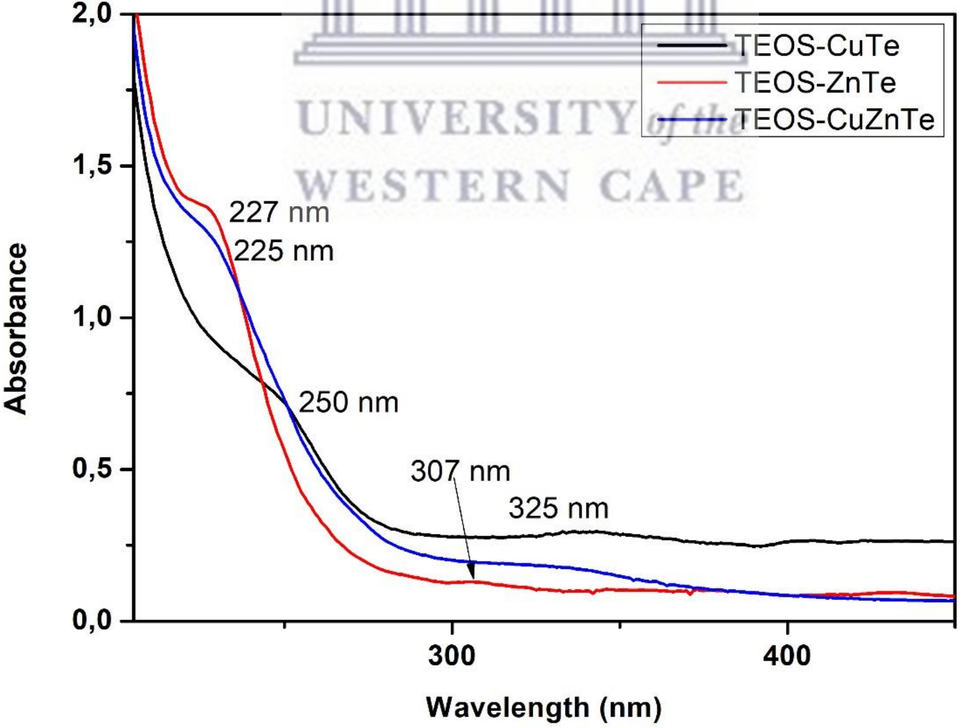

Figure 5.2: UV-vis spectra of TEOS-CuTe, TEOS-ZnTe and TEOS-CuZnTe core-shell quantum dots.

5.3.2 Small-angle x-ray scattering

The particle size and size dispersion in aqueous media was investigated using small-angle x-ray scattering (SAXS) and dynamic light scattering (DLS). Furthermore, information regarding the stability of the nanoparticles in aqueous media (tendency to agglomerate) could also be obtained through these techniques. The results from the SAXS analysis was Fourier transformed using GIFT software, into a pair distance distribution function (PDDF) by volume and size distribution by number function NN(r). The results are shown in *Figure 5.3 to Figure 5.4*.

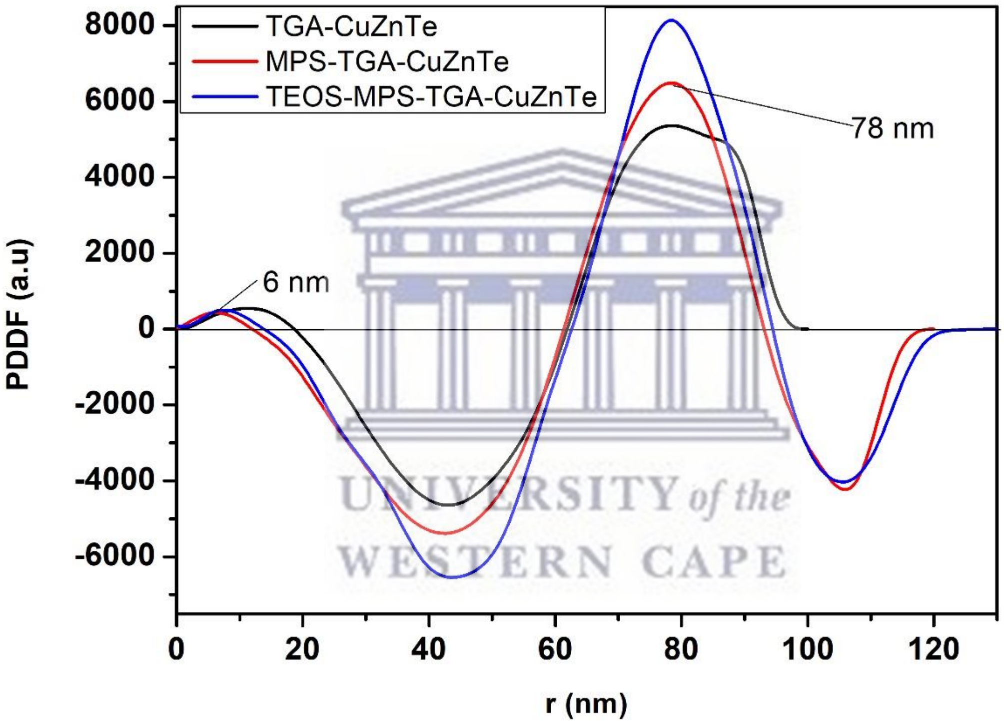

Figure 5.3: Representation of SAXS data in form of PDDF of TGA-CuZnTe (black-line), MPS-TGA-CuZnTe (red-line) and TEOS-MPS-TGA-CuZnTe (blue-line).

In *Figure 5.3*, the PDDF curve of TGA-CuZnTe core-shell (black-line) showed the largest particles detected have a radius of 6 nm and 78 nm. From these results, TGA-CuZnTe shows a globular graph which shoes that quantum dots are spherical, there is an agglomeration of the quantum dots (Quyet Van Le, Jong Beom Kim, Soo Young Kim, Byeongdu Lee, 2017). The diameter of the TGA-CuZnTe ends at 100 nm and it does not have a capping reagent. The PDDF curve of MPS-TGA-CuZnTe (red-line) shows that the quantum dots are uniform and curve is globular with no agglomeration. The diameter of the MPS-TGA-CuZnTe is 120 nm which is 20 nm more than the TGA-CuZnTe QDs and the MPS-TGA-CuZnTe ha a curve in the negative region which indicates core-shell due to the addition of silica. TEOS-MPS-TGA-CuZnTe core-shell (blue-line) is globular and more narrow which indicates uniform distribution of the quantum dots. The size of the TEOS-MPS-TGA-CuZnTe quantum dots diameter is 140 nm, which is 20 more than MPS-TGA-CuZnTe and 40 more times than TGA-CuZnTe. At the first curve with the addition of the capping reagents it reduced, and the curve at 78 started increasing. This is an indication of growth of quantum dots, and the TGA-CuZnTe core-shell curve is asymmetrical having two peaks that shows agglomeration of the quantum dots (‘The SAXS Guide’, 2013; Gabriella and Pacoste, 2017). All the capping reagents goes to the negative reign which indicates the core-shell of quantum dots. The core-shell of the MPS-TGA-CuTe it has a smaller curve than that of TEOS-MPS-CuTe, this proves that the core-shell is thickened by the addition of TEOS. The Figure 5.4 illustrates that TGA-CuZnTe core-shell had a radius of 13 nm (diameter of 26 nm) when diluted in aqueous media. The MPS-TGA-CuTe QDs (red-line) have an average particle size of 27 nm in diameter (17 nm radius) in aqueous media. In the case of the TEOS-MPS-TGA-CuTe QDs (blue-line) the most abundant size within the particles is 18 nm in diameter when dispersed in aqueous solution (Gabriella and Pacoste, 2017).

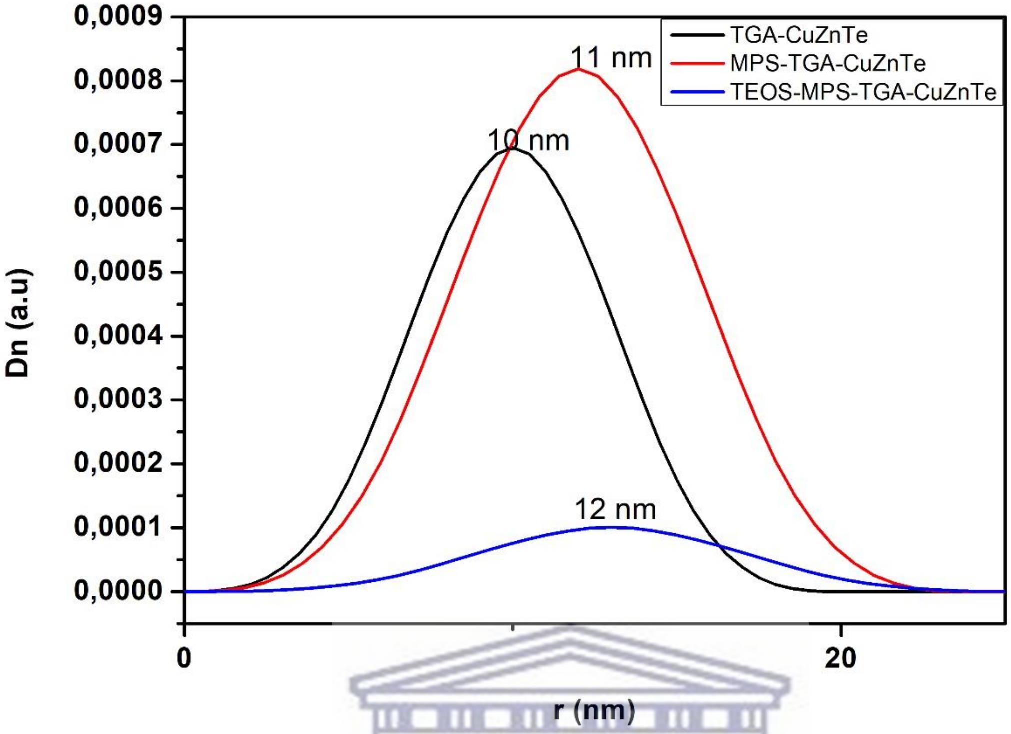

Figure 5.4: Representation of SAXS data in form of particle radius (r) distributed by number of particles for TGA-CuTe (black-line), MPS-TGA-CuTe (red-line) and TEOS-MPS-TGA-CuTe (blue-line).

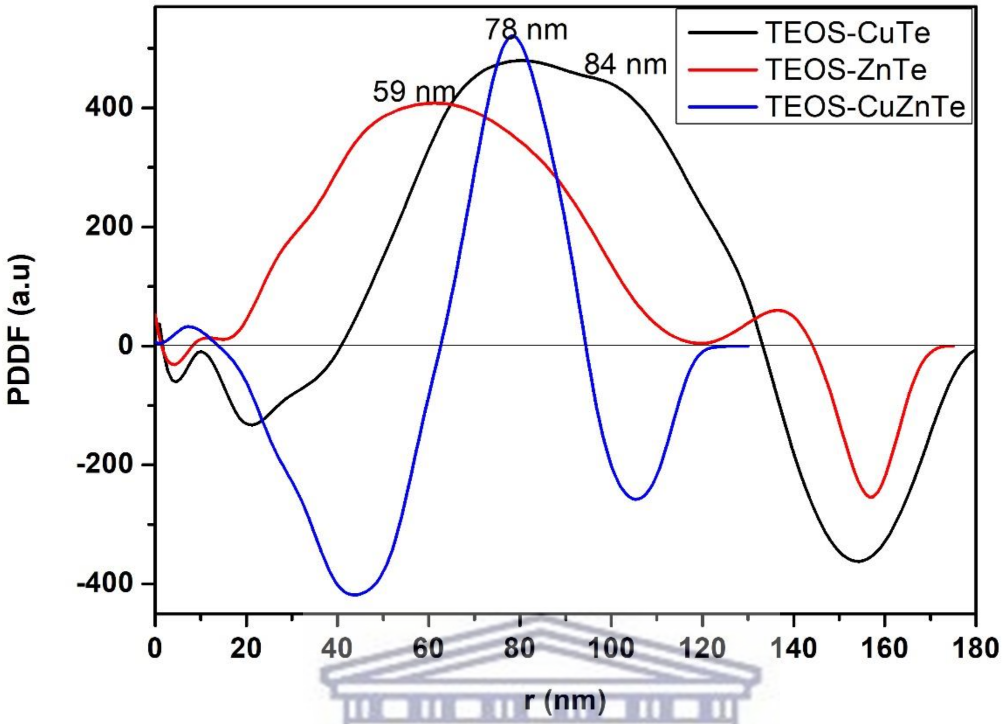

Figure 5.3: Representation of SAXS data in form of PDDF of TEOS-CuTe (black-line), TEOS-ZnTe (red-line) and TEOS-CuZnTe core-shell (blue-line).

In Figure 5.3, the 3 different quantum dots after the capping with tetraethyl orthosilicate (TEOS) are showed. With TEOS-CuTe QDs the graph shows agglomeration of the quantum dots with the curve it has a shoulder. The quantum dots have a globular shape which indicates that they are spherical. TEOS-ZnTe also have the same results as TEOS-CuTe which shows also the Zinc quantum dots are not stable. Addition to the information they both are capped with TEOS; this is indicated by the dip in the PDDF that goes to the negatives ('The SAXS Guide', 2013). With TEOS-CuZnTe core-shell quantum dots the curve only has one peak and its globular which shows that the quantum dots are spherical and they do not agglomerate and also the dip of the PDDF on to the negatives shows that they were successfully capped with TEOS. The CuZnTe core-shell QDs are the best of the three which also shows that Copper and Zinc with Telluride works well when combined than when separate.

5.3.3 Transmission electron microscopy

The size and shape of the products were examined by transmission electron microscopy (TEM). The TEM image of CuZnTe core-shell QDs is shown in *Figure 5.5, 5.6* and *5.7* respectively. *Figure 5.5* ***A)*** shows the image of the quantum dots that are of spherical in morphology. A degree of monodispersity and homogeneity in the particle distribution of TGA-capped CuZnTe core-shell QDs was achieved, as indicated in the image magnification (Adegoke *et al.*, 2016). The morphological assembly of the nanocrystals revealed the formation of a quasi-spherical pattern of particles (Dhar, Singh and Kumar, 2015). The average particle size distribution for TGA-CuZnTe core-shell QDs was estimated as 5.9nm. In contrast, the SAED Pattern Figure 5.5 C) shows well resolved bright rings corresponding to lattice planes this indicates that the degree of crystallinity is higher for the particles synthesized (Sovan Kumar Patra, BhavyaBhushanb and Priyam, 2016). Energy dispersion X-ray spectroscopy (EDX) is shown in Figure 5.5 B). In the EDX spectrum of quantum dots, peaks related to Cu, Zn, Te and S from the thioglycolic acid is observed. The excess Ni is due to physical absorption of Nickel from environment during sample preparation. Furthermore, the size and the shape of the resultant MPS-TGA-CuZnTe core-shell were obtained using TEM between a scale of 10 and 20 nm. The TEM image Figure 5.6 A) suggests that the measured size of the particles have an average size of 17 nm. The particles were of spherical shape but with the image is not in good condition. The size measured by TEM analysis was higher than the TGA-CuZnTe core-shell which corresponds with SAXSpace finds, this is due to the addition of silica to thicken the shell of the quantum dots. In the EDX spectrum of MPS-TGA-CuZnTe core-shell quantum dots, peaks related to Cu, Zn, Te, S and Si from the MPS is observed. A diameter of about 18-20 nm was obtained for the quantum dots as observed in Figure 5.7 A) with an existence of lattice fringes indicating that TEOS-MPS-TGA-CuZnTe core-shell quantum dots exhibited a crystalline structure (Han *et al.*, 2017). As shown in this Figure, there are some dark layers covering the nanoparticles due to excess capping agent on the surface of the quantum dots. The CuZnTe core-shell QDs could be uniformly coated on the surface of silica nanospheres. Such good dispersity of CuZnTe core-shell QDs on silica surface could effectively prevent themselves from agglutination, a problem that commonly occurs when employing ultra-small nanoparticles as the signal labels (Lu *et al.*, 2019). We attribute this stability to the effective silanization procedure, which modified the QD surface while retaining its morphological pattern (Adegoke *et al.,* 2016). The quantum dots do not agglomerate as seen in the *Figure 5.3,* these results are in correlation with the SAXS results.

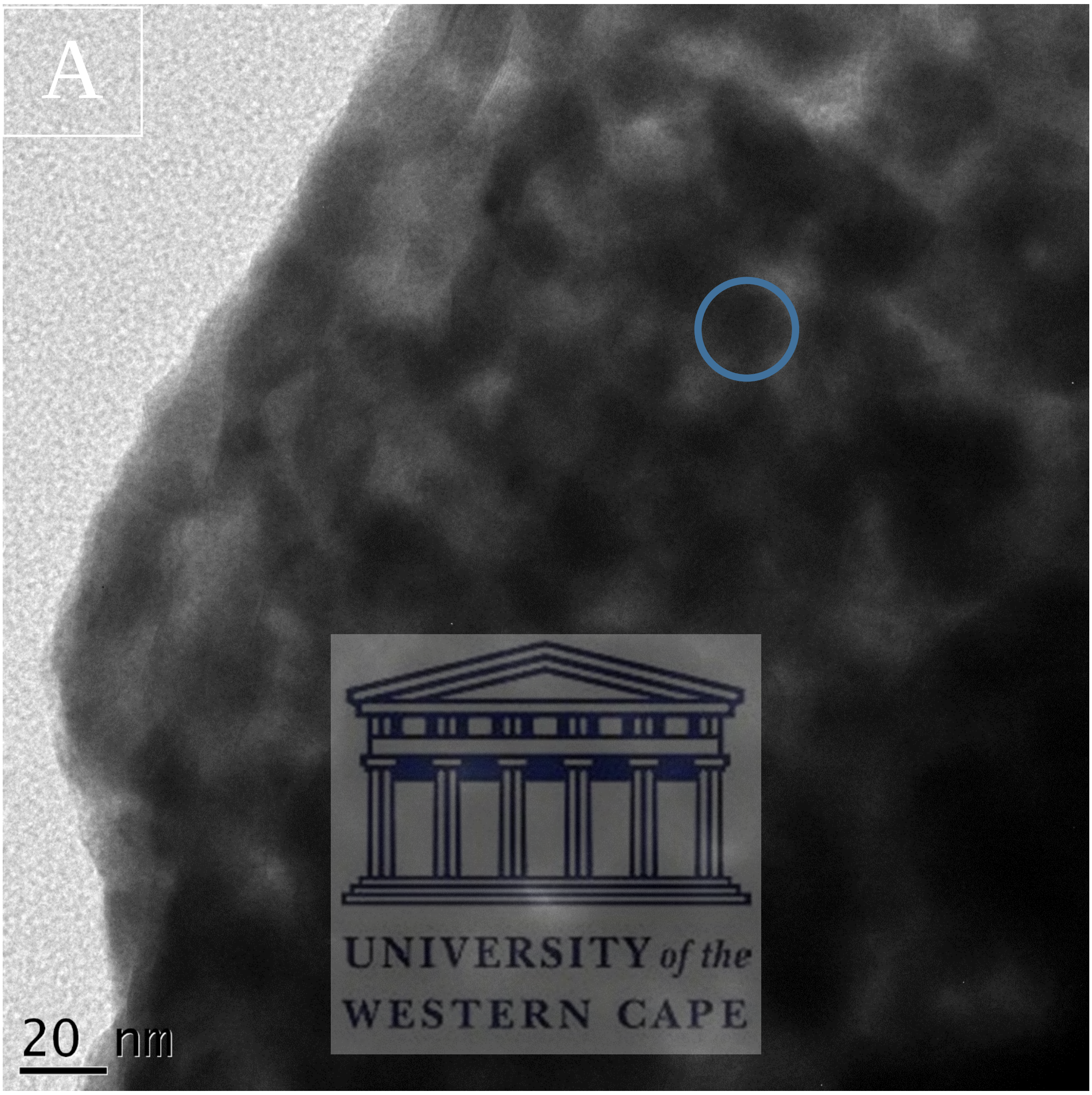
A
20 nm

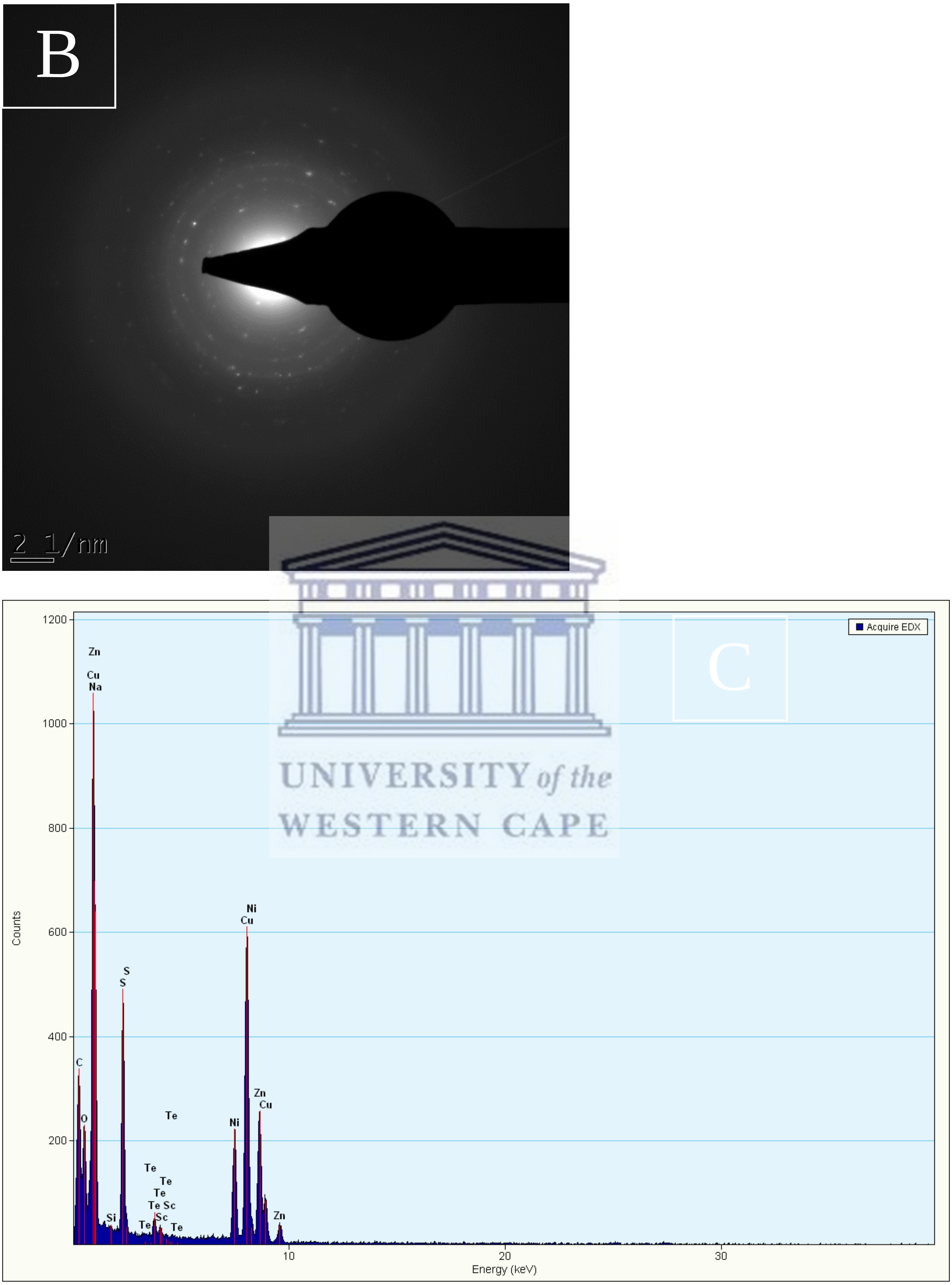

Figure 5.5: A) The TEM image, B) the SAED image and C) the Energy Dispersive X-ray (EDX) spectrum of TGA-CuZnTe core-shell.

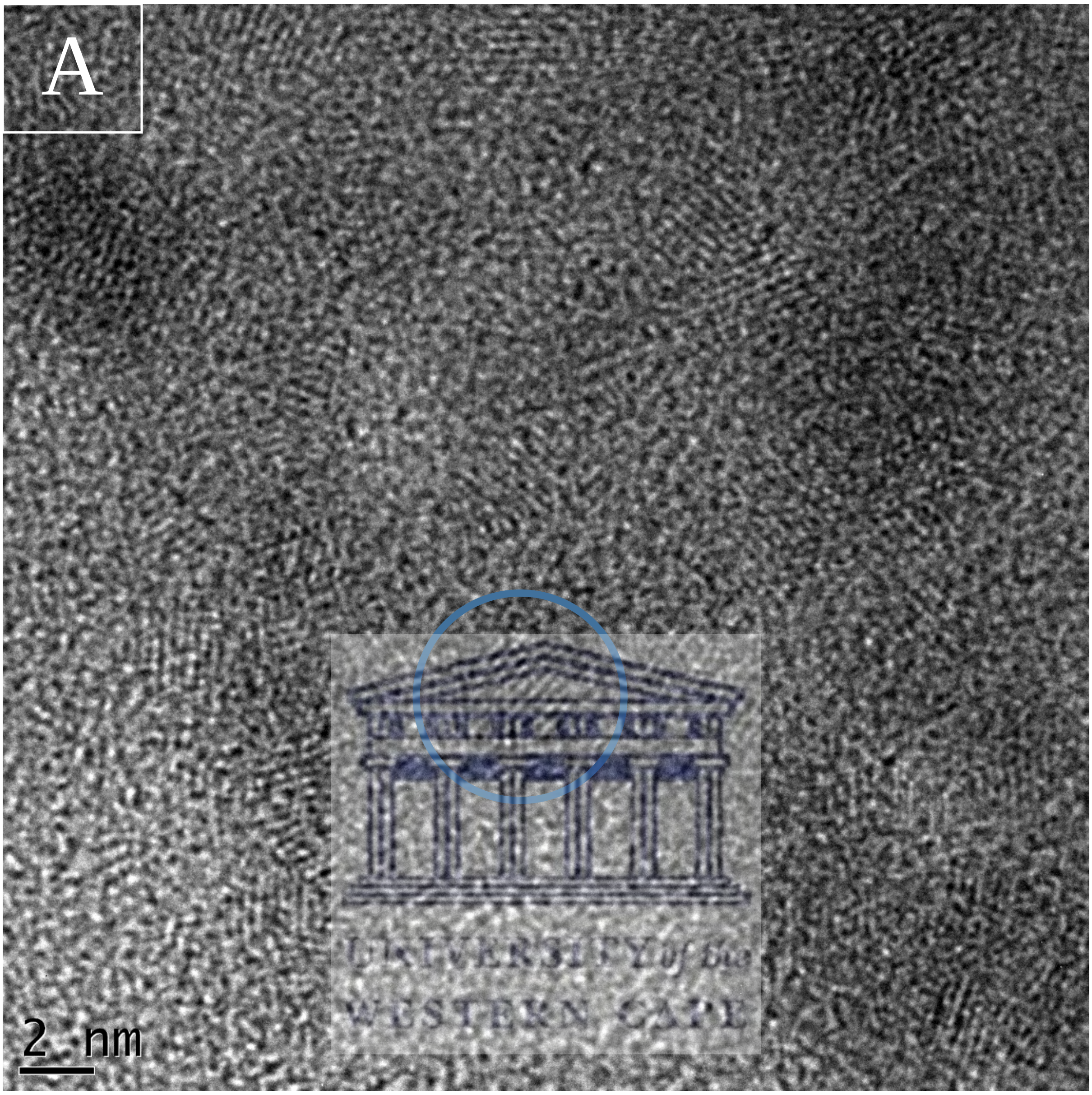
A
2 nm

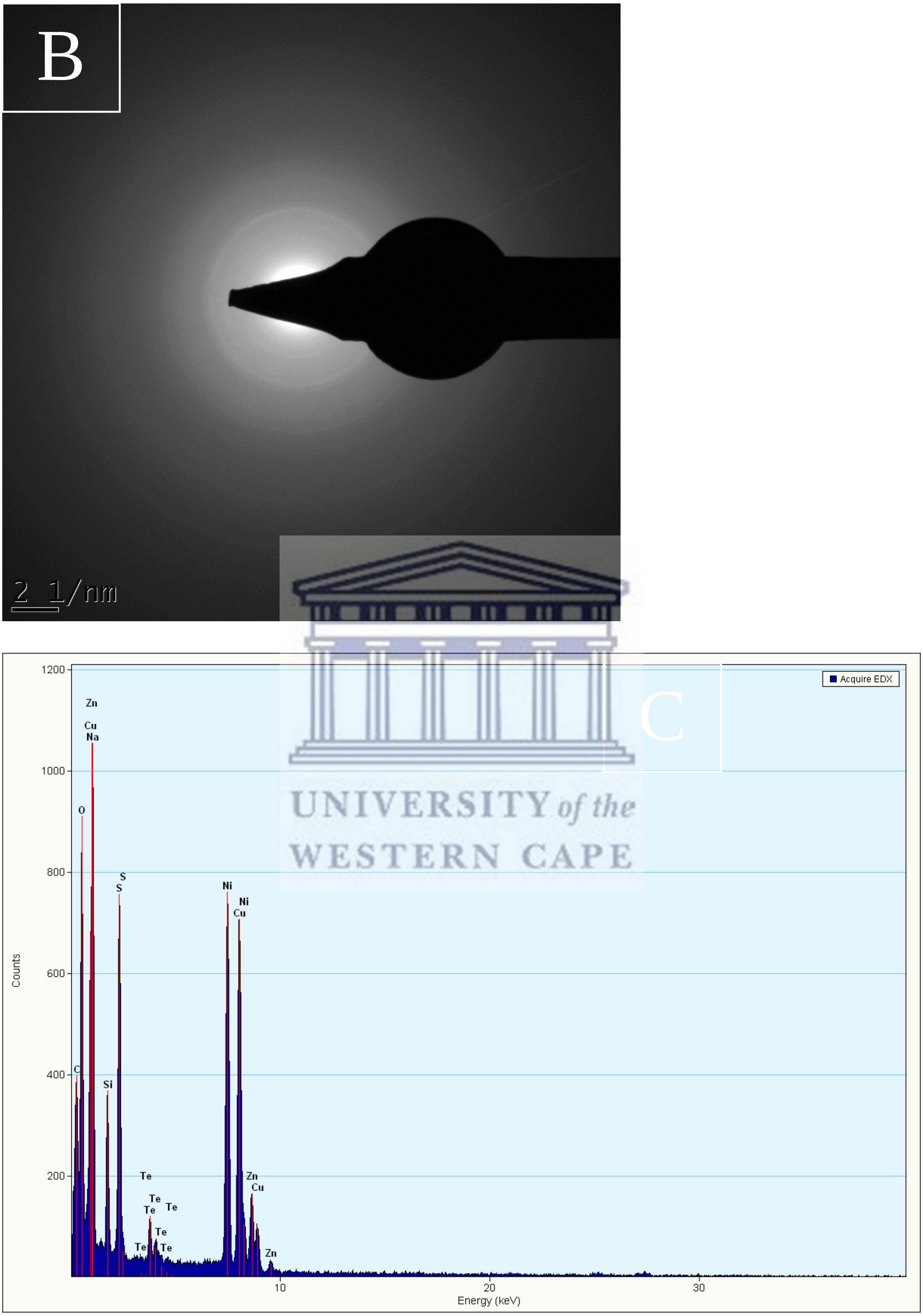

Figure 5.6: A) The TEM image, B) the SAED image and C) the Energy Dispersive X-ray (EDX) spectrum of MPS-TGA-CuZnTe core-shell.

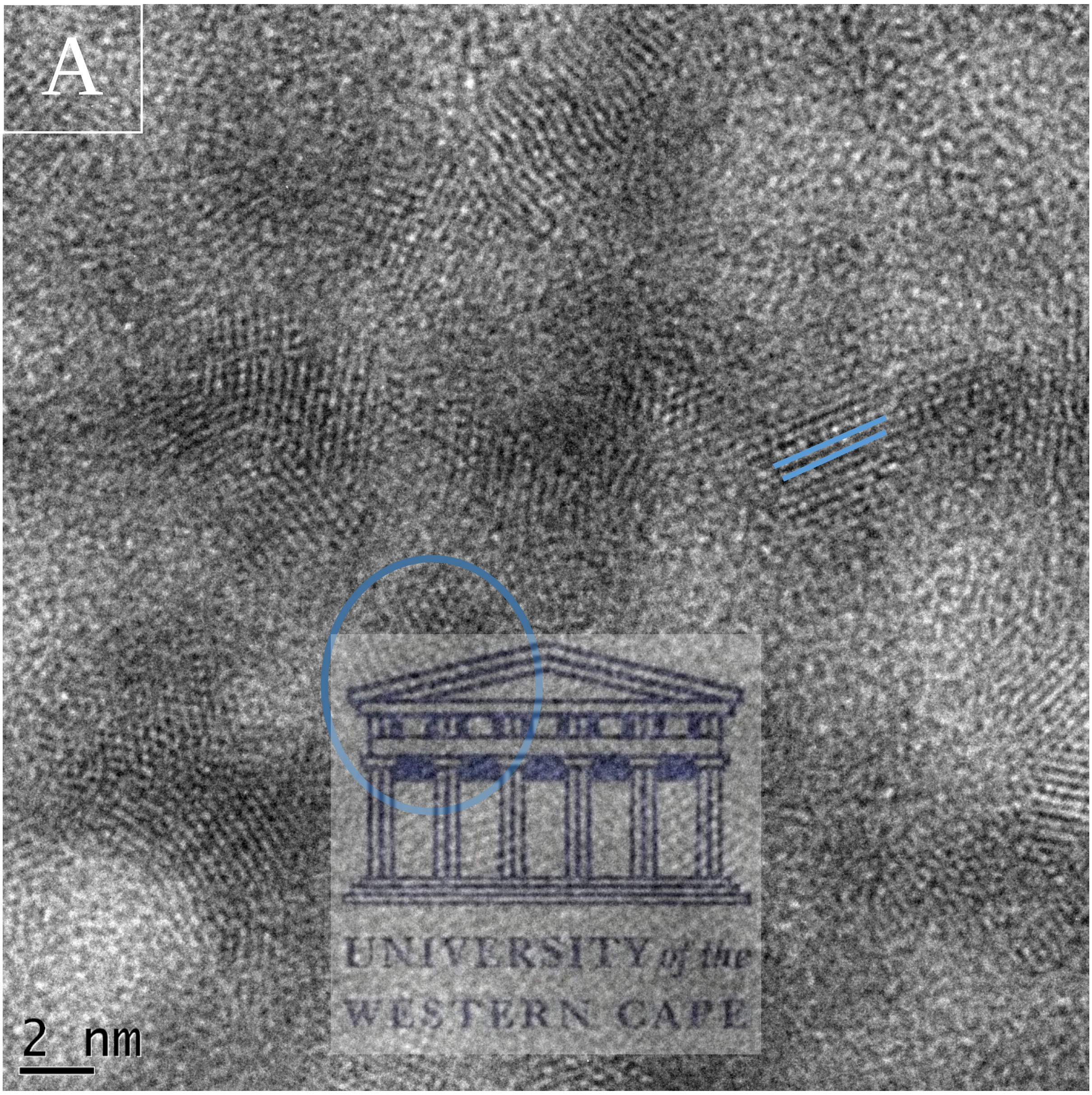
A
2 nm

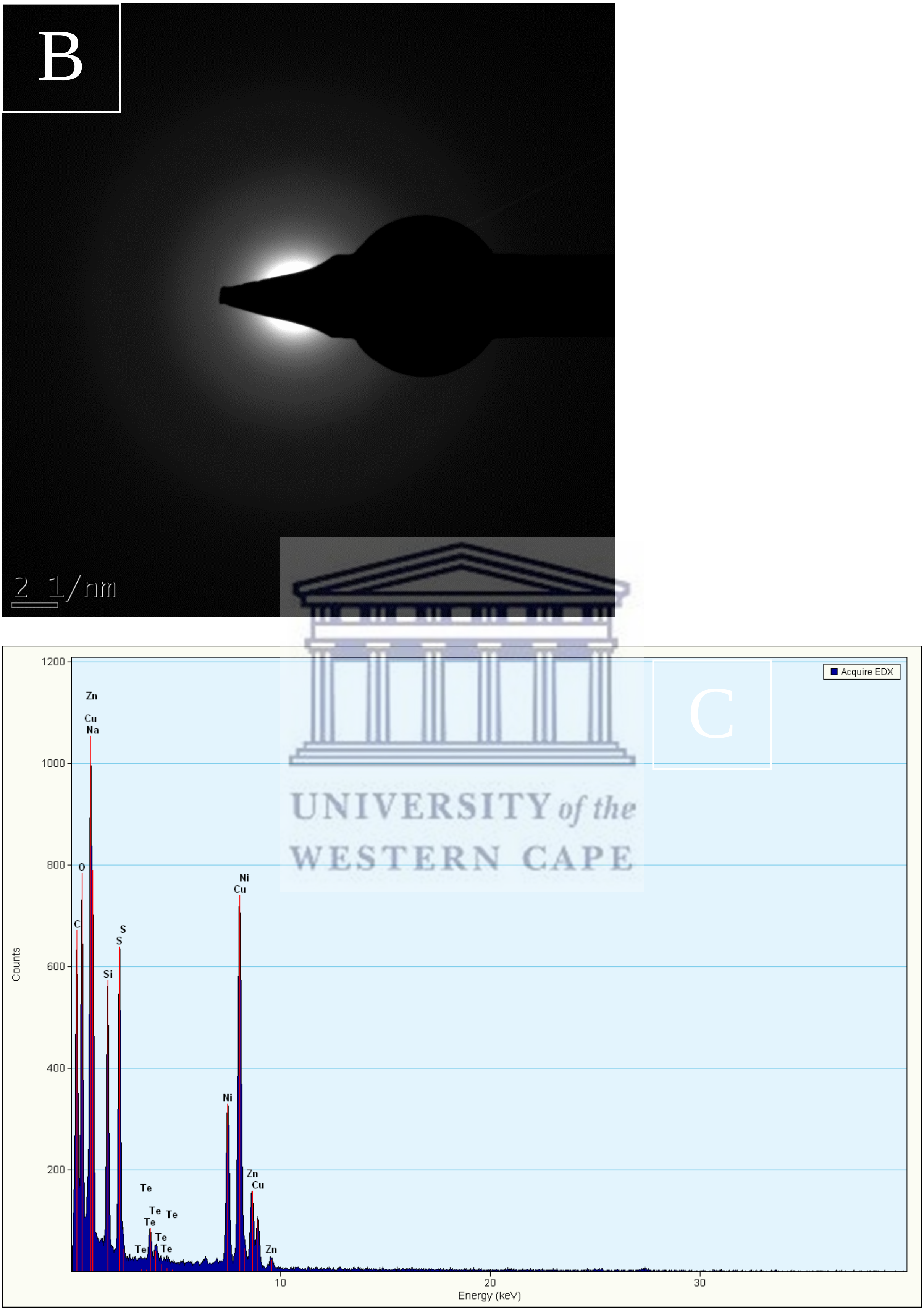

Figure 5.7: A) The TEM image, B) the SAED image and C) the Energy Dispersive X-ray (EDX) spectrum of TEOS-MPS-TGA-CuZnTe core-shell.

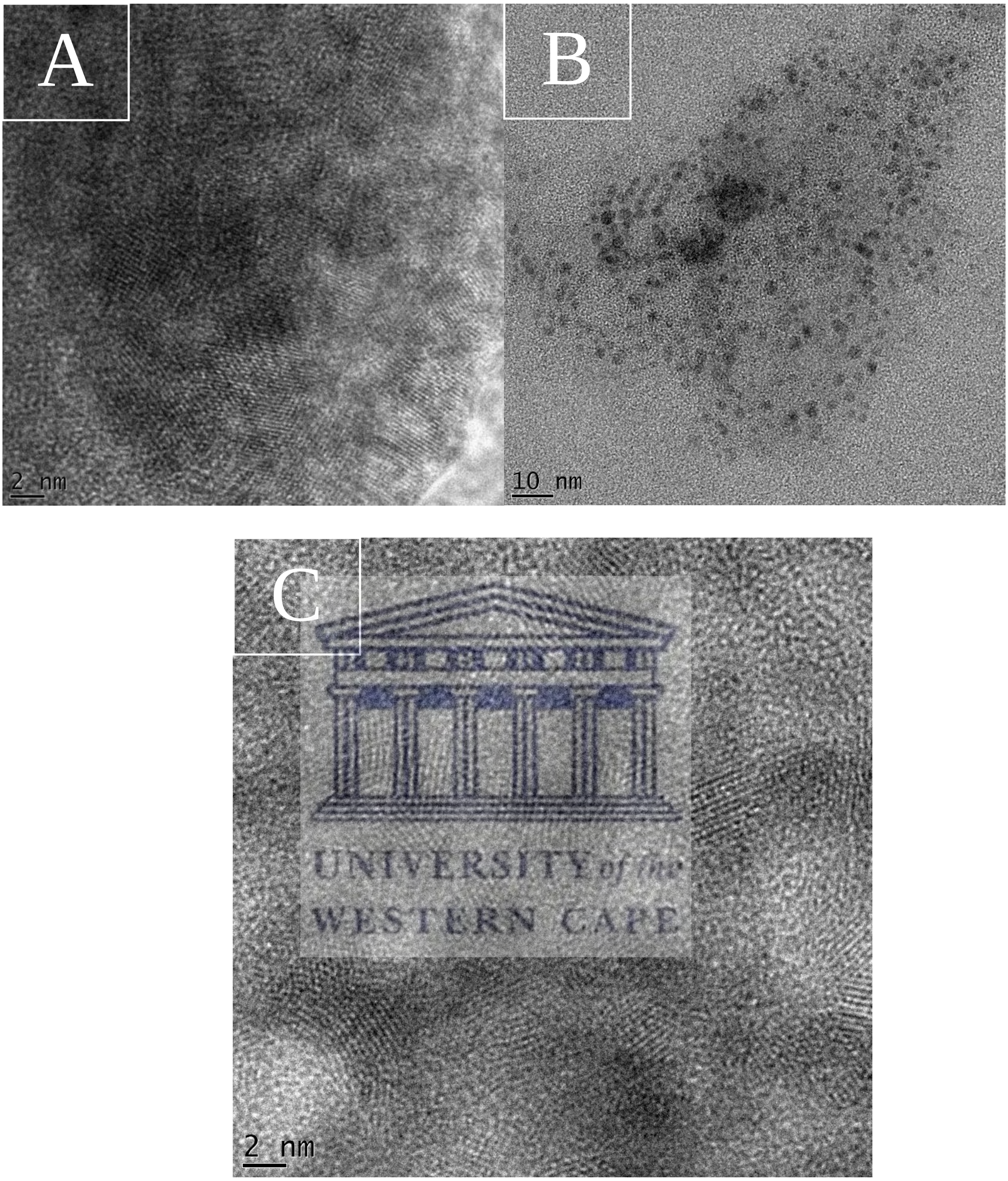

Figure 5.8: HRTEM micrographs of ***A)*** *TEOS-CuTe,* ***B)*** *TEOS-ZnTe and* ***C)*** *TEOS-CuZnTe core-shell.*

The TEM images of TEOS-CuTe, TEOS-ZnTe and TEOS-CuZnTe core-shell are shown in the figure above. Non- aggregated quantum dots with average size of 9.30 nm 6.80 nm and 5.30 for TEOS-CuZnTe core-shell, TEOS-ZnTe and TEOS-CuTe respectively were observed. The non-agglomeration of the quantum dots is a clear indication of successful capping by TEOS keeps the quantum dots apart. This retention of the capping agent is in agreement with the FTIR results which showed vibrations characteristic to functional groups in the capping reagent TEOS. Lattice fridges depicting high crystalline of the materials are also evident in the images.

5.3.4 Raman

Raman line shape: first-order and high-order Raman scattering. The Raman spectra of TGA-CuZnTe core-shell, MPS-TGA-CuZnTe core-shell and TEOS-MPS-TGA-CuZnTe core-shell with different shell thickness are presented in *Figure 5.8*. As shown in the Figure below the frequency 348 cm^{-1}, 483 cm^{-1} the first number stands for the experimentally measured frequency and the second one is the corresponding theoretical one, which is the vibration of the S-C_1 and the $C_1 – C_3$ stretches. The theoretical counterpart suggests that the frequency 483 cm^{-1} comes from the $HSCH_2COOH$ (Zhou, Williams and Wu, 2010). The frequency 1463 cm^{-1}, is due to the vibration of the COOH of the capping reagent TGA. The mode 1539 cm^{-1}, can be assigned to this COO− stretch in the SCH_2COO^-, which indicates that after the dissociation of the mercapto hydrogen atom and the deprotonation of the carboxylic acid group, some original $HSCH_2COOH$ molecules on the surface have turned into the SCH_2COO^- molecules (Zhou, Williams and Wu, 2010). The outstanding peak in the Raman spectrum of TGA-CuZnTe core-shell is attributed to the scattering of CuZnTe core-shell longitudinal optic phonons; the peak at 2487.9 cm^{-1}. With the TGA-CuZnTe core-shell capped by MPS shell, the intensity of the peak at 501 cm^{-1} and 2487.9 cm^{-1} increases. Some of the small peaks in TGA-CuZnTe core-shell start to fade when the quantum dots are capped with MPS. As the shell thickness further increases, it remains at 2487.9 cm^{-1} for the CuZnTe core-shell. In addition of TEOS to the quantum dots, a new peak at 428 cm^{-1} was also observed at the TEOS-MPS-TGA-CuZnTe core-shell(Lu *et al.*, 2007). In addition, there are features in Raman spectrum arises from Si substrate. These consist of abroad peak at 340 cm^{-1} due to stretching modes of Si - Si bonds and a sharp peak at 520 cm^{-1} due to the Si substrate (Musa, Qamhieh and Said, 2019). The shift is also due to the increase of the quantum dots when silica is being added (Eleanor Adachi1, Idemudia John Airuoyo2, Lakshmi Krishna2, 2016).

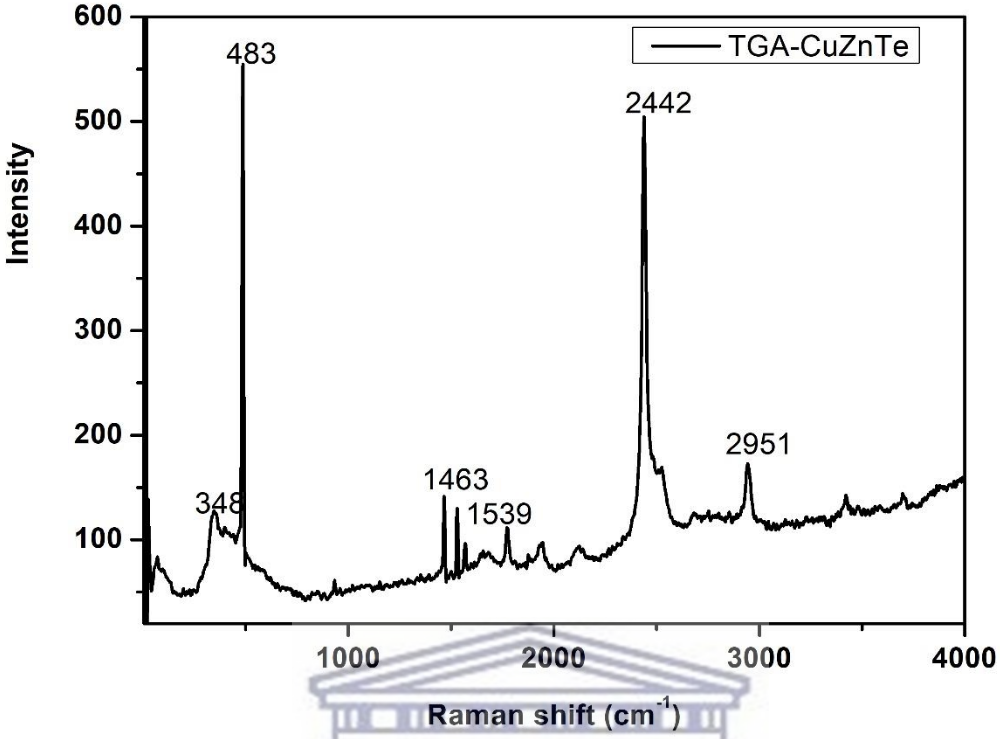
TGA-CuZnTe
483
2442
2951
1463
1539
348
Intensity
600
500
400
300
200
100
1000
2000
3000
4000
Raman shift (cm^{-1})

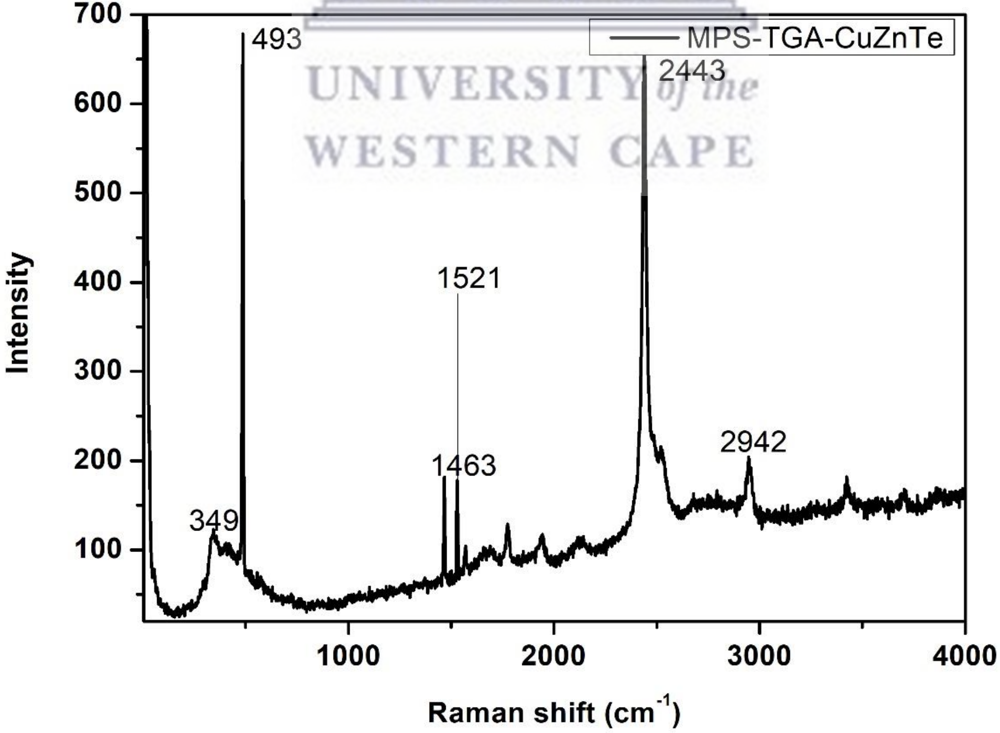
MPS-TGA-CuZnTe
493
2443
1521
1463
2942
349
Intensity
700
600
500
400
300
200
100
1000
2000
3000
4000
Raman shift (cm^{-1})

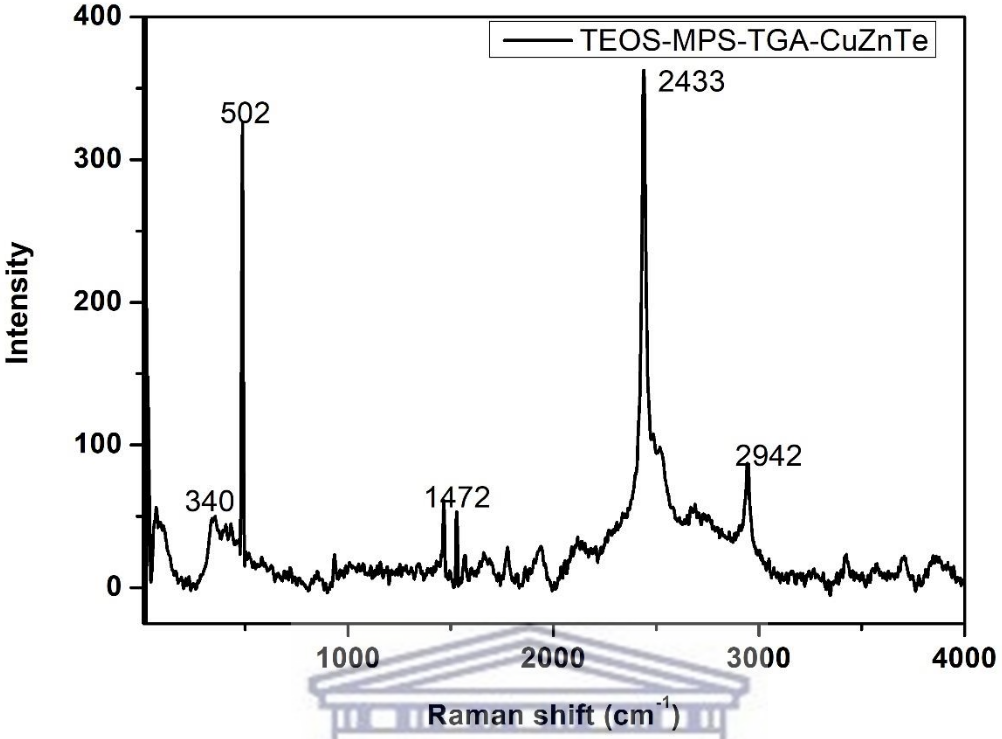

Figure 5.9: Raman spectra of development of synthesized quantum dots, TGA-CuZnTe core-shell, MPS-TGA-CuZnTe core-shell and TEOS-MPS-TGA-CuZnTe core-shell.

In *Figure 5.9,* is the comparison of the three quantum dots TEOS-CuTe, TEOS-ZnTe and TEOS-CuZnTe core-shell. In the Raman spectra of TEOS-CuTe as shown, with peaks at 867 cm^{-1}, 986 cm^{-1}, 1373 cm^{-1} and 2441 cm^{-1}. The peak at 867 cm^{-1} is attributed to C-C vibrations, the peak at 986 cm^{-1} may be due to Si-O-Si and the peak at 1373 cm^{-1} is attributed to CH_3. As indicated the strong vibration peak at 2433 cm^{-1} is assigned to S-H vibration band (Eleanor Adachi1, Idemudia John Airuoyo2, Lakshmi Krishna2, 2016). In the spectra of TEOS-MPS-TGA-CuZnTe core-shell a peak at 340 cm^{-1} was also observed and it arises from Si substrate at the (Lu *et al.*, 2007). These consist of a sharp peak at 502 cm^{-1} due to the Si-O-Si (Musa, Qamhieh and Said, 2019).

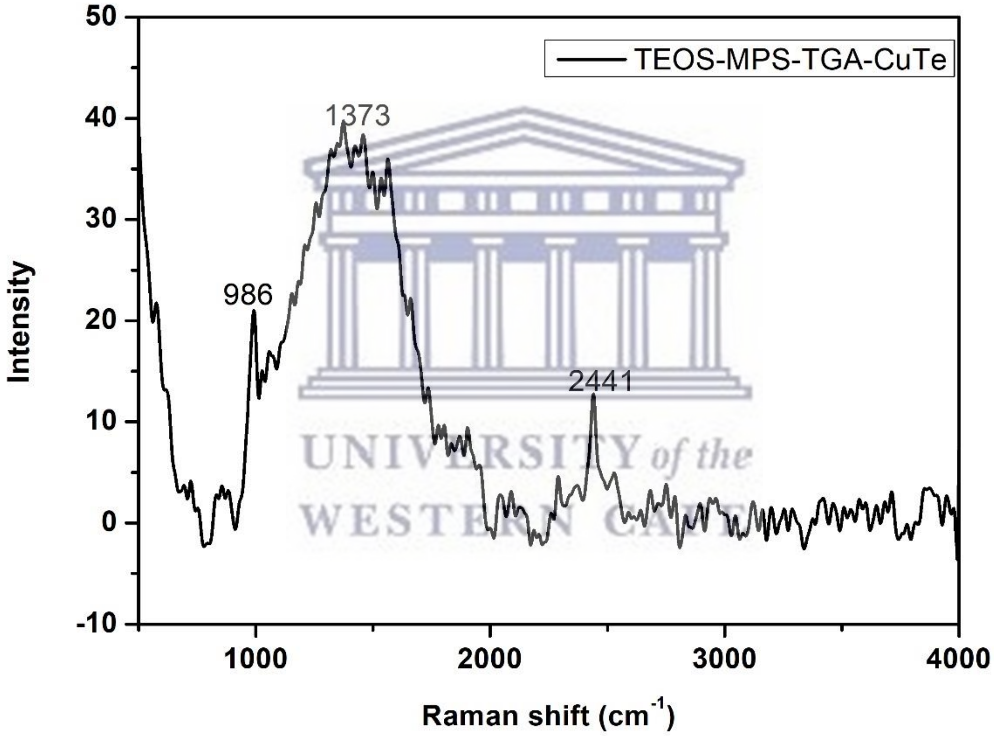

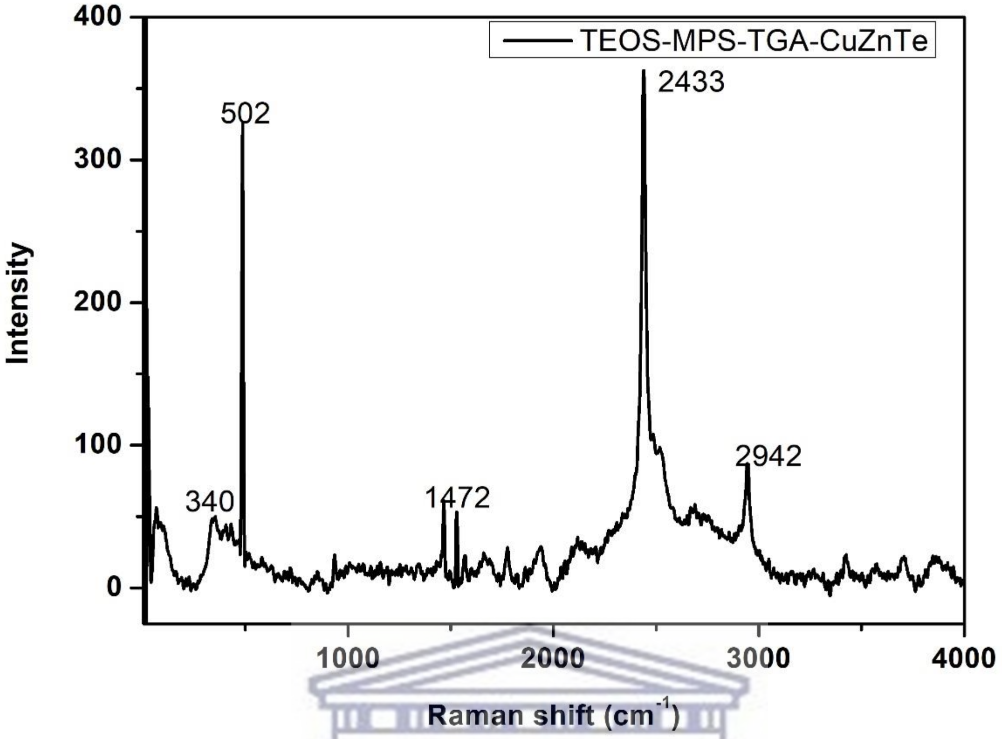

Figure 5.10: Raman spectra of development of synthesized quantum dots, TEOS-CuTe and TEOS-CuZnTe core-shell.

5.3.5 FTIR

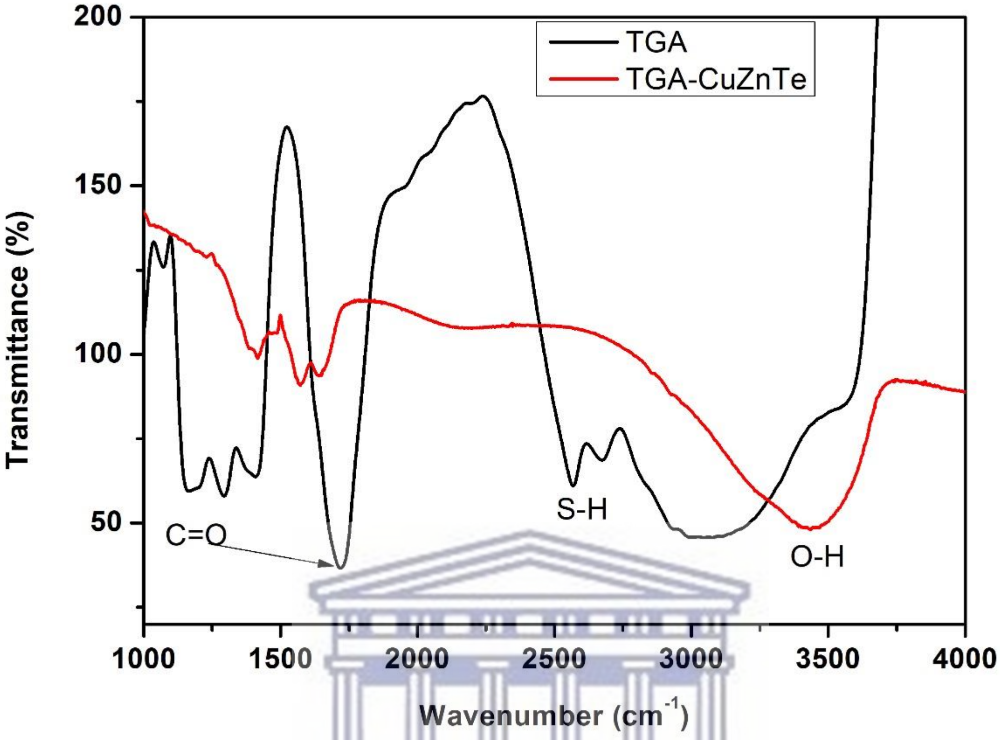

Figure 5.11: The FTIR spectrum showing the effect of capping reagents on the structure of quantum dots TGA-CuZnTe core-shell.

In chapter 3 and chapter 4, each capping reagent was explained in full detail. *Figure 5.9*, shows the FTIR spectra of TGA-CuZnTe core-shell, MPS-TGA-CuZnTe core-shell, and TEOS-MPS-TGA-CuZnTe core-shell, respectively. From the FTIR spectrum of TGA-CuZnTe core-shell and MPS-TGA-CuZnTe core-shell, a broad and intensive peak appeared at 3480 cm^{-1} was assigned to O–H stretching band, which might originate from water molecules adsorbed inside the quantum dots. Besides, peaks at 1385, 1726, and 2985 cm^{-1} were corresponded to C-H, C–H, and C=O vibration frequency, respectively. The FTIR spectrum of CuZnTe core-shell showed that the intensities of peaks corresponding to various functional groups were largely decreased, demonstrating that CuZnTe core-shell was successfully reduced. With the addition of silica to the quantum dots the Si-O-Si peak became broad indicating the thickening of the shell.

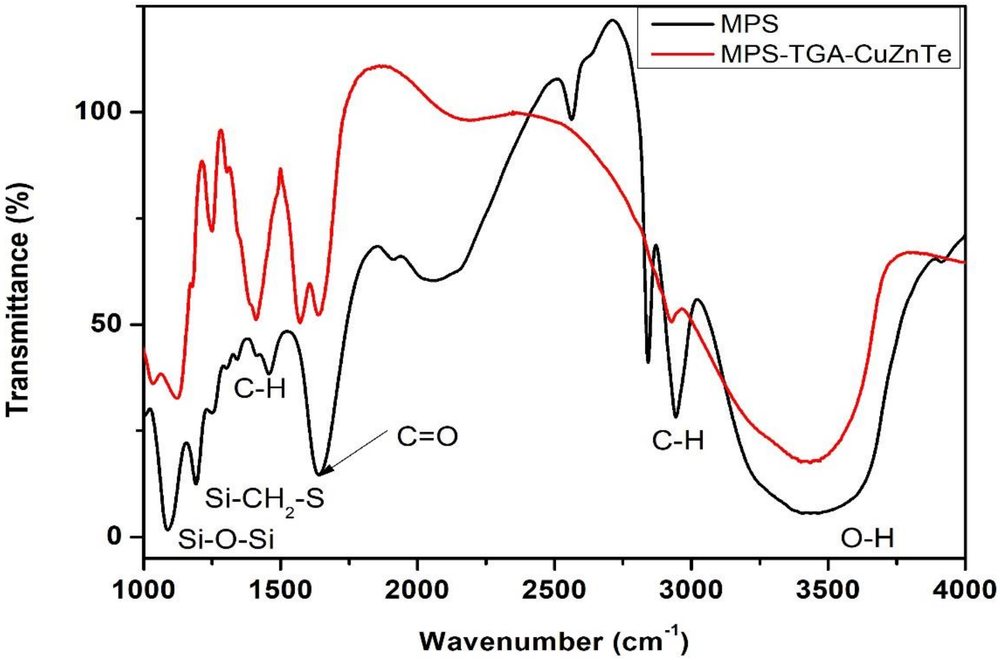

Figure 5.12: The FTIR spectrum showing the effect of capping reagents on the structure of quantum dots MPS-TGA-CuZnTe core-shell.

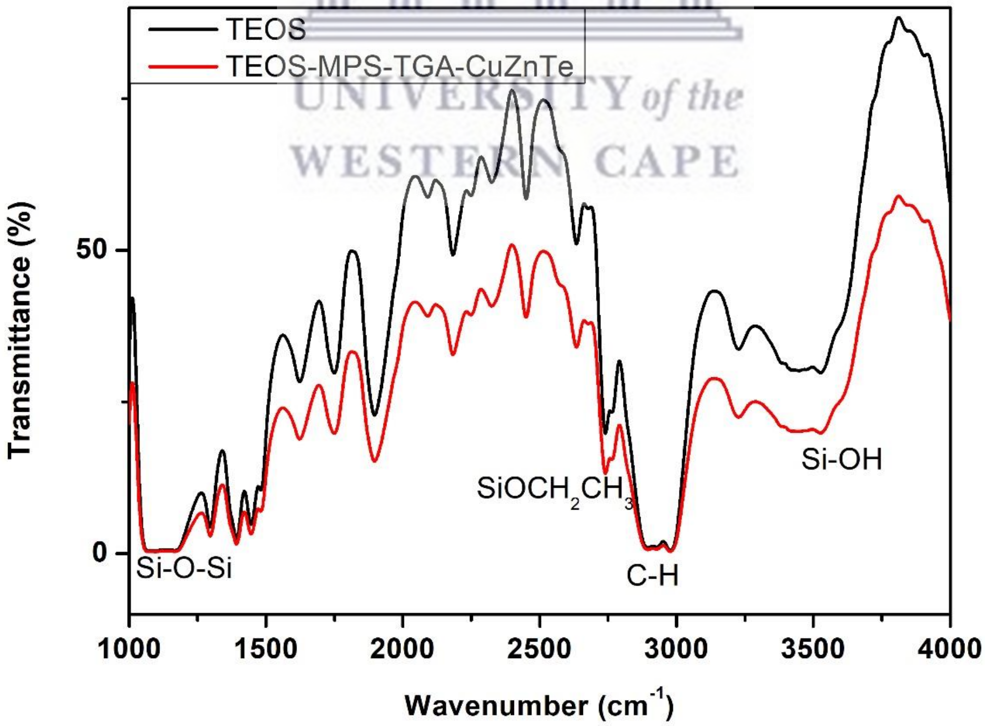

Figure 5.13: The FTIR spectrum showing the effect of capping reagents on the structure of quantum dots TEOS-MPS-TGA-CuZnTe core-shell.

The FTIR spectra of TEOS-CuTe, TEOS-ZnTe and TEOS-CuZnTe core-shell quantum dots in the region 1000 cm^{-1} to 4000 cm^{-1} are shown in the figure below. All the three quantum dots show bands in the region 1365 cm-1 to 1475cm^{-1}. These bands arise from the rock and scissor type bending vibrations of Si-O-Si groups from the Silica. The absorption bands between 2974 cm^{-1} have been assigned to the asymmetric stretching vibrations of the C-H bonds of the residual ethoxy moieties from TEOS (Tang *et al.*, 2017). There was a shift of the spectrum of TEOS-MPS-TGA-CuTe all the molecules shifted this indicates the addition of TEOS on the surface of the quantum dots. The results found in FTIR are in correlation with the results found in Raman, each capping reagent showed their compounds in both techniques.

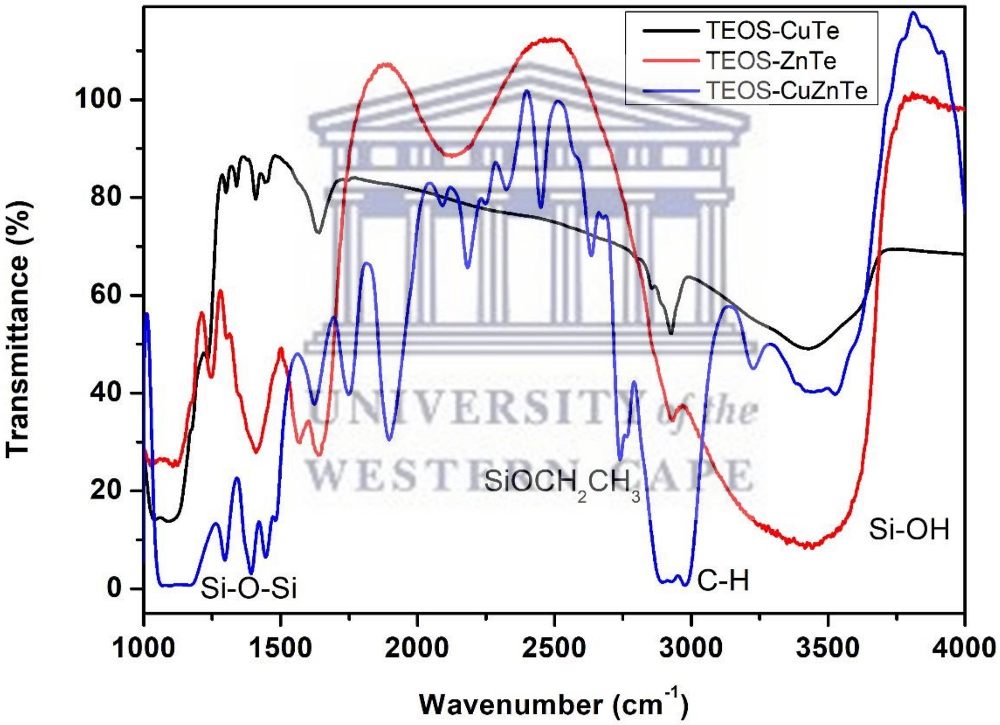

Figure 5.14: The FTIR spectrum showing different quantum dots, TGA-CuZnTe core-shell (black-line), MPS-TGA-CuZnTe core-shell (red-line) and TEOS-MPS-TGA-CuZnTe core-shell (blue-line).

5.3.6 Electrochemistry

The surface electrochemical properties of the CuZnTe core-shell quantum dots were evaluated directly onto the gold electrode surfaces. The surface concentration and dynamic kinetic properties of the quantum dots were evaluated using static cyclic and square-wave voltammetry techniques. In cyclic voltammetry (CV), a static 0.1 M phosphate buffer solution of pH 7.4 was used as the supporting electrolyte. *Figure 5.10 – 5.20,* presents the cyclic voltammetry profiles of CuZnTe core-shell quantum dot Coated on the surface of gold electrode, with a fixed potential window between 1200 mV to -1200 mV, and scan rates of 50 mV/s.

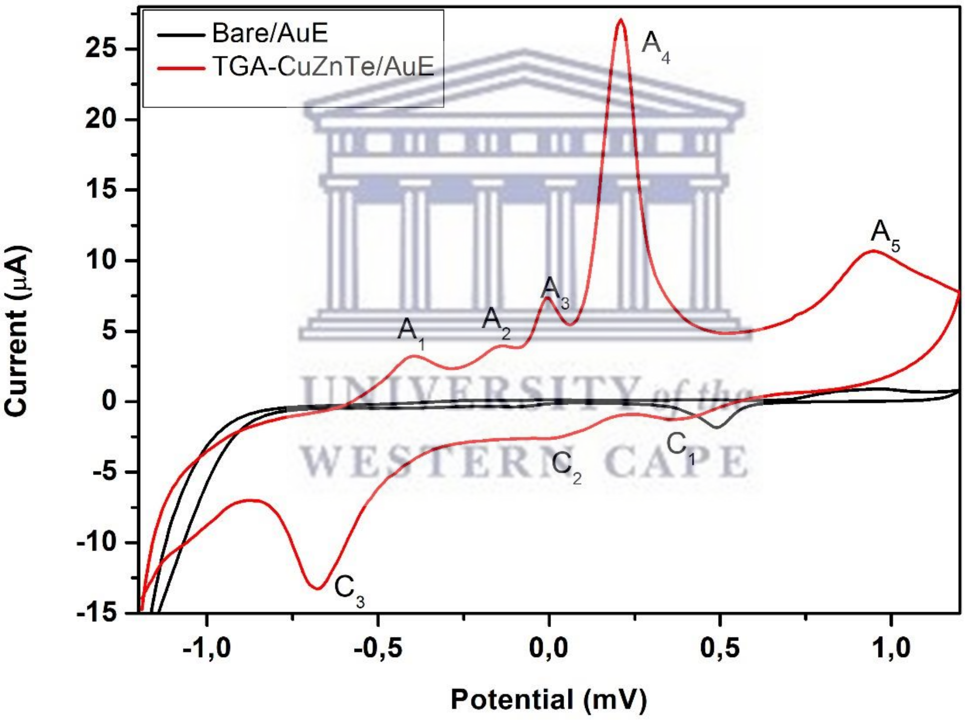

Figure 5.10: Cyclic voltammogram of bare AuE and AuE/TGA-CuZnTe core-shell QDs in 0.1M PBS, pH 7.4 at 50 mV/s.

The cyclic voltammetry of TGA-CuZnTe core-shell quantum dot solution on gold electrode was studied at a potential range of -1200 to +1200 mV and the results are shown in the figure above. Three anodic peaks are observed C_1, C_2 and C_3. In the reverse scan, five cathodic peak occurs A_1, A2, A_3, A_4, and A_5. Peaks A_5 and C_1 are peaks that are from the gold electrode as it is seen from the bare Au, the peak A_5 shifted significantly to more positive potentials while peak C_1 shifted to more negative potentials. This is an indication that the reactions responsible for these peaks are irreversible and points to an electrochemical decomposition of the TGA-CuZnTe core-shell quantum dots. The peak at C_3 is due to the reduction of Te^0 to Te^{2-}. The anodic peak A_1 at approximately −0.402 V represents the oxidation of elemental Zn (Ishizaki *et al.*, 2005). The peak A_2 at -00142 V is attributed to tellurium (Te^{2+}) and the reduction peak associated with reduction of Te^0 to Te^{2+} appeared at -0.677 V (Khene *et al.*, 2011). The peak A_3 is due to the oxidation of Te^{2+} to Te^{4+} (Ndangili, 2011). The redox couple (C_2/A_4) is attributed to the reaction of Cu(I) + e^- ↔ Cu (Xingli Zou, 2017).

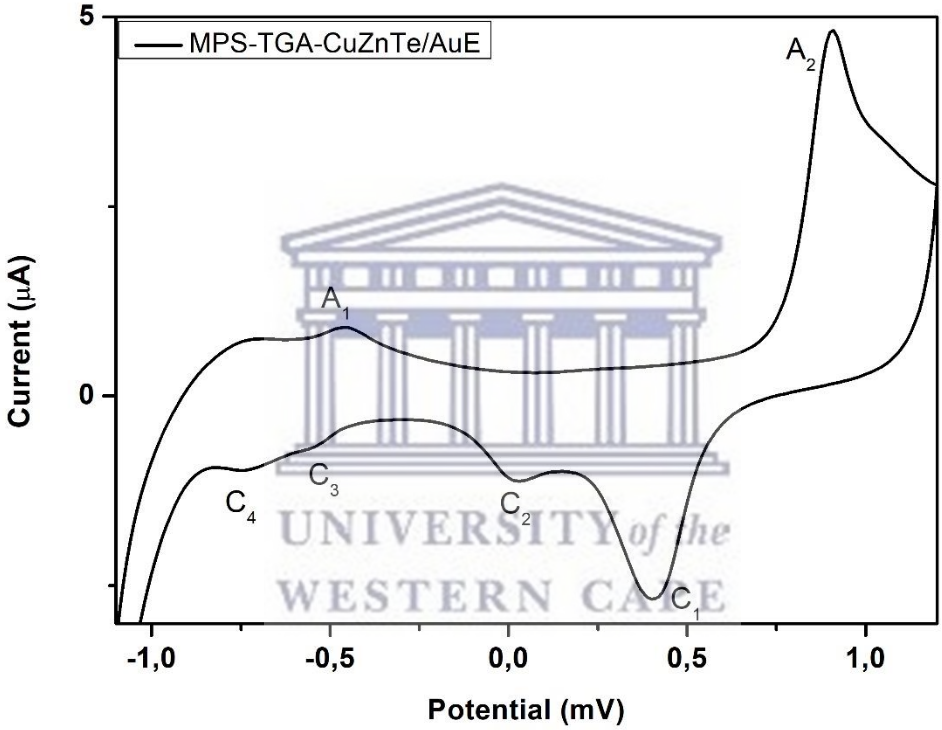

Figure 5.11: Cyclic voltammogram of AuE/MPS-TGA-CuZnTe core-shell QDs in 0.1M PBS, pH 7.4 at 50 mV/s.

Cyclic voltammetry is a simple and easy mean to show the changes of electrode behaviour after each assembly step, because the electron transfers between the solution species and the electrode must occur by tunnelling through either the barrier or the defects in the barrier voltammograms (CVs) of differently modified electrodes in PB solution. In *Figure 5.11*, a capping reagent MPS was added to the quantum dots for a silica core-shell and the behaviour was characterized using cyclic voltammetry. When MPS is formed on electrode, one can notice an obvious decrease in the cathodic and anodic peak currents. The reason is that the –SH of the MPS solution serving as binding site for the covalent attachment of MPS to electrode surface blocked electron transfer (Zhong *et al.*, 2005). It was observed that the was significant decrease in the current values, indicating that the electrode surface was blocked by a strong adsorption of the reagent and products of the oxidation reaction. Two anodic peaks were observed A_1 and A_2, A_1 is at approximately −0.402 V represents the oxidation of elemental Zn as mentioned above and A_2 is the gold peak. Form AuE/TGA-CuZnTe core-shell to AuE/MPS-TGA-CuZnTe core-shell there were peaks that disappeared. All the anodic peaks that were attibuted to Te on the AuE/TGA-CuZnTe core-shell disappeared, this is due to the silica that is being added to the quantum dots (Christine *et al.*, 2016). C_1 is a gold peak, C_2 is due to the oxidation of Copper and C_3 and C_4 are due to the reduction of Tellurium (Claude and Lyon, 2015). C_4 can also be due to the addition of MPS.

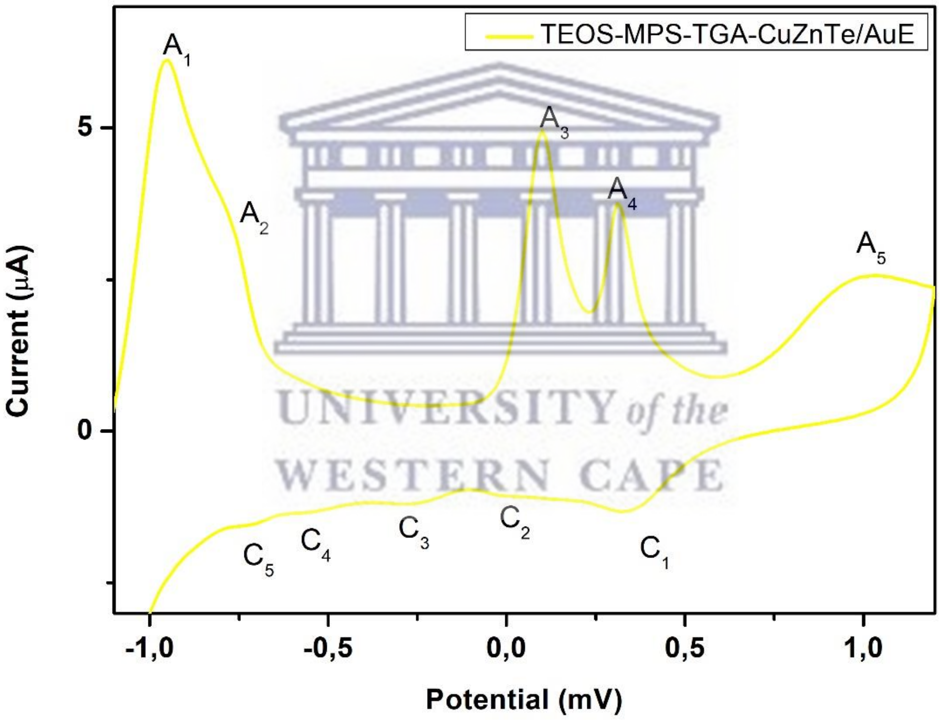

Figure 5.12: Cyclic voltammogram of AuE/TEOS-MPS-TGA-CuZnTe core-shell QDs in 0.1M PBS, pH 7.4 at 50 mV/s.

Figure 5.12 depicts cyclic voltammograms of TEOS-MPS-TGA-CuZnTe core-shell quantum dots immobilized onto the Au electrode and measured in 0.1 M PBS. On TEOS-MPS-TGA-CuZnTe core-shell new peaks were observed this may be due to the silica that is being added to shell of the quantum dots. With the TEOS addition, peaks that were present in TGA-CuZnTe core-shell are present now with the full silanization of the quantum dots. Five anodic peak were observed A_1, A_2, A_3, A_4 and A_5, A_1 is due to the addition of silica. A_2 is the oxidation of element

Zn as mention in *Figure 5.10*, the peak shifted to negative potential. The peak A_3 is due to the oxidation of Te^{2+} to Te^{4+} (Ndangili, 2011). The redox couple (C_2/A_4) is attributed to the reaction of Cu(I) + e^- ↔ Cu (Xingli Zou, 2017). A_5 and C_1 are anodic peak and cathodic peak of the gold electrode. Also five cathodic peaks were observed in *Figure 5.12*, C_2 is due to the oxidation of Copper where as C_3 is a new peak observed it may be due to the addition of TEOS. In all other cases the application of the coating improved the anodic behaviour of the samples (Sakai *et al.*, 2012). C_4 can also be due to the addition of MPS. C_4 and C_5 are due to the reduction of Tellurium (Claude and Lyon, 2015). The reduction peaks are seen to be shifting towards more positive potentials while the oxidation peaks are seen to be shifting to more negative potentials indicating an electron transfer and irreversible process.

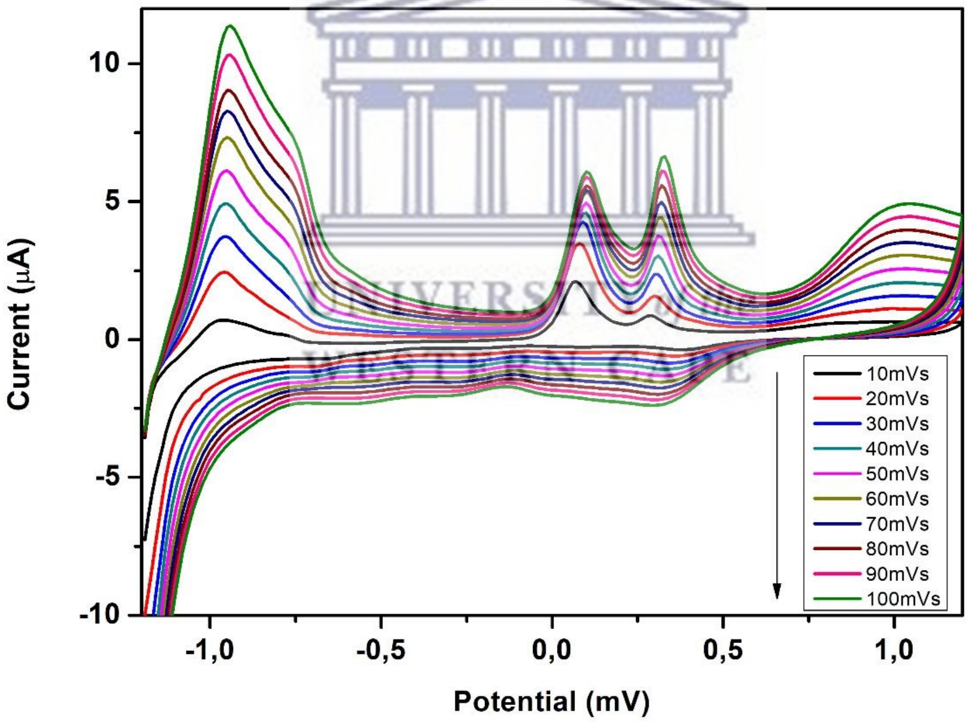

Figure 5.11: Multi-scan voltammograms of CuZnTe core-shell/AuE in 0.1 M PBS, pH 7.4 at 50 mV/s.

This was carried out to investigate electrochemistry of quantum dots in the potential window between -1.2 V to 1.2 V, scan rates of 10 mV/s to 100 mV/s. The quantum dots on to gold electrode was studied by cyclic voltammetry at different scan rates from 10-100 mV/s at a potential range from E = -1200 mV to E = 1200 mV in a traditional electrochemical setup consisting of Ag/AgCl as a reference electrode, Pt mesh wire as the counter electrode and a Gold electrode as the working electrode, dipped into PBS. *Figure 5.11* displays a multi-scan of the TEOS-MPS-TGA-CuZnTe core-shell QD and it can be seen that as the scan rate increases the anodic peaks shift to more positive potentials while the cathodic peaks shift to more negative potentials, this is an indication of slow electron transfer process and kinetic effects (Hossain and Norazmi, 2013).

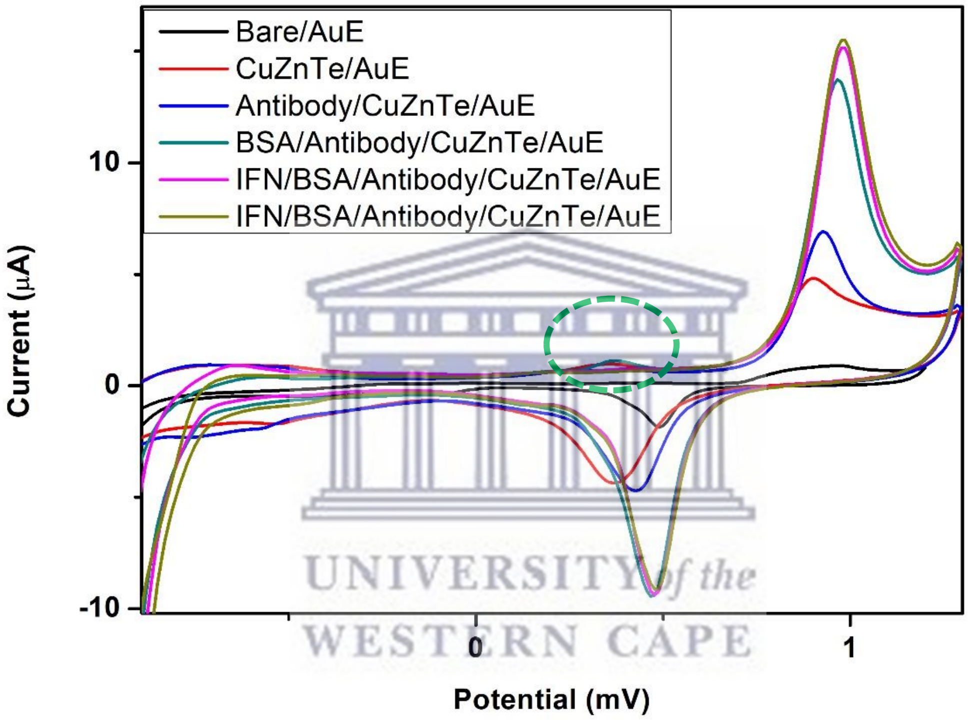

Figure 5.13: CV voltammogram of bare AuE, CuZnTe core-shell/AuE, antibody/CuZnTe core-shell/AuE, BSA/antibody/CuZnTe core-shell/AuE and IFN-γ/BSA/antibody/CuZnTe core-shell/AuE, respectively were carried out in 0.1 M PBS at pH 7.4.

Cyclic voltammetry is a simple and easy method to study the characteristics of the immunosensor at its different preparation phases. In *Figure 5.13* shows the cyclic voltammogram experiments of a bare gold electrode (AuE), CuZnTe core-shell/AuE, antibody/CuZnTe core-shell/AuE, BSA/antibody/CuZnTe core-shell/AuE and IFN-γ/BSA/antibody/CuZnTe core-shell/AuE, respectively were carried out in 0.1 M PBS (pH 7.4). Specifically, PBS solution (0.1 M, pH 7.0) was used as electrolyte, and 50 mV/s as scan rate. The degree of modification of the sensing interface was evaluated by monitoring changes in electrochemical features for a sensitive electrochemical readout. As shown in the figure above, a couple of reversible redox peaks appeared on the bare AuE, with PBS as the electrochemical probe, indicating the presence of a clean and activated AuE surface. After being modified by CuZnTe core-shell quantum dots, capable of promoting the electron transfer rate, the cyclic voltammetric (CV) signals revealed a great degree of current increase, indicating the covering of the AuE surface by CuZnTe core-shell QDs. It also indicated the excellent conductivity of AuE-CuZnTe core-shell QDs (Zhang *et al.*, 2015). When anti-human INF-γ antibody was attached to QDs on the surface of the sensor, the peak current of the sensor increased. This indicated successful deposition of anti-human INF-γ antibody on the electrode surface. Following that, the electrode was incubated in BSA solution, the peak current value showed a gradual increase which was attributed to that BSA occupied a large amounts of active sites on the surface of the Antibody/CuZnTe core-shell/AuE, forming major insulating BSA protein layers on the electrode to retard the electron transfer (Bhatia *et al.*, 1989; Simão *et al.*, 2016). Subsequently, it was found that the current response further decreased after the immunosensor was incubated in a solution with 2 ng/mL IFN-γ. This may originate from the insulating IFN-γ protein layers on the electrode that retards the electron transfer (Zhang *et al.*, 2015). To evaluate the feasibility of this electrochemical assay, the single-analyte sensing was firstly performed using DPV. As shown in *Figure 5.14*, the voltammogram (obtained from IFN-γ-BSA-Anti-CuZnTe core-shellQDs/Au) presents the well-shaped peak current at 275mV. After the treatment with different concentrations of IFN-γ, the decreased peak current was observed without its position change *Figure 5.15* (Xia *et al.*, 2015).

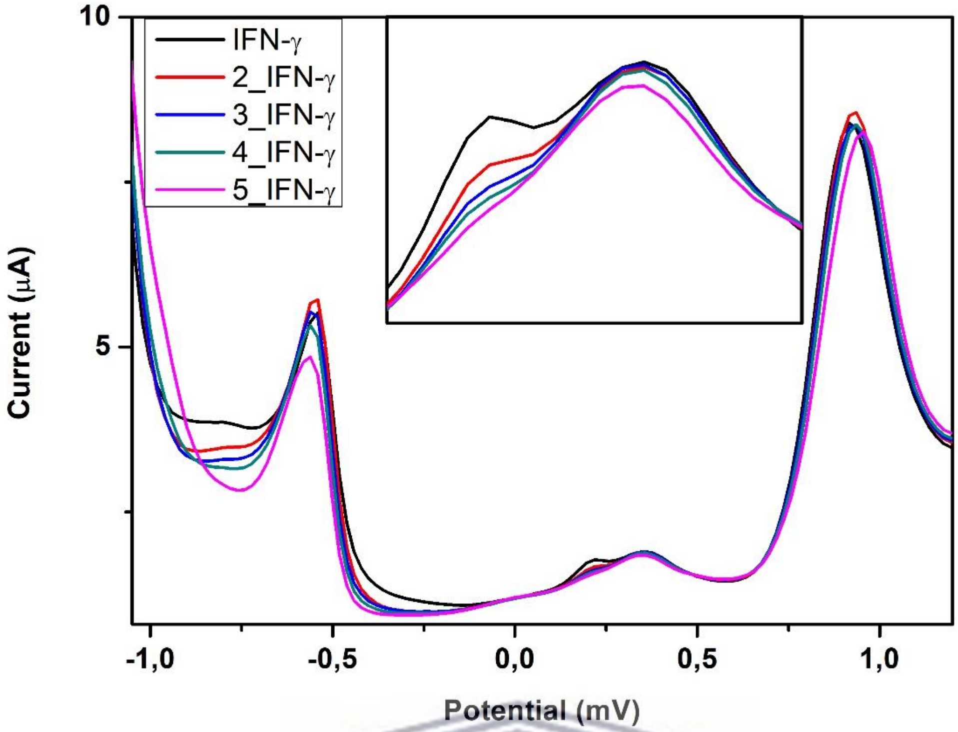

Figure 5.14: DPV after interactions with different concentrations of IFN-γ. Insets showed the corresponding DPV recorded of electrochemical immunoassay in 0.1 M, pH 7.0 PBS.

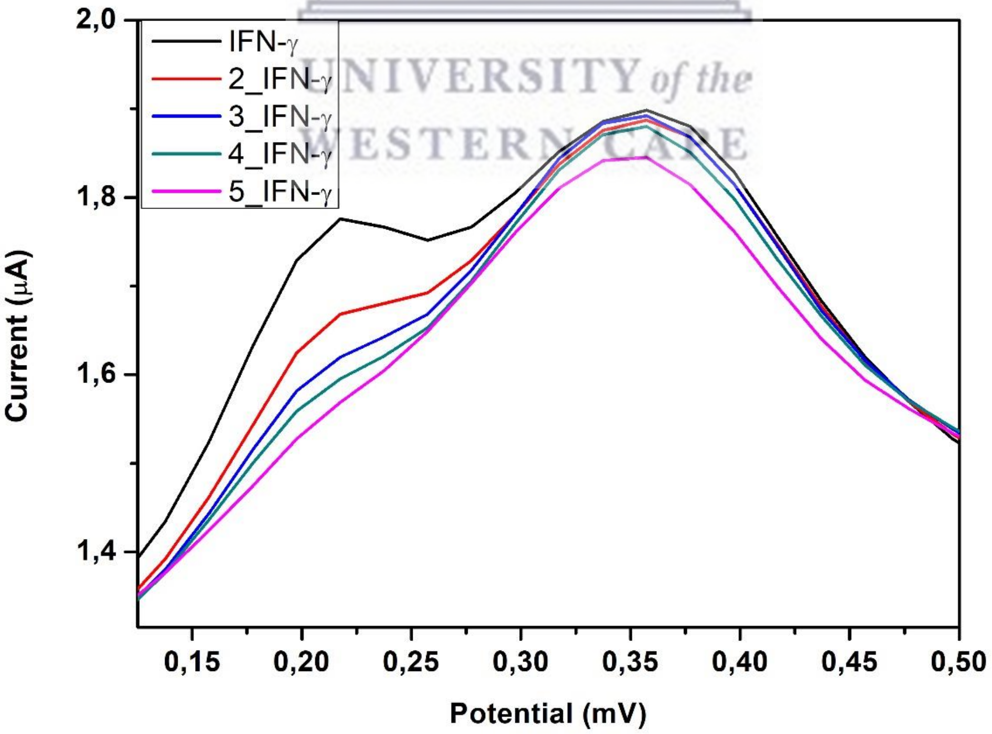

Figure 5.15: DPV after interactions with different concentrations of IFN-γ.

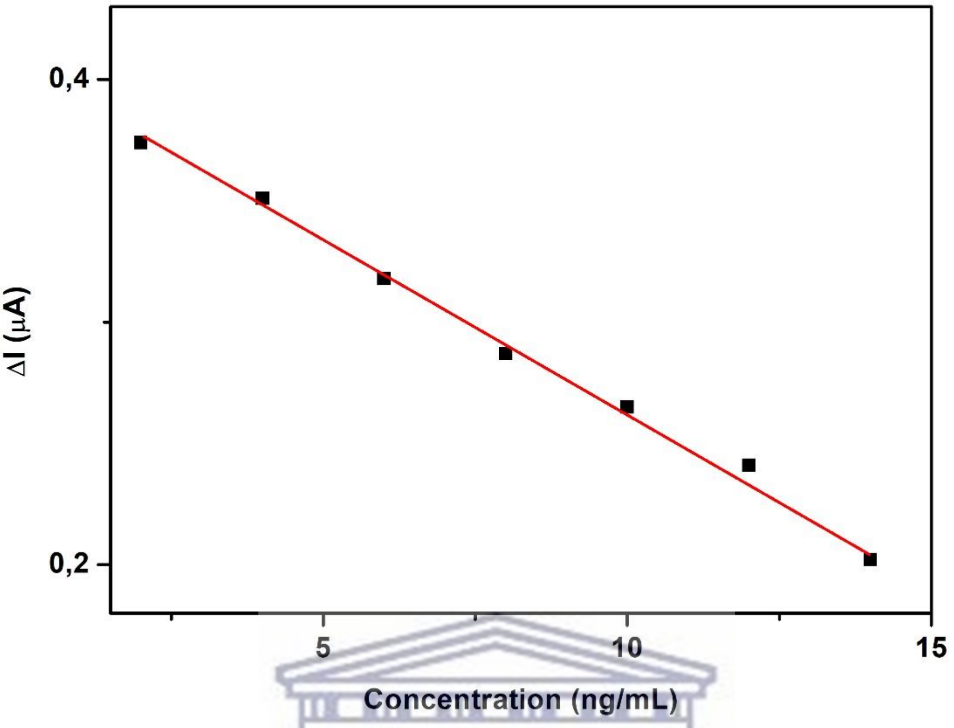

Figure 5.16: The calibration plot between the DPV peak current and the logarithm values of IFN-γ concentrations from 2 to 12 ng/ mL.

Figure 5.16, shows calibration plots obtained from the immunosensor with increasing concentrations of IFN-γ (2–12 ng/mL). Typically, IFN-γ was attached to the electrode surface through immunoreaction with anti-IFN-γ which was immobilized on the immunosensor previously. The insulating IFN-γ protein layer acting as a non-conductor obstructed the electron transfer between the electrolyte and electrode surface (Ding and Lu, 2018). Therefore, the DPV peak currents decreased proportionally with the increasing concentration of IFN-γ (*Figure 5.15*), which can be utilized as a quantitative measurement of IFN-γ concentration (Xia *et al.*, 2015; Zhang *et al.*, 2015). As shown in the figure above, the calibration plots show a good linear relationship between the peak current and the values of the analyte concentrations. The calibration plots of our study are 2– 12 ng/mL (*Figure 5.16*).

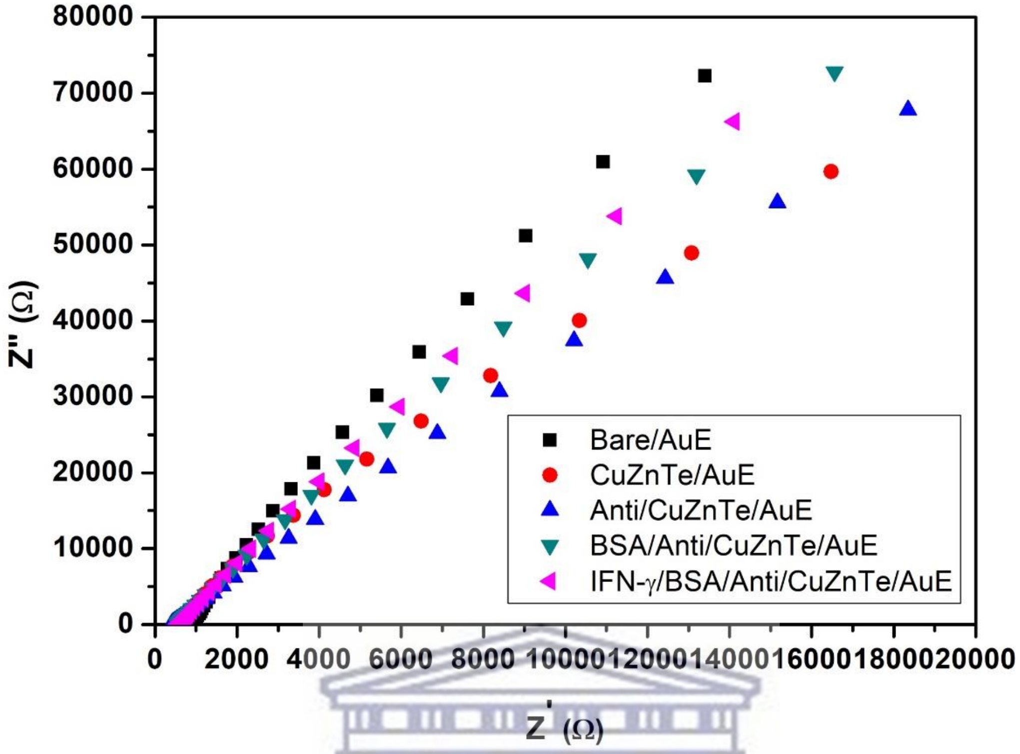

Figure 5.13: Nyquist plots obtained on AuE/Bare, CuZnTe core-shell/AuE, Antibody/CuZnTe core-shell/AuE, BSA Antibody/CuZnTe core-shell/AuE and IFN-γ/BSA/Antibody/CuZnTe core-shell/AuE.

Electrochemical impedance spectroscopy (EIS) is an effective technique to monitor the electrode surface features. The impedance spectra include a semi-circular portion and a linear portion, the semi-circular portion at higher frequencies corresponds to the electron-transfer-limited process, and the linear part at lower frequencies corresponds to the diffusion process. The semicircle diameters correspond to the electron-transfer resistance (Grossi and Riccò, 2017). In general, the change of impedance during the modification process was measured by EIS experiments. The Faradaic impedance spectra achieved in each modification process were shown in *Figure 5.17*. The diameter of semicircle calculated from the Nyquist plot corresponds to the electron transfer resistance (*R*ct). As can be deduced from the impedance spectrum obtained at bare AuE, the transfer resistance was low owing to the very small semicircle. The *R*ct value showed a slight increase when AuE was modified with CuZnTe core-shell QDs, indicating the successful formation of the quantum dots on the surface of AuE (Shenouda, Sayed and Sayed, 2015). The *R*ct showed a decrease for antibody/CuZnTe core-shell/AuE, the reason might be attributed to the fact that the synthesized Antibody (HRP-Ab4) possessed high conductivity and good electron transfer efficiency (Zhang *et al.*, 2016). *R*ct increased after the block treatment to antibody/CuZnTe core-shell/AuE with BSA. In contrast, the linear portion coinciding with the diffusion limited electron shift occurred at comparatively lower frequencies. When the fabricated immunosensor was used for the detection of IFN-γ, *R*ct was found to increase furtherly owing to that BSA and IFN-γ protein layers on the electrode retards the electron transfer. The impedance changes of the modification process indicated that CuZnTe core-shell quantum dots, Antibody, BSA, IFN-γ had been successively assembled onto the Gold electrode (Arshad *et al.,* 2016). The performance of fabricated immunosensor for the determination of IFN-γ at different concentrations was observed and the results were shown in *Figure 5.18*. As shown from the Nyquist plots of impedance spectra below, the diameter of semicircle increased with increasing concentrations of the IFN-γ. As can be seen from the calibration curve (*Figure 5.19*) of IFN-γ, the *R*ct change displayed a linear relationship with logarithm of IFN-γ ranging from 2 to 10 ng/mL. Linear equations are $y=2.6286-0.027x$ ($R=0.9992$). In the present work, the lowest detectable concentration is 0.33 ng/mL (defined as $DL = 3SB/m$, where m is the slope of the corresponding calibration curve and SB is the standard deviation of the blank). One can find that the proposed sensor in this work presents a relatively large linear range and low detection limit. The results indicated that this signal amplification method was efficient for the ultrasensitive electrochemical detection of IFN-γ. Therefore, the proposed immunosensor was a suitable means to quantify IFN-γ concentration.

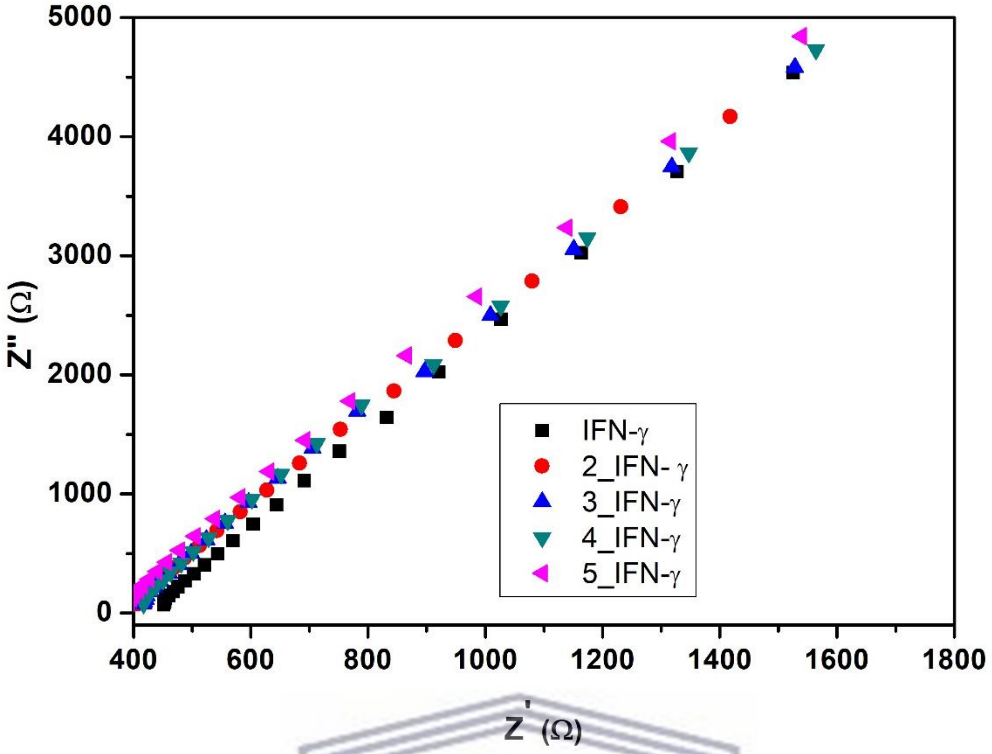

Figure 5.18: Impedance spectra of the as-prepared immunosensor upon incubated with different concentrations of IFN-γ (2, 4, 6, 8 and 10 ng/mL).

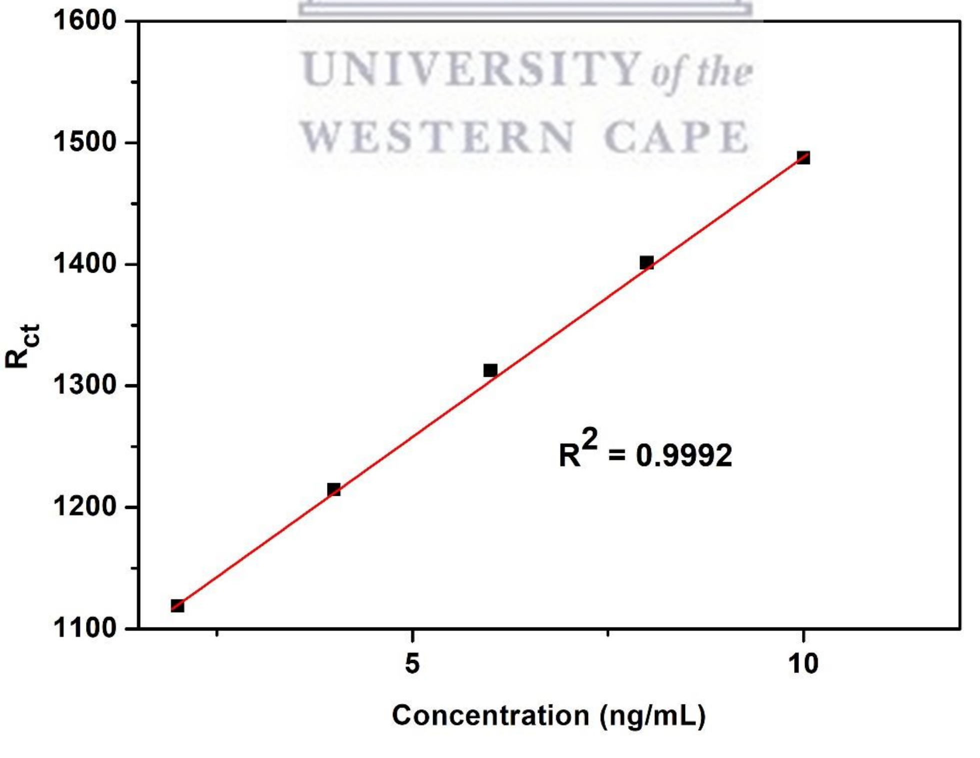

Figure 5.19: Calibration curve of the as-prepared immunosensor upon incubated with different concentrations of IFN-γ (2, 4, 6, 8 and 10 ng/mL).

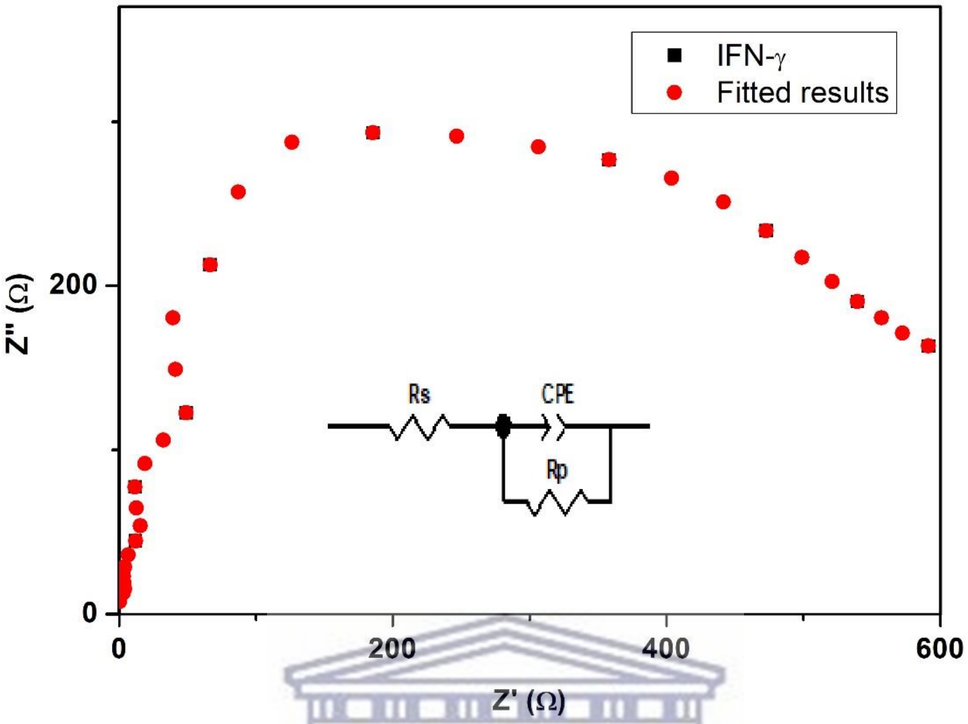

Zview software of Autolab was used to process impedance data on the base of Randles equivalent circuit. *Figure 5.20*, showed a modified Randles equivalent circuit and the corresponding fitted graph based on one measured spectrum, indicating that the circuit model was consistent with the measured system over the whole measured frequency range. The circuit consists of solution resistance (*R*s), Constant phase element (*CPE*), and solution resistance (*R*s). Usually, *R*s represents the bulk properties of electrolyte solution, and the CPE element represents a non-ideal capacitor and replaces the capacitance due to its roughness and heterogeneous surface (Ricardo Adriano Dorledo de Faria, Hassan Iden, Luiz Guilherme Dias Heneine, 2019). The impedance data was fitted to Randles equivalent circuit with a constant phase element (CPE) instead of classical capacitance due to the complicated interface between electrode and electrolyte in this study. The result also indicated that Rct is a suitable signal for sensing the interfacial properties of the prepared immunosensor during all these modification steps.

5.5 Conclusion

In conclusion, an electrochemical impedance immunosensor for label-free detection of IFN-γ was developed for the first time. The as-proposed immunosensor was fabricated using CuZnTe core-shell quantum dots modified Gold electrode (AuE) on which IFN-γ monoclonal antibody was immobilized. The novel immunosensor, equipped with prominently conductivity and biocompatibility of the quantum dots, is ideal for the development of electrochemical immunosensor. Anti-IFN-γ can be attached to the modified electrode and used to specifically recognize IFN-γ. The goal was to achieve an accurate analysis of samples using a sandwich immunoreaction. The sandwich-type immunosensor provided a convenient, low-cost, and novel method for specific and highly sensitive detection of IFN-γ. This immunosensor was easy to fabricate without complicated procedures or expensive instruments and exhibited an excellent performance. The resultant IFN-γ immunosensor demonstrated various advantages such as simple manipulation, ultrahigh sensitivity, excellent specificity, wide linear range, good reproducibility and stability as well. As indicated by the recovery experiments, the proposed immunosensor with high accuracy demonstrated potential usage in the detection of IFN-γ in practical samples. This is the first report of developing an electrochemical IFN-γ biosensor with a ternary surface in biosensor developed. This immunosensor is able to detect IFN-γ with a linear sensing region of 2 ng/ml to 10 ng/ml and lower detection limit of 0.33 ng/ml (method detection limit technique) in buffer solution. The ability of the biosensor to accurately detect IFN-γ in protein matrices without sample pre-treatment is well-suited for rapid in-field biosensor detection strategies. Therefore, this novel, facile strategy reported here may hold great promise for applications in the clinical diagnosis with further development. Compared with the ELISA, our sensor has a lower detection limit, and thus provides a new promising platform for clinical immunoassay.

References

Adegoke, O. *et al.* (2016) 'Biosensors and Bioelectronics An ultrasensitive SiO 2 - encapsulated alloyed CdZnSeS quantum dot-molecular beacon nanobiosensor for norovirus', *Biosensors and Bioelectronic*. Elsevier, 86, pp. 135–142. doi: 10.1016/j.bios.2016.06.027.

Arshad, A. *et al.* (2016) 'Aqueous synthesis of tunable fluorescent , semiconductor CuInS 2 quantum dots for bioimaging', *Arabian Journal of Chemistry*. The Authors, pp. 4–11. doi: 10.1016/j.arabjc.2016.10.002.

Asano, H. *et al.* (2017) 'Synthesis of colloidal Zn(Te,Se) alloy quantum dots', *Materials Research Express*. IOP Publishing, 4(10), pp. 0–10. doi: 10.1088/2053-1591/aa8b84.

Bhatia, S. K. *et al.* (1989) 'Use of thiol-terminal silanes and heterobifunctional crosslinkers for immobilization of antibodies on silica surfaces', *Analytical Biochemistry*, 178(2), pp. 408–413. doi: 10.1016/0003-2697(89)90662-3.

Chang, C. *et al.* (2012) 'Biosensors and Bioelectronics Amplified surface plasmon resonance immunosensor for interferon-Gamma based on a streptavidin-incorporated aptamer', *Biosensors and Bioelectronic*. Elsevier, 37(1), pp. 68–74. doi: 10.1016/j.bios.2012.04.038.

Chen, X., Liu, F. and Jiang, Q. (2012) 'Synthesis and Properties of Water-Soluble Silica-Coated ZnSe / ZnS Semiconductor Quantum Dots', pp. 6–11. doi: 10.1007/s10904-011-9606-3.

Christine, A. *et al.* (2016) 'The electrochemical behavior of core-shell CdSe / CdS magic-sized quantum dots linked to cyclodextrin for studies o .... The electrochemical behavior of core-shell CdSe / CdS magic-sized quantum dots linked to cyclodextrin for studies of the encapsulation of bioactive compounds', *Journal of Solid State Electrochemistry*. Journal of Solid State Electrochemistry, (April). doi: 10.1007/s10008-016-3221-8.

Claude, L. U. and Lyon, B. (2015) 'Development of electrochemical biosensors for environmental pollutant and food safety monitoring Zhenzhong Guo To cite this version : HAL Id : tel-01128300 Délivrée par'.

Crevel, R. Van, Ottenhoff, T. H. M. and Meer, J. W. M. Van Der (2002) 'Innate Immunity to Mycobacterium tuberculosis', 15(2), pp. 294–309. doi: 10.1128/CMR.15.2.294.

Dhar, R., Singh, S. and Kumar, A. (2015) 'Effect of capping agents on optical and antibacterial properties of cadmium selenide quantum dots', 38(5), pp. 1247–1252.

Ding, S. and Lu, M. (2018) 'Highly sensitive biosensors with interdigitated electrode arrays'.

Dingran Chang, Sandy Zakaria, Mimi Deng, Nicholas Allen, K. T. and Y. L. (2016) 'Integrating Deoxyribozymes into Colorimetric Sensing Platforms'. doi: 10.3390/s16122061.

Eleanor Adachi1, Idemudia John Airuoyo2, Lakshmi Krishna2, R. C. (2016) 'Developing a Process for Studying Annealing Effects on Mobilities in Silicon Quantum Dots', 1527(1986), p. 163111.

Gabriella, L. and Pacoste, C. (2017) 'Development of Copper Selenide Quantum Dots-Based Therapeutic Drug Monitoring Biosensors for Toremifene – In the Department of Chemistry , University of the Western Cape'.

Goletti, D. *et al.* (2016) 'Tuberculosis biomarkers : from diagnosis to protection', 8. doi: 10.4081/idr.2016.6568.

Grossi, M. and Riccò, B. (2017) 'Electrical impedance spectroscopy (EIS) for biological analysis and food characterization : a review', pp. 303–325.

Han, A. Z. *et al.* (2017) 'SC', *Sensors & Actuators: B. Chemical*. Elsevier B.V. doi: 10.1016/j.snb.2017.11.157.

Hossain, M. and Norazmi, M. (2013) 'Pattern Recognition Receptors and Cytokines in Mycobacterium tuberculosis Infection — The Double-Edged Sword ?', 2013.

Ishizaki, T. *et al.* (2005) 'An investigation into the effect of ionic species on the formation of ZnTe from a citric acid electrolyte', 50, pp. 3509–3516. doi: 10.1016/j.electacta.2004.12.028.

Li, G. *et al.* (2017) 'Evaluation of a New IFN- γ Release Assay for Rapid Diagnosis of Active Tuberculosis in a High-Incidence Setting', 7(April). doi: 10.3389/fcimb.2017.00117.

Liu, C. *et al.* (2015) 'An electrochemical aptasensor for detection of IFN-γ using graphene and a dual signal amplification strategy based on the exonuclease-mediated surface-initiated enzymatic polymerization', *Analyst*, 140(22), pp. 7784–7791. doi: 10.1039/c5an01591j.

Lu, L. *et al.* (2007) 'Raman analysis of CdSe / CdS core – shell quantum dots with different CdS shell thickness', 406221. doi: 10.1088/0953-8984/19/40/406221.

Lu, X. *et al.* (2019) 'Analytica Chimica Acta Target-driven switch-on fl uorescence aptasensor for trace a fl atoxin B1 determination based on highly fl uorescent ternary CdZnTe quantum dots', *Analytica Chimica Acta*. Elsevier Ltd, 1047, pp. 163–171. doi: 10.1016/j.aca.2018.10.002.

Musa, I., Qamhieh, N. and Said, K. (2019) 'Results in Physics Germanium antimony quantum dots morphology and Raman spectroscopy fabricated by inert gas condensation', *Results in Physics*. Elsevier, 13(April), p. 102311. doi: 10.1016/j.rinp.2019.102311.

Ndangili, P. M. (2011) 'Electrochemical and optical modulation of selenide and telluride ternary alloy quantum dots genosensors', (November).

Nwabisa, A. (2010) 'DEVELOPMENT OF ELECTROCHEMICAL ZnSe QUANTUM DOTS BIOSENSORS FOR LOW-LEVEL DETECTION OF 17 β -ESTRADIOL ESTROGENIC', (November).

Quyet Van Le, Jong Beom Kim, Soo Young Kim, Byeongdu Lee, and D. R. L. (2017) 'Structural Investigation of Cesium Lead Halide Perovskites for High-Efficiency Quantum Dot Light Emitting Diodes'. doi: 10.1021/acs.jpclett.7b01709.

Ram, C. *et al.* (2017) 'Computational study of leading edge jet impingement cooling with a conical converging hole for blade cooling', *ARPN Journal of Engineering and Applied Sciences*, 12(22), pp. 6397–6406. doi: 10.1039/b000000x.

Ricardo Adriano Dorledo de Faria, Hassan Iden, Luiz Guilherme Dias Heneine, T. M. & Y. M. (2019) '3-Aminophenylboronic Acid Functionalized Sensitive Glucose Detection'. doi: 10.3390/s19071686.

Sakai, R. T. *et al.* (2012) 'Progress in Organic Coatings Electrochemical study of TEOS , TEOS / MPTS , MPTS / MMA and TEOS / MPTS / MMA films on tin coated steel in 3 . 5 % NaCl solution', *Progress in Organic Coatings*. Elsevier B.V., 74(2), pp. 288–301. doi: 10.1016/j.porgcoat.2012.01.001.

Shenouda, A. Y., Sayed, E. and Sayed, M. El (2015) 'Electrodeposition , characterization and photo electrochemical properties of CdSe and CdTe', *Ain Shams Engineering Journal*. Faculty of Engineering, Ain Shams University, 6(1), pp. 341–346. doi:

10.1016/j.asej.2014.07.010.

Simão, E. P. *et al.* (2016) 'Biosensor based on cysteine monolayer and monoclonal antibody for specific detection of aflatoxin b1 in rice', *Journal of the Brazilian Chemical Society*, 27(6), pp. 1040–1047. doi: 10.5935/0103-5053.20150361.

Smith, I. (2003) 'Mycobacterium tuberculosis Pathogenesis and Molecular Determinants of Virulence', 16(3), pp. 463–496. doi: 10.1128/CMR.16.3.463.

Sovan Kumar Patra, BhavyaBhushanb and Priyam, A. (2016) 'Dalton Transactions'. doi: 10.1039/b000000x.

Tang, X. *et al.* (2017) 'Ultrathin and Highly Passivating Silica Shells for Luminescent and Water-Soluble CdSe/CdS Nanorods'. doi: 10.1021/acs.langmuir.7b00615.

'The SAXS Guide' (2013).

Varshney, R. *et al.* (no date) 'Characterization of Copper Nanoparticles Synthesized by a Novel Microbiological Method'.

Wang, M., Chen, Z. and Cao, C. (2014) 'Preparation of magnetic CuInS 2 – ZnS nanocomposites for bioimaging', 120, pp. 50–53. doi: 10.1016/j.matlet.2014.01.031.

Wang, X. *et al.* (2017) 'Fabrication of Electrochemical Immunosensor for Interferon- γ Determination and Its Application of Tuberculosis Diagnosis', 12(April 1993), pp. 7262–7271. doi: 10.20964/2017.08.67.

Wang, Y., Mazurek, G. H. and Alocilja, E. C. (2016) 'Measurement of Interferon Gamma Concentration Using an Electrochemical Immunosensor', 163(5), pp. 140–145. doi: 10.1149/2.0271605jes.

WHO (2015) 'Global Tuberculosis Report'.

Xia, J. *et al.* (2015) 'Biosensors and Bioelectronics Single electrode biosensor for simultaneous determination of inter- feron gamma and lysozyme', *Biosensors and Bioelectronic*. Elsevier, 68, pp. 55–61. doi: 10.1016/j.bios.2014.12.045.

Xingli Zou, X. L. and X. X. (2017) 'We are IntechOpen , the world ' s leading publisher of Open Access books Built by scientists , for scientists TOP 1 %'.

Ying Liu, Timothy Kwa, and A. R. (2012) 'NIH Public Access', 33(30), pp. 1–18. doi: 10.1016/j.biomaterials.2012.06.089.Simultaneous.

Zhang, B. *et al.* (2008) 'A novel method to enhance quantum yield of silica-coated quantum dots for biodetection'. doi: 10.1088/0957-4484/19/46/465604.

Zhang, Y. *et al.* (2015) 'Fabrication of an interferon-gamma-based ITO detector for latent tuberculosis diagnosis with high stability and lower cost'. doi: 10.1007/s10008-015-2936-2.

Zhang, Y. *et al.* (2016) 'Electrochemical immunosensor for interferon- γ based on disposable ITO detector and HRP-antibody-conjugated nano gold as signal tag', *Materials Science & Engineering C*. Elsevier B.V., 59, pp. 577–584. doi: 10.1016/j.msec.2015.10.066.

Zhong, X. *et al.* (2005) 'Glucose biosensor based on self-assembled gold nanoparticles and polymer onto gold substrate', 104, pp. 191–198. doi: 10.1016/j.snb.2004.04.114.

Zhou, J. G., Williams, Q. L. and Wu, R. (2010) 'Thioglycolic acid on the gold (111) surface and Raman vibrational spectra', *Journal of Chemical Physics*, 132(6), pp. 1–8. doi: 10.1063/1.3319711.

Zi, L. *et al.* (2014) ‘Thioglycolic acid-capped CuInS 2 / ZnS quantum dots as fluorescent probe for cobalt ion detection’, *Journal of Luminescence*. Elsevier, 148, pp. 359–363. doi: 10.1016/j.jlumin.2013.12.051.

Chapter six

Summary

This chapter revisits the specific objectives of the study to report whether the aims of this dissertation was achieved, and to give an overview of the success and shortcomings of the study. Also reported here is an indication of which areas of this study warrant further investigations in the future.

5.5 Conclusion

In this study, a rare chemistry of telluride has been explored as a source of precursor for synthesis of novel biocompatible and water soluble silica coated quantum dots. The telluride has also been used to tailor the optical and electrochemical properties of copper and zinc quantum dots. In the process, this study has introduced novel biocompatible and water soluble binary-capped (CuTe) and (ZnTe) quantum dots. One of the main problems encountered in the development of QD-based systems is the selection of a suitable capping ligand in order to achieve adequate solubility of QDs in the dispersion media. In the process of the aqueous synthesis, thiols were predominantly employed as the capping agents. Thioglycolic acid (TGA), was used in such synthesis where the thiol-end of the molecule binds to the particle surface, the other end-groups such as carboxylate (COO-) or hydroxide (OH) remains free, which imparts biocompatibility and opens up a window to interact and integrate with other biomolecules. A significant research effort has been devoted to prepare core-shell type QDs with a cross-linked shell that would protect the QDs much better than thiol-based coating. To protect the surface of the quantum dots the most widely used approach is silica coating. Silanization of quantum dots showed a great success in protecting their surface characteristics. The silanization of QDs was done in laborious process that goes through multiple steps. The first step involved was the activation of QD surface for attaching the first layer of silane molecules to QD surface. The (3-mercaptopropyl) trimethoxysilane (MPS) was used as the first layer of silica followed by thickening of the shell tetraethyl orthosilicate (TEOS). Electrostatic repulsion arising from functional groups on the surface of the quantum dot particles kept them non-agglomerated. Retention of the capping agent on the quantum dot surface was confirmed by FTIR studies, which showed characteristic bands related to C-H, C=O, Si-O-Si, Si-CH_2-S as well as –O-H groups. The electrochemical studies of the binary CuTe quantum dots, ZnTe quantum dots and the ternary CuZnTe core-shell quantum dots reveal that ternary quantum dots were stable and showed a significant enhancement in the conductivity of CuZnTe core-shell solution compared to that of CuTe and ZnTe, all studied in solution. The fluorescence and UV-vis studies of the quantum dots showed that the ternary quantum dots have distinctive band at 325 nm at it was the only one that had a red shift. After the addition of TEOS it increased to the longer wavelengths. With the SAXS, it was showed that the CuZnTe core-shell are the only quantum dots do not agglomerate after the addition of the capping reagents, also it showed a very narrow tube that indicated that the quantum dots are uniform. These results were in correlation with TEM results that showed that the ternary quantum dots do not agglomerate and also they are uniformly dispersed. Successful detection of the studied analytes on the binary and ternary quantum dot platforms widens the scope of biocompatible nanostructured platforms upon which other biomolecules of interest can be immobilized for a wide range of analytical purposes. In this work, a QDs-based electrochemical biosensor was successfully constructed for the detection of Interferon gamma in aqueous solution. The CuZnTe core-shell QDs contributed to retaining the antibody properties in immobilizer. This was confirmed through cyclic voltammetry studies. We demonstrated the feasibility of the immunosensor by measuring the amount of IFN-γ in samples with known concentrations. This immunosensor was easy to fabricate without complicated procedures or expensive instruments and exhibited an excellent performance. The resultant IFN-γ immunosensor demonstrated various advantages such as simple manipulation, ultrahigh sensitivity, excellent specificity, wide linear range, good reproducibility and stability as well. We observed a linear relationship between the electrochemical signal and IFN-γ concentration from 2 ng/mL to 10 ng/mL and lower detection limit of 0.33 ng/ml (method detection limit technique) in buffer solution. Specificity was high and measurement of IFN-γ concentrations took less time than one reported before. A high-sensitivity biosensor for IFN-γ such as the one described in this work can be used in a variety of medical and biological applications. Blood and serum IFN-γ levels have been used to monitor the progression of diseases such as tuberculosis and malaria. IFN-γ levels of tuberculous in patients, for instance, have been shown to be around 1048pg/mL before treatment and 2233pg/mL after treatment. The fact that our sensor requires a very small sample volume and gives an almost instantaneous result makes it convenient in medical settings. This biosensor platform provides advantage of not only chemical stability, but also the ability to be extended to other related targets. Because antibody can be generated for such a wide variety of targets – ions, peptides, viruses, etc. – one would only need to change the antibody while keeping the rest of the sensor identical in order to detect another analyte of interest. The proposed sensor therefore has a potential application in medical diagnostics, infectious disease monitoring and biomedical applications. These characteristics suggest that, with optimization, this immunosensor may have clinical utility. This makes the sensor more suitable for determining the presence of IFN-γ in a sample, rather than determining the exact concentration of the sample. This could contribute to reduce waiting times which is beneficial both to patients and doctors involved, as well as cost-effective.

5.5 Recommendations for future studies

The following aspects of the electro-biosensors for the determination of Interferon gamma, a first line tuberculosis treatment drug presented in this work warrant further investigations:

- More work needs to be done to improve the electro-activity of sensor through the synthesis of higher generations.

- It would a great work if the work could be done without the use of antibody.

- Work on the material to check if it is good for people with different metabolisms.

- Test the sensor to see if it will be good for other disease.